eman ta zabal zazu

Universidad del País Vasco

Euskal Herriko Unibertsitatea

# The Role of Graphene for Advanced Electrochemical Energy Storage Devices

**Doctor of philosophy**

by

**Juan Luis Gómez Urbano**

Thesis supervisors:

**Prof. Teófilo Rojo**

**Dr. Daniel Carriazo**

**Leioa 2022**

Universidad del País Vasco Euskal Herriko Unibertsitatea | NAZIOARTEKO BIKAINTASUN CAMPUSA CAMPUS DE EXCELENCIA INTERNACIONAL

| TESI ZUZENDARIAREN BAIMENA TESIA AURKEZTEKO | AUTORIZACIÓN DEL/LA DIRECTORA/A DE TESIS PARA SU PRESENTACIÓN |
|---|---|

Zuzendariaren izen-abizenak /Nombre y apellidos del director: Teófilo Rojo Aparicio

IFZ /NIF: 14887108J

Tesiaren izenburua / Título de la tesis: The role of graphene for advanced electrochemical energy storage devices

Doktorego programa / Programa de doctorado: Ciencia y Tecnología de los Materiales

Doktoregaiaren izen-abizenak / Nombre y apellidos del/la doctorando/a: Juan Luis Gómez Urbano

| | |
|---|---|
| Unibertsitateak horretarako jartzen duen tresnak emandako ANTZEKOTASUN TXOSTENA ikusita, baimena ematen dut goian aipatzen den tesia aurkez dadin, horretarako baldintza guztiak betetzen baititu. | Visto el INFORME DE SIMILITUD obtenido de la herramienta que a tal efecto pone a disposición la universidad, autorizo la presentación de la tesis doctoral arriba indicada, dado que reúne las condiciones necesarias para su defensa. |

Tokia eta data / Lugar y fecha: Leioa, 16/12/2021

TEOFILO ROJO APARICIO - 14887108J

Firmado digitalmente por TEOFILO ROJO APARICIO - 14887108J
Fecha: 2022.01.24 12:39:46 +01'00'

Sin. / Fdo.: Tesiaren zuzendaria / El/La director/a de la tesis

Universidad del País Vasco | Euskal Herriko Unibertsitatea

NAZIOARTEKO BIKAINTASUN CAMPUSA
CAMPUS DE EXCELENCIA INTERNACIONAL

| TESI ZUZENDARIAREN BAIMENA TESIA AURKEZTEKO | AUTORIZACIÓN DEL/LA DIRECTORA/A DE TESIS PARA SU PRESENTACIÓN |
|---|---|

Zuzendariaren izen-abizenak /Nombre y apellidos del director: Daniel Carriazo Martín

IFZ /NIF: 07877188X

Tesiaren izenburua / Título de la tesis: The role of graphene for advanced electrochemical energy storage devices

Doktorego programa / Programa de doctorado: Ciencia y Tecnología de los Materiales

Doktoregaiaren izen-abizenak / Nombre y apellidos del/la doctorando/a: Juan Luis Gómez Urbano

| | |
|---|---|
| Unibertsitateak horretarako jartzen duen tresnak emandako ANTZEKOTASUN TXOSTENA ikusita, baimena ematen dut goian aipatzen den tesia aurkez dadin, horretarako baldintza guztiak betetzen baititu. | Visto el INFORME DE SIMILITUD obtenido de la herramienta que a tal efecto pone a disposición la universidad, autorizo la presentación de la tesis doctoral arriba indicada, dado que reúne las condiciones necesarias para su defensa. |

Tokia eta data / Lugar y fecha: Vitoria, 15/12/2021

Sin. / Fdo.: Tesiaren zuzendaria / El/La director/a de la tesis

Universidad del País Vasco Euskal Herriko Unibertsitatea

NAZIOARTEKO BIKAINTASUN CAMPUSA
CAMPUS DE EXCELENCIA INTERNACIONAL

# AUTORIZACIÓN DE LA COMISIÓN ACADÉMICA DEL PROGRAMA DE DOCTORADO

La Comisión Académica del Programa de Doctorado en Ciencia y Tecnología de los Materiales en reunión celebrada el día 15 de Diciembre de 2021, ha acordado dar la conformidad a la presentación de la Tesis Doctoral titulada: *The role of graphene for advanced electrochemical energy storage devices*, dirigida por el Dr. Teófilo Rojo Aparicio y el Dr. Daniel Carriazo Martín, y presentada por D. Juan Luis Gómez Urbano adscrito al Departamento de Química Orgánica e Inorgánica

En Leioa a 15 de Diciembre de 2021

EL/LA RESPONSABLE DEL PROGRAMA DE DOCTORADO

LUIS MARIA LEZAMA DIAGO

Firmado digitalmente por LUIS MARIA LEZAMA DIAGO
Nombre de reconocimiento (DN): c=ES, o=UPV - EHU, ou=PDI, ou=Ziurtagiri onartua - Certificado reconocido, ou=Ziurtagiri korporatibo onartua - Cert. corporativo reconocido, ou=Condiciones de uso en www.izenpe.com nola erabili jakiteko, dnQualifier=-dni 30580768Z -cif Q4818001B, cn=LUIS MARIA LEZAMA DIAGO, givenName=LUIS MARIA, sn=LEZAMA, serialNumber=30580768Z
Fecha: 2021.12.22 15:51:54 +01'00'

Fdo.: Luis María Lezama Diago

Universidad del País Vasco Euskal Herriko Unibertsitatea

NAZIOARTEKO BIKAINTASUN CAMPUSA
CAMPUS DE EXCELENCIA INTERNACIONAL

**AUTORIZACIÓN DEL DEPARTAMENTO**

El Consejo del Departamento de Química Orgánica e Inorgánica en reunión celebrada el día 21 de enero de 2022 ha acordado dar la conformidad a la admisión a trámite de presentación de la Tesis Doctoral titulada: *The role of graphene for advanced electrochemical energy storage devices* dirigida por el Dr. Teófilo Rojo Aparicio y el Dr. Daniel Carriazo Martín y presentada por D. Juan Luis Gómez Urbano ante este Departamento.

En Leioa a 21 de enero de 2022

VºBº DIRECTORA DEL DEPARTAMENTO

IZASKUN GIL DE MURO ZABALA - 30644624E

Firmado digitalmente por IZASKUN GIL DE MURO ZABALA - 30644624E
Fecha: 2022.01.21 12:20:11 +01'00'

Fdo.: Izaskun Gil de Muro Zabala

SECRETARIA DEL DEPARTAMENTO

MARIA ISABEL MORENO BENITEZ - 29034387S

Firmado digitalmente por MARIA ISABEL MORENO BENITEZ - 29034387S
Fecha: 2022.01.21 12:42:44 +01'00'

Fdo.: María Isabel Moreno Benítez

Universidad del País Vasco Euskal Herriko Unibertsitatea

NAZIOARTEKO BIKAINTASUN CAMPUSA
CAMPUS DE EXCELENCIA INTERNACIONAL

# ACTA DE GRADO DE DOCTOR O DOCTORA
# ACTA DE DEFENSA DE TESIS DOCTORAL

DOCTORANDO DON. Juan Luis Gómez Urbano

TITULO DE LA TESIS: The Role of Graphene for Advanced Electrochemical Energy Storage Devices

El Tribunal designado por la Comisión de Postgrado de la UPV/EHU para calificar la Tesis Doctoral arriba indicada y reunido en el día de la fecha, una vez efectuada la defensa por el/la doctorando/a y contestadas las objeciones y/o sugerencias que se le han formulado, ha otorgado por_____la calificación de:

*unanimidad ó mayoría*

| |
|---|
| |

*SOBRESALIENTE / NOTABLE / APROBADO / NO APTO*

Idioma/s de defensa (en caso de más de un idioma, especificar porcentaje defendido en cada idioma):

Castellano _____

Euskera _____

Otros Idiomas (especificar cuál/cuales y porcentaje) _____

En _____a _____de _____de _____

EL/LA PRESIDENTE/A, EL/LA SECRETARIO/A,

Fdo.: Fdo.:

Dr/a: _____ Dr/a: _____

VOCAL 1º, VOCAL 2º, VOCAL 3º,

Fdo.: Fdo.: Fdo.:

Dr/a: _____Dr/a:_____Dr/a:_____

EL/LA DOCTORANDO/A,

Fdo.: _____

*“Patria est, ubicumque bene est”*

# Acknowledgments

Al final de este camino sólo me queda agradecer a todos aquellos que me han acompañado y lo han hecho posible. Por suerte tengo mucho que agradecer.

En primer lugar, quiero agradecer al CIC energiGUNE, dónde he pasados los últimos seis años. Así mismo, agradezco a la UPV/EHU y en especial a **Luis Lezama** por su disponibilidad, accesibilidad, pronta respuesta y simpatía. Quiero agradecer a mis directores **Prof. Teófilo Rojo** y **Dr. Daniel Carriazo** por darme la oportunidad de iniciar mi carrera investigadora, al igual que al Ministerio Universidades por el contrato pre-doctoral (FPU16/03498) y la ayuda asociada para estancias breves (EST19/00316).

Quiero dar un doble agradecimiento al Dr. Daniel Carriazo por tantos buenos consejos científicos y por poder haber sido el principal apoyo sobre el que se ha sustentado este trabajo. Así como a Dani, no quiero olvidar agradecer a las primeras personas que me formaron y a los que considero mis mentores. A **Juan Luis Gómez Cámer** por enseñarme perseverancia y electroquímica; a **Noel Diez** por enseñarme buen humor y ciencia de los materiales; y a **Cristina Botas** por enseñarme valentía y casi todo lo que sé sobre el grafeno.

Gracias a todos mis compañeros del CIC, a los que están y a los que se han ido, por hacer que los momentos difíciles, no lo parezcan tanto. Gracias a **Mikel Iturriza** por ser la primera persona que puedo considerar mi amigo en Vitoria; a **Xabi** por el humor negro; a **Jose Coca** por compartir inquietudes sobre Cthulu; a **Esti** por los aceituneros de Jaén y las socis; a **Ainhoa** por su vitalidad; a **Carlos** por ser los ganadores de los cócteles navideños; a **Nicola** por tantos días en terrazas y por la fuerza a través de la alegría; a **María Jáuregui** por tantos rayos y Kurt; a **María Echeverría** por las fotos y echarnos unas risas en los pitis; a **Fran** también por las fotos y por los días de conversaciones interesantes; a **Marina**, a **Roshan**, a **Emanuele**, a **Marian**, a **Sergio**, a **Mikel Arrese**, a **Eku**, a **Alex**, a **Oier Arcelus**, a **Oier Lakuntza**, a **Pierre**, a **Silvia**, a **Sona**, a **María Martínez**, a **Gene**, a **Nahom**, a **Montse Garcelán**, a **Montse Casas**, a **Sergio**, a **Joseba** y a todos los que me dejo sin nombrar

Un especial agradecimiento a los miembros del grupo de Supercaps por haber trabajado codo con codo conmigo durante todos estos años y haberme hecho entender cómo de importante es la colaboración y el buen ambiente en la

investigación. Gracias a **Gelines** por ser mi principal compañera durante todo este proceso; a **Miguel** por la atmósfera de tranquilidad que crea a su alrededor; a **María Arnaiz** porque me debe un salmorejo; a **Jon Ajuria** por su actitud hacia la vida y la ciencia; a **Roman** por compartir conmigo su punto de vista realista sobre la ciencia; y a **Violeta** por insuflar nueva vida al grupo con su fuerza.

I'm also very grateful for the days I spent during my stay in Jena at the group of Prof. Andrea Balducci. Special thanks to **Andrea Balducci** for accepting me in his group, for his kindness and for building such a great working atmosphere. Thanks to **Timo** and **Annika** for making me feel like at home in Jena, to **Christian** for all he taught me and his constant nice mood; to **Sandesh** for his strength and perseverance; to **Fabian** for the Schnitzel; to **Lukas M.** for being such a great person, to **Lukas K.** for the code and to **Binson** for the walks home. Sorry for all the people I forgot to mention, I'm quite happy to have spent three months there with you. Danke schön!

Gracias a mi familia por haberme hecho como soy, por haber estado siempre ahí apoyándome y mandándome ánimos desde la distancia. Gracias a mis amigos de la Rambla con los que he crecido; a **Pérez** por ser un pilar al que volver, a **Lasas** por inspirarme sin que él lo sepa, a **Víctor** por tocar la guitarra mal, a **Fali** por cortarse el pelo, a **Parra** por enseñarme que muchas veces es mejor estar callado que decir tonterías, a **Fernández** por ser un ejemplo de superación, a **Puli** por haber compartido conmigo tantos momentos musicales y a **María Jiménez** por el viaje a Senegal que nos espera. Espero que la vida siga sin separar nuestros caminos como no lo ha conseguido hasta ahora a pesar de la distancia y el tiempo.

También a los amigos que encontré en Vitoria y que han hecho que me sienta como en casa. En especial a **Álvaro**, amigo es una palabra que se queda corta para describirte, gracias por hacerme no entender, sino sentir, que la verdadera patria son los amigos. Gracias **Andrés** por tus inventos, tantas videollamadas, tu humor y nuestro futuro empresarial. A **Kenari**, **Roger**, a **Justo**, a **Diego**, a **Sarai**, a **Mikel**, a **Alberto** y a **Oscar**.

Dejo para el final el mayor agradecimiento a **Iciar**: amiga, compañera de trabajo, pareja y tantos otros títulos que necesitaría otra tesis para enumerar. Nunca voy a olvidar que tú siempre estuviste a mi lado durante toda esta etapa. Gracias por ser en gran parte la fuerza que me impulsa. Gracias por enseñarme tanto sin pretenderlo. Gracias por ser una parte tan importante de mi vida.

Gracias a todos.

# Summary

Novel energy storage devices beyond Li-ion are emerging in order to meet the ever-growing energy demand of our society. However, most of these technologies are under development and still face some important challenges such as long-term stability. For this purpose, it is very important to find new active materials specifically adapted to overcome the drawbacks associated to each technology. Among them, graphene oxide is a promising candidate due to its easy manufacture, outstanding mechanical properties and great tunability. Within this context, this thesis explores the impact that the integration of graphene oxide and its derivatives have on the performance of different energy storage systems; namely lithium-sulfur batteries, sodium-oxygen batteries, supercapacitors and lithium-ion hybrid capacitors. State of the art, fundaments framework and objectives are included in the **Chapter I**.

**Chapter II** focuses in the preparation of graphene-based composites with high sulfur loadings and its application as cathodes for high-energy and long cycle life Lithium-Sulfur batteries. The graphene sheets wrap the sulfur particles with the aim of circumvent some of the drawbacks associated to this technology. In **Section 2.2**, hydrothermally reduced graphene oxide/sulfur composites are prepared, whereas submicrometer-sized sulfur particles are produced by a green and scalable method. The resulting composites exhibit improved stability while retaining most of the initial capacity, even if the amount of sulfur in the cathodes is higher than that usually reported in the state-of-the-art. This section is adapted from the research article "*Hydrothermally reduced graphene oxide for the effective wrapping of sulfur particles showing long term stability as electrodes for Li-S batteries*" published in Carbon (2018). In **Section 2.3**, with the aim of increasing the sulfur loading of the composites, graphene-based aerogels are explored as sulfur conductive matrix. Either the incorporation of carbon nanotubes or the thermal reduction of the graphene leads to a significant improvement of the areal capacity of the cathodes. This section is adapted from the research article "*Graphene oxide-carbon nanotubes aerogels with high sulfur loadings suitable as binder-free cathodes for high performance lithium-sulfur batteries*" published in Journal of Power sources (2019).

**Chapter III** explores the use of three-dimensional graphene architectures as electrocatalyst to host the reaction in the Sodium-Oxygen batteries. In this chapter the cycle life of the battery is extended due to the addition of graphene. Pore size

distribution of graphene-based oxygen cathodes show to have a great influence over the electrochemical performance of Na-$O_2$ batteries in terms of cycle life, delivered capacity and energy efficiency. Especially, a quick freezing of the GO suspension guarantee the presence of active sites for ORR and OER reactions and provides enough channels for the diffusion of $O_2$ and $Na^+$ ions. This chapter is adapted from the research article "*Pathways towards high performance Na–$O_2$ batteries: tailoring graphene aerogel cathode porosity & nanostructure*" published in Journal of Materials Chemistry A (2019).

In **Chapter IV** activated carbon-graphene composites are developed from cigarette filter wastes and its potential as electrodes for high energy EDLCs is investigated. The incorporation of graphene into the carbon composites does not only increase its electronic conductivity but it also induces morphological and textural changes that favor the adsorption/desorption of electrolyte ions. The use of ionic liquids as electrolyte along with the wide pore size distribution of the graphene-activated carbon allows a stable performance even at 3.4 V. This chapter is adapted from the research article "*Nanostructured carbon composites from cigarette filter wastes and graphene oxide suitable as electrodes for 3.4 V supercapacitors*" published in Batteries & Supercaps (2021).

**Chapter V** is devoted to the preparation of carbon composites from the pyrolysis and activation of coffee waste and graphene oxide, and their evaluation as potential electrodes for dual-carbon lithium-ion capacitors. The energy, power and cyclability output of the LIC are enhanced due to the exhaustive optimization of some important parameters such as particle size, electronic conductivity or mass loading of the battery-type electrode; and the optimum combination of specific surface area and pore size distribution for the capacitor-type electrode. This chapter is adapted from the research article "*Graphene-coffee waste derived carbon composites as electrodes for optimized lithium ion capacitors*" published in Carbon (2020).

**Chapter VI** includes an overview of the work, the conclusions and a perspective about the potential use of graphene in energy storage systems.

# Table of contents

# Chapter I. Introduction and objectives



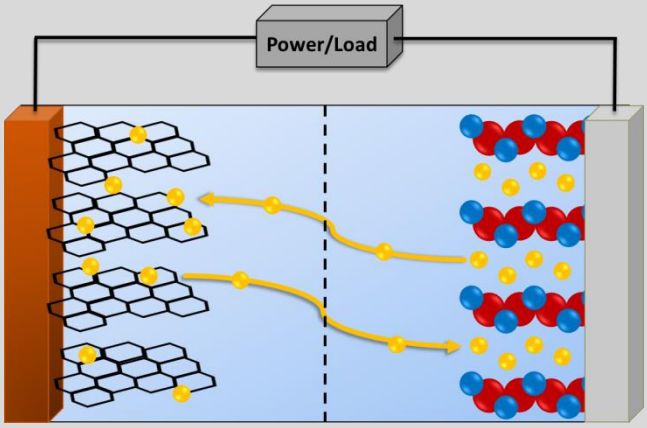

## 1.1. Energy Storage

Reliable energy supply is of paramount importance in our society to carry out daily activities such as heating, lighting, or transportation. Since XIX century, the exponentially-growing global energy demand has being mainly covered by the use of fossil fuels. However, our dependence on these fuels is associated to some important issues such as their limited availability, its geopolitical dependence and also to the environmental concerns derived from the pollutants evolved through their combustion [1,2]. On this regard, the oil's crisis of the 80's pushed the development of alternative renewable energy sources such as solar, wind or geothermal energy. However, renewable energies are intermittent and strongly depend on the weather conditions. As an illustrative example, the energy peak produced through solar energy is shifted with respect to the maximum of the energy demand (**Figure 1.1**).

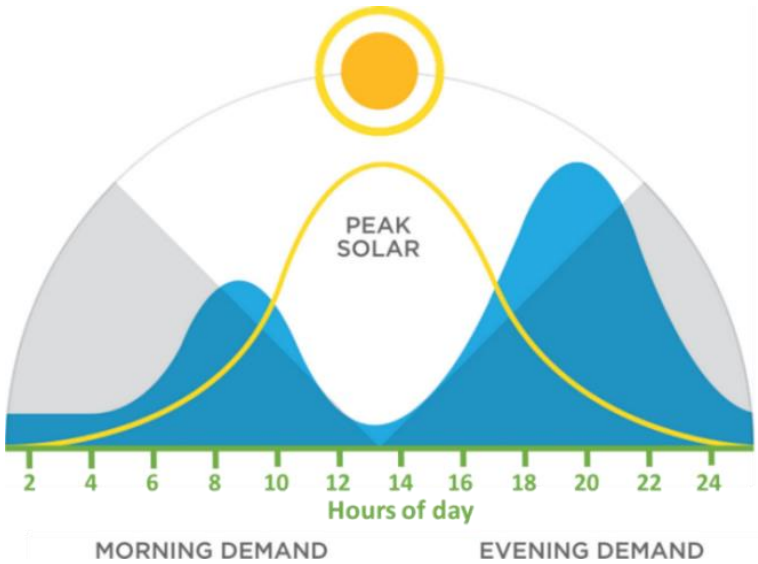


***Figure 1.1.*** *Energy demand and maximum solar energy generation during daily hours (modified from [3]).*

Energy storage systems (ESS) are the solution for this production/demand mismatching, which limits the expansion of renewable energies at global scale. Moreover, ESS can support services for consumers during power crises due to natural disasters, as well as lessens the prices of electricity to support the peak demand by

storing energy during off peak hours at low cost [4]. Additionally, ESS will play a crucial role on the replacement of conventional internal combustion engine-run vehicles by electric vehicles (EVs), contributing on the reduction of greenhouse gases emission and the pollution levels in big cities [5,6]. ESS can be classified regarding the use of energy in a specific form: mechanical, electrochemical, electrical or thermal [7].

Electrochemical energy storage (EES) devices involve the reversible transformation from electrical to chemical energy and vice versa. The main representatives of this type of systems are secondary (rechargeable) batteries, which are used to power most of the portable electronic devices (laptops, cell phones, etc.) or as starter in vehicles. Complementary to rechargeable batteries, electrochemical capacitors [8], offer a much higher power density and work without interruption for an almost unlimited lifespan. Electrochemical capacitors are generally found in high power applications since they can release a large amount of energy in a short period of time (starter systems for EVs, microelectronics, defibrillators or camera flash) [9].

Own to their features, electrochemical capacitors and secondary batteries have been appointed as the main candidates to promote the use of renewable energy sources and EVs to attain a sustainable energy development of our society [10].

## 1.2. Batteries

Batteries are devices that store the energy through chemical reactions. They are classified into primary batteries and secondary batteries. In the former ones the energy is released as electricity only once and after that the battery is “dead”. In the last ones, also known as rechargeable batteries the electrochemical process is, up to some extent, reversible. Chemical species can be electrochemically regenerated, or charged, to its initial state by running a current into the battery, converting electric energy in chemical energy ready to be released again. Cells are considered the electrochemical units and batteries usually contain a stack of them connected in series or parallel. Cells are formed by a cathode and an anode separated by a membrane embedded in an electrolyte [11]. The term cathode refers to the electrode where reduction process occurs, while term anode is used for the electrode where the oxidation redox reaction takes place. However, in secondary batteries, this classification can lead to confusion, because the electrodes known as “anode” and “cathode” should be adapted to the charge or discharge processes. For this reason, it

is more appropriate to name them as negative and positive electrode, on the basis of the electric potential values. But it should be also kept in mind that in most of the published works, the term “anode” and “cathode” are directly correlated to the negative and positive electrodes, respectively.

A schematic representation of a battery operation is depicted in **Scheme 1.1**. During the discharge step, the active materials in the negative electrode are oxidized. The ions move internally along the electrolyte and diffuse through the separator membrane to the positive electrode, where reduction reactions take place; simultaneously, electrons move through the external circuit to the positive electrode, giving rise to an electric current. Upon charge, electrons are forced to move in the opposite way, producing the inverse redox reactions.

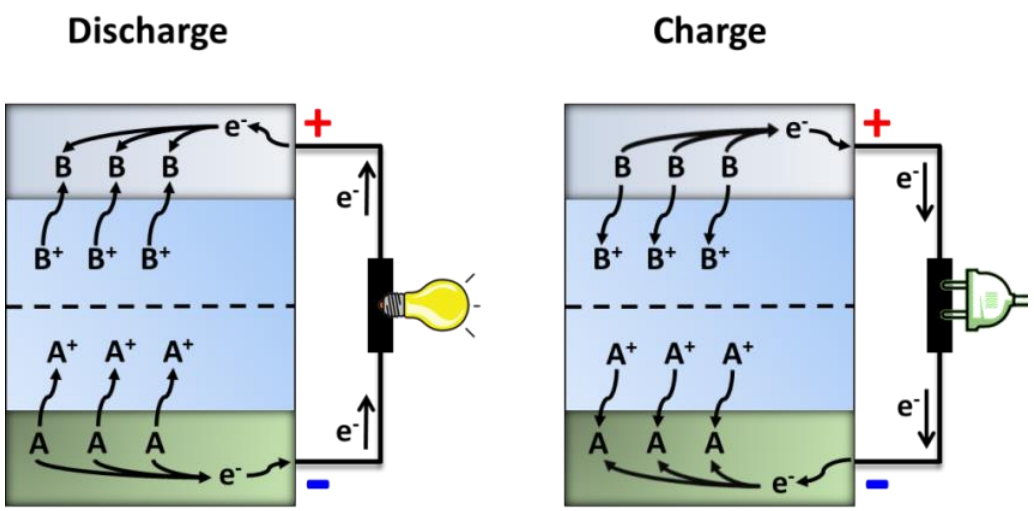


***Scheme 1.1.*** *Generic operation model for a battery during discharge and charge*

The term capacity refers the amount of charge that can be stored in a battery and it is expressed in coulombs (C) or in ampere hour (Ah), whereas 1C= 1As = 1/3600 Ah. Generally, the capacity delivered by a given active material is normalized per its mass ($C_g$= Ah $g^{-1}$). The maximum achievable capacity or theoretical capacity ($C_{theo}$) can be calculated according to Faraday’s law as follows:

$$C_{theo} = \frac{F \cdot n_e}{MW_{AM}} \quad (1.1)$$

Where $MW_{AM}$ is the molecular weight of the active material, $n_e$ is the number of electrons involved in the reaction and F is the Faraday's constant. However, the theoretical capacity is rarely achieved due to many different factors such as side reactions, internal resistance of the cell or active materials polarization. Experimental capacity ($C_{exp}$) is calculated form the charge/discharge time (in hours) measured from the galvanostatic charge/discharge curves registered at a constant current density (A $g^{-1}$).

$$C_{exp} = \left(\frac{A}{g}\right) \cdot (h) = \frac{Ah}{g} \quad (1.2)$$

The current density applied during galvanostatic measurements is commonly expressed in terms of C-rate like:

$$I_g = M \cdot C_{theo} \quad (1.3)$$

Where $I_g$ is the gravimetric current density in A $g^{-1}$ and M is a multiple or fraction of $C_{theo}$. As an example, an electrode in which $C_{theo}$ is 372 mAh $g^{-1}$, the rates 1C and 0.1C correspond to current densities of 372 and 37.2 mA $g^{-1}$, respectively.

Theoretical energy of a single cell ($E_{theo}$) is the product of the capacity and the cell voltage.

$$E_{theo} = C_{theo} \cdot V_{theo} \quad (1.4)$$

Cell voltage ($V_{theo}$) can be calculated from the individual theoretical potential of each of the active materials included in the cell.

$$V_{theo} = E^0_{Cathode} - E^0_{Anode} \quad (1.5)$$

In a simplified case under ideal conditions, the discharge of the battery proceeds at the theoretical voltage until the active materials are consumed and the capacity is fully extracted, leading to an abrupt voltage drop to 0 V (**Scheme 1.2a**). However, in a real

system, the voltage measured under discharge load, is lower than the theoretical voltage due to internal resistance of the cell as well as polarization effects at both electrodes. A plateau is generally observed in the voltage curve when the effect of change in reactants and reaction products is minimal until the active materials are nearly exhausted (**Scheme 1.2b**). A multi-step curve, showing more than one plateau region, is characteristic of electrochemical systems in which a change in the reaction mechanism and reduction potential of the active materials occurs (**Scheme 1.2c**). A slopping region is typical when the composition of the active materials, reactants, internal resistance etc. changes upon cell discharge (**Scheme 1.2d**).

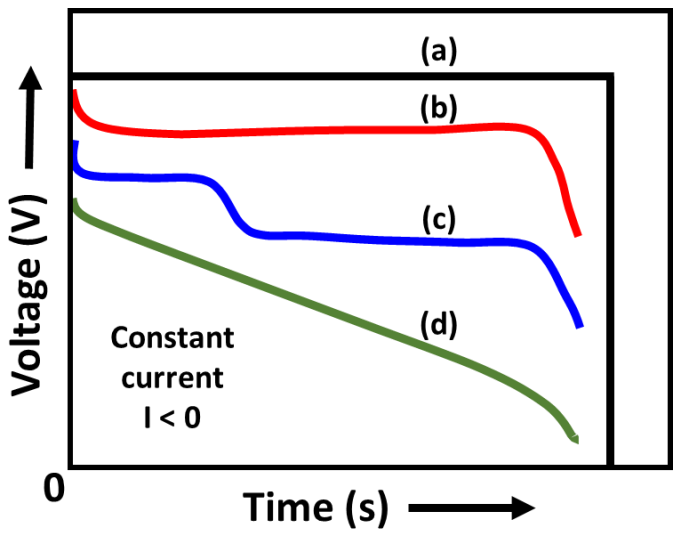


***Scheme 1.2.*** *Characteristic galvanostatic discharge curves of batteries.*

As above discussed, neither theoretical voltage nor theoretical capacity can be experimentally reached. Thus, the theoretical energy density cannot be either achieved [12].

### 1.2.1. Lithium-ion batteries

Since Sony commercialized the first lithium-ion battery (LiB) in 1991, they have been the most commonly used energy storage technology in portable electronics and cordless devices. LIBs show higher energy density, higher voltage and lower self-discharge compared to other energy storage systems. These features are associated to some intrinsic cell components. Lithium is the third lightest element and has one of the smallest ionic radii of any single charged ion, enabling a good diffusion of the lithium ions into the active materials in the electrodes. It has the lowest reduction potential of any element, allowing Li-based batteries to have the highest possible cell potential [13].

Most commercially available lithium-ion batteries contain a carbonaceous material as negative electrode, a layered $LiMO_2$ (M=Co, Mn, Ni) compound as positive electrode and a lithium-containing salt dissolved in organic solvent as electrolyte. During discharge, $LiMO_2$ is at some extent delithiated (**equation 1.6**) while lithium ions are intercalated in the carbon-based matrix (**equation 1.7**) in the negative electrode. Opposite reactions take place during charge. This simultaneous intercalation-deintercalation of lithium ions in both electrodes is the reason why lithium-ion batteries are sometimes denoted as “rocking chair” batteries [14].

$$LiMO_2 \rightleftarrows Li_{1-x}MO_2 + xLi^+ + xe^- \quad \textbf{(1.6)}$$

$$xe^- + nC + xLi^+ \leftrightarrows Li_xC_n \quad \textbf{(1.7)}$$

Among the different carbonaceous materials that can be selected as negative electrode, graphite is the most commonly used due to its low price, chemical stability and low reduction potential. On the other hand, $LiCoO_2$, one of the first commercialized cathodes for LiBs, is still present in most commercial devices due to its high reliability, moderate theoretical gravimetric capacity and high operation potential. Regarding the electrolyte, lithium hexafluorophosphate ($LiPF_6$) dissolved in a mixture of carbonate-based solvents, is mostly employed [15]. Diagram of a conventional LIB is depicted in **Scheme 1.3**.

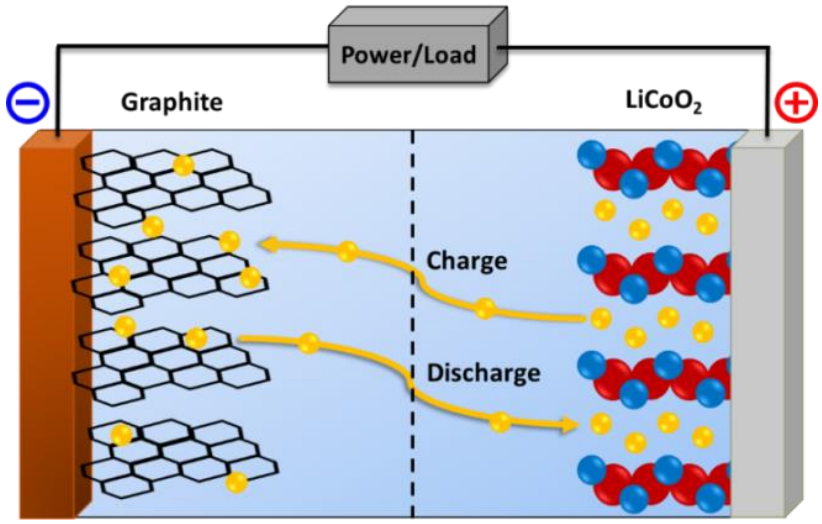


***Scheme 1.3.*** *Operation of a conventional Lithium-ion battery.*

However, besides the aforementioned advantages, conventional lithium-ion batteries based on the $Li^+$ intercalation mechanism cannot provide the fast charge needed for certain number of applications. In addition, the use of critical raw materials such as cobalt hinders their global use in stationary and grid storage applications. Research on new materials for the anode and cathode side and exploring new battery chemistries will play a crucial role on the development of a more efficient, cheaper and environmentally friendly new generation of batteries. Among them, sodium-ion batteries, lithium-sulfur batteries, metal-oxygen batteries or redox-flow batteries can be mentioned as the most representative ones [16].

### 1.2.2. Lithium-sulfur batteries

Lithium-sulfur (Li-S) batteries use sulfur as the positive electrode, metallic lithium as the negative electrode and a lithium containing organic salt as electrolyte. The replacement of metal oxide intercalation cathodes by elemental sulfur, $S_8$, provides some advantages. First, regardless the bad reputation of sulfur, it is a non-toxic substance, since not mutagen or carcinogenic effects have been reported, and continuous exposition to low amounts is recognized as safe [17]. Second, sulfur is cheap and is one of the most abundant elements in the earth's crust. Moreover, sulfur

is a major by-product of oil refining and gas processing; crude oil grades contain sulfur that has to be removed through purification processes to fulfil the refined products standards [18]. Third, and most important, the theoretical specific capacity of sulfur is very high (1,675 mAh $g^{-1}$) since two electrons are shared in the course of the electrochemical reaction and the molecular weight of sulfur is relatively low. Combined with the high theoretical capacity of metallic lithium (3,861 mAh $g^{-1}$), Li-S batteries exhibit one of the highest theoretical gravimetric energy densities among all the battery chemistries (ca. 2,600 Wh $Kg^{-1}$). Therefore, Li-S batteries are considered among the most promising next generation of lithium batteries [19,20]. Some relevant parameters for Li-ion and Li-S cathodes are listed in **Table 1.1**.

***Table 1.1.*** *Some relevant parameters for conventional Li-ion and Li-S cathode materials [21].*

| *Battery* | *Cathode* | Cost | Cell Voltage (V) | Theoretical Capacity (mAh $g^{-1}$) | Practical Capacity (mAh $g^{-1}$) |
|---|---|---|---|---|---|
| Li-ion | $LiCoO_2$ | High | 3.6 | 274 | 160 |
| | $LiMn_2O_4$ | Low | 3.9 | 148 | 105 |
| | $LiFePO_4$ | Low | 3.4 | 170 | 155 |
| Li-S | **Sulfur** | **Very Low** | **2.1** | **1,675** | **600-800** |

Regarding the operation principles, during the discharge reaction, lithium metal is oxidized at the negative electrode to produce lithium ions and electrons (**Reaction 1.8**). Lithium ions migrate to the positive electrode through the electrolyte to the positive electrode where sulfur is reduced to lithium sulfide ($Li_2S$) (**Reaction 1.9**), while the electrons travel through the external circuit generating an electrical current. Overall discharge reaction is represented in **Reaction 1.10**.

Negative electrode $$2Li \rightarrow 2Li^+ + 2e^- \quad (\textbf{\textit{1.8}})$$

Positive electrode $$S + 2Li^+ + 2e^- \rightarrow Li_2S \quad (\textbf{\textit{1.9}})$$

Overall discharge reaction: $$2Li + S \rightarrow Li_2S \quad (\textbf{\textit{1.10}})$$

Reduction of elemental sulfur into $Li_2S$ does not take place directly but through the formation of several polysulfide intermediates ($Li_2S_x$). During discharge, two plateaus and a sloppy region are generally observed due to the progressive reduction of sulfur into $Li_2S$. The first plateau at ca. 2.3 V vs. $Li^+/Li$ corresponds to the ring opening of $S_8$ and reduction into high order polysulfides ($Li_2S_8$, $Li_2S_6$). High order polysulfides are furtherly reduced to $Li_2S_4$ in the slopping region, and as the reaction continues, low order polysulfides ($Li_2S_2$, $Li_2S$) start appearing in the second plateau at ca. 2.1 V vs. $Li^+/Li$ until reaction finishes due to the complete reduction of sulfur into $Li_2S$ (**Scheme 1.4**) [22].

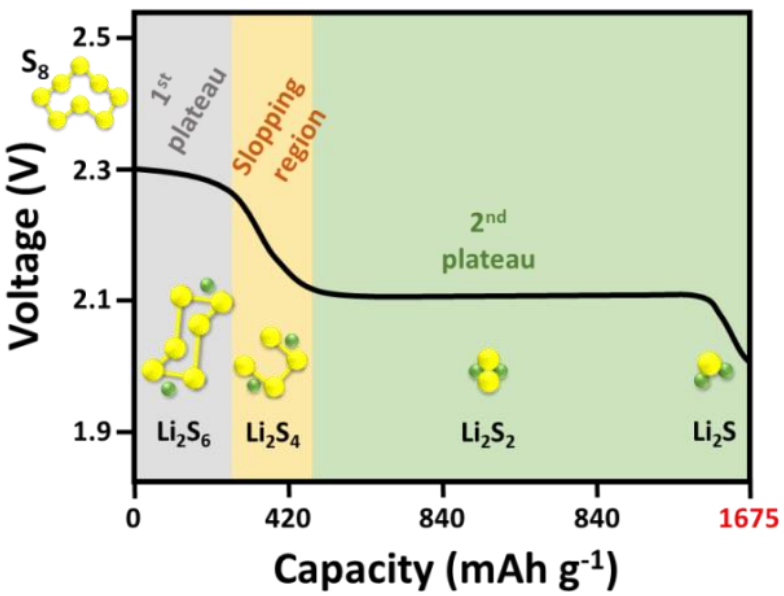


***Scheme 1.4.*** *Li-S ideal galvanostatic discharge curve.*

In this technology, the inherent electrochemical advantages of sulfur coexist with the challenges associated to the non-metallic feature of this element. First, sulfur and its reduction products ($Li_2S$) are electrical insulators, requiring the use of carbon additives to improve the electronic conductivity of the electrodes, which unfortunately contribute to increase the "dead weight" of the electrochemical cell, and therefore decrease its specific energy density. In the second place, $Li_2S$ volume is a 76% larger than that of sulfur. This volume expansion/contraction during the battery discharge

and charge, respectively, can progressively deteriorate the cathode life and lead to electrode cracking, loss of active material or even the short-circuit of the cell [23–25]. Last, the major challenge associated with the use of sulfur, is the so-called "Shuttle effect". High-order lithium polysulfides are very soluble in most commonly used organic electrolytes, so, they tend to diffuse from the cathode to the anode due to concentration gradient and potential difference. Then, long chain polysulfides are reduced with metallic lithium, giving rise to low order lithium polysulfides that diffuse back to the cathode and are again oxidized to high order lithium polysulfides. These polysulfides can be even further reduced to insoluble $Li_2S$ or $Li_2S_2$ that can precipitate at the anode surface. This process takes place repeatedly during cycling, degrading metallic lithium and leading to active material lost in the cathode. This effect results in a progressive deterioration of the coulombic efficiency, a poor cycle life and a strong capacity fading of the cell [26,27]. Discharge, charge and shuttle effect mechanisms for a Li-S battery are summarized in **Scheme 1.5**.

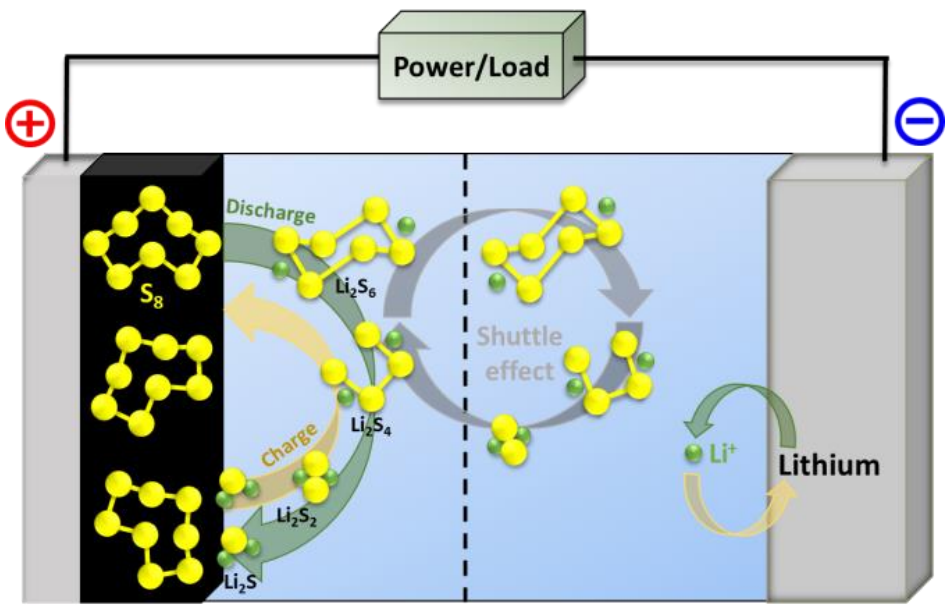


***Scheme 1.5.*** *Diagram of reaction mechanisms for a Li-S battery.*

To overcome all these issues, much effort has been devoted for optimization of the cathode material. Most of them, involve the preparation of composites by mixing of sulfur with other materials (polymers, transition metals, carbons) [28–32]. On the anode-side, the use of bare metallic lithium has associated some important challenges. The solid electrolyte interface layer (SEI) formed upon the reaction between lithium and the electrolyte produce irreversible loss of active material and the heterogeneous deposition of lithium ions on the anode side can lead to lithium dendrite formation (ramified structures that grow beyond the surface of the anode) that limit the lifetime of the battery and compromise its safety [33].

### 1.2.3. Metal-oxygen batteries

Metal-oxygen batteries (M-$O_2$) rely on the electrochemical reduction of molecular oxygen ($O_2$) in the cathode and the use of an electropositive metal as anode. Well known examples of M-$O_2$ batteries are primary cells in aqueous electrolytes such as Zn-$O_2$, Al-$O_2$ or Mg-$O_2$ batteries. Unfortunately, these devices cannot be recharged due to the irreversible electrochemical reactions that take place in both anode and cathode during discharge. On this regard, non-aqueous metal-oxygen batteries based on the use of alkali metals such as Li or Na, have been recently identified as promising next generation of batteries due to their outstanding theoretical energy density and their ability to be recharged [34]. These cells are formed by combining an alkali metal anode with an “air-cathode”; generally, a porous material with high surface area to enable the gas diffusion and promote the reaction between sodium and oxygen. The chemical processes behind the operation involve the metal (e.g. Li or Na) oxidation in the anode during the discharge, and ions reaction with molecular oxygen at the cathode. The reduction of molecular oxygen, usually denoted as oxygen reduction reaction (ORR), lead to the formation of superoxide ($O_2^-$) and peroxide ($O_2^{-2}$) anions simultaneously. These oxygen reactive species generated by the ORR combine with the metal cation and the precipitation of metal oxides occurs at the surface of the “air-cathode”. Upon charge, alkali metal oxides decompose reversibly into oxygen gas (OER) and alkali metal [35,36]. The working mechanism of a generic rechargeable M-$O_2$ battery is depicted in **Scheme 1.6**.

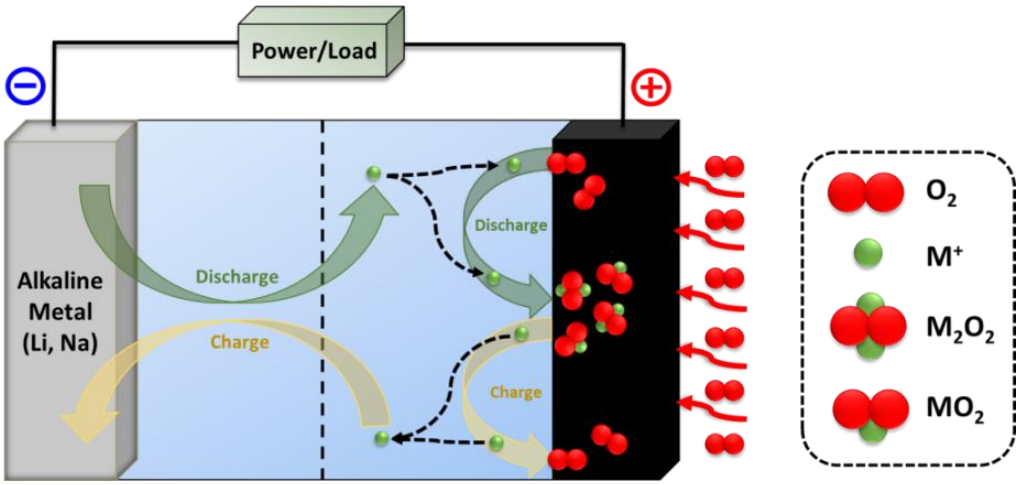


***Scheme 1.6.*** *Schematic representation of the working principles of rechargeable M-$O_2$ batteries.*

Among the different M-$O_2$ configurations, lithium-oxygen batteries (Li-$O_2$), firstly reported in 1996, have attracted considerable attention [37]. During discharge, metallic lithium is oxidized to $Li^+$ in the negative electrode, which reacts with the $O_2^-$ from the ORR to form $LiO_2$ in the cathode. However, $LiO_2$ is unstable and further reacts with another $Li^+$ to form $Li_2O_2$. As consequence, Li-$O_2$ batteries have an outstanding theoretical energy density of ca. 3,500 Wh $kg^{-1}$, which is almost ten times higher than that of conventional LiBs. However, several drawbacks related to battery operation such as Li dendrite growth, side reactions, stability of the electrolyte and poor kinetics have limited its practical application [38]. Moreover, relying on quasi-reversible oxygen/peroxide ($O_2/O_2^-$) electrochemistry, Li-$O_2$ cells suffer from high charging overpotential that results in poor energy efficiency. In other words, more energy is required to recharge the battery compared with the energy that can be obtained on discharge. This high charging overpotential also contributes to instability of the cells components, leading to a low cycling performance [39].

In 2012, the Na-$O_2$ technology emerged as a promising alternative just by replacing the metallic Li by Na as the negative electrode [40]. Sodium shows higher ionic conductivity, is more abundant and cheaper than lithium. Moreover, Na-$O_2$ batteries perform through the formation of superoxide discharge product ($NaO_2$, **Reaction 1.11**) instead of peroxide, ($Li_2O_2$, **Reaction 1.12**).

Na-$O_2$ discharge $$O_2 + Na^+ + 1e^- \rightarrow NaO_2$$ **(*1.11*)**

Li-$O_2$ discharge $$O_2 + 2Li^+ + 2e^- \rightarrow Li_2O_2$$ **(*1.12*)**

The one electron-based oxygen reduction undergone in Na-$O_2$ battery decrease the energy density of the battery to 1,100 Wh $kg^{-1}$, but fasten the reaction kinetics, decrease overpotential and improve stability and efficiency. Na-$O_2$ batteries, however, are still a novel technology and will need further development before widespread commercialization. The major challenge of Na-$O_2$ batteries is related to cyclability, since more than 100 cycles are rarely achieved. This poor cycling life is associated to the different cell components (anode, cathode, and electrolyte). Despite the aforementioned positive features, metallic sodium is more reactive than lithium, which may lead to premature cell failure due to dendrite growth and poor cycling rate performance due to parasitic reactions [41]. The $O_2^-$ radical which is formed upon discharge is highly reactive and may decompose most of the commonly used aprotic electrolytes and attack both the anode and the cathode. Moreover, the excessive accumulation of discharge products in the oxygen cathode can also lead to pore clogging, hindering reversible cycling. In addition, a rationally designed cathode is needed to provide efficient $Na^+$ and $O_2$ diffusion pathways at the time that serve as catalyst for ORR and OER reactions [42]. Regarding cell setup, most of the cells used in the Na-$O_2$ research field are homemade or noncommercially available. This leads to a wide variability in the reported results, which varies from lab to lab [43]. In summary, a thorough design and optimization of each cell component and a better understanding of the reaction mechanism will be crucial for the development of this promising technology.

## 1.3. Electrochemical capacitors

The discovery of electrical capacitors dates from 1957, when a group of engineers from the General Electric Company firstly described the electric double layer effect undergone in porous carbon electrodes. In 1969, Sohio Corporation manufactured the first commercial electric double layer capacitor using a porous carbon in a non-aqueous solvent. Finally, in 1978, NEC (a Japanese multinational Information Technology provider) baptized these types of high electrochemical capacitors as “supercapacitor” [44]. From then, the terms supercapacitor or ultracapacitor, are used

to generally denote electrochemical capacitors (EC). Supercapacitors can be classified in three main subcategories depending on their energy storage mechanism: electrical double layer capacitors (EDLCs), pseudocapacitors and metal-ion hybrid capacitors.

### 1.3.1. Electrical double layer capacitors

Electric double layer capacitors are formed by two electrodes, which in most of the cases are two similar porous carbon-based materials, separated by a semi-permeable membrane impregnated in an electrolyte. Energy is electrostatically stored by the adsorption of positive and negative charges at the interface electrode/electrolyte rather than in a chemical form. Owing to the non-faradaic charge storage mechanism, which does not involve any chemical reaction, these devices can stand millions of cycles with an outstanding power density. When a potential difference is applied to an EDLC, opposite ion charges in the electrolyte are attracted by the as-generated potential difference, permeating the membrane and getting stored in the pores of the carbon materials, thus forming the electric double layer [45] as represented in **Scheme 1.7**.

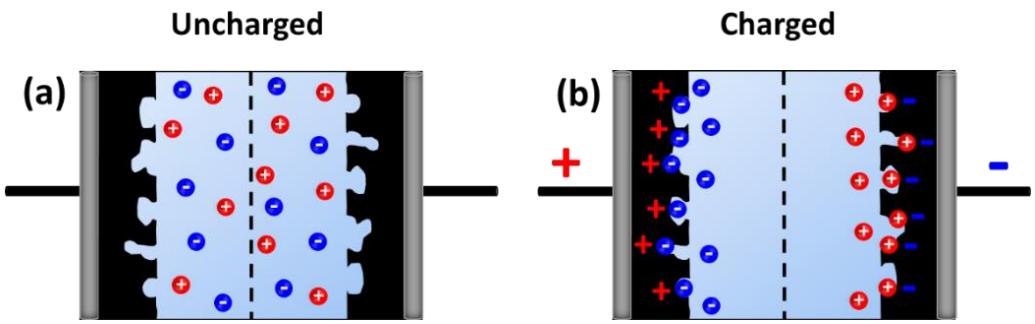


***Scheme 1.7.*** *Activated carbon-based EDLC in its uncharged* ***(a)*** *and charged state* ***(b)****.*

As each electrode-electrolyte interface represents a conventional capacitor, the full cell can be considered as two capacitors connected in series, and therefore, the charge stored in the cell in farads, or capacitance ($C_{cell}$) can be calculated following the **Equation 1.13**, where $C_+$ and $C_-$ are the capacitance values of the positive and negative electrodes respectively.

$$\frac{1}{C_{Cell}} = \frac{1}{C_+} + \frac{1}{C_-} \quad \textbf{(1.13)}$$

Energy stored on an EDLC is directly related to capacitance and exponentially proportional to operational working voltage window as stated in **Equation 1.14**. Meanwhile, power is delivered energy per unit of time like expressed in **Equation 1.15**.

$$E = \frac{1}{2} C \cdot V^2 \quad \textbf{(1.14)}$$

$$P = {}^{E}/_{t} \quad \textbf{(1.15)}$$

Extended research has been devoted to increase capacitance and voltage on EDLC devices to achieve higher energy densities. While capacitance is mainly related with the nature of the electrode materials, operational working voltage is highly dependent on the selected electrolyte. Each electrode capacitance ($C_e$) can be described by the Helmholtz model:

$$C_e = \varepsilon_0 \varepsilon_r \cdot \frac{S}{d} \quad \textbf{(1.16)}$$

Where $\varepsilon_0$ is the permittivity of vacuum, $\varepsilon_r$ the relative permittivity of the electrolyte, S is the surface area of the electrode/electrolyte interface and d is the effective thickness of the double layer. The influence of surface area over capacitance is the main reason why activated carbons (ACs) are the preferred choice for EDLCs electrodes. However, only a fraction of the surface area is available to form the electric double layer, and consequently the capacitance calculated on the basis of **Equation (1.16)** is usually overestimated. This is generally related to the adequacy of pore size distribution with electrolyte ions size. For example, an excessively small pore size will hinder the access of electrolyte ions, what entails an underuse of the whole surface area. Therefore, electrode materials for EDLCs must account with large specific surface area and an appropriate pore size distribution that fits the ions size of selected electrolyte [50]. Additionally, electrolyte selection is no trivial issue since it mainly determines the operational working voltage of the cell. Aqueous-based electrolyte rarely exceeds 1 V (due to water decomposition), while organic electrolytes and ionic liquids (ILs) can work above 2.5 V. More in detail, the ions of aqueous electrolytes

generally account with a small size and a higher electronic conductivity, allowing higher capacitance and power values than that obtained for organic electrolytes, especially at higher rates. In any case, organic electrolytes are still the preferred choice for commercial supercapacitors due to its wider operating potential windows (2.5 – 2.8 V). However, organic electrolytes, generally based on ammonium salts dissolved in acetonitrile (ACN), still exhibit some volatility, safety and toxicity issues [46]. On the other hand, ionic liquids have recently received significant interest as alternative electrolytes for supercapacitors due to several advantages that include negligible volatility, non-flammability and good thermal and electrochemical stability (3.0 - 3.5 V). Nevertheless, the specific capacitance of the final EDLC can be compromise due to the lower ionic conductivities and larger size of the ILs ions [47,48].

Regarding their characterization, cyclic voltammetry (CV) is one of the most used electrochemical techniques to evaluate the EDLC performance. A differential in potential in terms of scan rate ($V_{Scan\ rate}$ = V $s^{-1}$) is applied and the current generated due to electric double layer formation is registered. The resulting current can be directly related to the cell capacitance from the following equation:

$$C_{Cell} = \frac{I}{V_{Scan\ rate}} \qquad \textbf{(1.17)}$$

For an ideal EDLC, a perfect rectangular shaped curve should be observed under the electrolyte stability limits. Consequently, this technique is very useful for a first assessment of the new materials and to determine the stability voltage window for a certain system. However, galvanostatic measurements, applying a constant current, are considered a more accurate technique for the evaluation of critical operational parameters such as energy, power or cycle life. While for batteries an almost constant voltage (plateau) is attained during discharge, EDLCs show a linear dependency between voltage and its state of discharge. Comparison between ideal CV and galvanostatic curves for batteries and EDLC are shown in **Scheme 1.8** [49].

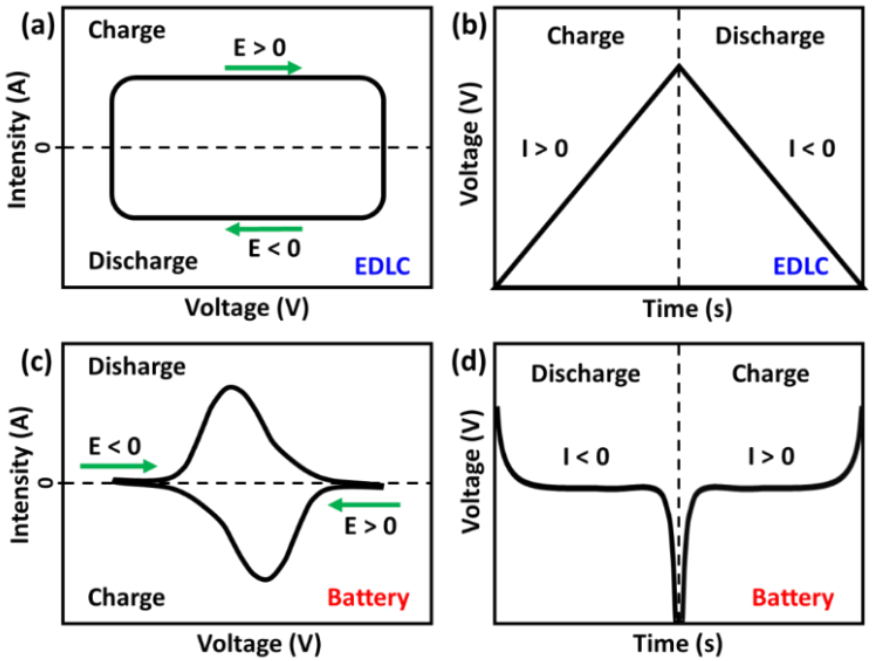


***Scheme 1.8.*** *CV (**a**) and galvanostatic (**b**) characteristic profiles for EDLCs and batteries (**c** and **d**).*

### 1.3.2. Pseudocapacitors

In pseudocapacitors charge is stored via fast and reversible faradaic processes which involve charge transfer between electrode and electrolyte. When a potential is applied, reduction and oxidation reactions take place on the electrode material, resulting in faradaic current passing through the capacitor cell. This non-diffusion limited process enables much faster redox reactions, allowing higher capacitance values than EDLCs [50]. Active electrode materials showing pseudocapacitive behavior are transition metal oxides ($RuO_2$, $MnO_2$) and conducting polymers. A typical pseudocapacitive reaction is represented in **Equation 1.18**.

$$RuO_2 + xH^+ + xe^- \leftrightarrows RuO_{2-x}(OH)_x \qquad (\mathbf{1.18})$$

### 1.3.3. Metal-ion Hybrid Capacitors

Metal-ion hybrid supercapacitors are devices that combine a battery-type electrode with a capacitive one in the same cell. So, hybrids are built in an asymmetric configuration. While one electrode store charge electrostatically, the other one undergoes faradaic charge storage [51]. Metal-ion hybrid capacitors are a promising technology since they exhibit intermediate properties between both technologies and fill the gap for a number of applications where moderate energy densities at high powers are demanded [52,53]. Lithium-ion capacitors (LICs), firstly reported by Amattuci and coworkers [54], have gained considerable attention due to the synergistic effects achieved when merging LiB and EDLC technologies. LICs include a typical negative electrode from a LiBs and a positive capacitive-type electrode from the EDLC, both impregnated with an organic electrolyte containing a lithium-ion conducting salt. As depicted in **Scheme 1.9**, the charge/discharge processes in LICs involve faradaic and non-faradaic electrochemical processes. During charging, lithium ions are intercalated in the anode materials while the anions in the electrolyte are adsorbed on the surface of the porous positive electrode. During discharge, electric current is produced through the spontaneous reverse processes [55].

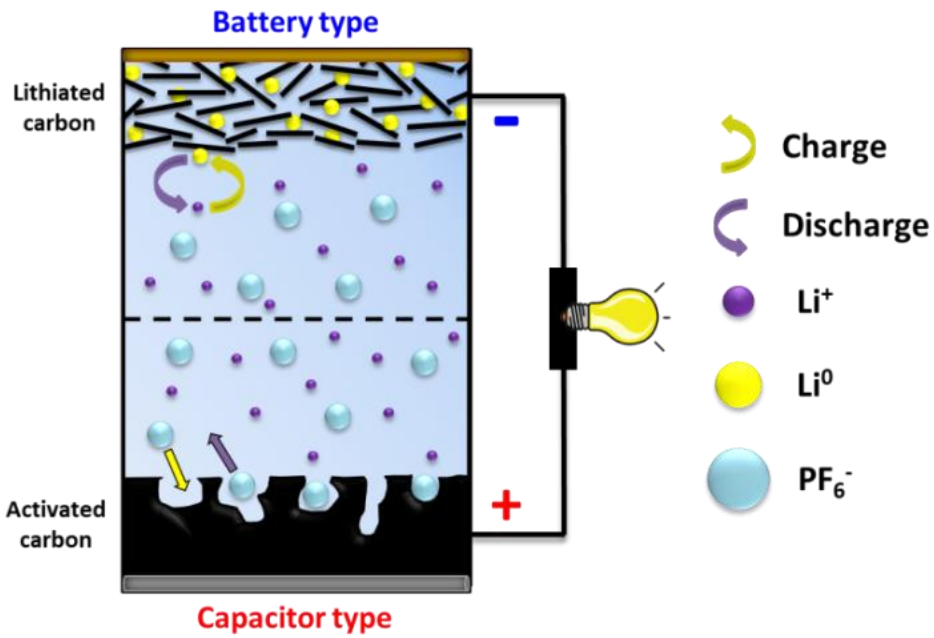


***Scheme 1.9.*** *Lithium-ion capacitor operation diagram.*

In an ideal LIC, cell voltage shows a linear dependence with time, similar to what occurs in EDLCs. The amount of stored energy is proportional to the capacitance, C, and to the square of the operating upper, $V^2_{max}$, and lower voltages, $V^2_{min}$, according to the following equation:

$$E = \frac{1}{2} C (V_{max}^2 - V_{min}^2) \quad \textbf{(1.19)}$$

Due to the larger operational potentials compared to EDLC, LICs exhibit much higher energy densities. And the electrostatic charge storage process in the positive electrode enables faster charge-discharge rates compared to LIBs. The advantages of LICs can be summarized as follows (i) higher energy density and low self-discharge rate (<5% voltage drop at room temperature) compared to EDLCs; (ii) higher power density when compared to LiBs; (iii) long-term stability and (iv) wide operating temperature ranging from -20 to 70 °C [56]. Ragone plots, showing energy to power density values, are commonly used to compare the performance of different devices or electrochemical storage systems. Ragone plot in **Figure 1.2** clearly evidences the "bridging" opportunities of LICs.

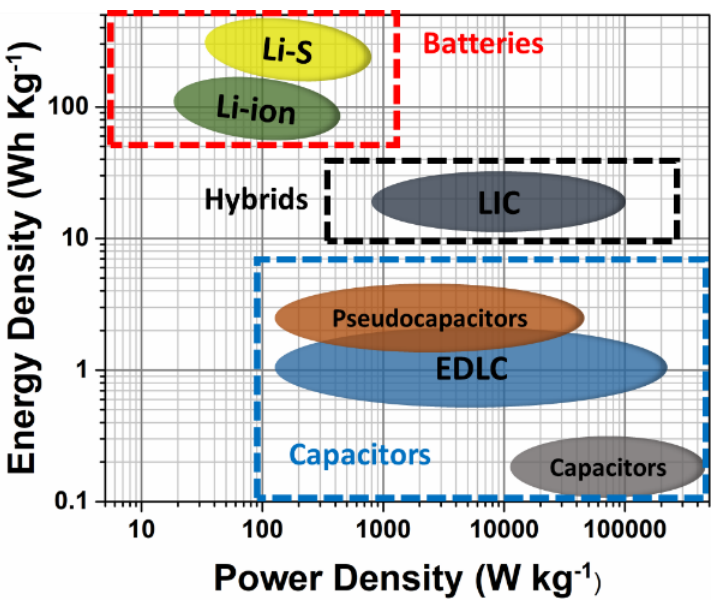


***Figure 1.2**. Ragone plot comparing performance of representative energy storage devices.*

Although this technology is already commercialized [57], there are still some issues to be solved, the main one is related with the mismatched kinetics between positive and negative electrodes. The energy density of the LIC is limited by the specific capacitance of the capacitive-type electrode, since specific capacity of the battery-type electrode is much higher. On the other hand, the power density is limited by the battery-type electrode which shows sluggish kinetics behavior [58]. Thus, a thorough selection and optimization of positive and negative electrode materials are needed. For the positive electrode, as for EDLCs, activated carbons are the preferred choice since possess the merits of: (i) a high specific surface area to gain high specific capacitance; (ii) a high operating voltage to ensure a high energy density; (iii) a superior electronic conductivity to achieve a high power; and (iv) an excellent electrolyte accessibility through the intrapore space [59]. On the other hand, a low operating voltage and a good rate capability is desired for battery-type electrode materials in the LIC. Negative electrodes, borrowed from LIBs anodes, can be classified into three kinds according to their $Li^+$ storage behaviors: insertion-type (pre-lithiated carbons, LTO, $TiO_2$), conversion-type ($SnO_2$, $Fe_3O_4$, $Nb_2O_5$) and alloy-type (Si, Sn) [60]. Despite the great variety of electrode materials reported, it is remarkable that dual carbon LICs (DC-LICs), in which both electrodes are based on carbonaceous materials, exhibit a safer performance, better long-term cycling stability, greater reliability and higher power densities than other LICs configurations [56,61]. However, pre-lithiation of the battery-type electrode is required to enable the operation of DC-LICs since both the carbonaceous materials used do not contain lithium ions. Pre-lithiation process can be challenging and raise the price of LICs manufacture [62]. However, it also allows the use of alternative carbon materials with low first cycle coulombic efficiencies, since irreversible reactions associated with SEI formation takes place during this preliminary step. This is the case of non-graphitizable carbons, also known as hard carbons (HCs), which has demonstrated to be a suitable alternative to conventional graphite anodes owing to their large storage capacity, low working potential and good cycling stability [63]. Another, challenge associated to LICs, especially at the lab-scale, is the so-called "platting" process. When potential of the battery-electrode reaches negative values, formation of metallic lithium is favored. As result life performance of the LIC can be seriously affected, but most important, the presence of metallic lithium in the cell entails serious safety hazards. A careful control of the pre-lithiation process and matching the kinetics of both electrodes need to be considered to avoid lithium platting and ensure the correct operation of the LIC [64].

## 1.4. Graphene

### 1.4.1. Structure and properties of graphene

Graphene is an allotrope of carbon where $sp^2$-hybridized carbon atoms arranged in a flat bidimensional honeycomb lattice. Graphene sheets layers, with a carbon atom thickness of only 3.32 Å, can be also considered as a basic structural building block for several well-known carbon structures, such as graphite, carbon nanotubes or fullerenes (**Scheme 1.10**).

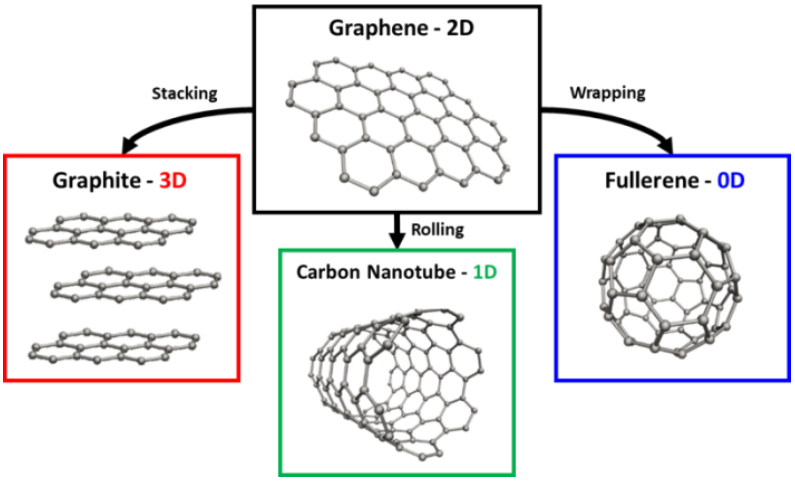


***Scheme 1.10.*** *Graphene as building block for different carbon structures.*

Since first unambiguously obtained and partially characterized by Andre Geim and Konstantin Novoselov in 2004 [65], graphene has attracted much interest due to its outstanding properties and wide range of applications:

- Graphene is an excellent electric conductor due to its conjugated bidimensional pi system. In fact, free-standing graphene has high electrical charge carrier mobility up to ~ 200,000 $cm^2 V^{-1}s^{-1}$ [66].
- The thermal conductivity of graphene could reach ~ 5,000 $W m^{-1}K^{-1}$. As a result, graphene could be used for thermal management in microelectronics or as an

ultrahigh thermal conductive filler to improve thermal conductivity of polymer composites [67].

- Graphene presents optic transparency, absorbing only the 2.3% of the white light. This feature appoints graphene as a potential candidate to replace conventional transparent electrodes (indium tin oxide) in solar cells [68].
- Regarding the mechanical properties, the flexibility of graphene adds another advantage over the conventional rigid electrodes, and extends its application to flexible, wearable electronics. Additionally, graphene can be used as a reinforcement filler to enhance the mechanical properties of other materials thanks to its outstanding mechanical strength (Young's modulus, ~1 TPa) [69].
- The theoretical specific surface area of graphene is as high as 2,630 $m^2 g^{-1}$ [70], which renders this bidimensional material highly desirable for its use in the sorption of gases or water purification.

It is worth to remark that all these promising features only apply to pure single-atom thick layer of graphene, which is usually called just as "graphene" or "pristine graphene". As several layers of graphene stack together due to pi-pi conjugation, these properties may vary and progressively approach those of graphite. Attending to that, it is well accepted in the scientific literature to use the term "multilayer graphene" when 2 to 10 layers are stacked together [71]. If the number of layers is above 10, it would be correct to use the term "graphitic material" or "carbon thin film". In order to properly classify the different emerging graphene-based materials, terms like graphene nanoribbons, graphene nanosheets or graphene quantum dots have been widely used in literature. This nomenclature refers to their aspect ratio. However, they are often indiscriminately used, which leads to confusion.

### 1.4.2. Preparation of graphene-based materials

Since graphene does not occur naturally, different synthetic routes have been explored for the preparation of single-layer carbon sheets. This is not a trivial issue due to the great stacking tendency of the graphene layers, the instability of monolayer graphene and the high dependency of graphene properties over its preparation method. Despite great efforts have been devoted to find an approach that allows to obtain large amounts of highly pure graphene so far none of them have fully succeed,

which has hindered its integration in real systems. Within this context, in last decade, several preparation methods of graphene have been described to fulfil these requirements. Following the nomenclature used for the preparation of nanostructured materials, the synthesis of graphene and its relatives can be classified into two main categories, bottom-up and top-down approaches [72].

In bottom-up approaches individual constituents, like inorganic/organic molecules, are assembled to build the bidimensional carbon layer. Methods based on the controlled growth of graphene from decomposition of carbon precursors over a substrate like chemical vapor deposition (CVD) or epitaxial growth are the most representative techniques for bottom-up approaches. These techniques allow the production of high-quality graphene (monolayer, non-defective, transparent, flexible). Nevertheless, the high cost and extremely low yield of these manufacture processes greatly hinder their use for the large scale production of graphene, limiting their use for certain applications like microelectronics in which small quantities of high quality graphene are needed [73].

On the other hand, top-down approaches use as precursor carbonaceous materials that already contain graphene on its structure, e.g. graphite, and break in down into its individual units. These processes can be classified according to the method used for the exfoliation: mechanical, electrochemical or chemical. All of them allow getting a considerably high amount of product at a very low cost, but resultant graphene-based materials generally show a larger amount of defects compared to those obtained by bottom-up approaches [74]. Graphene production through the graphite oxide exfoliation route (chemical exfoliation) is the most used one due to its low-cost, large-scale production and easy manipulation. The resultant product from this method is graphene oxide (GO), one of the most commonly used precursors for the production of graphene-based materials.

### 1.4.3. Graphene oxide

Graphene oxide is generally produced in two steps. In the first one, graphite is oxidized to graphite oxide, and in the second one, graphite oxide is exfoliated to graphene oxide. The most commonly used oxidation route of graphite is the "Hummers' method" [75], which consists on the sequential addition of strong oxidizing agents ($H_2SO_4$, $KMnO_4$, $NaNO_3$) to a certain amount of graphite. As a result, graphite is

oxidized and oxygen functional groups are intercalated between the graphene layers, reducing the Van der Waals energy forces due to the increase of the interlayer distance [76]. The oxygen functional groups present on the surface of graphene layers are mainly hydroxyl and epoxy groups on the inner part of the sheets and smaller amounts of carboxyl, carbonyl, phenol, lactone and quinone groups mainly located at the edges sites [77]. Resultant graphite oxide can be easily exfoliated to GO by different methods such as sonication in a solvent. However, most oxygen functionalities from graphite oxide remain anchored on the surface of the graphene layers. For this reason, the term "graphene oxide" is generally used (see **Scheme 1.11**).

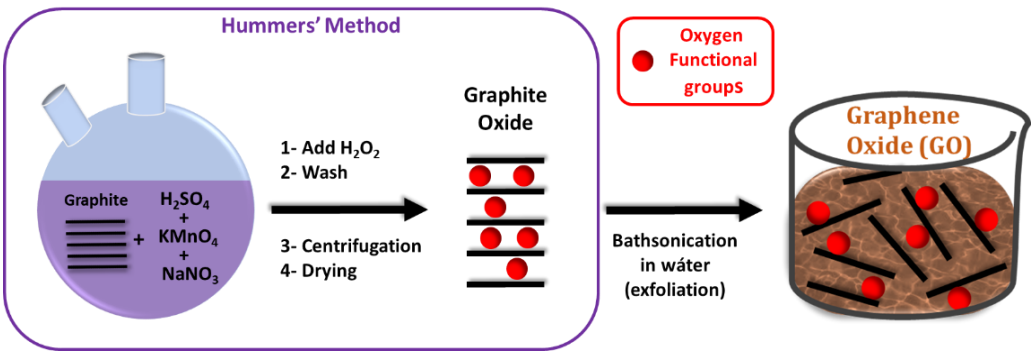


***Scheme 1.11.*** *Schematic representation of a conventional route followed for the preparation of GO.*

The presence of oxygen functional groups improves its dispersibility in polar solvents and increase its reactivity for further surface chemical modifications, which is especially interesting for the design of sensors or biomedicines [78]. Nevertheless, graphene oxide is an insulator due to the disrupted $sp^2$ bonding networks which limits the direct application of GO in electrically active materials and devices. To recover a good electronic conductivity comparable to graphite, GO needs to be reduced to restore its pi-pi conjugated structure. For this purpose, thermal or chemical treatments are generally used to remove the oxygen functional groups, and in this case the term "reduced graphene oxide" (rGO) is used to distinguish it from non-defective pristine graphene [79].

## 1.5. Objectives and goals

In short, there is an urgent need to develop new and more efficient energy storage devices. For this purpose, new chemistries beyond Li-ion are arising. Among them, lithium-sulfur batteries, sodium-oxygen batteries, electric double layer capacitors and lithium-ion capacitors are quite promising. However, these technologies still need a further development to meet the ever-growing energy demand of modern society. For this purpose, it is crucial the search for new electrode materials tailored to the requirements of each device. On this regard, graphene oxide is a promising candidate thanks to its easy manufacture, low price, outstanding mechanical properties and great tunability. Thus, the main objective of this thesis relies in the use of graphene oxide and its derivatives to surpass the intrinsic challenges of the aforementioned energy storage devices and enhance their practical energy and power densities. Since each energy storage technology is based on different mechanisms and, subsequently, individual strategies are needed, each chapter of the thesis is dedicated to a specific technology. The common thread of the chapters is the use and evaluation of graphene-based materials in the electrodes. **Chapter I** includes and introduction and the State of the Art of the topic and the objectives of this thesis. **Chapter II** objective is the preparation of high sulfur loaded graphene-sulfur composites and its further application as cathodes for high-energy and long-life Li-S batteries. **Chapter III** aims to produce three-dimensional graphene supports as oxygen cathodes for Na-$O_2$ batteries. **Chapter IV** is devoted to the preparation of activated carbon-graphene composites using cigarette filter wastes as precursor and evaluate its potential application as electrodes for high energy EDLCs. **Chapter V** objective is the preparation of carbon composites from the pyrolysis and activation of coffee waste and graphene oxide, and their evaluation as potential electrodes for dual-carbon lithium-ion capacitors. Finally, in **Chapter VI**, a general discussion is followed; results are examined and put into perspective. Conclusions of this thesis are summarized.

## 1.6. Bibliography

[1] S. Tagliapietra, M. Hafner, The Geopolitics of the Global Energy Transition, Springer Nature, 2020. http://search.ebscohost.com/login.aspx?direct=true&site=edspub-live&scope=site&type=44&db=edspub&authtype=ip,guest&custid=ns011247&groupid=main&profile=eds&bquery=AN%2026155814 (accessed March 4, 2021).

[2] M. Bazilian, M. Bradshaw, J. Gabriel, A. Goldthau, K. Westphal, Four scenarios of the energy transition: Drivers, consequences, and implications for geopolitics, Wires Clim. Change. 11 (2020) e625. https://doi.org/10.1002/wcc.625.
[3] X. Xie, Z. Dou, M. Huang, Viability of Large Scale Renewable Energy Installations in Victoria, ENG5006 Eng. Proj. B. (2018) 25.
[4] Z. Yang, J. Zhang, M.C.W. Kintner-Meyer, X. Lu, D. Choi, J.P. Lemmon, J. Liu, Electrochemical Energy Storage for Green Grid, Chem. Rev. 111 (2011) 3577–3613. https://doi.org/10.1021/cr100290v.
[5] M.A. Hannan, M.M. Hoque, A. Mohamed, A. Ayob, Review of energy storage systems for electric vehicle applications: Issues and challenges, Renew. Sustain. Energy Rev. 69 (2017) 771–789. https://doi.org/10.1016/j.rser.2016.11.171.
[6] D. Parra, M. Swierczynski, D.I. Stroe, Stuart.A. Norman, A. Abdon, J. Worlitschek, T. O'Doherty, L. Rodrigues, M. Gillott, X. Zhang, C. Bauer, M.K. Patel, An interdisciplinary review of energy storage for communities: Challenges and perspectives, Renew. Sustain. Energy Rev. 79 (2017) 730–749. https://doi.org/10.1016/j.rser.2017.05.003.
[7] E. Hossain, H.M.R. Faruque, Md.S.H. Sunny, N. Mohammad, N. Nawar, A Comprehensive Review on Energy Storage Systems: Types, Comparison, Current Scenario, Applications, Barriers, and Potential Solutions, Policies, and Future Prospects, Energies. 13 (2020) 3651. https://doi.org/10.3390/en13143651.
[8] J.R. Miller, P. Simon, MATERIALS SCIENCE: Electrochemical Capacitors for Energy Management, Science. 321 (2008) 651–652. https://doi.org/10.1126/science.1158736.
[9] J. Libich, J. Máca, J. Vondrák, O. Čech, M. Sedlaříková, Supercapacitors: Properties and applications, J. Energy Storage. 17 (2018) 224–227. https://doi.org/10.1016/j.est.2018.03.012.
[10] J.B. Goodenough, Electrochemical energy storage in a sustainable modern society, Energy Env. Sci. 7 (2014) 14–18. https://doi.org/10.1039/C3EE42613K.
[11] T.B. Reddy, D. Linden, Linden's Handbook of batteries, 4th eddition, McGraw-Hill, 2011.
[12] A. Ponrouch, M.R. Palacín, Post-Li batteries: promises and challenges, Philos. Trans. R. Soc. Math. Phys. Eng. Sci. 377 (2019) 20180297. https://doi.org/10.1098/rsta.2018.0297.
[13] N. Nitta, F. Wu, J.T. Lee, G. Yushin, Li-ion battery materials: present and future, Mater. Today. 18 (2015) 252–264. https://doi.org/10.1016/j.mattod.2014.10.040.
[14] A. Mauger, C.M. Julien, J.B. Goodenough, K. Zaghib, Tribute to Michel Armand: from Rocking Chair – Li-ion to Solid-State Lithium Batteries, J. Electrochem. Soc. 167 (2020) 070507. https://doi.org/10.1149/2.0072007JES.
[15] M. Li, J. Lu, Z. Chen, K. Amine, 30 Years of Lithium-Ion Batteries, Adv. Mater. 30 (2018) 1800561. https://doi.org/10.1002/adma.201800561.

[16] T. Placke, R. Kloepsch, S. Dühnen, M. Winter, Lithium ion, lithium metal, and alternative rechargeable battery technologies: the odyssey for high energy density, J. Solid State Electrochem. 21 (2017) 1939–1964. https://doi.org/10.1007/s10008-017-3610-7.

[17] Roth, Sulphur safety data sheet, (2017). https://www.carlroth.com/medias/SDB-4669-GB-EN.pdf?context=bWFzdGVyfHNlY3VyaXR5RGF0YXNoZWV0c3wyNTE2MjR8YXBwbGljYXRpb24vcGRmfHNlY3VyaXR5RGF0YXNoZWV0cy9oMGUvaDIwLzg5Nzc3MjIxMTQwNzgucGRmfGQ1YTlmNjk3Y2E4NDgwMzU4NTZmNmEwN2M1MTZlOWVlMjQyZjBjOTQ4ZWJlNTI5OWVjNTQ5MjAxMzg4ZWQ0Yzc (accessed April 3, 2021).

[18] D.A. Boyd, Sulfur and Its Role In Modern Materials Science, Angew. Chem. Int. Ed. 55 (2016) 15486–15502. https://doi.org/10.1002/anie.201604615.

[19] A. Manthiram, Y. Fu, S.-H. Chung, C. Zu, Y.-S. Su, Rechargeable Lithium–Sulfur Batteries, Chem. Rev. 114 (2014) 11751–11787. https://doi.org/10.1021/cr500062v.

[20] B. Liu, R. Fang, D. Xie, W. Zhang, H. Huang, Y. Xia, X. Wang, X. Xia, J. Tu, Revisiting Scientific Issues for Industrial Applications of Lithium-Sulfur Batteries, Energy Environ. Mater. 1 (2018) 196–208. https://doi.org/10.1002/eem2.12021.

[21] X. Zhao, G. Cheruvally, C. Kim, K.-K. Cho, H.-J. Ahn, K.-W. Kim, J.-H. Ahn, Lithium/Sulfur Secondary Batteries: A Review, J. Electrochem. Sci. Technol. 7 (2016) 97–114. https://doi.org/10.5229/JECST.2016.7.2.97.

[22] M. Wild, L. O'Neill, T. Zhang, R. Purkayastha, G. Minton, M. Marinescu, G.J. Offer, Lithium sulfur batteries, a mechanistic review, Energy Environ. Sci. 8 (2015) 3477–3494. https://doi.org/10.1039/C5EE01388G.

[23] R. Fang, S. Zhao, Z. Sun, D.-W. Wang, H.-M. Cheng, F. Li, More Reliable Lithium-Sulfur Batteries: Status, Solutions and Prospects, Adv. Mater. 29 (2017) 1606823. https://doi.org/10.1002/adma.201606823.

[24] Z.W. Seh, Y. Sun, Q. Zhang, Y. Cui, Designing high-energy lithium–sulfur batteries, Chem Soc Rev. 45 (2016) 5605–5634. https://doi.org/10.1039/C5CS00410A.

[25] G. Xu, B. Ding, J. Pan, P. Nie, L. Shen, X. Zhang, High performance lithium–sulfur batteries: advances and challenges, J. Mater. Chem. A. 2 (2014) 12662. https://doi.org/10.1039/C4TA02097A.

[26] B. Gong, X. Song, Y. Shi, J. Liu, C. Hao, Understanding the Inhibition of the Shuttle Effect of Sulfides (S ≤ 3) in Lithium–Sulfur Batteries by Heteroatom-Doped Graphene: First-Principles Study, J. Phys. Chem. C. 124 (2020) 3644–3649. https://doi.org/10.1021/acs.jpcc.9b10314.

[27] W. Ren, W. Ma, S. Zhang, B. Tang, Recent advances in shuttle effect inhibition for lithium sulfur batteries, Energy Storage Mater. 23 (2019) 707–732. https://doi.org/10.1016/j.ensm.2019.02.022.

[28] L. Zhang, Y. Wang, Z. Niu, J. Chen, Advanced nanostructured carbon-based materials for rechargeable lithium-sulfur batteries, Carbon. 141 (2019) 400–416. https://doi.org/10.1016/j.carbon.2018.09.067.
[29] H. Wang, W. Zhang, J. Xu, Z. Guo, Advances in Polar Materials for Lithium-Sulfur Batteries, Adv. Funct. Mater. 28 (2018) 1707520. https://doi.org/10.1002/adfm.201707520.
[30] L. Zhou, D.L. Danilov, R. Eichel, P.H.L. Notten, Host Materials Anchoring Polysulfides in Li–S Batteries Reviewed, Adv. Energy Mater. (2020) 2001304. https://doi.org/10.1002/aenm.202001304.
[31] M. Wang, X. Xia, Y. Zhong, J. Wu, R. Xu, Z. Yao, D. Wang, W. Tang, X. Wang, J. Tu, Porous Carbon Hosts for Lithium–Sulfur Batteries, Chem. – Eur. J. 25 (2019) 3710–3725. https://doi.org/10.1002/chem.201803153.
[32] J.E. Knoop, S. Ahn, Recent advances in nanomaterials for high-performance Li–S batteries, J. Energy Chem. 47 (2020) 86–106. https://doi.org/10.1016/j.jechem.2019.11.018.
[33] X.-B. Cheng, J.-Q. Huang, Q. Zhang, Review—Li Metal Anode in Working Lithium-Sulfur Batteries, J. Electrochem. Soc. 165 (2018) A6058–A6072. https://doi.org/10.1149/2.0111801jes.
[34] D. Sharon, D. Hirshberg, M. Afri, A.A. Frimer, M. Noked, D. Aurbach, Aprotic metal-oxygen batteries: recent findings and insights, J. Solid State Electrochem. 21 (2017) 1861–1878. https://doi.org/10.1007/s10008-017-3590-7.
[35] J.L. Gómez Urbano, M. Enterría, I. Monterrubio, I. Ruiz de Larramendi, D. Carriazo, N. Ortiz Vitoriano, T. Rojo, An Overview of Engineered Graphene-Based Cathodes: Boosting Oxygen Reduction and Evolution Reactions in Lithium– and Sodium–Oxygen Batteries, ChemSusChem. 13 (2020) 1203–1225. https://doi.org/10.1002/cssc.201902972.
[36] K. Song, D.A. Agyeman, M. Park, J. Yang, Y.-M. Kang, High-Energy-Density Metal-Oxygen Batteries: Lithium-Oxygen Batteries vs Sodium-Oxygen Batteries, Adv. Mater. 29 (2017) 1606572. https://doi.org/10.1002/adma.201606572.
[37] K.M. Abraham, Z. Jiang, A Polymer Electrolyte-Based Rechargeable Lithium/Oxygen Battery, J. Electrochem. Soc. 143 (1996) 1–5. https://doi.org/10.1149/1.1836378.
[38] C. Wang, Z. Xie, Z. Zhou, Lithium-air batteries : Challenges coexist with opportunities Lithium-air batteries : Challenges coexist with opportunities, APL Mater. 7 (2019) 040701.
[39] H. Yadegari, X. Sun, Sodium–Oxygen Batteries: Recent Developments and Remaining Challenges, Trends Chem. 2 (2020) 241–253. https://doi.org/10.1016/j.trechm.2019.12.003.
[40] P. Hartmann, C.L. Bender, M. Vraˇ, A.K. Dürr, A. Garsuch, J. Janek, P. Adelhelm, A rechargeable room-temperature sodium superoxide ( NaO 2 ) battery, Nat. Mater. 12 (2012) 228–232.

[41] S. Zhao, L. Li, F. Li, S.-L. Chou, Recent progress on understanding and constructing reliable Na anode for aprotic Na-O2 batteries: A mini review, Electrochem. Commun. 118 (2020) 106797. https://doi.org/10.1016/j.elecom.2020.106797.
[42] H. Yadegari, X. Sun, Recent Advances on Sodium–Oxygen Batteries: A Chemical Perspective, Acc. Chem. Res. 51 (2018) 1532–1540. https://doi.org/10.1021/acs.accounts.8b00139.
[43] W.D. McCulloch, N. Xiao, G. Gourdin, Y. Wu, Alkali-Oxygen Batteries Based on Reversible Superoxide Chemistry, Chem. - Eur. J. 24 (2018) 17627–17637. https://doi.org/10.1002/chem.201802101.
[44] A.K. Samantara, S. Ratha, Historical Background and Present Status of the Supercapacitors, in: Mater. Dev. Act. Compon. Supercapacitor, Springer Singapore, Singapore, 2018: pp. 9–10. https://doi.org/10.1007/978-981-10-7263-5_2.
[45] M. Salanne, B. Rotenberg, K. Naoi, K. Kaneko, P.-L. Taberna, C.P. Grey, B. Dunn, P. Simon, Efficient storage mechanisms for building better supercapacitors, Nat. Energy. 1 (2016) 16070. https://doi.org/10.1038/nenergy.2016.70.
[46] R. Ramachandran, F. Wang, Electrochemical Capacitor Performance: Influence of Aqueous Electrolytes, in: Supercapacitors - Theor. Pract. Solut., IntechOpen, 2017.
[47] L. Yu, G.Z. Chen, Ionic Liquid-Based Electrolytes for Supercapacitor and Supercapattery, Front. Chem. 7 (2019) 272. https://doi.org/10.3389/fchem.2019.00272.
[48] A. Brandt, S. Pohlmann, A. Varzi, A. Balducci, S. Passerini, Ionic liquids in supercapacitors, MRS Bull. 38 (2013) 554–559. https://doi.org/10.1557/mrs.2013.151.
[49] Q. Abbas, M. Mirzaeian, M.R.C. Hunt, P. Hall, R. Raza, Current State and Future Prospects for Electrochemical Energy Storage and Conversion Systems, Energies. 13 (2020) 5847. https://doi.org/10.3390/en13215847.
[50] S. Fleischmann, J.B. Mitchell, R. Wang, C. Zhan, D. Jiang, V. Presser, V. Augustyn, Pseudocapacitance: From Fundamental Understanding to High Power Energy Storage Materials, Chem. Rev. 120 (2020) 6738–6782. https://doi.org/10.1021/acs.chemrev.0c00170.
[51] D. Tie, S. Huang, J. Wang, J. Ma, J. Zhang, Y. Zhao, Hybrid energy storage devices: Advanced electrode materials and matching principles, Energy Storage Mater. 21 (2019) 22–40. https://doi.org/10.1016/j.ensm.2018.12.018.
[52] H. Wang, C. Zhu, D. Chao, Q. Yan, H.J. Fan, Nonaqueous Hybrid Lithium-Ion and Sodium-Ion Capacitors, Adv. Mater. 29 (2017) 1702093. https://doi.org/10.1002/adma.201702093.
[53] M. Soltani, S.H. Beheshti, A comprehensive review of lithium ion capacitor: development, modelling, thermal management and applications, J. Energy Storage. 34 (2021) 102019. https://doi.org/10.1016/j.est.2020.102019.

[54] G.G. Amatucci, F. Badway, A. Du Pasquier, T. Zheng, An Asymmetric Hybrid Nonaqueous Energy Storage Cell, J. Electrochem. Soc. 148 (2001) A930. https://doi.org/10.1149/1.1383553.
[55] J.J. Lamb, O.S. Burheim, Lithium-Ion Capacitors: A Review of Design and Active Materials, Energies. 14 (2021) 979. https://doi.org/10.3390/en14040979.
[56] G. Li, Z. Yang, Z. Yin, H. Guo, Z. Wang, G. Yan, Y. Liu, L. Li, J. Wang, Non-aqueous dual-carbon lithium-ion capacitors: a review, J. Mater. Chem. A. 7 (2019) 15541–15563. https://doi.org/10.1039/C9TA01246J.
[57] P. Han, G. Xu, X. Han, J. Zhao, X. Zhou, G. Cui, Lithium Ion Capacitors in Organic Electrolyte System: Scientific Problems, Material Development, and Key Technologies, Adv. Energy Mater. 8 (2018) 1801243. https://doi.org/10.1002/aenm.201801243.
[58] J. Xu, B. Gao, K.-F. Huo, P.K. Chu, Recent Progress in Electrode Materials for Nonaqueous Lithium-Ion Capacitors, J. Nanosci. Nanotechnol. 20 (2020) 2652–2667. https://doi.org/10.1166/jnn.2020.17475.
[59] B. Li, J. Zheng, H. Zhang, L. Jin, D. Yang, H. Lv, C. Shen, A. Shellikeri, Y. Zheng, R. Gong, J.P. Zheng, C. Zhang, Electrode Materials, Electrolytes, and Challenges in Nonaqueous Lithium-Ion Capacitors, Adv. Mater. 30 (2018) 1705670. https://doi.org/10.1002/adma.201705670.
[60] C. Han, H. Li, R. Shi, L. Xu, J. Li, F. Kang, B. Li, Nanostructured Anode Materials for Non-aqueous Lithium Ion Hybrid Capacitors, Energy Environ. Mater. 1 (2018) 75–87. https://doi.org/10.1002/eem2.12009.
[61] S.S. Zhang, Dual-Carbon Lithium-Ion Capacitors: Principle, Materials, and Technologies, Batter. Supercaps. 3 (2020) 1137–1146. https://doi.org/10.1002/batt.202000133.
[62] L. Jin, C. Shen, A. Shellikeri, Q. Wu, J. Zheng, P. Andrei, J.-G. Zhang, J.P. Zheng, Progress and perspectives on pre-lithiation technologies for lithium ion capacitors, Energy Environ. Sci. 13 (2020) 2341–2362. https://doi.org/10.1039/D0EE00807A.
[63] J. Zhang, X. Liu, J. Wang, J. Shi, Z. Shi, Different types of pre-lithiated hard carbon as negative electrode material for lithium-ion capacitors, Electrochimica Acta. 187 (2016) 134–142. https://doi.org/10.1016/j.electacta.2015.11.055.
[64] A. Cappetto, W.J. Cao, J.F. Luo, M. Hagen, D. Adams, A. Shelikeri, K. Xu, J.P. Zheng, Performance of wide temperature range electrolytes for Li-Ion capacitor pouch cells, J. Power Sources. 359 (2017) 205–214. https://doi.org/10.1016/j.jpowsour.2017.05.071.
[65] K.S. Novoselov, A.K. Geim, S.V. Morozov, D. Jiang, Y. Zhang, S.V. Dubonos, I.V. Grigorieva, A.A. Firsov, Electric Field Effect in Atomically Thin Carbon Films, Sci. New Ser. 306 (2004) 666–669.
[66] M.S. Fuhrer, C.N. Lau, A.H. MacDonald, Graphene: Materially Better Carbon, MRS Bull. 35 (2010) 289–295. https://doi.org/10.1557/mrs2010.551.

[67] Y. Sun, L. Chen, L. Cui, Y. Zhang, X. Du, Molecular dynamics simulation of the effect of oxygen-containing functional groups on the thermal conductivity of reduced graphene oxide, Comput. Mater. Sci. 148 (2018) 176–183. https://doi.org/10.1016/j.commatsci.2018.02.037.

[68] T. Mahmoudi, Y. Wang, Y.-B. Hahn, Graphene and its derivatives for solar cells application, Nano Energy. 47 (2018) 51–65. https://doi.org/10.1016/j.nanoen.2018.02.047.

[69] C. Lee, X. Wei, J.W. Kysar, J. Hone, Measurement of the Elastic Properties and Intrinsic Strength of Monolayer Graphene, Science. 321 (2008) 385–388. https://doi.org/10.1126/science.1157996.

[70] S. Zhang, H. Wang, J. Liu, C. Bao, Measuring the specific surface area of monolayer graphene oxide in water, Mater. Lett. 261 (2020) 127098. https://doi.org/10.1016/j.matlet.2019.127098.

[71] A. Bianco, H.-M. Cheng, T. Enoki, Y. Gogotsi, R.H. Hurt, N. Koratkar, T. Kyotani, M. Monthioux, C.R. Park, J.M.D. Tascon, J. Zhang, All in the graphene family – A recommended nomenclature for two-dimensional carbon materials, Carbon. 65 (2013) 1–6. https://doi.org/10.1016/j.carbon.2013.08.038.

[72] S.S. Shams, R. Zhang, J. Zhu, Graphene synthesis: a Review, Mater. Sci.-Pol. 33 (2015) 566–578. https://doi.org/10.1515/msp-2015-0079.

[73] G. Ruhl, S. Wittmann, M. Koenig, D. Neumaier, The integration of graphene into microelectronic devices, Beilstein J. Nanotechnol. 8 (2017) 1056–1064. https://doi.org/10.3762/bjnano.8.107.

[74] Z. Zhang, A. Fraser, S. Ye, G. Merle, J. Barralet, Top-down bottom-up graphene synthesis, Nano Futur. 3 (2019) 042003. https://doi.org/10.1088/2399-1984/ab4eff.

[75] W.S. Hummers Jr, R.E. Offeman, Preparation of graphitic oxide, J. Am. Chem. Soc. 80 (1958) 1339–1339.

[76] T. Tene, G. Tubon Usca, M. Guevara, R. Molina, F. Veltri, M. Arias, L.S. Caputi, C. Vacacela Gomez, Toward Large-Scale Production of Oxidized Graphene, Nanomaterials. 10 (2020) 279. https://doi.org/10.3390/nano10020279.

[77] Q. Zhang, Y. Gao, Z. Xu, S. Wang, H. Kobayashi, J. Wang, The Effects of Oxygen Functional Groups on Graphene Oxide on the Efficient Adsorption of Radioactive Iodine, Materials. 13 (2020) 5770. https://doi.org/10.3390/ma13245770.

[78] D. Chen, H. Feng, J. Li, Graphene Oxide: Preparation, Functionalization, and Electrochemical Applications, Chem. Rev. 112 (2012) 6027–6053. https://doi.org/10.1021/cr300115g.

[79] A.T. Smith, A.M. LaChance, S. Zeng, B. Liu, L. Sun, Synthesis, properties, and applications of graphene oxide/reduced graphene oxide and their nanocomposites, Nano Mater. Sci. 1 (2019) 31–47. https://doi.org/10.1016/j.nanoms.2019.02.004.

# Chapter II. Lithium-sulfur batteries



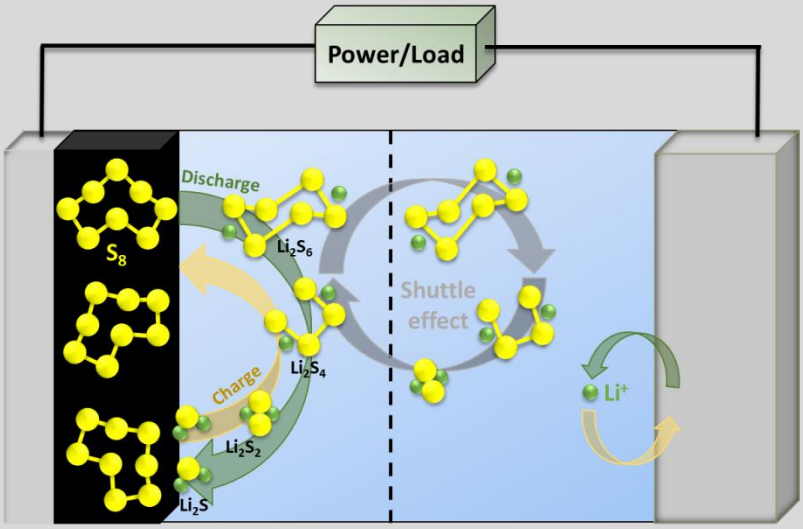

## 2.1. State-of-the-art of graphene-based materials for Li-S cathodes

Lithium-sulfur technology is moving forward by leaps and bounds towards overpassing conventional Li-ion batteries. However, shuttle effect, isolating nature of sulfur and large volume changes in the cathode during cycling largely hinder its large-scale commercialization. To solve these challenges, the encapsulation of sulfur into a conductive matrix has demonstrated to be a versatile approach [1]. On this regard, graphene-based materials have been appointed as a promising material to encapsulate sulfur particles. Their excellent electrical conductivity and mechanical properties can mitigate the isolating nature of sulfur and buffer the volume changes during cycling [2]. This can considerably increase the conductivity of the composite and boost it rate capability, allowing higher sulfur utilizations. Pristine graphene, referring to one-layer atom thickness defect-free graphene, has been considered as a promising encapsulating material do its unparalleled conductivity and electron transferring ability [3]. These features render graphene/S cathodes superior rate performance and sulfur utilization compared with other carbonaceous materials [4–6]. However, the non-polar nature of defect-free graphene also results in a poor compatibility with polysulfides, resulting in a fast capacity decay due to the unrestricted shuttle effect taking place in the cells [7,8]. On the other hand, GO, accounting with a low-associated cost and easy of fabrication, can benefit from the wide range of oxygen functional groups which endow this material with higher polarity than pristine graphene, allowing the chemical bonding of polysulfides [9,10]. Additionally, the hydrophilic nature of GO allow the incorporation of sulfur via multiple liquid methods, increasing sulfur loading and promoting homogenization [11–14]; as well as facilitate the fabrication of hierarchically porous structures such as aerogels [15–17]. Nevertheless, GO shows a lower electronic conductivity than pristine graphene or other carbonaceous materials. The combination with carbonaceous conductive additives (CNTs [18–20], porous carbons [17,21,22] or carbon spheres [23]) and its partial reduction using chemicals [24] or thermal [25] treatments have been proved to be effective approaches to improve the electronic conductivity without compromising the polarity of GO. Moreover, functional groups can serve as anchoring point for heteroatoms [26–28] or catalysts that promote sulfur conversion and/or polysulfide trapping [29–35]. **Table 2.1** summarizes the electrochemical performance of most representative graphene-based/sulfur cathodes.

***Table 2.1.*** *Summary of some representative works employing graphene-based/S cathodes including relevant electrochemical parameters for Li-S batteries.*

| Material | Sulfur content [wt.%]* | Sulfur mass loading [mg $cm^{-2}$] | Initial specific capacity (C-rate) [mAh $g^{-1}$]** | Initial areal capacity [mAh $cm^{-2}$] | Reversible capacity (after nth) [mAh $g^{-1}$] | Nº Cycles (% Retention) | Ref |
|---|---|---|---|---|---|---|---|
| PC-Graphene/S | 48.0 | - | 1400 (0.1C) | - | 380 at 1C (after 800 cy) | 800 (76%) | [5] |
| Graphene/S | 36.5 | 0.86 | 1500 (100 mA $g^{-1}$) | 1.29 | 840 at 200 mA $g^{-1}$ (after 100 cy) | 100 (53%) | [7] |
| rGO-CNF/S | 85.0 | 15.8 | 1360 (0.1C) | 21.5 | 1028 at 0.5C (after 600 cy) | 600 (83%) | [15] |
| NrGO-Graphene/S | 70.0 | 8.20 | 1256 (0.1C) | 10.3 | 804 at 0.4C (after 300 cy) | 300 (82%) | [16] |
| PC-GO/S | 70.0 | 2.00 | 1386 (0.1C) | 2.77 | 670 at 0.2C (after 400 cy) | 400 (68%) | [17] |
| NrGO-CNT/S | 53.5 | 1.60 | 1049 (0.1C) | 1.68 | 464 at 0.5C (after 500 cy) | 500 (61%) | [20] |
| PC-rGO/S | 41.2 | 1.23 | 1500 (0.1C) | 1.85 | 341 at 1C (after 500 cy) | 500 (43%) | [22] |
| NrGO/S | 53.2 | 1.20 | 1413 (0.1C) | 1.69 | 526 at 1C (after 1000 cy) | 1000 (61%) | [26] |
| rGO-$TiO_2$/S | 50.4 | 1.30 | 1116 (0.2C) | 1.46 | 831 at 1C (after 200 cy) | 200 (98%) | [33] |
| rGO-VN/S | 56.0 | 3.00 | 1447 (0.2C) | 4.35 | 917 at 1C (after 200 cy) | 200 (81%) | [34] |

*Sulfur content in the electrode

**C-rate according to the theoretical specific capacity of sulfur (1C= 1675 mA $g^{-1}$)

It should be highlighted, that despite the large initial specific capacities achieved in some of the works (1000 – 1500 mAh $g^{-1}$), the sulfur content in those cathodes is generally below the 60 wt.%, while sulfur loadings are rarely above 2 mg $cm^{-2}$. As result, besides some exceptions [15,16,36–38], areal capacities reported in literature are considerably lower than that of conventional Li-ion batteries (4 mAh $cm^{-2}$). Thus, researches on new graphene-based cathodes that can host large sulfur loadings are crucial to meet the requirements of practical Li-S batteries.

## 2.2. HrGO wrapping sulfur particles

Taking into account the aforementioned issues, this section of the thesis is devoted to the preparation of high sulfur loaded graphene-sulfur composites to be used as cathodes for Li-S batteries. Partially reduced graphene oxide obtained by the hydrothermal treatment of a home-made GO suspension is investigated as sulfur host. By controlling the time and reaction temperature, the hydrothermal treatment partially reduces graphene oxide (HrGO) sheets and thus increase their electronic conductivity compared to GO. Moreover, this methodology uses water as the reducing agent, thus avoiding the use of toxic/hazardous chemicals and giving rise to a clean HrGO dispersion that can be directly used in subsequent water-based processes. In this approach, a colloidal suspension of sulfur particles is mixed with HrGO to form the final composite. Sulfur suspension is prepared through a green route using sodium thiosulfate as sulfur precursor in the presence of polyvinyl pyrrolidone (PVP) as capping agent to control the growth of sulfur particles.

### 2.2.1. Sulfur composites and electrodes preparation

Graphite oxide was obtained through a modified Hummers' method [39]. Briefly, 240 mL of concentrated $H_2SO_4$ and 5 g of sodium nitrate $NaNO_3$ were added slowly under vigorous stirring to a 250 mL round bottom flask containing 5 g of graphite powder. Then, 30 g of $KMnO_4$ was added to the reaction mixture while the flask was held on an ice bath, followed by stirring for 3 h at 30 °C. Afterwards, 1 L of $H_2O_2$ (3%) was added to the flask. The resulting graphite oxide was treated with 5% HCl and then washed several times with distilled water followed by centrifugation until neutral pH. After drying, graphite oxide was dispersed in 200 mL of water and ultrasonicated at 30 °C for 2 h, yielding an aqueous GO dispersion with a concentration of 2.3 g $L^{-1}$. HrGO was obtained by hydrothermal reduction of the GO suspension (1 g $L^{-1}$) in a Teflon-lined reactor at 150 °C for 3 h.

On the other hand, a sulfur colloidal dispersion was prepared by disproportionation reaction of 3 g of sodium thiosulfate ($Na_2S_2O_3$) dissolved in 0.5 L of water by the further addition of 24 mL of concentrated hydrochloric acid (**Reaction 2.1**).

$$Na_2S_2O_3(aq) + HCl(aq) \rightarrow \downarrow \boldsymbol{S}(\boldsymbol{s}) + SO_2(g) + NaCl(aq) + H_2O \qquad \textbf{(2.1)}$$

Shape and size of sulfur particles in the dispersion were controlled by adding 1.6 g of PVP. Finally, for the preparation of HrGO-PVP/S composite, 40 mL of HrGO suspension were mixed with 20 mg of commercial conductive carbon (Super C, C65) and in-situ prepared sulfur dispersion. Synthetic route followed for the preparation of HrGO-PVP/S composite is depicted in **Scheme 2.1**. For the sake of comparison, PVP-free composite (HrGO/S), non-reduced graphene composite (GO/S) and a sample prepared in the absence of graphene (Sulfur) were prepared.

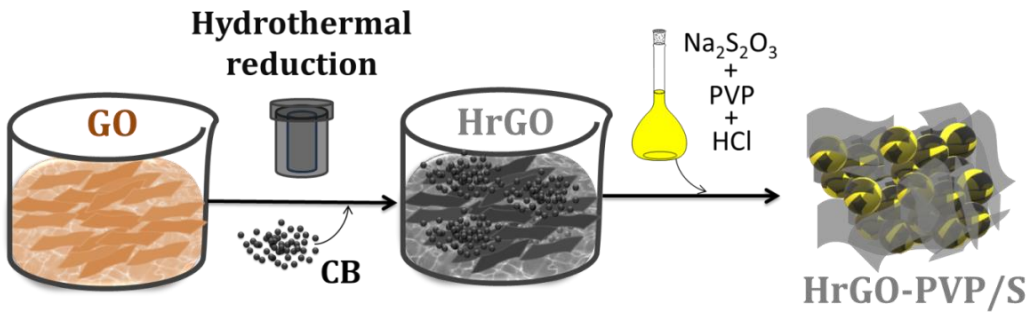


***Scheme 2.1.*** *Schematic representation of the synthetic route followed for the preparation of HrGO-PVP/S.*

In order to prepare laminates for further electrochemical characterization, composites were mixed with carbon black and polyvinylidene difluoride (PVDF) in N-methyl-2-pyrrolidone (NMP) in an 80:10:10 mass ratio. These slurries were then deposited onto a carbon-coated aluminum foil using the doctor blade technique and dried under vacuum overnight. Electrode discs of 12 mm in diameter and typical sulfur mass loadings of 1.3-1.6 mg $cm^{-2}$ were cut and further dried prior to cell assembly. CR2032 type coin cells were assembled in an argon-filled glovebox using lithium discs as counter and reference electrode. The electrolyte used was a 1 M solution of lithium bis(trifluoromethanesulfonyl)imide (LiTFSI) in a 1:1 (v/v) mixture of 1,2-dimethoxy ethane (DME) and dimethyl 1,3-dioxolane (DOL) containing 2 wt.% $LiNO_3$. The sulfur/electrolyte ratio was optimized to 1/20 for this kind of composites. Capacity and current density values are referred to the mass of elemental sulfur in the electrodes.

### 2.2.2. Physicochemical characterization of graphene-sulfur composites

From **Figure 2.1** it can be noticed that under the mild selected hydrothermal conditions, the partially reduced graphene oxide still maintains a good dispersion in water, which could favor the homogeneous wrapping of sulfur particles. Moreover, the change in color from light-brown to black undergone by the GO suspension evidenced the removal of oxygenated functional groups [40].

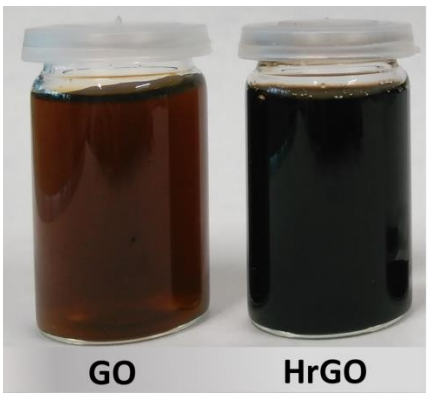


***Figure 2.1.*** *Digital photographs of GO (left side) and HrGO (right side) suspensions.*

Nuclear magnetic resonance (NMR) studies were conducted to gain quantitative information about the nature and ratio of the oxygenated functional groups present on the graphene-based matrixes. The solid-state NMR spectra recorded for HrGO and GO samples are shown in **Figure 2.2**. The spectra were deconvoluted considering several signals at different chemical shifts. The assignment of chemical shifts to the different functional groups is based in the very good agreement existing between the experimental values obtained from the NMR experiments and the values reported in the literature [41–43]. From the intensity of the signals and the contribution of each deconvolution peak to the overall curve, it can be inferred that under selected hydrothermal conditions, superheated water catalyzes bond cleavage of the oxygen moieties in the GO, leading to a significant reduction of the overall number of oxygen-containing functional groups. The difference is nevertheless non homogeneous, being the ether groups the most prompted for reduction. According to the NMR spectrum

registered for the HrGO sample, a 37 wt.% of oxygen can be estimated in this sample, which is significantly lower than the 50 wt.% measured for the pristine GO.

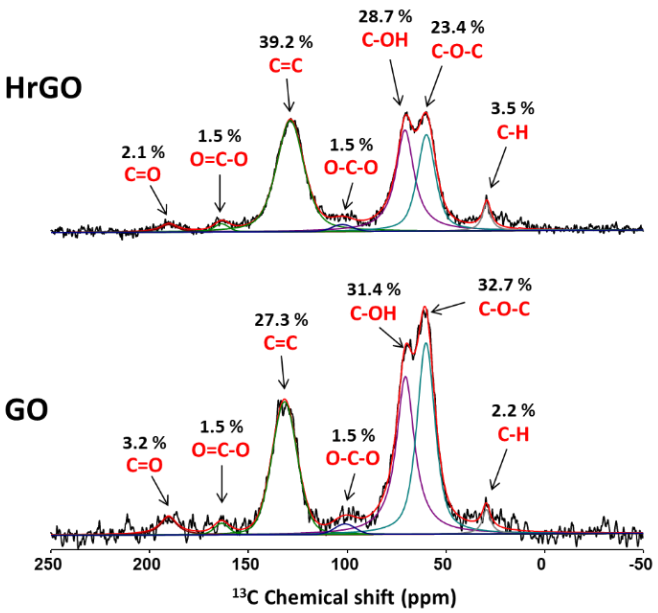


***Figure 2.2.*** *$^{13}$C solid state NMR of HrGO and GO samples. The result of the deconvolution is shown in the spectra together with the signal assignments and the relative populations.*

After the incorporation of sulfur into the graphene-based matrix, elemental analysis was performed to determine the amount of sulfur in the composites. The data show that the sulfur content in the GO/S, HrGO/S and HrGO-PVP/S samples correspond to 92.0, 90.3 and 85.6 wt.%, respectively. It is worth highlighting that the overall sulfur content obtained in both composites and electrodes in the present study is among the highest reported in literature [44–49]. X-Ray diffraction (XRD) patterns of the composites were registered and depicted in **Figure 2.3a**. They clearly show very intense diffraction peaks associated to the crystalline orthorhombic phase of sulfur (JCPDS No. 08-0247). Raman spectra recorded for the composites further confirm the presence of sulfur and graphene-based matrix within the composites (**Figure 2.3b**). All the spectra clearly show three sharp peaks registered at ca. 152, 217 and 472 $cm^{-1}$, which are assigned to the $e_2$, $a_1$ and $e_1$ symmetry vibration modes of S-S bonds in orthorhombic sulfur, according to literature [50]. In addition, two broad Raman peaks

assigned to the D-band and G-band of graphite are observed at about 1598 and 1350 $cm^{-1}$, respectively [51]. When D/G area ratios were calculated from the curve integration, values of ca. 1.12, 1.23 and 1.22 were obtained for the GO/S, HrGO/S and HrGO-PVP/S samples, respectively. These results support the reduction undergone by GO upon hydrothermal treatment since ratio of D to G band increases after thermal treatment of graphene-based materials due to removal of oxygen functionalities in form of $CO_2$/CO gases which induce the formation of defects in the rGO lattice.

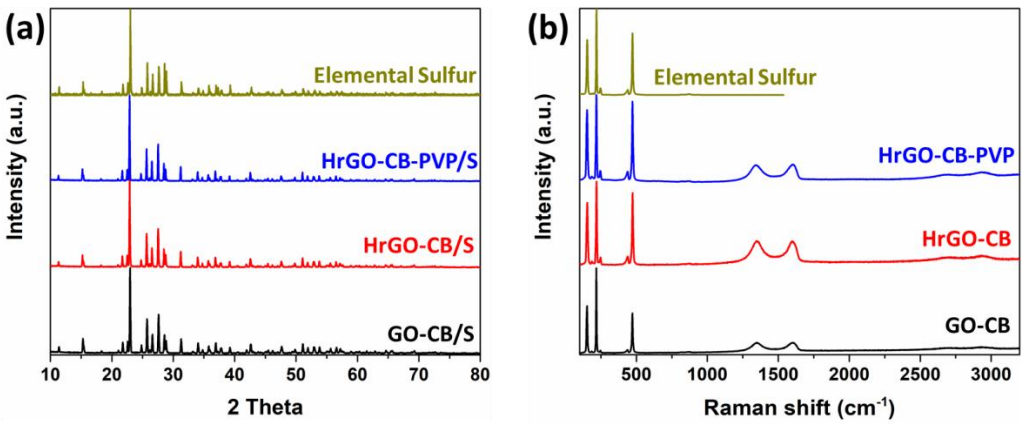


***Figure 2.3.*** *XRD* ***(a)*** *and Raman* ***(b)*** *measurements for labelled sulfur-based composites.*

The morphology and microstructure of these samples were furtherly evaluated by scanning electron microscopy (SEM). As it can be noticed from **Figure 2.4**, spherical-shaped sulfur particles efficiently covered by graphene sheets were obtained. Great morphological similarities between GO/S (**Figure 2.4a**) and HrGO/S (**Figure 2.4b**) can be attributed to the good dispersibility of both GO and HrGO in water, which allows a good covering of the sulfur particles. In addition, higher roughness of the graphene-based matrix is noticed for the HrGO composite, which is typical from reduced graphene oxide materials. In both cases, sulfur particles of 5-10 µm size were obtained. On the other hand, HrGO-PVP/S pictures (**Figure 2.4c** and **d)**, shows that PVP acted efficiently as capping agent, resulting on a considerable reduction of the particle size. In this later case, sulfur particle diameters were determined to be approximately 600 nm, which is almost one order of magnitude smaller compared to the composites prepared in the absence of PVP.

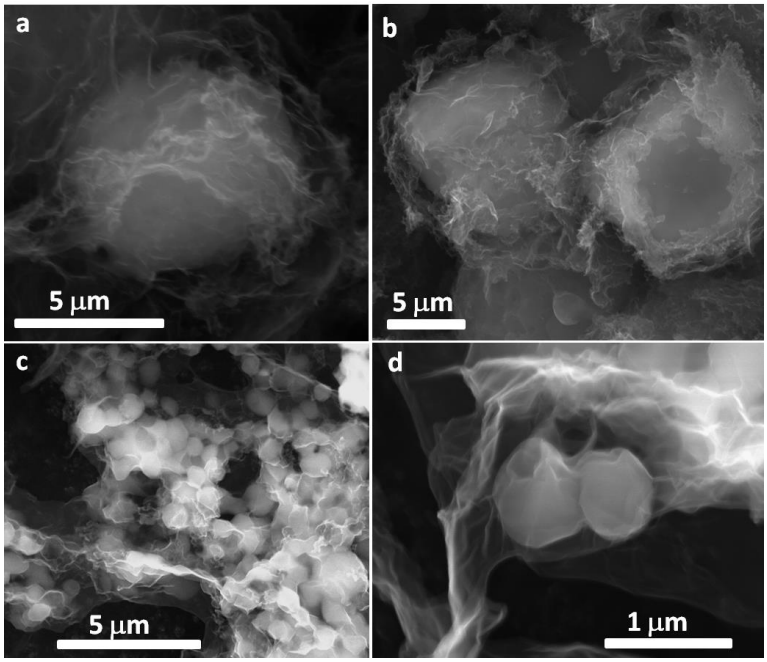


***Figure 2.4.*** *SEM images of GO/S (**a**), HrGO/S (**b**) and HrGO-PVP/S (**c** and **d**).*

### 2.2.3. Electrochemical characterization of graphene-sulfur composites

In order to test the electrochemical performance of the different samples, coin cells were assembled and galvanostatically cycled at a current density of 0.2C (1C = 1675 mA $g^{-1}$). **Figure 2.5a** shows representative galvanostatic charge-discharge profiles of each composite. Characteristic Li-S discharge plateaus are observed at ca. 2.3 and 2.1 V for the HrGO-based composites, corresponding to high-order and low-order polysulfide formation, respectively. However, for GO/S composite and sulfur pristine sample, the first discharge plateau is inappreciable and large polarization is observed. This results in shortened charge/discharge processes, thus considerably reducing specific capacity values. This behavior could be strongly related to the low electronic conductivity associated to large amount of oxygen functional groups in the GO matrix and the isolating nature of sulfur. **Figure 2.5b** shows the cycling performance and coulombic efficiency of the different composites under galvanostatic cycling tests with two activation cycles at a current density of 0.1C and then the subsequent cycles at 0.2C. The initial capacity was 213, 877, 975 and 1021 mAh $g^{-1}$ for Sulfur, GO/S, HrGO/S and HrGO-PVP/S, respectively. It can be appreciated that the low

conductivity of elemental sulfur results in an extremely low specific capacity during the whole cycling. Regarding the graphene-based composites, after the first activation cycles, GO/S shows a drastic capacity drop of a 43% due to the increment of current density, remarking the poor conductivity of the GO. On the other side, capacity drop of the more conductive HrGO composites is only 7% in both cases. For the first cycle at 0.5C, HrGO-based composites exhibited higher specific capacities, 944 mAh $g^{-1}$ (HrGO-PVP/S) and 825 mAh $g^{-1}$ (HrGO/S), than the GO-based composite (503 mAh $g^{-1}$). After 100 cycles, the HrGO-PVP/S composite maintained 631 mAh $g^{-1}$ (67%), while HrGO/S and GO/S retained 517 (63%) and 420 mAh $g^{-1}$ (84%), respectively. The larger number of polar groups present in the GO may favor the trapping of polysulfide species; however, its poorer electronic conductivity leads to lower capacity values. It is worth noting the high coulombic efficiency observed for all composites is close to 100%.

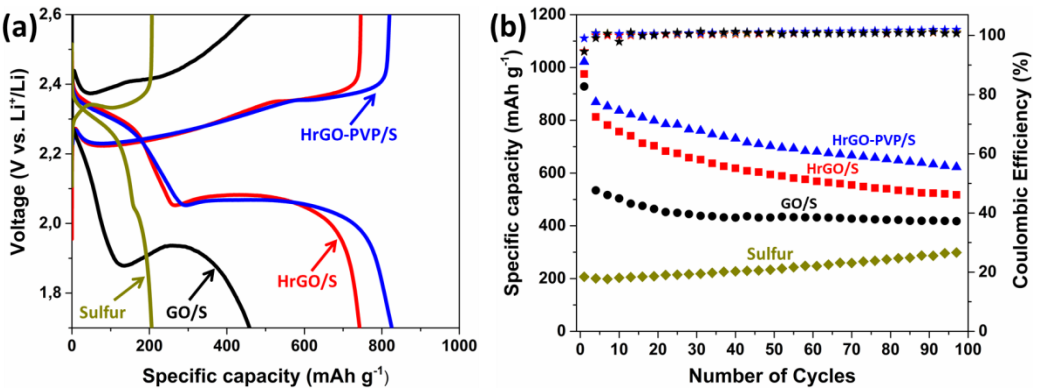


***Figure 2.5.*** *Galvanostatic curves of the 10th cycle (**a**) and specific capacity evolution upon cycling measured at 0.2C (**b**) of labelled sulfur-based composites.*

**Figure 2.6** shows long-term cycling tests performed at the high current density of 1C for the graphene-based composites. On one hand, the low conductivity of the GO/S does not support the high-density current employed and values below 200 mAh $g^{-1}$ are obtained during the cycling process with a very unstable coulombic efficiency. On the other hand, HrGO-based composites demonstrate stable cycling after some initial activation cycles. In the case of HrGO/S more than 100 activation cycles are needed and strong capacity fluctuations are observed after reaching its maximum specific capacity (435 mAh $g^{-1}$). In contrast, the smaller sulfur particle size of HrGO-PVP/S

result in a faster activation of only 50 cycles and higher maximum gravimetric capacity value of 503 mAh $g^{-1}$. This result is very promising attending to the high current employed (1.675 A $g^{-1}$), and the high sulfur content on the electrode. It is worth noting that for HrGO-PVP/S, a 35% capacity loss was observed after the activation process, corresponding to a capacity degradation of 0.07% per cycle. Nevertheless, the coulombic efficiency dropped below 95% after 150 cycles, indicating a progressive failure trapping polysulfides in the graphene-based matrix, most probably due to the sulfur redistribution upon long term cycling at high current density.

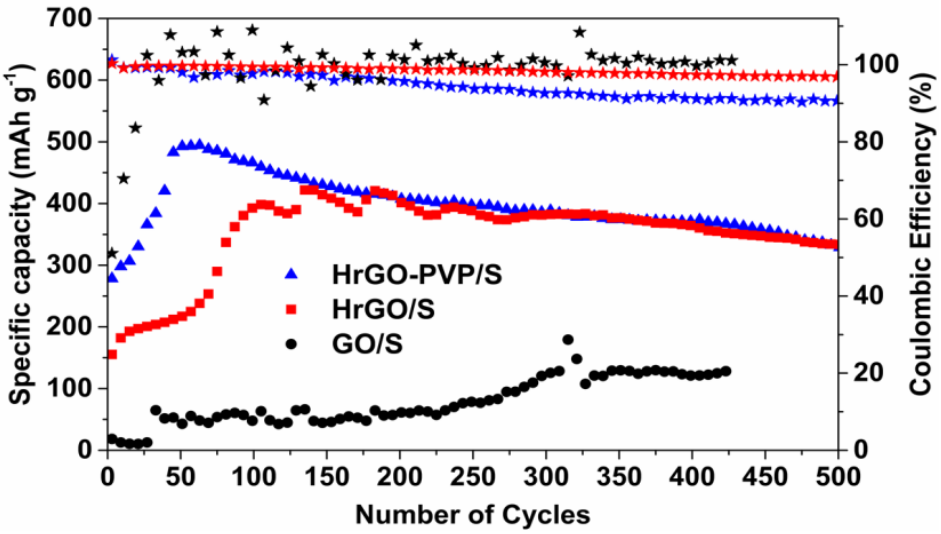


***Figure 2.6.*** *Long-term cyclability studio at 1C for labelled sulfur-based electrodes.*

Due to its promising electrochemical performance, capacity evolution at different current densities was evaluated for the HrGO-PVP/S composite (**Figure 2.7**). By increasing charge/discharge rates from 0.1C to 1C every 10 cycles, the material shows high reversible capacities of 1,033 mAh $g^{-1}$ at 0.1C, 716 mAh $g^{-1}$ at 0.2C, 654 mAh $g^{-1}$ at 0.5C and 588 mAh $g^{-1}$ at 1C, recovering 719 mAh $g^{-1}$ when the current was restored to 0.1C. The stable behavior and little capacity drop at high current densities indicate good electronic conductivity, provided by the partially reduced graphene-based matrix, and fast reaction kinetics, favored by the small particle size and homogeneous distribution of sulfur. Reduced particle size provides a better electrochemical

performance due to several factors. First, electronic contact between the matrix and sulfur particles is improved considerably with the consequent increment of conductivity, leading to higher capacity values. Second, a decrease of sulfur particle size entails a shortening of the diffusion pathways, which results beneficial in terms of high current density behavior. Third, sub-micrometer particle size results in better coverage by the conductive matrix, creating a barrier that prevents the migration of high-order polysulfides [25].

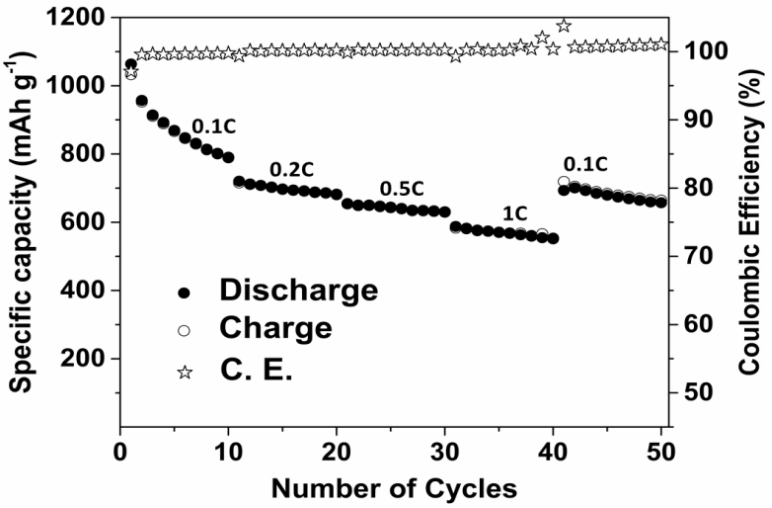


***Figure 2.7.****HrGO-PVP/S composite galvanostatically cycled at several C-rates.*

For the sake of comparison in **Table 2.2** are summarized some representative results obtained in previous studies, which followed a similar procedure for both the electrode (lamination) and the composite preparation (sulfur obtained from $Na_2S_2O_3$) and with sulfur loading above 70 wt.%. However, even if these composites reach a high sulfur loading, it is worth to note that the final sulfur content in the electrodes is significantly decreased from the addition of inactive materials such as binders or conductive carbons during the lamination process. Taking this into account, only one of the studies reported higher electrode sulfur content [52]. Besides, none of them reaches specific (630 mAh $g^{-1}$) or areal capacities (ca. 1 mAh $cm^{-2}$) as high as reported in this study at the 100$^{th}$ cycle at 0.2C. In addition, number of cycles reported not

exceed 200$^{th}$ in any of the cases, while in this work 500$^{th}$ cycles are reached with an outstanding stability at high current density (1.675 A g$^{-1}$).

***Table 2.2.*** *State-of-the-art of different high-sulfur content composites prepared by lamination using $Na_2S_2O_3$ as sulfur precursor.*

| Material | %S in the composite (wt.%) | %S in the electrode (wt.%) | Sulfur loading (mg cm$^2$) | Specific capacity* (mAh g$^{-1}$) | Areal capacity* (mAh cm$^{-2}$) | Number of cycles | Reference |
|---|---|---|---|---|---|---|---|
| **GO/S** | 86 | 60 | 1.0 | 390 | 0.39 | 200 | [13] |
| **GO-CB/S** | 70 | 56 | - | 560 | - | 140 | [14] |
| **GO/S** | 80 | 56 | - | 400 | - | 100 | [47] |
| **rGO/S** | 91 | 77 | 2 | 430 | 0.86 | 100 | [52] |
| **rGO-PPy/S** | 73 | 44 | 0.7-0.9 | 450 | 0.32 - 0.40 | 200 | [53] |
| **HrGO-PVP/S** | **86** | **69** | **1.5** | **630** | **0.95** | **500** | **This work** |

*Specific and areal capacities calculated at 0.2C and referred to the 100$^{th}$ cycle

The influence of graphene-based matrix reduction degree and sulfur particle size over cell resistance was furtherly evaluated by electrochemical impedance spectroscopy (EIS). Measurements were conducted in three-electrode cells in the fully charged state to monitor the changes in electrode resistance during the first cycles (**Figure 2.8**). The characteristic resistances for the different electrochemical processes were calculated according to the equivalent circuit shown in **Figure 2.8a**. EIS spectra of all composites after activation cycles at 0.1C (**Figure 2.8b**) show two semicircles at high and medium frequency and a linear region at the low frequency range. The value of resistance registered at the highest frequency corresponds to the electrolyte resistance ($R_e$). The semicircle at high frequencies is related to the interphase contact resistance ($R_{SL}$) and associated capacitance ($C_{SL}$), and the middle-frequency semicircle corresponds to the charge transfer resistance ($R_{CT}$) and its double layer capacitance ($C_{DL}$). GO/S composite exhibits much larger impedance than the materials based on HrGO, showing a clear difference in the size of the high frequency semicircle, related to surface layer resistance. This could indicate lower conductivity of GO compared to HrGO or could be the result of a stronger interaction of functional groups present in larger amount on the GO's surface [54]. On the other hand, HrGO-based composites show smaller high frequency semicircles, less resistive due to higher reduction degree. **Figure 2.8c** shows the impedance response evolution of HrGO-PVP/S composite upon cycling. After the

first cycle a change on the interfacial properties and on the charge transfer is evident. Both $R_{SL}$ and $R_{CT}$ are reduced during the redistribution of sulfur active materials on the graphene network, favored by the good conductivity of HrGO and the small particle size of precipitated sulfur capped by the PVP. During the following cycles, impedance spectra of HrGO-PVP/S electrode vary very little, only with minor decrease in charge transfer resistance.

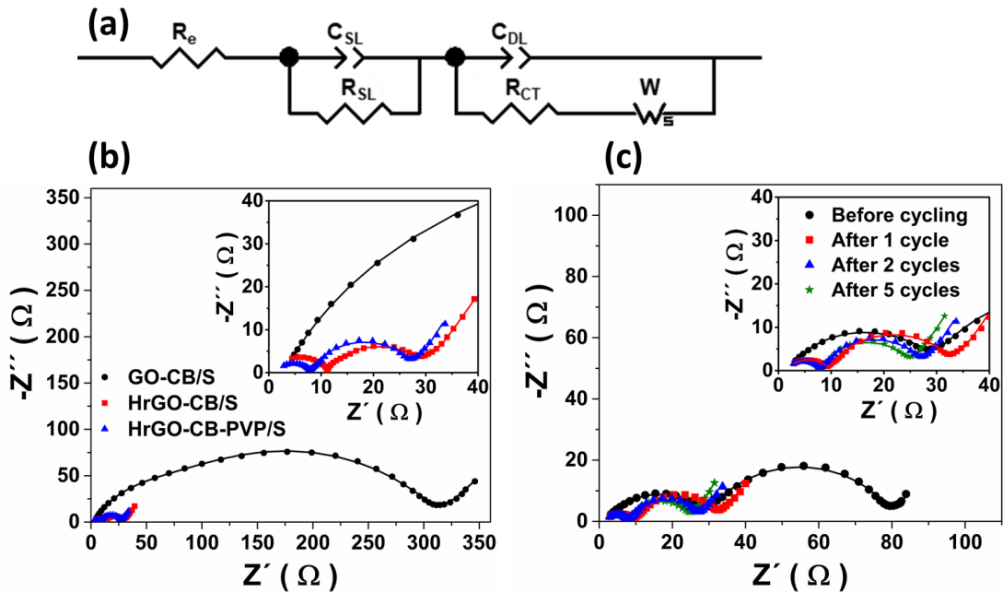


***Figure 2.8.*** *Equivalent circuit (**a**) and Nyquist plots for the noted samples after activation cycles at 0.1C (**b**) and for HrGO-PVP/S upon cycling (**c**).*

The parameters extracted by fitting the EIS data of HrGO-PVP upon cycling are shown in **Table 2.2**. In this model, nonideal behavior of porous and rough surfaces are compensated using constant phase elements (CPE) instead of capacitors. Thus, $C_{SL}$-T and $C_{DL}$-T reflect "pseudocapacitance" values, while $C_{SL}$-P and $C_{DL}$-P are their corresponding phase parameters. A phase parameter close to 1 or 0 reflects a behavior close to a pure capacitor or to a resistance, respectively. According to Gao et al. [47], the adsorption of polysulfide species also affect the capacitance, therefore its interpretation is more complex. The interphase contact resistance, $R_{SL}$, decreases from the first cycle at 0.1C, 8.334 Ω, to the second cycle at 0.2C, 6.885 Ω, then the

resistance increased slightly to 7.264 Ω. These changes reflect a redistribution of the sulfur at the initial cycles, followed by a relatively stable situation with growth of a thin insulating $Li_2S$ surface layer, explaining the increased interphase resistance. On the contrary, charge transfer resistance, $R_{CT}$, decreases slightly but continuously during the five cycles, suggesting minor losses of active material due to dissolution. Warburg impedance fitting returns three parameters, W-R, W-T and W-P, related to the diffusion resistance, diffusion coefficient and the phase parameter. The term associated to diffusion resistance, interestingly does not follow the trend of $R_{CT}$, but that of the interphase resistance, $R_{SL}$. The term assigned to the diffusion coefficient remains virtually unaltered after one cycle at 0.1C and after a second cycle at 0.2C, to increase considerably after the fifth cycle at 0.2C, pointing at a weakened $Li^+$ diffusion upon cycling as the interphase resistance increases.

***Table 2.3.*** *Summary of some relevant parameters calculated from the fitting of the electrochemical impedance spectroscopy curves.*

| | $R_e$ (Ω) | $R_{SL}$ (Ω) | $C_{SL}$-T | $C_{SL}$-P | $R_{CT}$ (Ω) | $C_{DL}$-T | $C_{DL}$-P | W-R | W-T | W-P |
|---|---|---|---|---|---|---|---|---|---|---|
| **After 1 cycle** | 1.3 | 8.3 | 4.9E-5 | 0.66 | 23.8 | 4.3E-3 | 0.76 | 59.2 | 124.7 | 0.70 |
| **After 2 cycles** | 1.3 | 6.8 | 2.9E-5 | 0.70 | 19.7 | 4.7E-3 | 0.79 | 54.8 | 122.1 | 0.72 |
| **After 5 cycles** | 1.0 | 7.3 | 3.6E-5 | 0.67 | 17.0 | 5.2E-3 | 0.82 | 93.8 | 245.8 | 0.70 |

## 2.3. Graphene-based aerogels as sulfur matrix

In the last section, the composites prepared from partially reduced graphene oxide have demonstrated to enhance the performance of Li-S batteries in terms of cyclability, rate performance and specific capacity values. However, even if the sulfur content in the processed electrodes is considerably high (ca. 70%), the sulfur loading (1.5 – 1.7 mg $cm^{-2}$) is still insufficient to fulfill the requirements of practical Li-S batteries [36]. Taking this into account, this section is devoted to the preparation of three-dimensional, self-standing graphene aerogels as high-sulfur loading cathodes. The processing of graphene-based electrodes as macroporous sponges not only can help to increase the amount of sulfur loaded, but also facilitate the diffusion of the

electrolyte to the whole surface of the cathode [55]. Moreover, the absence of binder within the electrodes can be also strongly beneficial, since binders are not active materials but in contrast it may have a negative impact by blocking pores and decreasing electronic conductivity [56]. The large amount of oxygen functionalities of graphene oxide allows this material to be processed as self-standing aerogels by a simple freeze-freeze drying process. However, as previously remarked, the high oxygen content in the GO may be a double-edged sword. On one hand, it can favor the chemical trapping of polysulfides by chemical bonding, improving the efficiency and capacity retention of the cell; but in the other hand, decreases its electric conductivity, leading to lower sulfur utilization and rate capability. On this regard, two different approaches are followed to improve the electric conductivity of the GO-based aerogels. The first one relies on the incorporation of CNTs within the graphene-based architecture, which is expected to lead to an improvement of the electronic conductivity of the samples due to the generation of a conductive network along the graphene oxide sheets [57]. The second one is based on the partial reduction of GO self-standing discs by thermal treatment which would lead to the removal of oxygenated functional groups present in the GO structure, and partially restoring the $sp^2$ graphitic character of the materials with its subsequent improvement on the electronic conductivity [58].

### 2.3.1. Graphene-based aerogels and composites preparation

Graphene-based aerogels have been prepared from a commercially available GO suspension supplied by Graphenea. For the preparation of GO-CNT aerogels, 2 mg of CNT (Sigma Aldrich, MWCNT) were added to 40 ml of a GO suspension (2 mg $mL^{-1}$) and vigorously stirred overnight. Then, suspension was frozen by its immersion in liquid nitrogen and then freeze-dried for 72 h. Aerogels obtained after the drying process were compacted and subsequently punched out to obtain discs of 12 mm in diameter. On the other hand, GO aerogels were prepared following the same route but in the absence of CNT. Reduced GO aerogels (hereafter denoted as rGO) were obtained by the thermal treatment of GO aerogel discs at 700 °C for 1 h under dynamic argon atmosphere (**Scheme 2.2**).

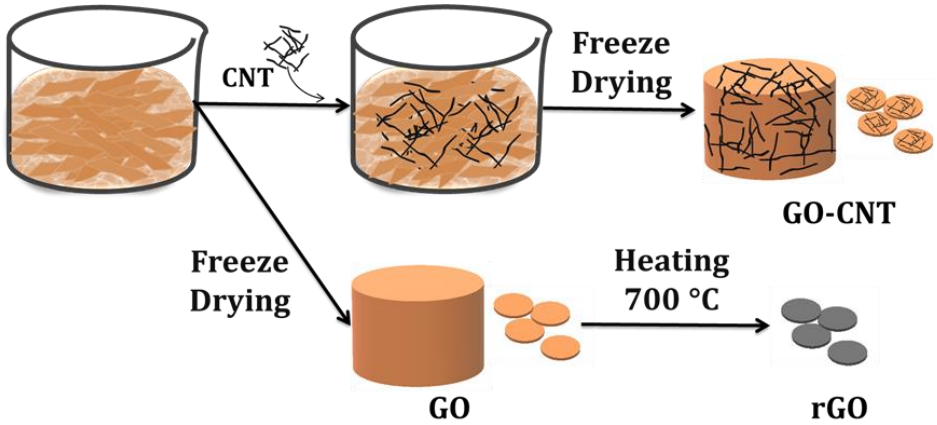


***Scheme 2.2.*** *Schematic representation of the preparation method followed for the preparation of GO-CNT, GO and rGO discs*

Sulfur composites were prepared by melt diffusion using the different graphene aerogels as supports. Briefly, a certain amount of commercial sulfur is dispersed in 2 mL of toluene under heating at 90 °C. Subsequently, single self-standing graphene-based aerogel pellets were added to the sulfur dispersion and heated until completely dry, then transferred to a furnace and heated at 155 °C for 12 h in order to obtain the different electrodes. Resulting self-standing electrodes, with typical thickness values of 300 ± 20 µm, were directly assembled as cathodes for Li-S batteries in CR2032 type coin cells. Lithium discs were used as counter and reference electrodes while the electrolyte used was 1M LiTFSI in a mixture 1:1 (v/v) of DME/DOL. The sulfur/electrolyte ratio was optimized to 1/30. Capacity and current density values are referred to the mass of elemental sulfur in the electrodes.

### 2.3.2. Physicochemical characterization of self-standing cathodes

As described in the previous section, composites were prepared by melt diffusion of sulfur into the graphene-based self-standing aerogels. The aerogels used to support sulfur were prepared by compacting and punching out different pieces of the monoliths obtained by the freeze/freeze-drying of both graphene oxide (**Figure 2.9a**) and graphene oxide-CNT suspensions. In order to compare the impact of the addition of a small amount of CNT *versus* the thermal reduction effect, some GO discs (**Figure 2.9b**) were thermally treated at 700 °C to yield rGO (**Figure 2.9c**). The partial reduction

is noticed by the color change, which turns from brown to black when aerogels are submitted to the thermal reduction treatment. It is worth noticing that the aspects of the aerogel wafers do not change significantly after the deposition of sulfur (**Figure 2.9d**), suggesting a good and homogeneous dispersion of sulfur within the surface of the three different aerogels.

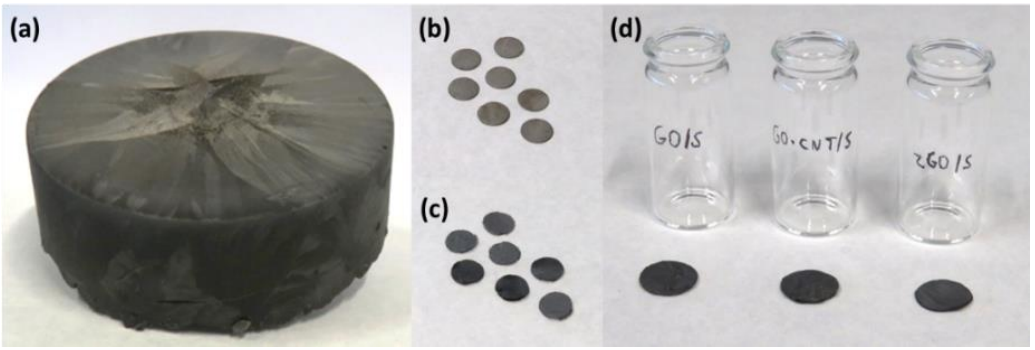


***Figure 2.9.*** *Digital photographs of GO monolithic aerogel [6.5 cm width / 2.5 cm height] (**a**), GO pellets (**b**), rGO pellets (**c**) and labeled composite electrodes (**d**) after the incorporation of sulfur.*

Morphology and microstructure of the sulfur-free aerogels were evaluated by SEM (**Figure 2.10**). Uniform graphene-sheet like morphology is observed for the different samples. However, a slight increase on the roughness is observed due to the thermal treatment from GO (**Figure 2.10a**) to rGO (**Figure 2.10b**). On the other hand, the incorporation of CNT does not show to have any influence over GO-CNT aerogel (**Figure 2.10c**) morphology.

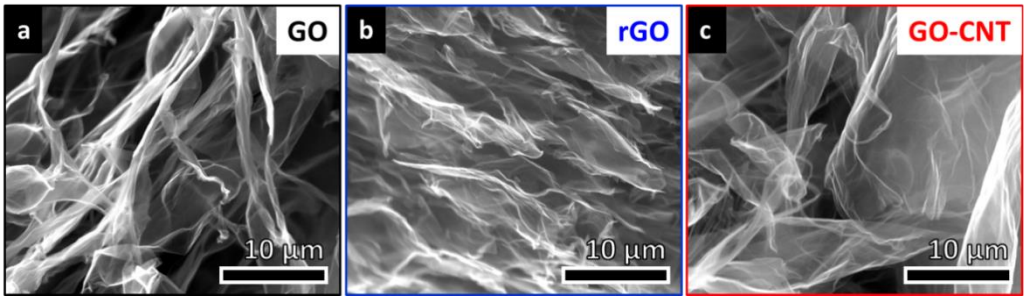


***Figure 2.10.*** *SEM images of GO (**a**), rGO (**b**) and GO-CNT (**c**) aerogels.*

Nitrogen adsorption-desorption isotherms registered for the three samples are depicted in **Figure 2.11a**. All of them show similar adsorption profiles matching with type-II isotherms according to the IUPAC classification [59]. These isotherms are characteristic of materials that contain macropores which, in these cases, are due to the interparticle voids generated between graphene sheets. BET specific surface area calculated for the different samples give values of 21, 47 and 53 $m^2 g^{-1}$ for the GO, rGO and GO-CNT, respectively. In good agreement with previous publications [60], the slight increase on the specific surface area observed in the thermally reduced sample is related to the partial reorientation and slight wrinkle of the graphene. On the other hand, the increase experimented by the GO-CNT sample can be assigned to the pillaring effect of CNT between some graphene-type layers, as previously observed [61]. The XRD patterns measured for the three different graphene-based aerogels are shown in **Figure 2.11b**. A prominent peak is observed between 15 and 30 degrees for the three composites, which can be indexed as the C(002) reflection corresponding to hexagonal structure of graphite [62]. In the case of GO and GO-CNT, the peak appears at ca. 17 degrees while for rGO at ca. 26 degrees. This shift towards larger angle is ascribed to the graphene interlayered distance, which is reduced upon thermal reduction treatment. In addition, the different orientation of the graphene sheets, characteristic of non-reduced graphene oxides, broads the peak at 17 degrees with respect to 26 degrees peak for rGO [63,64].

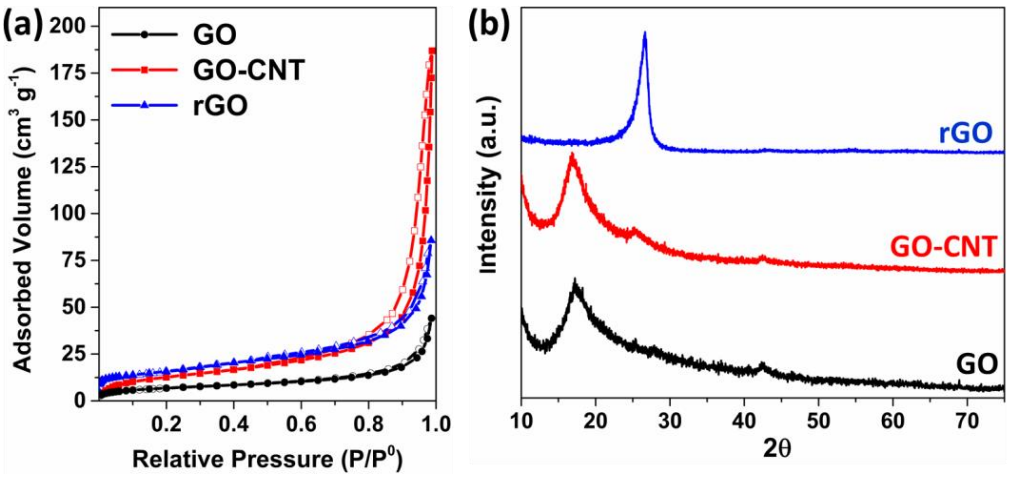


***Figure 2.11.*** *Nitrogen adsorption/desorption isotherms (**a**) and XRD spectra (**b**) for labelled graphene-based aerogels*

After sulfur infiltration on the graphene-based aerogels, sulfur content was measured by elemental analysis, showing values of ca. 70 % in weight for all the composites. Self-standing cathodes do not need to be further processed together with non-active materials such as binder or conductive additive, thus allowing higher sulfur content in the final electrode. Morphology and microstructure of the composites were evaluated by SEM (**Figure 2.12**). No significant morphological differences are observed between GO/S (**Figure 2.12a**) and rGO/S (**Figure 2.12b**), indicating that the pristine porous structure of GO is maintained after sulfur infiltration. Similar results are obtained in the case of the sample that contain CNTs; it seems that the incorporation of the CNT within the graphene aerogels (GO-CNT/S) do not significantly modify the macroporous structure of the composites as noticed from the cross-section image included in **Figure 2.12c**. High-magnification image using back scattered electron detector (**Figure 2.12d**) confirms the presence of CNTs uniformly distributed within the graphene layers. Moreover, the absence of sulfur agglomerates suggest that sulfur has been homogeneously distributed along the surface of the graphene sheets within the aerogels.

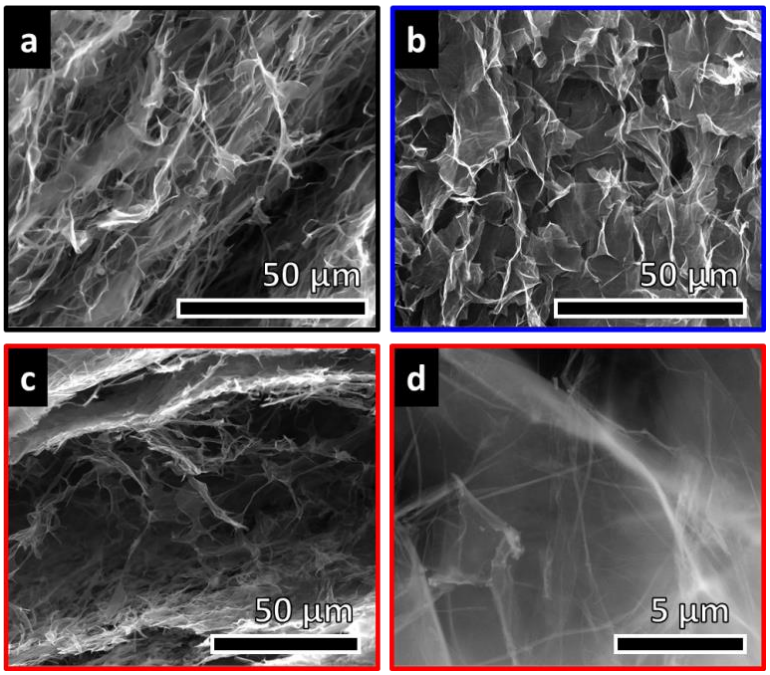


***Figure 2.12.*** *SEM pictures of GO/S (**a**), rGO/S (**b**) and GO-CNT/S (**c**) aerogels. Back scattered SEM image of GO-CNT/S registered at higher magnification (**d**).*

XRD study performed for the composites containing sulfur (**Figure 2.13a**), shows intense and narrow diffraction peaks ascribed to the orthorhombic phase of sulfur (JCPDS No. 08-0247). The Raman spectra registered for these materials (**Figure 2.13b**) show two broad Raman peaks observed at about 1351 and 1599 $cm^{-1}$, assigned to the G and D bands of graphite, respectively. From $I_D/I_G$ calculation, values of ca. 0.88, 0.90 and 0.99 were obtained for GO/S, GO-CNT/S and rGO/S respectively, indicating the reduction process undergone by GO to rGO in thermal treatment. A closer view at the Raman spectra registered within the 100-650 $cm^{-1}$ range (**Figure 2.13c**) show three peaks at ca. 155, 220 and 475 $cm^{-1}$ assigned to the $e_2$, $a_1$ and $e_1$ symmetry vibration modes of S-S bonds in orthorhombic sulfur [50]. In good agreement with previous works, the low intensity of the peaks suggests that crystalline sulfur clusters are homogeneously dispersed along the graphene surface [65,66].

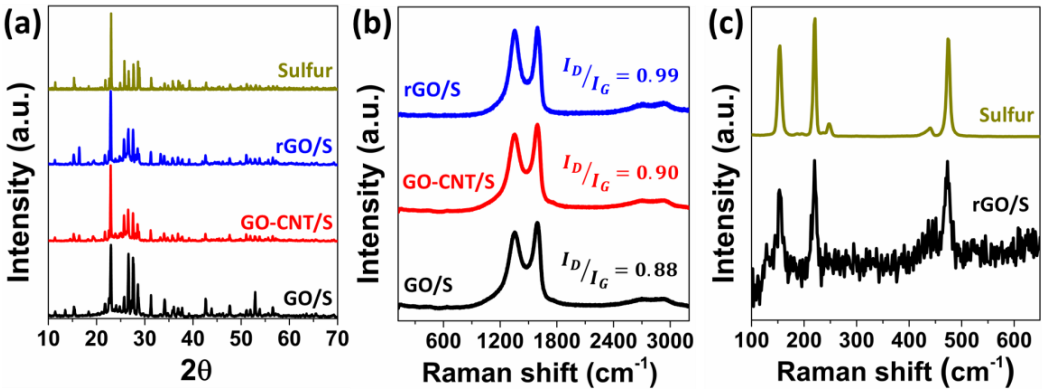


***Figure 2.13.*** *XRD (**a**) and Raman (**b**) measurements for labelled sulfur containing aerogels; and Raman spectra after several acquisitions of rGO/S aerogel (**c**).*

### 2.3.3. Electrochemical characterization of self-standing cathodes

To determine the influence of the addition of CNT and thermal reduction over GO electrodes, EIS study was performed in a three electrodes cell to the as-described materials. Obtained data were fitted using the equivalent circuit depicted in **Figure 2.14a**, which assumes an electrolyte or uncompensated resistance ($R_e$), a surface layer resistance ($R_{SL}$) and a charge transfer resistance ($R_{CT}$). It can be noted that GO/S (**Figure 2.14b**) and GO-CNT/S (**Figure 2.14c**) show a similar spectrum which is related to their non-reduced nature. Nevertheless, as predicted previously, CNT presence contributes

to create a conductive framework on the GO-CNT structure, decreasing considerably the resistance of the system. On the other side, rGO/S (**Figure 2.14d**) spectrum shows to be different from the previous one due to its reduced structure resultant from the thermal treatment. Although resistance on the first cycle is very large, a subsequent decrease is observed for the following cycles, indicating greater stability and a large activation time for the electrode to reach its maximum potential.

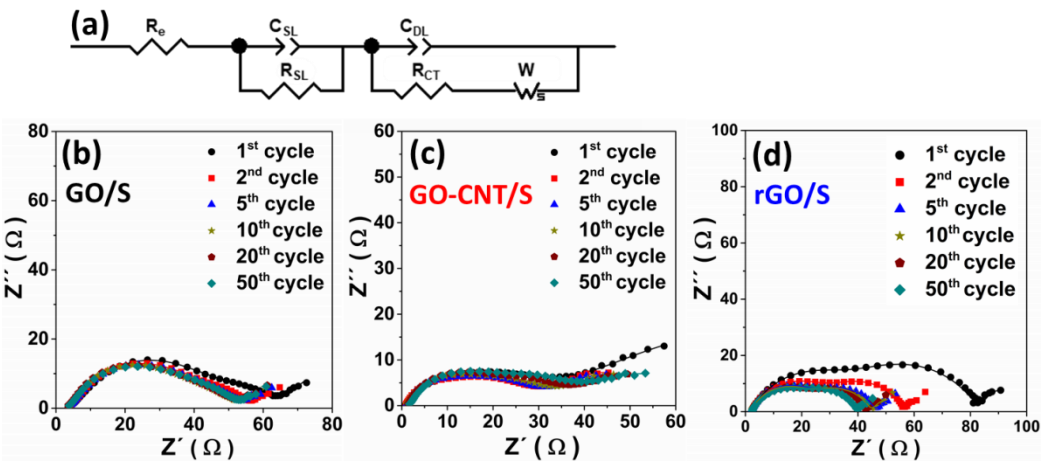


***Figure 2.14.*** *Equivalent circuit (**a**) and Nyquist plots for GO/S (**b**), GO-CNT/S (**c**) and rGO/S (**d**) self-standing electrodes.*

Charge transfer resistance and goodness of the fitting values are referred in **Table 2.4**.

***Table 2.4.*** *Charge transfer resistance values and goodness of the fitting (chi$^2$) of the composites upon cycling*

| Samples | | Cycle 1 | Cycle 2 | Cycle 5 | Cycle 10 | Cycle 20 | Cycle 50 |
|---|---|---|---|---|---|---|---|
| GO/S | $R_{CT}$ (Ω) | 44.25 | 36.46 | 34.30 | 31.98 | 32.33 | 35.13 |
| | $\chi^2$ | 6.73E-5 | 5.78E-5 | 4.11E-5 | 3.51E-5 | 5.98E-5 | 4.73E-5 |
| GO-CNT/S | $R_{CT}$ (Ω) | 25.00 | 20.68 | 19.42 | 17.42 | 17.61 | 21.93 |
| | $\chi^2$ | 4.52E-5 | 1.69E-5 | 2.99E-5 | 4.06E-5 | 4.46E-5 | 6.63E-5 |
| rGO/S | $R_{CT}$ (Ω) | 34.85 | 27.21 | 22.85 | 20.54 | 19.14 | 19.04 |
| | $\chi^2$ | 3.42E-4 | 1.32E-4 | 9.01E-5 | 1.04E-4 | 1.05E-4 | 1.19E-4 |

For a better comparison of the electrochemical performances, the three samples were cycled at different C-rates using electrodes with similar areal mass loadings (4 mg $cm^{-2}$) (**Figure 2.15a**). GO-CNT/S and rGO/S obtain similar initial areal capacities of 3.75 and 3.25 mAh $cm^{-2}$ respectively at 0.05C. On the other side, the lack of conductivity of GO results in much lower initial areal capacity values (ca. 1 mAh $cm^{-2}$). When increasing current density to 0.1C and 0.2C, it can be noted that the addition of CNT and thermal reduction leads to similar areal capacity values of ca. 2 mAh $cm^{-2}$ and ca. 1.75 mAh $cm^{-2}$ respectively. However, when increasing to 0.5C and 1C it can be perceived that carbon nanotubes do not provide enough conductivity to support the applied current and consequently lower capacity values are obtained for GO-CNT/S with respect to rGO/S which maintains values above 1 mAh $cm^{-2}$ at 0.5C and almost 0.75 mAh $cm^{-2}$ at 1C. Besides, it is worth noting that GO-CNT/S electrode exhibit a better cycling stability compared to rGO/S, which shows some capacity fluctuations. In addition, when returning to 0.1C, the GO-CNT/S electrode recovers the initial capacity with ca. 2 mAh $cm^{-2}$ in the 65$^{th}$ cycle with a capacity loss of only 3.3% in the last 20 cycles at 0.1C, while rGO/S electrode shows stronger fading, reaching values of ca. 1.75 mAh $cm^{-2}$ in the 65$^{th}$ cycle (9% capacity loss). From voltage curves represented in **Figure 2.15b** for the 50$^{th}$ cycle, two typical Li-S plateaus are observed at 2.25 and 2.05 V for GO-CNT/S and rGO/S, which correspond to the formation of high and low-order polysulfides respectively. For GO/S, greater polarization and the disappearance of the first plateau are observed, which could be attributed to the lack of conductivity.

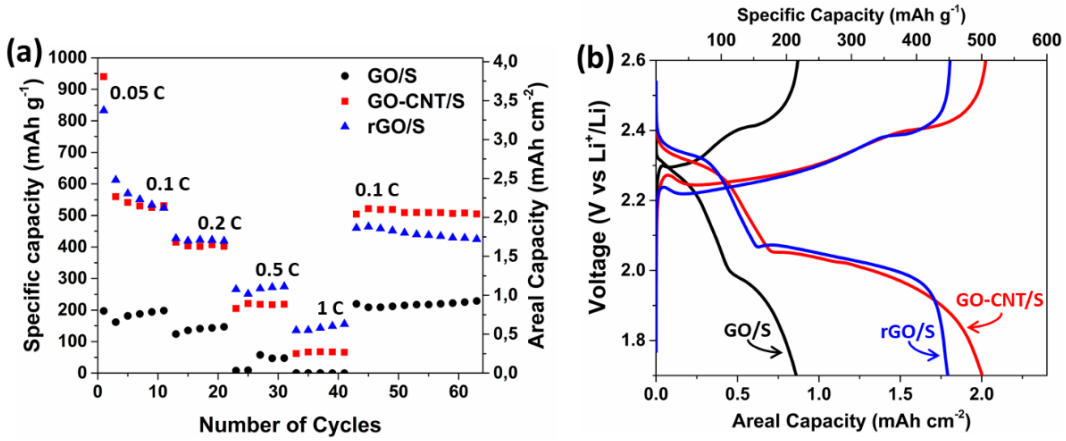


***Figure 2.15.*** *Specific capacity calculated at different C-rates (**a**) and corresponding galvanostatic charge-discharge curves registered at the 50$^{th}$ cycle (**b**) for noted graphene/sulfur cathodes.*

Cycling stability and capacity loss of the samples were further evaluated at 0.1C for 100 cycles as represented in **Figure 2.16a**. A similar electrochemical behavior is again observed for GO-CNT/S and rGO/S, with areal capacity values of 2.2 and 2 mAh $cm^{-2}$ after 100 cycles respectively. However, it can be noted that materials without CNT need an activation period while GO-CNT/S electrode present a very stable charge/discharge behavior. Likewise, very good capacity retentions are obtained for the samples with a capacity loss of 2.8, 7.7 and 17.1% for GO/S, GO-CNT/S and rGO/S respectively between 20$^{th}$ and 100$^{th}$ cycle. The great cycling stability derived from the addition of CNT is also showed from coulombic efficiency calculation (**Figure 2.16b**). Greater instabilities are observed for materials without CNT, especially in the first cycles for rGO/S due to the low activation process and in the case of GO/S, during the whole experiment because of its low conductivity.

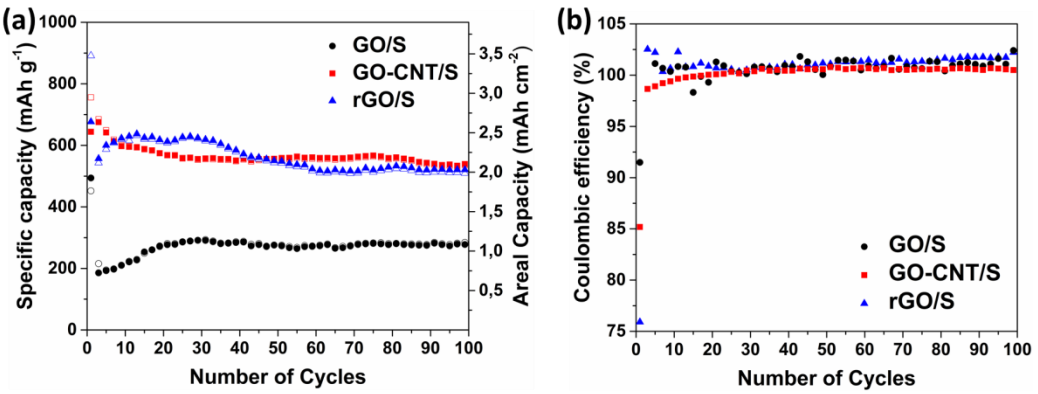


***Figure 2.16.*** *Specific capacity evolution registered at 0.1C for the indicated composites (**a**) and their associated Coulombic efficiencies (**b**).*

The superior electrochemical behavior observed in these materials, in terms of areal capacity and capacity retention, compared to other reported electrode materials, processed as laminates [6,11,26,52], can be ascribed to the use of porous graphene-based architectures. Such three dimensional porous graphene structures are not only suitable to host large amounts of sulfur but also provide effective activation sites for sulfur reduction and re-precipitation, while trapping the high-order polysulfides in the matrix [55]. This argument was further justified by post-cycling SEM images (**Figure 2.17**) of the cycled electrodes after 100 cycles at 0.1C (corresponding to electrodes

cycled in **Figure 2.16**). Backscattered SEM images at low magnification of GO/S (**Figure 2.17a**), GO-CNT/S (**Figure 2.17b**) and rGO/S (**Figure 2.17c**) show a clean and homogenous surface, with no major morphological changes after the cycling process. From a visual examination of the cycled electrodes (**Figure 2.17a**, **b** and **c** inset), no damages were observed and a good physical integrity was maintained after the cycling process. Since all the electrodes maintain a good structural integrity, it can be said that this behavior arises from the aerogel structure and not from further thermal treatment or additives addition. Also, it is worth noting that no agglomerations of re-precipitated sulfur have been observed in any of the cases. From GO-CNT/S cathode observation at high magnification (**Figure 2.17d** and **e**) after cycling, it can be appreciated how sulfur particles have re-precipitated orderly and homogenously in a sub-micrometer size in the graphene matrix, which could be the major reason of the good capacity retention observed.

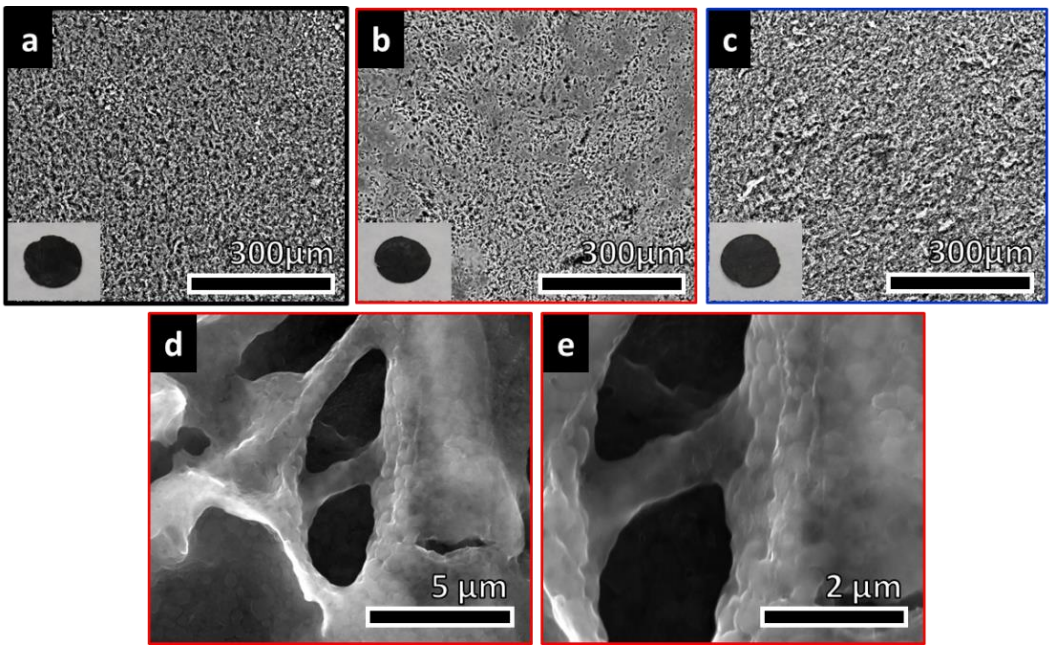


***Figure 2.17.*** *Backscattered SEM images acquired for GO/S (**a**), GO-CNT/S (**b**) and rGO/S (**c**) after 100 cycles, and high magnification SEM images of GO-CNT/S (**d** and **e**).*

## 2.4. A brief outlook and perspectives

In this chapter two different strategies have been followed for the encapsulation of sulfur into graphene-based matrices in order to mitigate the challenges associated to the Li-S technology. For the sake of clarity, encapsulation of in-situ synthesized sulfur particles (**Section 2.2**) is hereafter denoted as Strategy 1, while the use of aerogels as self-standing cathodes (**Section 2.3**) will be denoted as Strategy 2. In **Table 2.5** are summarized some relevant parameters for Li-S cell design followed in Strategy 1 and 2.

***Table 2.5.*** *Summary of some relevant parameters for Li-S cell design followed in Strategies 1 and 2.*

| | Sulfur infiltration method | Electrode processing method | S/electrolyte ratio ($mg_S$:µL) | Sulfur mass loading (mg $cm^{-2}$) | %S in the composite (wt.%) | %S in the electrode (wt.%) |
|---|---|---|---|---|---|---|
| **Strategy 1** | • $Na_2S_2O_3$ dimutation | Casting in Aluminum | 1:20 | 1.45 ± 0.15 | 85 - 92 | 68 - 70 |
| **Strategy 2** | • Dissolution of sulfur in toluene<br>• Melt Diffusion | None | 1:30 | 4.20 ± 0.20 | 68 - 72 | 68-72 |

The first difference arises on the sulfur infiltration method in the graphenic matrix. On this regard, Strategy 1 is based on the disproportionation of an aqueous solution of $Na_2S_2O_3$ to form submicrometer-sized sulfur particles. This is considered a green, scalable and easy approach since no hazardous chemicals are used. On the contrary, sulfur infiltration techniques are greatly limited in Strategy 2 due to the self-standing nature of the electrodes. For this purpose, a simple approach relies on the dissolution of sulfur in an organic solvent and further sulfur adsorption of the graphene pellets by soaking. However, the nonpolar nature of sulfur greatly constricts the list of suitable solvents [67]. For this reason, toluene is used in Strategy 2 even if it is considered a highly toxic and flammable chemical. A further melt diffusion procedure at 155 °C for 12 hours is needed to assure the correct redistribution of sulfur in the graphene-based matrix. Despite the use of toluene, it is necessary to emphasize that this method allow the deposition of a thin sulfur film along the graphene matrix, which favors its utilization and limits the migration of polysulfides. Powdered composite resulting from sulfur infiltration in Strategy 1 needs to be processed into a slurry in order to be casted

in aluminum. Nowadays, casting is the preferred choice for the lab-scale and large-scale electrodes manufacture [68]. However, conductive carbons and binders employed for slurry fabrication increase the fraction of inactive materials, leading to a reduction of the energy density of the cell. In fact, even if sulfur content of the composites is ca. 88%, after electrode processing this value is reduced to ca. 70%. Additionally, the most used electrolyte salt in Li-S batteries, LiTFSI, can corrode aluminum current collectors, which can result in progressive capacity fading, parasitic reactions and cell failure, as reported elsewhere [69]. Contrary, self-standing electrodes processed by the Strategy 2 do not need binders nor being deposited on current collectors and can be directly assembled as Li-S cathodes. Additionally, sulfur loading in the electrodes processed as self-standing binder-free pellets is higher (ca. 4 mg $cm^{-2}$) when compared to laminates (ca. 1.5 mg $cm^{-2}$). As a consequence, even if Strategy 1 can provide higher specific capacities than that of Strategy 2 (**Figure 2.18a**); areal capacities for latter materials are almost two times higher (**Figure 2.18b**). However, due to its open porous structure, aerogels need a higher amount of electrolyte to ensure the correct diffusion of the lithium ions, which would also result in a decrease of the practical energy density of the cell.

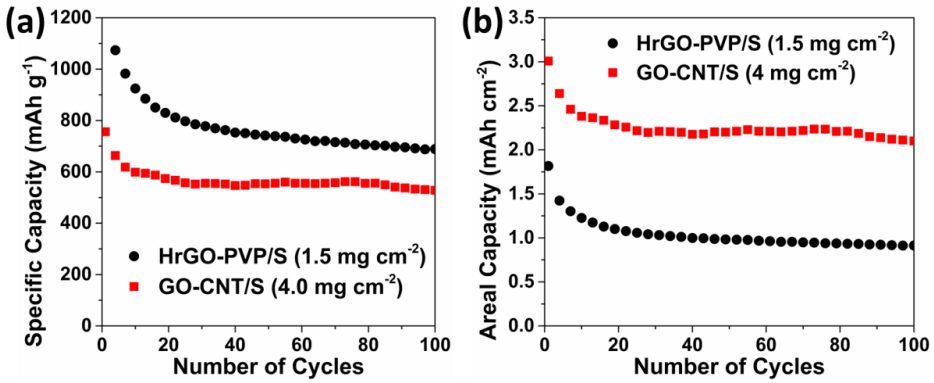


***Figure 2.18.*** *Specific capacity (**a**) and corresponding areal capacity (**b**) evolution upon cycling at 0.1C for noted Li-S cathodes.*

Summarizing, both strategies report advantages and disadvantages toward its utilization for practical Li-S batteries. And, regardless the strategy used, graphene has been proved to be an excellent sulfur host matrix, to improve the electrochemical performance of these systems.

## 2.5. Summary and conclusions

In this chapter, the role of graphene in Li-S batteries has been explored. For this purpose, two different strategies have been followed. In the first approach composites of partially reduced graphene oxide and sulfur have been successfully prepared following a simple and environmentally friendly approach. PVP assisted synthesis of sulfur particles limited its particle growing and allowed its homogeneous distribution within the graphene matrix. The partially reduced nature of HrGO maintaining certain amount of polar functional groups on graphene sheets allowed combining good electronic conductivity with good dispersibility which helped for the homogeneous and effective wrapping of sulfur particles. The composite was able to deliver more than 500 cycles at 1C with good capacity retention as well as acceptable rate capability. Regarding the second approach, Graphene-CNT-sulfur composites have been prepared as self-standing films and used as binder-free cathodes in Li-S batteries. The graphene-based-sulfur electrodes are easily obtained by freeze and freeze drying graphene oxide-CNT suspension, and then impregnated with sulfur by melt diffusion to reach a sulfur content over 70 wt.% and sulfur loadings of 4 mg $cm^{-2}$. Similar performances were found for those samples with CNTs than those thermally reduced, both significantly improving the performance of the composites formed by non-treated GO samples. The incorporation of just 2 wt.% of CNTs demonstrates to significantly enhance both the capacity and the capacity retention compared to the CNT-free samples. Large areal capacities above 2.0 mAh $cm^{-2}$ after 100 cycles are obtained for both thermally reduced and CNT containing samples.

## 2.6. Bibliography

[1] S. Li, Z. Fan, Encapsulation methods of sulfur particles for lithium-sulfur batteries: A review, Energy Storage Mater. 34 (2021) 107–127. https://doi.org/10.1016/j.ensm.2020.09.005.

[2] M. Yu, R. Li, M. Wu, G. Shi, Graphene materials for lithium–sulfur batteries, Energy Storage Mater. 1 (2015) 51–73. https://doi.org/10.1016/j.ensm.2015.08.004.

[3] Y. Ren, H. Shui, C. Peng, H. Liu, Y. Hu, Solubility of elemental sulfur in pure organic solvents and organic solvent–ionic liquid mixtures from 293.15 to 353.15K, Fluid Phase Equilibria. 312 (2011) 31–36. https://doi.org/10.1016/j.fluid.2011.09.012.

[4] Z. Xiao, G. Ning, Z. Yu, X. Xie, L. Zhao, X. Ma, M. Zhang, C. Xu, Sponge-like graphene cubes: S reservoir with large polysulfide diffusion resistance for lithium-

sulfur batteries, Carbon. 155 (2019) 100–107. https://doi.org/10.1016/j.carbon.2019.08.016.

[5] J. Wang, Y. Liu, M. Cheng, H. Zhao, J. Wang, Z. Zhao, X. Duan, C. Wang, J. Wang, Hierarchical porous carbon-graphene-based Lithium–Sulfur batteries, Electrochimica Acta. 318 (2019) 161–168. https://doi.org/10.1016/j.electacta.2019.05.090.

[6] C. Li, J. Yu, S.-L. Xue, Z. Cheng, G. Sun, J. Zhang, R. Huang, L. Qu, Wood-inspired multi-channel tubular graphene network for high-performance lithium-sulfur batteries, Carbon. 139 (2018) 522–530. https://doi.org/10.1016/j.carbon.2018.07.023.

[7] Y. Feng, H. Zhang, Y. Zhang, X. Qu, C–S Bonds in Sulfur-Embedded Graphene, Carbon Nanotubes, and Flake Graphite Cathodes for Lithium–Sulfur Batteries, ACS Omega. 4 (2019) 16352–16359. https://doi.org/10.1021/acsomega.9b01862.

[8] T. Lin, Y. Tang, Y. Wang, H. Bi, Z. Liu, F. Huang, X. Xie, M. Jiang, Scotch-tape-like exfoliation of graphite assisted with elemental sulfur and graphene–sulfur composites for high-performance lithium-sulfur batteries, Energy Environ. Sci. 6 (2013) 1283–1290. https://doi.org/10.1039/c3ee24324a.

[9] L. Chen, R. Yang, Y. Yan, Y. Zou, X. Li, Q. Deng, Y. Xu, Controlling hydroxyl content of reduced graphene oxide for superior cathode performance of lithium sulfur batteries, Electrochimica Acta. 362 (2020) 137112. https://doi.org/10.1016/j.electacta.2020.137112.

[10] L. Ji, M. Rao, H. Zheng, L. Zhang, Y. Li, W. Duan, J. Guo, E.J. Cairns, Y. Zhang, Graphene Oxide as a Sulfur Immobilizer in High Performance Lithium/Sulfur Cells, J. Am. Chem. Soc. 133 (2011) 18522–18525. https://doi.org/10.1021/ja206955k.

[11] J.M. Chabu, K. Zeng, W. Chen, A. Mustapha, Y. Li, Y.-N. Liu, A novel graphene oxide-wrapped sulfur composites cathode with ultra-high sulfur content for lithium–sulfur battery, Appl. Surf. Sci. 493 (2019) 533–540. https://doi.org/10.1016/j.apsusc.2019.07.061.

[12] Z.W. Lu, Y.H. Wang, Z. Dai, X.P. Li, C.Y. Zhang, G.Z. Sun, C.S. Gong, X.J. Pan, W. Lan, J.Y. Zhou, E.Q. Xie, One-pot sulfur-containing ion assisted microwave synthesis of reduced graphene oxide@nano-sulfur fibrous hybrids for high-performance lithium-sulfur batteries, Electrochimica Acta. 325 (2019) 134920. https://doi.org/10.1016/j.electacta.2019.134920.

[13] H. Wu, Y. Huang, M. Zong, X. Ding, J. Ding, X. Sun, Electrostatic self-assembly of graphene oxide wrapped sulfur particles for lithium–sulfur batteries, Mater. Res. Bull. 64 (2015) 12–16. https://doi.org/10.1016/j.materresbull.2014.12.036.

[14] H. Wang, Y. Yang, Y. Liang, J.T. Robinson, Y. Li, A. Jackson, Y. Cui, H. Dai, Graphene-Wrapped Sulfur Particles as a Rechargeable Lithium–Sulfur Battery Cathode Material with High Capacity and Cycling Stability, Nano Lett. 11 (2011) 2644–2647. https://doi.org/10.1021/nl200658a.

[15] J. Tan, D. Li, Y. Liu, P. Zhang, Z. Qu, Y. Yan, H. Hu, H. Cheng, J. Zhang, M. Dong, C. Wang, J. Fan, Z. Li, Z. Guo, M. Liu, A self-supported 3D aerogel network lithium–sulfur battery cathode: sulfur spheres wrapped with phosphorus doped graphene and bridged with carbon nanofibers, J. Mater. Chem. A. 8 (2020) 7980–7990. https://doi.org/10.1039/D0TA00284D.

[16] R. Fang, S. Zhao, K. Chen, D.-W. Wang, F. Li, Binary graphene-based cathode structure for high-performance lithium-sulfur batteries, J. Phys. Energy. 2 (2020) 015003. https://doi.org/10.1088/2515-7655/ab5997.

[17] J. Kim, Y. Kang, S.-W. Song, J. Suk, Freestanding sulfur-graphene oxide/carbon composite paper as a stable cathode for high performance lithium-sulfur batteries, Electrochimica Acta. 299 (2019) 27–33. https://doi.org/10.1016/j.electacta.2018.12.165.

[18] Y. Chen, S. Lu, X. Wu, J. Liu, Flexible Carbon Nanotube–Graphene/Sulfur Composite Film: Free-Standing Cathode for High-Performance Lithium/Sulfur Batteries, J. Phys. Chem. C. 119 (2015) 10288–10294. https://doi.org/10.1021/acs.jpcc.5b02596.

[19] H. Köse, B.Ş. Kurt, Ş. Dombaycıoğlu, A.O. Aydın, Rational design of cathode structure based on free-standing S/rGO/CNT nanocomposite for Li-S batteries, Synth. Met. 267 (2020) 116471. https://doi.org/10.1016/j.synthmet.2020.116471.

[20] Z. Zhang, L.-L. Kong, S. Liu, G.-R. Li, X.-P. Gao, A High-Efficiency Sulfur/Carbon Composite Based on 3D Graphene Nanosheet@Carbon Nanotube Matrix as Cathode for Lithium-Sulfur Battery, Adv. Energy Mater. 7 (2017) 1602543. https://doi.org/10.1002/aenm.201602543.

[21] N. Wang, J. Wang, J. Zhao, J. Wang, J. Pan, J. Huang, Synthesis of porous-carbon@reduced graphene oxide with superior electrochemical behaviors for lithium-sulfur batteries, J. Alloys Compd. 851 (2021) 156832. https://doi.org/10.1016/j.jallcom.2020.156832.

[22] Y. Yan, M. Shi, Y. Zou, Y. Wei, L. Chen, C. Fan, R. Yang, Y. Xu, Tunable hierarchical porous carbon aerogel / graphene composites cathode matrix for Li-S batteries, J. Alloys Compd. 791 (2019) 952–961. https://doi.org/10.1016/j.jallcom.2019.03.396.

[23] S. Liu, K. Xie, Z. Chen, Y. Li, X. Hong, J. Xu, L. Zhou, J. Yuan, C. Zheng, A 3D nanostructure of graphene interconnected with hollow carbon spheres for high performance lithium–sulfur batteries, J Mater Chem A. 3 (2015) 11395–11402. https://doi.org/10.1039/C5TA00897B.

[24] W. Qian, Q. Gao, W. Tian, H. Zhang, Y. Tan, Z. Li, One-pot in situ chemical reduction of graphene oxide and recombination of sulphur as a cathode material for a Li–S battery, J. Mater. Chem. A. 4 (2016) 15140–15147. https://doi.org/10.1039/C6TA03555H.

[25] Z. Li, H. Sun, Y. Pang, M. Yu, S. Zheng, Investigation on Fabrication of Reduced Graphene Oxide-Sulfur Composite Cathodes for Li-S Battery via Hydrothermal and

Thermal Reduction Methods, Materials. 14 (2021) 861. https://doi.org/10.3390/ma14040861.

[26] M. Shi, S. Zhang, Y. Jiang, Z. Jiang, L. Zhang, J. Chang, T. Wei, Z. Fan, Sandwiching Sulfur into the Dents Between N, O Co-Doped Graphene Layered Blocks with Strong Physicochemical Confinements for Stable and High-Rate Li–S Batteries, Nano-Micro Lett. 12 (2020) 146. https://doi.org/10.1007/s40820-020-00477-3.

[27] P. Shi, Y. Wang, X. Liang, Y. Sun, S. Cheng, C. Chen, H. Xiang, Simultaneously exfoliated boron doped graphene sheets to encapsulate sulfur for applications in lithium sulfur batteries, ACS Sustain. Chem. Eng. 6 (2018) 9661–9670. https://doi.org/10.1021/acssuschemeng.8b00378.

[28] B. Gong, X. Song, Y. Shi, J. Liu, C. Hao, Understanding the Inhibition of the Shuttle Effect of Sulfides (S ≤ 3) in Lithium–Sulfur Batteries by Heteroatom-Doped Graphene: First-Principles Study, J. Phys. Chem. C. 124 (2020) 3644–3649. https://doi.org/10.1021/acs.jpcc.9b10314.

[29] W. Sun, Y. Xu, X. Chen, Y. Xu, F. Wu, Y. Wang, Reduced graphene oxide modified with naphthoquinone for effective immobilization of polysulfides in high-performance Li-S batteries, Chem. Eng. J. 383 (2020) 123111. https://doi.org/10.1016/j.cej.2019.123111.

[30] W. Wang, G. -c. Li, Q. Wang, G. -r. Li, S. -h. Ye, X. -p. Gao, Sulfur-Polypyrrole/Graphene Multi-Composites as Cathode for Lithium-Sulfur Battery, J. Electrochem. Soc. 160 (2013) A805–A810. https://doi.org/10.1149/2.059306jes.

[31] P. Xiao, F. Bu, G. Yang, Y. Zhang, Y. Xu, Integration of Graphene, Nano Sulfur, and Conducting Polymer into Compact, Flexible Lithium-Sulfur Battery Cathodes with Ultrahigh Volumetric Capacity and Superior Cycling Stability for Foldable Devices, Adv. Mater. (2017) 1703324. https://doi.org/10.1002/adma.201703324.

[32] M. Yu, A. Wang, F. Tian, H. Song, Y. Wang, C. Li, J.-D. Hong, G. Shi, Dual-protection of a graphene-sulfur composite by a compact graphene skin and an atomic layer deposited oxide coating for a lithium-sulfur battery, Nanoscale. 7 (2015) 5292–5298. https://doi.org/10.1039/C5NR00166H.

[33] Y. Li, Q. Cai, L. Wang, Q. Li, X. Peng, B. Gao, K. Huo, P.K. Chu, Mesoporous $TiO_2$ Nanocrystals/Graphene as an Efficient Sulfur Host Material for High-Performance Lithium–Sulfur Batteries, ACS Appl. Mater. Interfaces. 8 (2016) 23784–23792. https://doi.org/10.1021/acsami.6b09479.

[34] Z. Sun, J. Zhang, L. Yin, G. Hu, R. Fang, H.-M. Cheng, F. Li, Conductive porous vanadium nitride/graphene composite as chemical anchor of polysulfides for lithium-sulfur batteries, Nat. Commun. 8 (2017) 14627. https://doi.org/10.1038/ncomms14627.

[35] X. Li, Z. Pan, Z. Li, X. Wang, B. Saravanakumar, Y. Zhong, L. Xing, M. Xu, C. Guo, W. Li, Coral-like reduced graphene oxide/tungsten sulfide hybrid as a cathode host of high performance lithium-sulfur battery, J. Power Sources. 420 (2019) 22–28. https://doi.org/10.1016/j.jpowsour.2019.02.089.

[36] M. Rana, S.A. Ahad, M. Li, B. Luo, L. Wang, I. Gentle, R. Knibbe, Review on areal capacities and long-term cycling performances of lithium sulfur battery at high sulfur loading, Energy Storage Mater. 18 (2019) 289–310. https://doi.org/10.1016/j.ensm.2018.12.024.

[37] Y. Hu, W. Chen, T. Lei, Y. Jiao, J. Huang, A. Hu, C. Gong, C. Yan, X. Wang, J. Xiong, Strategies toward High-Loading Lithium–Sulfur Battery, Adv. Energy Mater. 10 (2020) 2000082. https://doi.org/10.1002/aenm.202000082.

[38] M. Li, Y. Dai, X. Pei, W. Chen, Three-dimensional hollow reduced graphene oxide spheres with a hierarchically porous structure for high-performance lithium–sulfur batteries, Inorg. Chem. Front. 6 (2019) 2528–2538. https://doi.org/10.1039/C9QI00656G.

[39] C. Botas, P. Álvarez, C. Blanco, R. Santamaría, M. Granda, P. Ares, F. Rodríguez-Reinoso, R. Menéndez, The effect of the parent graphite on the structure of graphene oxide, Carbon. 50 (2012) 275–282. https://doi.org/10.1016/j.carbon.2011.08.045.

[40] W. Chen, L. Yan, P.R. Bangal, Preparation of graphene by the rapid and mild thermal reduction of graphene oxide induced by microwaves, Carbon. 48 (2010) 1146–1152. https://doi.org/10.1016/j.carbon.2009.11.037.

[41] Y. Li, H. Chen, L.Y. Voo, J. Ji, G. Zhang, G. Zhang, F. Zhang, X. Fan, Synthesis of partially hydrogenated graphene and brominated graphene, J. Mater. Chem. 22 (2012) 15021. https://doi.org/10.1039/c2jm32307a.

[42] W. Cai, R. Piner, F.J. Stadermann, S. Park, M.A. Shaibat, Y. Ishii, D. Yang, A. Velamakanni, S. Jin An, M. Stoller, J. An, D. Chen, R.S. Ruoff, Synthesis and Solid-State NMR structural characterization of 13C-labeled graphite oxide, Science. 321 (2008) 1815.

[43] H. He, T. Riedl, A. Lerf, J. Klinowski, Solid-State NMR Studies of the Structure of Graphite Oxide, J. Phys. Chem. 100 (1996) 19954–19958. https://doi.org/10.1021/jp961563t.

[44] B. Zhao, Y. Jiang, J. Xie, X. Ling, Y. Ding, S. Huang, Z. Chen, Y. Jiang, A double-shelled structure confining sulfur for lithium-sulfur batteries, J. Alloys Compd. 811 (2019) 151434. https://doi.org/10.1016/j.jallcom.2019.07.146.

[45] S. Li, H. Li, G. Zhu, B. Jin, H. Liu, Q. Jiang, Improved electrochemical performance of Li-S battery with carbon and polymer-modified cathode, Appl. Surf. Sci. 479 (2019) 265–272. https://doi.org/10.1016/j.apsusc.2019.02.109.

[46] H. Yang, Q. Li, C. Guo, A. Naveed, J. Yang, Y. Nuli, J. Wang, Safer lithium–sulfur battery based on nonflammable electrolyte with sulfur composite cathode, Chem. Commun. 54 (2018) 4132–4135. https://doi.org/10.1039/C7CC09942H.

[47] X. Gao, J. Li, D. Guan, C. Yuan, A Scalable Graphene Sulfur Composite Synthesis for Rechargeable Lithium Batteries with Good Capacity and Excellent Columbic Efficiency, ACS Appl. Mater. Interfaces. 6 (2014) 4154–4159. https://doi.org/10.1021/am4057979.

[48] Nanchang Institute of Technology, Tianxiang Avenue No.289, 330099, Nanchang, China, W. Zhang, Preparation and Optimization of Nanoporous Hollow Carbon spheres /S Composite Cathode Materials for Li-S battery, Int. J. Electrochem. Sci. (2019) 4693–4704. https://doi.org/10.20964/2019.05.52.

[49] P. Półrolniczak, D. Kasprzak, J. Kaźmierczak-Raźna, M. Walkowiak, P. Nowicki, R. Pietrzak, Composite sulfur cathode for Li-S batteries comprising hierarchical carbon obtained from waste PET bottles, Synth. Met. 261 (2020) 116305. https://doi.org/10.1016/j.synthmet.2020.116305.

[50] B.A. Trofimov, L.M. Sinegovskaya, N.K. Gusarova, Vibrations of the S–S bond in elemental sulfur and organic polysulfides: a structural guide, J. Sulfur Chem. 30 (2009) 518–554. https://doi.org/10.1080/17415990902998579.

[51] J.-B. Wu, M.-L. Lin, X. Cong, H.-N. Liu, P.-H. Tan, Raman spectroscopy of graphene-based materials and its applications in related devices, Chem. Soc. Rev. 47 (2018) 1822–1873. https://doi.org/10.1039/C6CS00915H.

[52] Y. Liu, J. Guo, J. Zhang, Q. Su, G. Du, Graphene-wrapped sulfur nanospheres with ultra-high sulfur loading for high energy density lithium–sulfur batteries, Appl. Surf. Sci. 324 (2015) 399–404. https://doi.org/10.1016/j.apsusc.2014.10.176.

[53] W. Wang, G. Li, Q. Wang, G. Li, S. Ye, X. Gao, Sulfur-polypyrrole/graphene multi-composites as cathode for lithium-sulfur battery, J. Electrochem. Soc. 160 (2013) A805–A810.

[54] Z. Deng, Z. Zhang, Y. Lai, J. Liu, J. Li, Y. Liu, Electrochemical Impedance Spectroscopy Study of a Lithium/Sulfur Battery: Modeling and Analysis of Capacity Fading, J. Electrochem. Soc. 160 (2013) A553–A558. https://doi.org/10.1149/2.026304jes.

[55] C. Sun, yingqi Liu, J. Sheng, Q. Huang, W. Lv, G. Zhou, H.-M. Cheng, Status and prospects of porous graphene networks for lithium-sulfur batteries, Mater. Horiz. 7 (2020) 2487–2518. https://doi.org/10.1039/D0MH00815J.

[56] M. Lacey, F. Jeschull, K. Edstrom, D. Brandell, Porosity Blocking in Highly Porous Carbon Black by PVdF Binder and Its Implications for the Li−S System, J. Phys. Chem. C. 118 (2014) 25890–25898. https://doi.org/10.1021/jp508137m.

[57] L. Huilin, Q. Guo, Y. Li, D. Tian, Enhancement of electrical and thermal properties of graphene by aligned carbon nanotubes, Mater. Res. Express. 7 (2020) 015046. https://doi.org/10.1088/2053-1591/ab6639.

[58] P. Zhang, Z. Li, S. Zhang, G. Shao, Recent Advances in Effective Reduction of Graphene Oxide for Highly Improved Performance Toward Electrochemical Energy Storage, Energy Environ. Mater. 1 (2018) 5–12. https://doi.org/10.1002/eem2.12001.

[59] M. Thommes, K. Kaneko, A.V. Neimark, J.P. Olivier, F. Rodriguez-Reinoso, J. Rouquerol, K.S.W. Sing, Physisorption of gases, with special reference to the evaluation of surface area and pore size distribution (IUPAC Technical Report), Pure Appl. Chem. 87 (2015) 1051–1069. https://doi.org/10.1515/pac-2014-1117.

[60] J. Wang, B. Chen, Adsorption and coadsorption of organic pollutants and a heavy metal by graphene oxide and reduced graphene materials, Chem. Eng. J. 281 (2015) 379–388. https://doi.org/10.1016/j.cej.2015.06.102.
[61] P. Saikia, K. Dutta, A.K. Guha, S.K. Dolui, P. Barman, L.J. Borthakur, High-performance aqueous electrolyte based supercapacitor of carboxylic acid functionalized carbon-nanotubes and graphene nano composite, Mater. Chem. Phys. 258 (2021) 123786. https://doi.org/10.1016/j.matchemphys.2020.123786.
[62] Ch.N. Barnakov, G.P. Khokhlova, A.N. Popova, S.A. Sozinov, Z.R. Ismagilov, XRD Characterization of the Structure of Graphites and Carbon Materials Obtained by the Low-Temperature Graphitization of Coal Tar Pitch, Eurasian Chem.-Technol. J. 17 (2015) 87. https://doi.org/10.18321/ectj198.
[63] M. Aziz, F.S. Abdul Halim, J. Jaafar, Preparation and Characterization of Graphene Membrane Electrode Assembly, J. Teknol. 69 (2014). https://doi.org/10.11113/jt.v69.3388.
[64] C. Botas, P. Álvarez, C. Blanco, R. Santamaría, M. Granda, M.D. Gutiérrez, F. Rodríguez-Reinoso, R. Menéndez, Critical temperatures in the synthesis of graphene-like materials by thermal exfoliation–reduction of graphite oxide, Carbon. 52 (2013) 476–485. https://doi.org/10.1016/j.carbon.2012.09.059.
[65] Q. (Ray) Zeng, D.-W. Wang, K.-H. Wu, Y. Li, F. Condi de Godoi, I.R. Gentle, Synergy of nanoconfinement and surface oxygen in recrystallization of sulfur melt in carbon nanocapsules and the related Li–S cathode properties, J. Mater. Chem. A. 2 (2014) 6439. https://doi.org/10.1039/c4ta00314d.
[66] X. Yang, W. Zhu, G. Cao, X. Zhao, Preparation of a carbon nanofibers–carbon matrix–sulfur composite as the cathode material of lithium–sulfur batteries, RSC Adv. 6 (2016) 7159–7171. https://doi.org/10.1039/C5RA24129D.
[67] R. Wang, B. Shen, H. Sun, J. Zhao, Measurement and Correlation of the Solubilities of Sulfur $S_8$ in 10 Solvents, J. Chem. Eng. Data. 63 (2018) 553–558. https://doi.org/10.1021/acs.jced.7b00699.
[68] W.B. Hawley, J. Li, Electrode manufacturing for lithium-ion batteries—Analysis of current and next generation processing, J. Energy Storage. 25 (2019) 100862. https://doi.org/10.1016/j.est.2019.100862.
[69] M. Morita, T. Shibata, N. Yoshimoto, M. Ishikawa, Anodic behavior of aluminum current collector in LiTFSI solutions with different solvent compositions, J. Power Sources. 119–121 (2003) 784–788. https://doi.org/10.1016/S0378-7753(03)00253-2.

# Chapter III. Sodium-Oxygen Batteries



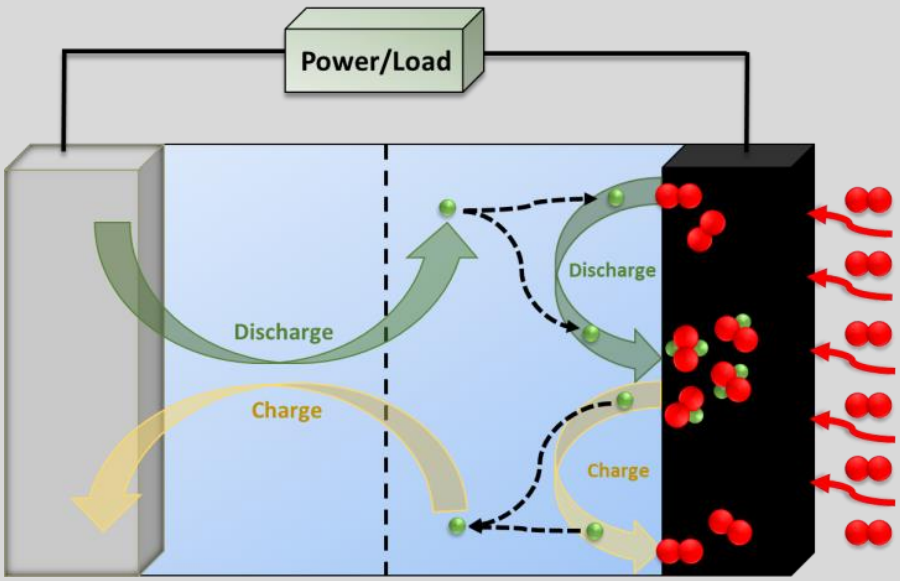

## 3.1. State-of-the-art of graphene-based cathodes for Na-$O_2$ batteries

Although significant progress has been achieved in the last years, there are still many challenges to overcome in order to reach the final commercialization of Na-$O_2$ batteries. One of the most limiting and challenging factors is the development of bifunctional cathodes towards oxygen reduction and evolution reactions [1,2]. Besides the overall cell performance, the utilization of a suitable cathode material is required to accommodate the maximum amount of discharge products without pore clogging and subsequent cell failure [3,4]. Porous carbon materials have been largely used due to their low cost, high surface area, chemical stability and high conductivity [5–9]. Among carbon-based materials, graphene has been appointed as a very versatile and promising air cathode in M-$O_2$ batteries due to its high electronic conductivity (~ 2,000 S $m^{-1}$), specific surface area (> 2,600 $m^2$ $g^{-1}$), mechanical strength, low density and intrinsic catalytic activity towards ORR/OER reactions [10,11]. Moreover, graphene confers the suitable electrode channels for $O_2$ diffusion, facilitates the impregnation of the electrolyte and offers high number of active sites for the formation/deposition and decomposition of the discharge products [12–14]. To improve the catalytic activity of graphene in M-$O_2$ batteries, different routes have been explored, such as the introduction of ORR/OER catalysts like noble metal nanoparticles [15–17]. Even though such nanoparticles have demonstrated highly catalytic activity, they suffer from high cost, low selectivity, poor durability and detrimental environmental impact. In this context, metal-free carbon catalysts incorporating nitrogen atoms in the carbon lattice/bulk are a great alternative since heteroatoms can modify the acid/base and electronic characteristic of the electrodes [18,19]. But in practical terms, the effective access to the large and active 2D surface of graphene is subjected to careful engineering of both the morphology and the 3D structure. This is extremely important in M-$O_2$ batteries; an optimum air cathode should maximize the oxygen diffusion towards the three-phase boundary (i.e., electrolyte/electrode/oxygen interface) and accommodate a large amount of discharge product during ORR [20–22]. On this regard, graphene-based aerogels have been appointed as promising oxygen cathodes [23–25]. However, to fully exploit the outstanding features of Na-$O_2$ batteries, a comprehensive research on the role of graphene-based cathodes textural properties over battery performance is still needed.

## 3.2. Graphene-based aerogels as Na-$O_2$ cathodes

In the present work, an easy and sustainable preparation procedure of different rGO aerogels was followed to use directly as self-standing, binder-free cathodes for Na-$O_2$ batteries. In this context, the self-assembly in aqueous solution of 2D graphene-based sheets to form 3D nanomaterials is expected to prevent individual graphene sheets to stack while provides low-density materials with controlled porosity. Moreover, avoiding the utilization of either binder or current collector offer several advantages such as reducing the total weight of the battery which is essential to develop practical Na-$O_2$ batteries, since a lower fraction of inactive materials allow greater cell energy densities. On the other hand, the role of specific surface area and pore size distribution of the graphene-based cathodes over their electrochemical performance in Na-$O_2$ cells is studied and disclosed.

### 3.2.1. Material and electrode preparation of the rGO-based electrodes

Graphene oxide suspensions were prepared by following the modified Hummers' method described in **Section 2.2.1**. Graphene oxide suspensions (2 mg $mL^{-1}$) were suddenly frozen with liquid nitrogen at -196 °C ($N_2$-rGO) or slowly in a freezer at -75 °C (F-rGO). Furtherly, frozen suspensions were freeze-dried for 72 hours to obtain the graphene-based aerogels. For the shake of comparison, a third sample was prepared by drop-casting GO suspension on silicon rubber and kept at room temperature until totally dry (Film). Discs of 12 mm in diameter were cut from GO aerogels or Film and thermally treated in a tubular furnace at 800 °C for 1 h to obtain the oxygen electrodes (see **Scheme 3.1**).

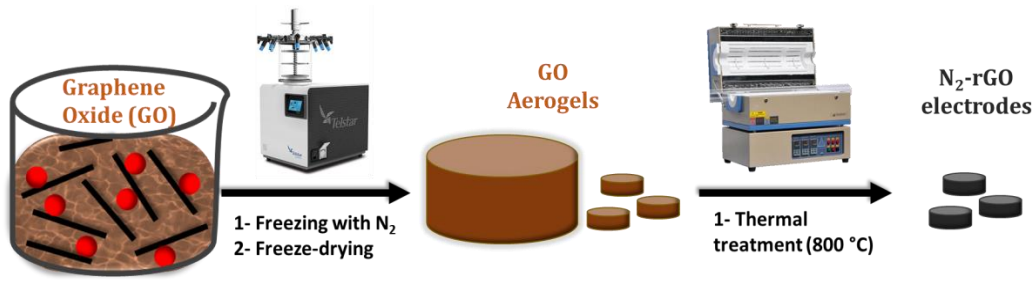


***Scheme 3.1.*** *Synthetic route followed for the preparation of $N_2$-rGO electrodes.*

Graphene-based discs were assembled as positive electrode and metallic sodium as counter and reference electrode in a pressurized 2-electrode Swagelok-type cell. A 0.1 M solution of sodium perchlorate ($NaClO_4$) in DME was used as electrolyte. After the assembly, cells were pressurized with pure oxygen to ~1 atm before the electrochemical measurements. The discharge and charge experiments were performed at a current of 100 mA $g^{-1}$ (~ 150-300 µA $cm^{-2}$) with a potential cut-off between 1.8 to 3.2 V vs. $Na/Na^+$.

### 3.2.2. Physicochemical characterization of the rGO-based electrodes

The morphology of the self-standing binder-free rGO cathodes was studied by scanning electron microscopy (**Figure 3.1**). The film shows a smooth and uniform surface with no visible porosity (**Figure 3.1a**) and a thickness around 12 µm as measured by cross-sectional SEM imaging (inset **Figure 3.1a**). In contrast, F-rGO electrode displays large platelet-like structures incorporating voids of ca. 100 µm (**Figure 3.1b**) while $N_2$-rGO presents a smooth morphology with smaller pores of around 30 µm (**Figure 3.1c**). The appearance of narrow pores in $N_2$-rGO is probably caused by the presence of small and randomly oriented aggregates of graphene sheets formed during sudden freezing of the GO suspensions.

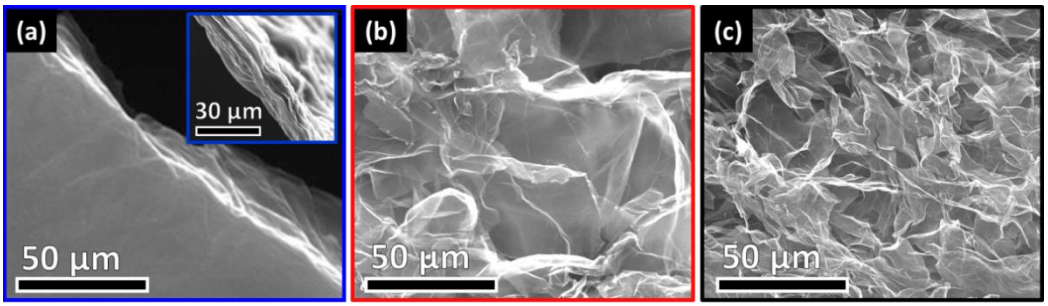


***Figure 3.1.*** *SEM images of the rGO film (**a**), and both aerogels: F-rGO (**b**) and $N_2$-rGO (**c**).*

The textural properties of the rGO electrodes were studied by nitrogen gas adsorption. **Figure 3.2a** displays the $N_2$ adsorption-desorption isotherms measured at -196 ˚C. According to the IUPAC classification [26], the film and F-rGO samples yield a type-II

isotherm which is ascribed to non-porous or macroporous solids. In contrast, $N_2$-rGO present a mixture between type-I and II isotherms revealing the presence of both micro and macroporous. The electrode prepared by freeze-casting at lower temperature ($N_2$-rGO) bear H3-type hysteresis indicating the presence of non-rigid aggregates of graphene sheets bearing slit-shape pores in-between the sheets. The electrode froze at -75 °C (F-rGO) yields an H4 hysteresis loop indicating also the existence of interparticle porosity, but narrow pore size. The pore size distribution was further studied by bidimensional non-local density functional theory (2D-NLDFT) analysis (**Figure 3.2b**). The aerogels present an adsorption maximum at 0.9 nm suggesting the presence of micropores. It is worth to remark that much larger micropore volume is observed for $N_2$-rGO sample. Regarding mesoporosity, F-rGO mesopores are narrower than 5 nm while $N_2$-rGO displays much wider mesopore size distribution, with sizes ranging from 2 to 25 nm.

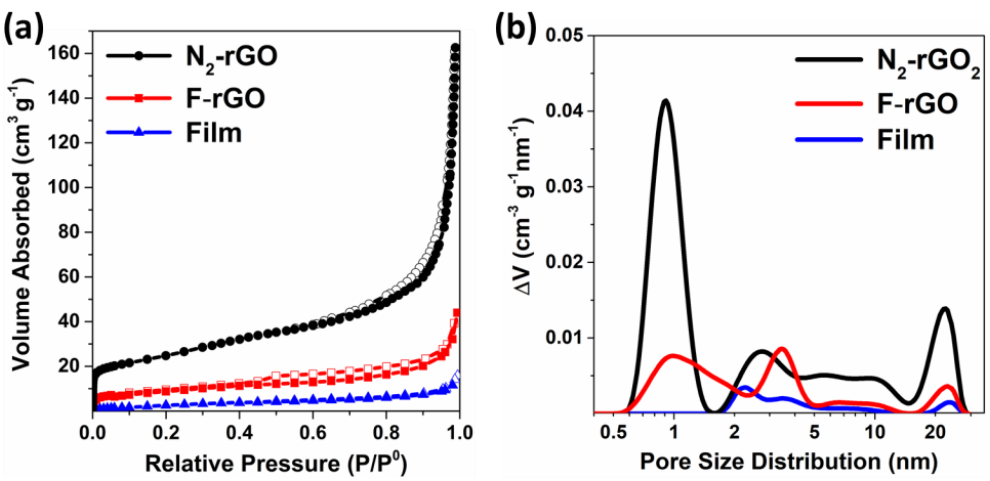


***Figure 3.2.*** *Nitrogen adsorption/desorption isotherms (**a**) and PSD (**b**) of the noted rGO-based samples*

A larger average mesopore size and mesopore volume for $N_2$-rGO aerogel is further confirmed by calculating the equivalent mesopore diameter (**Table 3.1**, $D_{meso}$). The mesopore size shifts from 8.8 nm for F-rGO to 11.3 nm for $N_2$-rGO. Higher total pore volume ($V_T$), specific surface ($S_{BET}$) and external areas ($S_{EXT}$) have been observed for the 3D porous aerogels when compared to that of the Film (**Table 3.1**). The Film presents negligible gas adsorption in the whole pressure range and, consequently, can be

considered a non-porous material. To study the macroporous nature of the materials, the apparent density ($\rho_a$) was calculated by measuring and weighting the electrodes while the true density ($\rho_t$, skeletal density with no contribution of pores) of the different samples was calculated by He pycnometry. The high pore volume of aerogels is confirmed by their low apparent density. $N_2$-rGO presents the largest real density which confirms a greater pore volume for this sample (**Table 3.1**, $V_P$). In addition of a developed porosity, $N_2$-rGO shows a narrower average macropore size (**Table 3.1**, $D_{Macro}$) than that of F-rGO (1263 nm vs 1630 nm). In view of the results obtained it can be attained that a quick freezing of the GO suspension during the pore casting ($N_2$-rGO) resulted in narrower macroporosity than that observed for a slow freezing (F-rGO). The ice crystals formed during $N_2$-rGO preparation are very small and highly dispersed as compared with the big crystals formed during the slow freezing. Regarding mesopores, the slow process provides time to the GO sheets to orientate leading to big aggregates and highly oriented mesoporous channels with narrow mesopore size distributions and large macropore size. In contrast, a sudden freeze of the suspension resulted in randomly-oriented small aggregates of GO sheets which gave rise to wide pore size distributions with large mesopores and narrow macropores.

***Table 3.1.*** *Most representative textural parameters measured for graphene-based electrodes by $N_2$ adsorption-desorption isotherms at -196 °C and He pycnometry at room temperature.*

| | **$N_2$ at -196 °C** | | | | **He at room temperature** | | | |
|---|---|---|---|---|---|---|---|---|
| | **$V_T$ ($cm^3\ g^{-1}$)** | **$S_{BET}$ ($m^2\ g^{-1}$)** | **$S_{EXT}$ ($cm^3\ g^{-1}$)** | **$\rho_a$ ($g\ cm^{-3}$)** | **$\rho_t$ ($g\ cm^{-3}$)** | **$V_P$ ($cm^3\ g^{-1}$)** | **$D_{Meso}$ (nm)** | **$D_{Macro}$ (nm)** |
| **Film** | 0.02 | 11 | 18 | 0.10 | 1.23 | 9.40 | 7.00 | 2090 |
| **F-rGO** | 0.07 | 32 | 35 | 0.05 | 1.85 | 14.3 | 8.80 | 1630 |
| **$N_2$-rGO** | 0.22 | 78 | 65 | 0.07 | 2.14 | 20.5 | 11.3 | 1263 |

The differences in the 3D structure arrangement of the GO sheets during the freeze-casting, therefore, not only lead to variations in the macroscopic morphology of the final electrodes by changing the aggregation behaviour of graphene sheets but also in the pore size (nanoscale). Thus, the as-prepared graphene-based materials present noticeable differences regarding porous properties, enabling a suitable evaluation of the influence of this key parameter over Na-$O_2$ battery performance.

### 3.2.3. Electrochemical characterization of the rGO-based electrodes

The cells were galvanostatically discharged to full capacity at 100 mA $g^{-1}$ in order to evaluate the oxygen reduction reaction kinetics of $NaO_2$ formation on graphene-based electrodes (**Figure 3.3a**). F-rGO and Film cathodes show large overpotentials (~ 300-400 mV; $E^0$ ($NaO_2$) = 2.27 V) and limited discharge capacities of 1.72 and 0.06 mAh $cm^{-2}$, respectively. On the other side, $N_2$-rGO presents much higher discharge capacity (6.61 mAh $cm^{-2}$) and lower overpotential (260 mV). The three studied materials present a similar potential drop at the beginning. This behaviour is related to the nucleation barrier needed to start forming the nucleation sites. Once these sites are available, the voltage increases and $NaO_2$ grows. The discharging stage ends with a sudden potential drop when the surface is totally covered and there are not more active sites for $NaO_2$ growth.

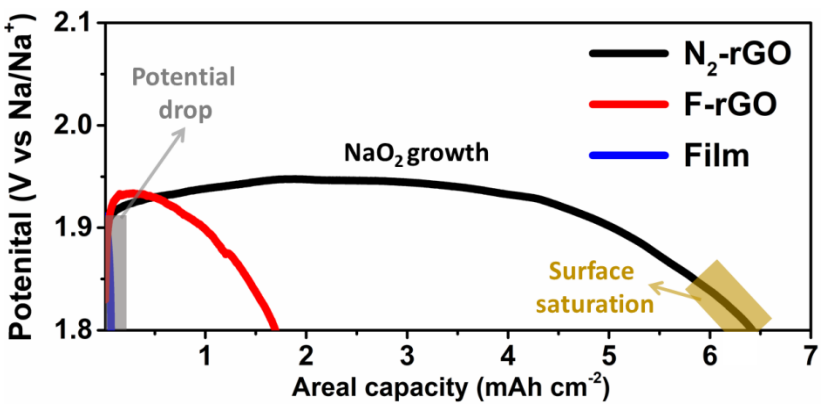


***Figure 3.3.*** *Galvanostatic discharge curves of noted graphene-based electrodes.*

Raman spectroscopy and $^{23}Na$ solid-state nuclear magnetic resonance analysis were used to identify the nature of the discharge products (**Figure 3.4**). Raman spectra show the presence of an intense peak at 1,156 $cm^{-1}$ for both $N_2$-rGO and F-rGO, which as previously reported [27], confirms $NaO_2$ as the main discharge product (**Figure 3.4a**). This peak is also verified for the Film but featuring much lower intensity, probably due to the low capacity achieved (**Figure 3.3**). In addition, two broad peaks corresponding to D and G bands were observed at 1,340 and 1,585 $cm^{-1}$, respectively. $I_D/I_G$ ratios of ca. 1 were obtained for the different electrodes, pointing out the remaining graphitic

character in all the samples, which favours the electronic transport from/to the cathode. As reported elsewhere [28,29], free-electrons located on lattice defects have demonstrated to act as active sites for the ORR as $O_2$ molecules oxidize preferentially at electron rich domains. On the other hand, suitable porosity is crucial to enhance molecular diffusion of $O_2$ molecules which are adsorbed on the surface/pores of carbon-based air cathodes prior to the charge transfer process. Bearing this in mind, the low overpotential discharge verified for $N_2$-rGO cathode points out the great influence of the 3D arrangement of the graphene sheets on the rGO aerogels when used as air electrodes. Regarding NMR analysis, the $^{23}$Na NMR spectra (**Figure 3.4b**) reveal that after discharge, $N_2$-rGO and F-rGO electrodes show a major resonance at -25 ppm attributed to $NaO_2$ [30] with two clear shoulders at around -16 and -5 ppm that can be ascribed to the formation of irreversible discharge subproducts [14]. The peak assigned to $NaO_2$ cannot be observed in the $^{23}$Na-NMR spectra of the Film since, as commented above, the discharge capacity is very low and the amount of $NaO_2$ might be below the detection limit.

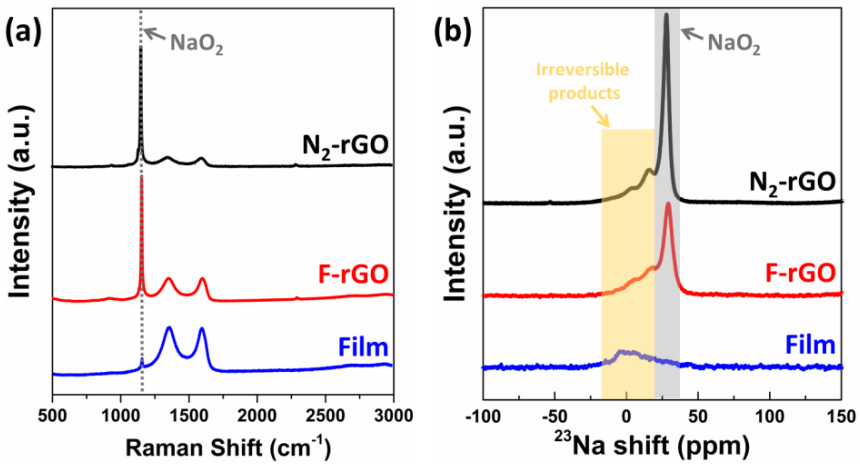


***Figure 3.4**. Raman (**a**) and $^{23}$Na NMR (**b**) spectra for the discharged rGO-based electrodes.*

Fully discharged electrodes were also studied by SEM imaging as depicted in **Figure 3.5**. It can be observed that discharge products in all the samples show a cube-type morphology, which in good agreement with literature [31,32], is characteristic of $NaO_2$ crystals. The number and size of superoxide cubes observed for the film (**Figure**

**3.5a**) is lower than in the case of the aerogels (**Figure 3.5b** and **c**), which can be related to its lower capacity. In the case of F-rGO (**Figure 3.5b**) and $N_2$-rGO (**Figure 3.5c**) discharged electrodes, the surface is covered by cubes ranging between 11 and 20 µm. It is worth to note that the deposition of $NaO_2$ on $N_2$-rGO cathode surface is greatly favoured since the surface of the aerogel is fully covered with cubes. These results can be ascribed to the 3D arrangement of the graphene sheets in the aerogel cathodes that expose a larger proportion of defects, which serve as nucleation sites for the growth of $NaO_2$. Thus, the porous network acts as diffusion channel for an enhanced $Na^+/O_2$ supply while lower restacking of graphene sheets provides accessible active sites for both ORR and OER reactions.

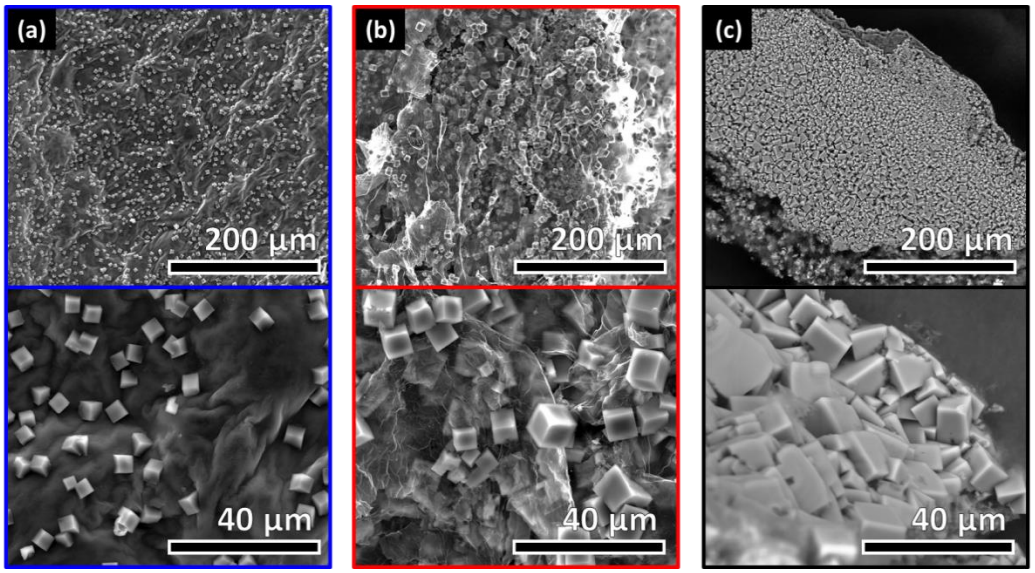


***Figure 3.5.*** *SEM pictures of galvanostatically discharged rGO-based electrodes; Film (**a**), F-rGO (**b**) and $N_2$-rGO (**c**).*

To evaluate the cycling performance of the graphene-based materials, cells were charge/discharged at 100 mA $g^{-1}$ with a capacity cut-off of 0.5 mAh $cm^{-2}$ (**Figure 3.6**). It can be attached from **Figure 3.6a** that film-based electrode is not capable to reach the capacity cut-off, showing an initial areal capacity of 0.3 mAh $cm^{-2}$ and it is only able to perform 2 charge/discharge cycles. Conversely, F-rGO and $N_2$-rGO deliver 0.5 mAh $cm^{-2}$ for 20 and 38 cycles, respectively. It is worth to remark that F-rGO electrode provides

both lower cycle life and worst C.E. evolution when compared to that of $N_2$-rGO. From galvanostatic charge/discharge curves it can be observed that the capacity of the non-porous Film (**Figure 3.6b**) is notably lower than that of the porous aerogels while the voltage hysteresis is much higher. On the other hand, F-rGO (**Figure 3.6c**) also presents higher voltage hysteresis than $N_2$-rGO (**Figure 3.6d**). More in detail, after first cycle stabilization, the average discharge and charge voltage plateaus of $N_2$-rGO fall into the range of 2.04-2.12 V and 2.36–2.44 V, respectively. These values correspond to charge overpotential of 240-370 mV (2$^{nd}$ to 38$^{th}$ cycle). In addition, $N_2$-rGO delivers 39 cycles followed by an overpotential increase (up to 510 mV at 39$^{th}$ cycle) and consequently capacity fade, probably due to accumulation of insoluble discharge products within the porous network. This finding further confirms the importance of building a tuned porous structure to improve the cycle life and stability of Na-$O_2$ cells.

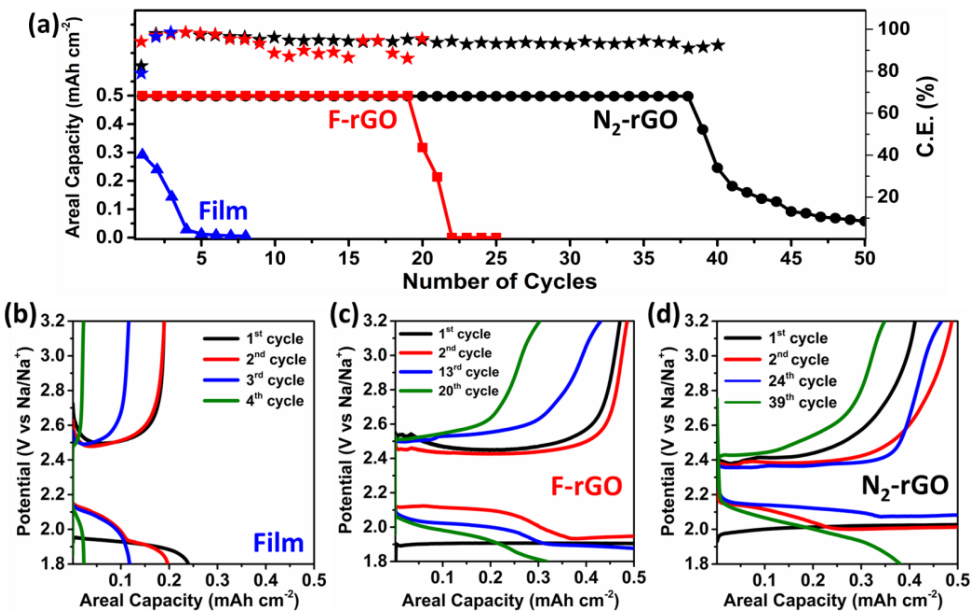


***Figure 3.6.*** *Evolution of discharge capacity and coulombic efficiency for noted samples (**a**) and representative galvanostatic charge/discharge curves of Film (**b**), F-rGO (**c**) and $N_2$-rGO (**d**) electrodes.*

In order to improve the cycle life of $N_2$-rGO cathode, shallow-cycling experiment (0.15 mAh cm$^{-2}$) was further conducted (**Figure 3.6a**). The cycle life of the Na-$O_2$ battery increases from 39 cycles (0.5 mAh cm$^{-2}$) to 128 cycles (0.15 mAh cm$^{-2}$) by

decreasing the capacity cut-off. The morphology of the discharge products after cycling was further examined by SEM imaging of the electrode in the uncharged state (**Figure 3.6b**). Two particle regimes are observed on the surface of $N_2$-rGO; ~ 12 µm cubes (**Figure 3.6c**) and ~ 3 µm rounded particles (**Figure 3.6c**); these latter particles were found in a greater extent. The appearance of different particle regimes might be due to the occurrence of two simultaneous processes; the dissolution of $NaO_2$ particles upon galvanostatic cycling (small particles) and appearance of new nucleation sites (big particles).

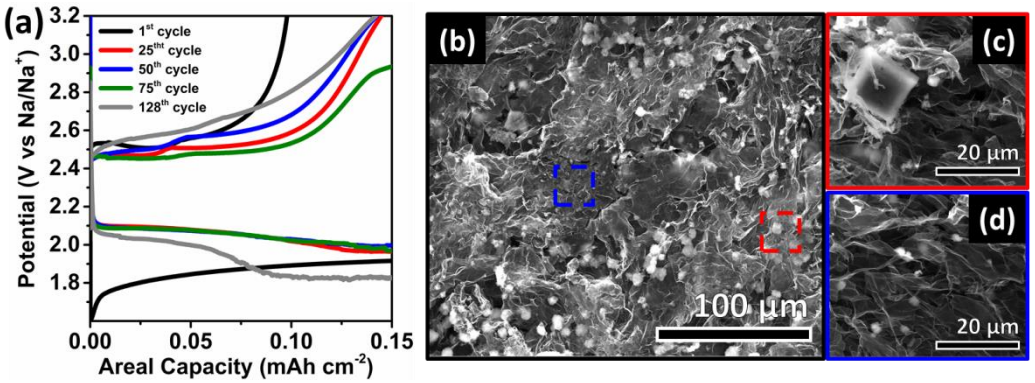


***Figure 3.7.*** *Representative galvanostatic charge/discharge curves of $N_2$-rGO sample when limiting capacity to 0.15 mAh $cm^{-2}$ (**a**) and SEM images of the electrode after 128$^{th}$ cycles at low (**b**) and high magnification (**c** and **d**).*

**Table 3.2** summarizes the state-of-the-art Na-$O_2$ battery performance using graphene-based materials. However, not all key parameters such as mass of active materials are given which hinders a reasonable evaluation. Among all the graphene-based materials reported in literature, the concentration of the electrolyte is the lowest reported, which have been shown to affect the discharge capacity and overpotential, i.e., higher concentration of electrolyte gives rise to greater discharge capacities and lower overpotentials [33]. However, a large amount of electrolyte could decrease the overall energy density of the cell, hindering a real implementation. In this work, even using the lowest concentration of electrolyte, one of the lowest charge overpotential has been attained (260 mV). Regarding the nature of the discharge products, most of the studies listed in **Table 3.2** observed the formation of $Na_2O_2$ and $Na_2CO_3$ on the surface of the air cathode [12,15,16,20,23]. Nevertheless, as previously reported [34–36], the

formation of $NaO_2$ as main discharge product results in lower voltage hysteresis and single flat plateau charge when compared with other discharge products. Similar to the herein studied aerogel cathodes, only three works identified the superoxide as main discharge product [13,14,17]. When comparing with pure graphene-based materials, results are similar to those reported previously but with lower overpotential and longer cycling life when limiting the discharge capacity [12,14]. The approach herein presented does not require of complex procedures, expensive metals or functionalization/doping, providing an efficient and sustainable method for $NaO_2$ air cathode manufacture. Overall, when comparing our result with current state-of-the-art in terms of rate, discharge capacity and cycle life; the presented pore-tuned 3D graphene-based aerogel yields an outstanding performance as Na-$O_2$ cathode.

***Table 3.2.*** *Representative electrochemical parameters summarized for the state-of-the-art of graphene-based materials used as cathodes in Na-$O_2$ batteries.*

| Material | Electrolyte | Discharge capacity | Discharge product | Number of cycles | Voltage Hysteresis (V) | Ref |
|---|---|---|---|---|---|---|
| GNS | 0.25M $NaPF_6$ in DME | 9268 mAh $g^{-1}$ [200 mA $g^{-1}$] | $Na_2O_2$ (Film) | 10 (at 300 mA $g^{-1}$ to 1200 mAh $g^{-1}$) | 1.5 | [12] |
| Printed rGO | 1M $NaCF_3SO_3$ DEGDME | 9.1 mAh $cm^{-2}$ [0.13 mA $cm^{-2}$] | $NaO_2$ (Cubes) | 120 (0.34 mA $cm^{-2}$ to 0.34 mAh $cm^{-2}$) | 0.4 | [13] |
| Porous rGO | 0.25M $NaClO_4$ in DME | 12 mAh $cm^{-2}$ [0.1 mA $cm^{-2}$] | $NaO_2$ (Cubes) | 17 (0.1 mA $cm^{-2}$ to 1 mAh $cm^{-2}$) | 0.4 | [14] |
| GNS/Pt | 0.25M $NaClO_4$ in DME | 12 mAh $cm^{-2}$ [0.1 mA $cm^{-2}$] | $Na_2CO_3$ (particles) | 10 (0.1 mA $cm^{-2}$ to 100 mAh $g^{-1}$) | 1.3 | [15] |
| rGO/Ag | 1M $NaClO_4$ in DME | 7574 mAh $g^{-1}$ [0.1 mA $cm^{-2}$] | $NaO_2$ and $Na_2O_2$ (particles) | 30 (0.2 mA $cm^{-2}$ to 0.125 mAh $cm^{-2}$) | 0.9 | [16] |
| B,N-doped rGO/$RuO_2$ | 1M $NaCF_3SO_3$ TEGDME | 3.8 mAh $cm^{-2}$ [0.05 mA $cm^{-2}$] | $NaO_2$ (Cubes) | 100 (0.05 mA $cm^{-2}$ to 0.5 mAh $cm^{-2}$) | 1.0 | [17] |
| N doped-GNS | 0.5M $NaSO_3CF_3$ in DEGDME | 6000 mAh $g^{-1}$ [150 mA $g^{-1}$] | $Na_2O_2$ (Particles) | 3 (75 mA $g^{-1}$ to 1150 mAh $g^{-1}$) | 0.6 | [19] |
| N-doped graphene aerogel | 0.3M $NaCF_3SO_3$ DEGDME | 9 mAh $cm^{-2}$ [0.08 mA $cm^{-2}$] | $Na_2O_2$ (Particles) | 100 (0.08 mA $cm^{-2}$ to 0.42 mAh $cm^{-2}$) | 0.2 | [23] |
| **$N_2$-rGO** | **0.1M $NaClO_4$ in DME** | **6.6 mAh $cm^{-2}$ [100 mA $g^{-1}$]** | **$NaO_2$ (Cubes)** | **40 (0.15 mA $cm^{-2}$ to 0.5 mAh $cm^{-2}$)** / **100 (0.15 mA $cm^{-2}$ to 0.15 mAh $cm^{-2}$)** | **0.3** | **This work** |

### 3.2.4. Discussion and proposed mechanisms

The rGO-based aerogels presented in this work, therefore, demonstrate to be competitive with all the above commented approaches due to their high conductivity, stability and the existence of unpaired electrons located in lattice defects which can catalyse both ORR and OER reactions. In addition, the influence of the pore size distribution of the present work correlates well with that previously reported for Li-$O_2$ battery cathodes by Xiao et al. [37]. They observed that both too large and too small pore size led to a less efficient use of mesopore volume. This observation is consistent with the results of this work since large mesopores existing in F-rGO cathode could lead to a loose of surface area for the adsorption of $O_2$ molecules and deposition of discharge products. As opposed to the trend observed in this work, Xiao´s group reported that narrow pore size distributions with an average pore size ~ 3.5 nm enhance Li-$O_2$ batteries efficiency. This might be due to the difference in size between Li and Na where Li ions could more easily access to smaller pores than Na ions [38]. On the other hand, lithium presents higher desolvation energies than sodium and may need higher adsorption energies (narrower pores) to get desolvated for the formation of metal oxides [39]. A recent report in Na-$O_2$ batteries furtherly confirm the results obtained in this study, since they observe that the highest discharge capacity was found for a carbonaceous cathode with a pore size of ca. 6 nm; this was over 100 times greater than that delivered by a cathode with a pore size less than 2 nm [40].

A diagram of the proposed discharge mechanisms for the rGO-based electrodes is depicted in **Scheme 3.2**. The fast capacity fade observed for the rGO film can be ascribed to the absence of accessible active sites to perform the ORR/OER reactions on the surface due to its non-porous nature. Thus, a high overpotential is observed in the discharge-charge profile of Film electrodes (see, **Figure 3.6b**). As previously reported [41], oxygen molecules diffusion through the graphene matrix can be seriously reduced due to restacking of the graphene sheets. The subsequent formation of $NaO_2$ nuclei is therefore hindered as the active sites in between the graphene sheets are blocked. In the case of F-rGO aerogel, the assembling of the graphene sheets leads to the formation of ordered domains in between oriented meso/macroporous channels. The thus formed porous network supplies a path for molecules to diffuse towards the active sites. Nevertheless, the oriented self-assembly of the sheets to form porous channels causes a partial stacking, limiting the exposure of the active sites. As a consequence, reduced effective area for oxygen to oxidation/reduction originates

relative high overpotential and low cycling stability (see, **Figure 3.6c**). For $N_2$-rGO aerogel-based electrodes, the disordered arrangement of the graphene sheets; i) maximize the exposed surface of active sites, ii) provides large pore volume, iii) wide mesopore size distribution and iv) narrow macropore size. These specific features clearly promote the occurrence of ORR/OER, enhance the molecular diffusion and favour the formation/redissolution of the $NaO_2$ cubes during the electrodes cycling. It can therefore be concluded that the improved performance of $N_2$-rGO when compared with F-rGO can be ascribed to the different spatial arrangement of the graphene sheets and, consequently, to specific meso-macroporosity.

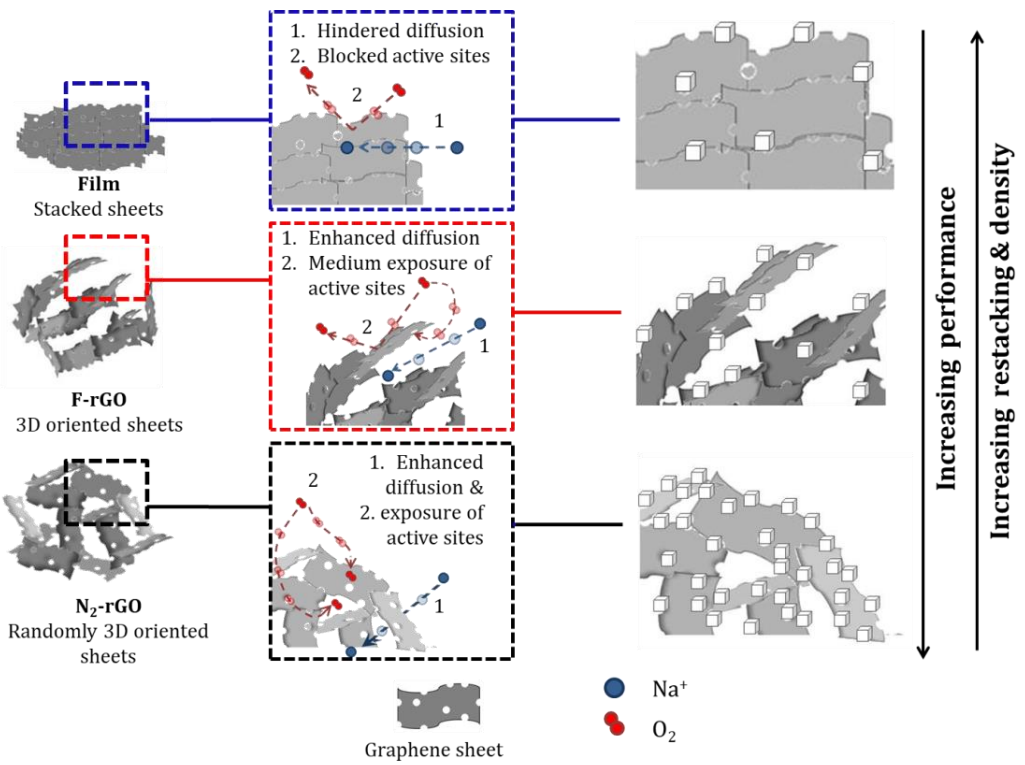


***Scheme 3.2.*** *Proposed discharge processes followed in the rGO-based electrodes.*

## 3.3. Summary and conclusions

In this chapter the preparation of graphene-based aerogels with tuned porosity and its successful implementation as oxygen electrodes for Na-$O_2$ batteries is demonstrated. The influence of experimental parameters like freezing temperature of the GO suspensions before freeze-drying has demonstrated to have a great influence over the textural properties of the resultant aerogels. Moreover, it was observed that air cathode porous properties play a key role on battery performance, influencing oxygen supply and hence oxygen reduction and evolution reaction kinetics (ORR/OER). Hence, a sudden freeze at very low temperature of the GO suspensions (-196 °C, $N_2$-rGO) leads to a discharge capacity of 6.61 mAh $cm^{-2}$, a good stability, and more than 100 cycles. The utilization of more progressive freezing (-75 °C, F-rGO) leads to significant reduction of both the discharge capacity and the cyclability. Such performance degradation is ascribed to large mesopores existing in the F-rGO cathode (>1,500 nm) which could lead to a loss of surface area for the adsorption of $O_2$ molecules and deposition of discharge products. The low capacity and cyclability of non-porous 2D rGO film as the cathode, highlights the importance of a good interconnected graphene-based matrix for practical Na-$O_2$ batteries. The enhanced performance of the $N_2$-rGO cathode is, therefore, related to three features; (i) highly accessible active sites for the ORR due to the tridimensional arrangement of the graphene sheets (low restacking), (ii) high pore volume (0.22 $cm^3\ g^{-1}$) and (iii) suitable mesopore (5– 25 nm) and macropore (ca. 1200 nm) size maximizing the surface area and molecules/ion diffusion.

## 3.4. Bibliography

[1] K. Song, D.A. Agyeman, M. Park, J. Yang, Y.-M. Kang, High-Energy-Density Metal-Oxygen Batteries: Lithium-Oxygen Batteries vs Sodium-Oxygen Batteries, Adv. Mater. 29 (2017) 1606572. https://doi.org/10.1002/adma.201606572.

[2] Z. Zheng, C. Wu, Q. Gu, K. Konstantinov, J. Wang, Research Progress and Future Perspectives on Rechargeable Na-O $_2$ and Na-CO $_2$ Batteries, ENERGY Environ. Mater. 4 (2021) 158–177. https://doi.org/10.1002/eem2.12139.

[3] H. Yadegari, Q. Sun, X. Sun, Sodium-Oxygen Batteries: A Comparative Review from Chemical and Electrochemical Fundamentals to Future Perspective, Adv. Mater. 28 (2016) 7065–7093. https://doi.org/10.1002/adma.201504373.

[4] B. Sun, C. Pompe, S. Dongmo, J. Zhang, K. Kretschmer, D. Schröder, J. Janek, G. Wang, Challenges for Developing Rechargeable Room-Temperature Sodium

Oxygen Batteries, Adv. Mater. Technol. 3 (2018) 1800110. https://doi.org/10.1002/admt.201800110.
[5] R.C. Alkire, P.N. Bartlett, J. Lipkowski, Electrochemistry of Carbon Electrodes, Advances in Electrochemical Sciences and Engineering, 2015.
[6] S. Liu, S. Liu, J. Luo, Carbon-based cathodes for sodium-air batteries, New Carbon Mater. 31 (2016) 264–270. https://doi.org/10.1016/S1872-5805(16)60012-4.
[7] E. Faktorovich-Simon, A. Natan, E. Peled, D. Golodnitsky, Comparison of the Catalytic Activity of Carbon, Spinel-Based, and Carbide Materials in the Na-Air Battery, Front. Mater. 6 (2019) 249. https://doi.org/10.3389/fmats.2019.00249.
[8] C. Shu, Y. Lin, B. Zhang, S.B. Abd Hamid, D. Su, Mesoporous boron-doped onion-like carbon as long-life oxygen electrode for sodium–oxygen batteries, J. Mater. Chem. A. 4 (2016) 6610–6619. https://doi.org/10.1039/C6TA00901H.
[9] B. Sun, K. Kretschmer, X. Xie, P. Munroe, Z. Peng, G. Wang, Hierarchical Porous Carbon Spheres for High-Performance Na–$O_2$ Batteries, Adv. Mater. 29 (2017) 1606816. https://doi.org/10.1002/adma.201606816.
[10] J.L. Gómez Urbano, M. Enterría, I. Monterrubio, I. Ruiz de Larramendi, D. Carriazo, N. Ortiz Vitoriano, T. Rojo, An Overview of Engineered Graphene-Based Cathodes: Boosting Oxygen Reduction and Evolution Reactions in Lithium– and Sodium–Oxygen Batteries, ChemSusChem. 13 (2020) 1203–1225. https://doi.org/10.1002/cssc.201902972.
[11] B. Kishore, B. Singh, S. Kumar, Graphene-based Nanocatalysts for Oxygen Reduction and Evolution Reactions in Metal-oxygen Batteries, Curr. Catal. 7 (2018) 158–166. https://doi.org/10.2174/2211544707666180807125616.
[12] W. Liu, Q. Sun, Y. Yang, J.-Y. Xie, Z.-W. Fu, An enhanced electrochemical performance of a sodium–air battery with graphene nanosheets as air electrode catalysts, Chem. Commun. 49 (2013) 1951. https://doi.org/10.1039/c3cc00085k.
[13] X. Lin, J. Wang, X. Gao, S. Wang, Q. Sun, J. Luo, C. Zhao, Y. Zhao, X. Yang, C. Wang, R. Li, X. Sun, 3D Printing of Free-Standing "$O_2$ Breathable" Air Electrodes for High-Capacity and Long-Life Na–$O_2$ Batteries, Chem. Mater. 32 (2020) 3018–3027. https://doi.org/10.1021/acs.chemmater.9b05360.
[14] T. Liu, G. Kim, M.T.L. Casford, C.P. Grey, Mechanistic Insights into the Challenges of Cycling a Nonaqueous Na–$O_2$ Battery, J. Phys. Chem. Lett. 7 (2016) 4841–4846. https://doi.org/10.1021/acs.jpclett.6b02267.
[15] S. Zhang, Z. Wen, K. Rui, C. Shen, Y. Lu, J. Yang, Graphene nanosheets loaded with Pt nanoparticles with enhanced electrochemical performance for sodium–oxygen batteries, J. Mater. Chem. A. 3 (2015) 2568–2571. https://doi.org/10.1039/C4TA05427J.
[16] S. Kumar, B. Kishore, N. Munichandraiah, Electrochemical studies of non-aqueous Na–$O_2$ cells employing Ag-RGO as the bifunctional catalyst, RSC Adv. 6 (2016) 63477–63479. https://doi.org/10.1039/C6RA13596J.

[17] F. Wu, Y. Xing, J. Lai, X. Zhang, Y. Ye, J. Qian, L. Li, R. Chen, Micrometer-Sized $RuO_2$ Catalysts Contributing to Formation of Amorphous Na-Deficient Sodium Peroxide in Na-$O_2$ Batteries, Adv. Funct. Mater. 27 (2017) 1700632. https://doi.org/10.1002/adfm.201700632.

[18] N.E. Benti, G.A. Tiruye, Y.S. Mekonnen, Boron and pyridinic nitrogen-doped graphene as potential catalysts for rechargeable non-aqueous sodium–air batteries, RSC Adv. 10 (2020) 21387–21398. https://doi.org/10.1039/D0RA03126G.

[19] Y. Li, H. Yadegari, X. Li, M.N. Banis, R. Li, X. Sun, Superior catalytic activity of nitrogen-doped graphene cathodes for high energy capacity sodium–air batteries, Chem. Commun. 49 (2013) 11731. https://doi.org/10.1039/c3cc46606j.

[20] A.C. Pozo-gonzalo, Y. Zhang, P. Howlett, D. Macfarlane, T. Rojo, J. Fang, N. Ortiz-vitoriano, J. Miguel, M. Echeverria, Controlling the three phase boundary in Na-oxygen batteries, ChemSusChem. 12 (2019) 4054–4063. https://doi.org/10.1002/cssc.201901351.

[21] W. Yin, Z. Fu, The Potential of Na–Air Batteries, ChemCatChem. 9 (2017) 1545–1553. https://doi.org/10.1002/cctc.201600646.

[22] H. Yadegari, M.N. Banis, B. Xiao, Q. Sun, X. Li, A. Lushington, B. Wang, R. Li, T.-K. Sham, X. Cui, X. Sun, Three-Dimensional Nanostructured Air Electrode for Sodium–Oxygen Batteries: A Mechanism Study toward the Cyclability of the Cell, Chem. Mater. 27 (2015) 3040–3047. https://doi.org/10.1021/acs.chemmater.5b00435.

[23] S. Zhang, Z. Wen, J. Jin, T. Zhang, J. Yang, C. Chen, Controlling uniform deposition of discharge products at the nanoscale for rechargeable Na–$O_2$ batteries, J. Mater. Chem. A. 4 (2016) 7238–7244. https://doi.org/10.1039/C6TA02336C.

[24] M. Enterría, J.L. Gómez-Urbano, J.M. Munuera, S. Villar-Rodil, D. Carriazo, J.I. Paredes, N. Ortiz-Vitoriano, Boosting the Performance of Graphene Cathodes in Na–$O_2$ Batteries by Exploiting the Multifunctional Character of Small Biomolecules, Small. 17 (2021) 2005034. https://doi.org/10.1002/smll.202005034.

[25] J.M. Munuera, J.I. Paredes, M. Enterría, S. Villar-Rodil, A.G. Kelly, Y. Nalawade, J.N. Coleman, T. Rojo, N. Ortiz-Vitoriano, A. Martínez-Alonso, J.M.D. Tascón, High Performance Na-$O_2$ Batteries and Printed Microsupercapacitors Based on Water-Processable, Biomolecule-Assisted Anodic Graphene, ACS Appl. Mater. Interfaces. 12 (2020) 494–506. https://doi.org/10.1021/acsami.9b15509.

[26] M. Thommes, K. Kaneko, A.V. Neimark, J.P. Olivier, F. Rodriguez-Reinoso, J. Rouquerol, K.S.W. Sing, Physisorption of gases, with special reference to the evaluation of surface area and pore size distribution (IUPAC Technical Report), Pure Appl. Chem. 87 (2015) 1051–1069. https://doi.org/10.1515/pac-2014-1117.

[27] E.F. Steigmeier, H.M. Bösch, W. Känzig, Molekiil- und Gitterschwingungen im Natriumhyperoxid, Z. Für Phys. 16 (1973) 107–112. https://doi.org/10.1007/bf02422692.

[28] H.R. Jiang, M.C. Wu, X.L. Zhou, X.H. Yan, T.S. Zhao, Computational insights into the effect of carbon structures at the atomic level for non-aqueous sodium-oxygen batteries, J. Power Sources. 325 (2016) 91–97. https://doi.org/10.1016/j.jpowsour.2016.05.132.

[29] L. Lutz, D.A.D. Corte, Y. Chen, D. Batuk, L.R. Johnson, A. Abakumov, L. Yate, E. Azaceta, P.G. Bruce, J. Tarascon, A. Grimaud, The Role of the Electrode Surface in Na–Air Batteries: Insights in Electrochemical Product Formation and Chemical Growth of $NaO_2$, Adv. Energy Mater. 8 (2018) 1701581. https://doi.org/10.1002/aenm.201701581.

[30] T.R. Krawietz, D.K. Murray, J.F. Haw, Alkali Metal Oxides, Peroxides, and Superoxides: A Multinuclear MAS NMR Study, J. Phys. Chem. A. 102 (1998) 8779–8785. https://doi.org/10.1021/jp9823190.

[31] Q. Sun, J. Liu, B. Xiao, B. Wang, M. Banis, H. Yadegari, K.R. Adair, R. Li, X. Sun, Visualizing the Oxidation Mechanism and Morphological Evolution of the Cubic-Shaped Superoxide Discharge Product in Na–Air Batteries, Adv. Funct. Mater. 29 (2019) 1808332. https://doi.org/10.1002/adfm.201808332.

[32] R. Tatara, G.M. Leverick, S. Feng, S. Wan, S. Terada, K. Dokko, M. Watanabe, Y. Shao-Horn, Tuning $NaO_2$ Cube Sizes by Controlling $Na^+$ and Solvent Activity in Na–$O_2$ Batteries, J. Phys. Chem. C. 122 (2018) 18316–18328. https://doi.org/10.1021/acs.jpcc.8b05418.

[33] J. Ma, W. Zhang, X. Wang, M. Tang, Z. Huang, J. Li, H. Zhang, X. Yang, Z. Guo, Y. Wang, Revealing the mechanism of saturated ether electrolyte for improving the long-cycling stability of Na-O2 batteries, Nano Energy. 84 (2021) 105927. https://doi.org/10.1016/j.nanoen.2021.105927.

[34] C.L. Bender, D. Schrçder, R. Pinedo, P. Adelhelm, J. Janek, One- or Two-Electron Transfer? The Ambiguous Nature of the Discharge Products in Sodium–Oxygen Batteries, Angew Chem Int Ed. 55 (2016) 4640–4649.

[35] H. Yadegari, X. Sun, Recent Advances on Sodium–Oxygen Batteries: A Chemical Perspective, Acc. Chem. Res. 51 (2018) 1532–1540. https://doi.org/10.1021/acs.accounts.8b00139.

[36] X. Bi, R. Wang, K. Amine, J. Lu, A Critical Review on Superoxide-Based Sodium–Oxygen Batteries, Small Methods. 3 (2019) 1800247. https://doi.org/10.1002/smtd.201800247.

[37] J. Xiao, D. Wang, W. Xu, D. Wang, R.E. Williford, J. Liu, J.-G. Zhang, Optimization of Air Electrode for Li/Air Batteries, J. Electrochem. Soc. 157 (2010) A487. https://doi.org/10.1149/1.3314375.

[38] T. Ogoshi, Y. Sakatsume, K. Onishi, R. Tang, K. Takahashi, H. Nishihara, Y. Nishina, B.D.L. Campéon, T. Kakuta, T.-A. Yamagishi, The carbonization of aromatic molecules with three-dimensional structures affords carbon materials with controlled pore sizes at the Angstrom-level, Commun. Chem. 4 (2021) 75. https://doi.org/10.1038/s42004-021-00515-0.

[39] K.L. Browning, R.L. Sacci, G.M. Veith, Energetics of $Na^+$ Transport through the Electrode/Cathode Interface in Single Solvent Electrolytes, J. Electrochem. Soc. 164 (2017) A580–A586. https://doi.org/10.1149/2.0311704jes.

[40] T.A. Ha, C. Pozo-Gonzalo, K. Nairn, D.R. MacFarlane, M. Forsyth, P.C. Howlett, An investigation of commercial carbon air cathode structure in ionic liquid based sodium oxygen batteries, Sci. Rep. 10 (2020) 7123. https://doi.org/10.1038/s41598-020-63473-y.

[41] E. Yoo, H. Zhou, Li−Air Rechargeable Battery Based on Metal-free Graphene Nanosheet Catalysts, ACS Nano. 5 (2011) 3020–3026. https://doi.org/10.1021/nn200084u.

# Chapter IV. Electrochemical Double Layer Capacitors



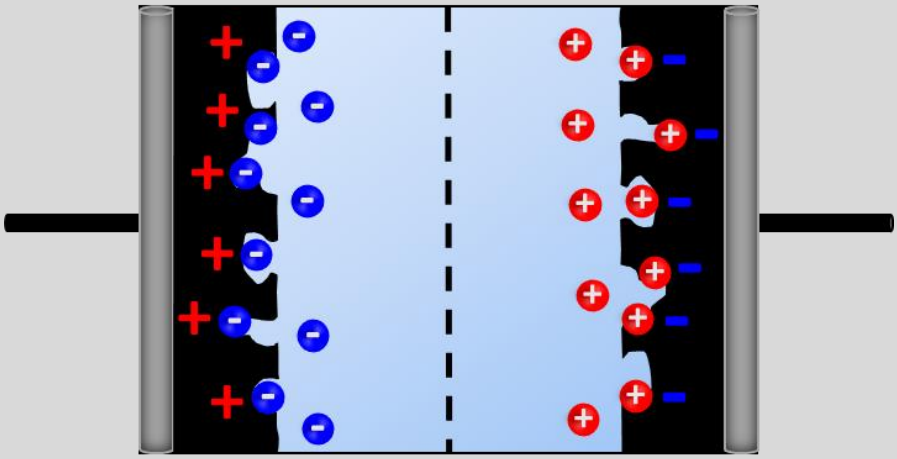

## 4.1. State-of-the-art of graphene-based EDLCs

High specific surface area materials plays a significant role in the enhancement of charge storage in EDLCs since electrostatic adsorption/desorption of ions mainly takes place on the surface of the electrode. The excellent mechanical and electrical properties of graphene combined with its high theoretical surface area of 2,630 $m^2 g^{-1}$ make it an ideal material for the fabrication of EDLCs [1]. However, the full utilization of the graphene surface is not possible, mainly due to the serious stacking between graphene sheets [2,3]. In order to tackle this issue, great efforts are being made to enhance the SSA of graphene and its derivatives like three-dimensional processing [4–8] or chemical activation [9–12]. However, multilayer structure and defects are inevitable in graphene electrodes as large-scale production of pristine graphene materials are widely considered difficult. Therefore, new methods are necessary to further improve the performance of graphene-based electrodes. Hybridization with other functional materials is one promising strategy to push the performance of graphene-based electrodes to a higher level [13]. In fact, enhanced energy density can be attained when combining graphene with pseudocapacitive materials that offer extra charge storage capability like metal oxides [14–20], metal sulfides [21–24] or polymers [25–29]. However, cyclic stability and power performance still remains a challenge for these composites [30]. On this regard, the formation of composites combining graphene and activated carbons, has demonstrated to bring several advantages [31–36]. On one hand, ACs have been the preferred choice as electrodes in high performing EDLCs due to its large SSA and low cost, as well as superior physical and chemical stability [37]. Additionally, ACs can be readily produced from worldwide abundant an easy accessible wastes such as orange peels [38], coffee waste [39], cigarette butts [40] or paper pulp [41]. On the other hand, the incorporation of graphene has been found to be useful for increasing the electronic conductivity of the composites by tailoring their particle morphology textural properties [42–44]. Nevertheless, most of the reported works relies on the use of aqueous-based electrolytes, which limits considerably the energy density of the EDLCs due to its narrower voltage window [45]. Thus, the evaluation of graphene-AC composites in non-aqueous electrolytes (organic, ionic liquids) is needed to subtract its maximal potential as electrodes for advanced EDLCs.

## 4.2. Cigarette butts-graphene derived activated carbons for EDLCs

In the light of the aforementioned, this section focuses on the preparation of activated carbon-graphene composites and its evaluation as electrodes for symmetric EDLCs in non-aqueous electrolytes. Cigarette butts (CBs) were chosen as AC precursor since are considered an extremely pollutant waste due to its low biodegradability rate and to the presence of highly toxic compounds (heavy metals, polycyclic aromatic hydrocarbons, hydrogen cyanide, etc.) that can be easily released to aquifers and soils. Moreover, CBs are one of the most abundant residues (see **Scheme 4.1**), yearly accounting approximately a million of tons worldwide [46]. Pyrolysis and activation of acetate cellulose, which is the main component of cigarette filters, for the production of ACs and its application on aqueous-based EDLCs has been previously presented as a promising revalorization strategy [47–50]. In this work, three different non-aqueous electrolytes (ammonium salt-based conventional organic electrolyte and two imidazolium-based ionic liquids), are used with the aim of extending the operational voltage window and thus, enhance the energy density of the devices. Moreover, addition of graphene as additive is expected not only to increase the conductivity of the carbon composite, but also to provide tailored morphological and textural properties towards the adsorption of large electrolyte ions in the electrolyte.

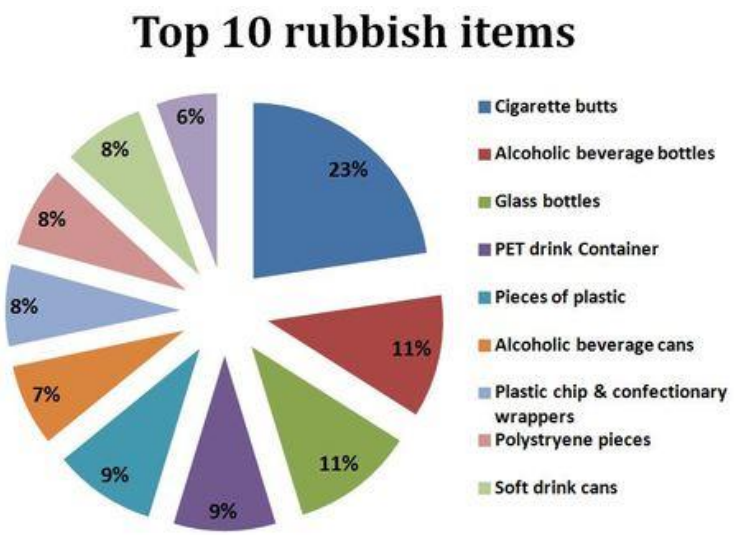


***Scheme 4.1.*** *Percentage of most common type of litters in the state of Victoria (Australia) in 2013 [51].*

### 4.2.1. Material and electrode preparation of the ACs

Commercial GO from Graphenea and cigarette butts, collected from ashtrays, served as carbon precursors. First, remaining tobacco rods, paper and ashes were removed from the cigarette filter. Then, filters were manually shredded into a fluffy mass of fibers. Cigar waste/GO composite was prepared by mixing 3.0 g of as-obtained fibers and 50 mL of 2 mg $mL^{-1}$ GO. Mixtures were kept 12 h before drying by freeze-freeze drying process. Dried precursor composite was pre-carbonized at 400 °C for 3 h under Ar atmosphere. Then carbon is grounded together with KOH in a mortar using a C:KOH mass ratio of 1:4 and then heated at 800 °C for 1 h under Ar atmosphere. The resulting material was washed once with a diluted solution of HCl and then several times with hot deionized water. Dry activated carbon (GO-FdAC) is obtained after freeze and freeze-drying the material (**Scheme 4.1**). For the sake of comparison, an activated carbon was also prepared following the same route but in the absence of GO (FdAC).

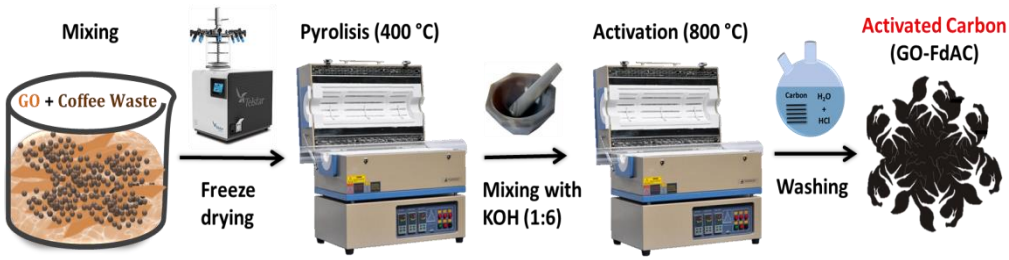


***Scheme 4.2.*** *Schematic representation of the synthetic route followed for the preparation of GO-FdAC.*

Electrodes of active materials were processed by rolling and pressing a mixture formed by these ACs together with Super P C65 and polytetrafluoroethylene in ethanol using a 90:5:5 mass ratio. Self-standing electrode discs (ϕ= 11 mm) were punched out from the paste and dried at 120 °C under vacuum overnight prior to cell assembly. AC-based electrodes (4 ± 1 mg $cm^{-2}$, 150 ± 30 µm) were evaluated as symmetric EDLCs using a two-electrode Swagelok-type cell. AC-based electrodes were also evaluated in a three-electrode Swagelok-type cell using an oversized Norit (Kuraray) disc as counter electrode and a silver wire as reference electrode ($Ag/Ag^{+}$). The chosen electrolytes were 1M tetraethylammonium tetrafluoroborate ($Et_4N$ $BF_4$) in acetonitrile (ACN), 1-ethyl-3-methylimidazolium tetrafluoroborate (EMIN $BF_4$) and 1-ethyl-3-methylimidazolium bis(trifluoromethanesulfonyl) imide (EMIN TFSI).

### 4.2.2. Morphological and physicochemical characterization of the ACs

As described in **Section 4.2.1**, cigarette filters were dispersed within the graphene oxide suspension to maximize the homogeneous distribution of the graphene sheets into the acetate cellulose fibers. Afterwards, the dried composite was submitted to a pre-carbonization step at 400 °C prior the chemical activation. As previously reported, this pre-carbonization step has been proved to enhance the SSA of the final ACs [52,53]. Morphology of pre-carbonized samples, without (FdAC precursor) and with graphene (GO-FdAC precursor) was evaluated by SEM imaging. It can be observed that FdAC precursor (**Figure 4.1a**) is formed by large-sized carbon particles (>100 µm) with smooth surface. The addition of graphene results in a significant reduction of the particle size (<50 µm), which it is also accompanied by a roughening of the carbon surface, and its homogenous coating by graphene sheets (**Figure 4.1b**). No significant morphological changes are observed by SEM upon activation of FdAC (**Figure 4.1c**). On the contrary, the incorporation of graphene sheets in the GO-FdAC sample (**Figure 4.1d**) seems to act as a template during acetate cellulose fibers carbonization. As result, GO-FdAC sample shows a pronounced flat-shaped morphology compared to that of FdAC sample.

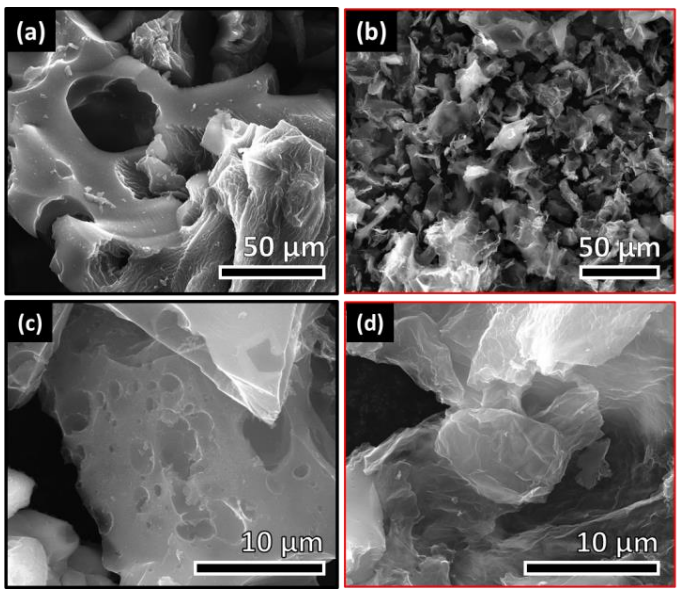


***Figure 4.1.*** *SEM images of filters (**a**) and graphene-filters mixture (**b**) carbonized at 400 °C; as well as FdAC (**c**) and GO-FdAC (**d**) activated carbons.*

TEM image of the GO-FdAC sample clearly shows the uniform growth of acetate cellulose-derived AC on the surface of the graphene sheets (**Figure 4.2a**). The Raman spectra (**Figure 4.2b**) registered for these materials were deconvoluted to better understand the structural differences between both samples. The fitted spectra show two characteristic D and G bands at ca. 1,345 and ca. 1,593 $cm^{-1}$, respectively. From the ratio between bands integrated areas ($A_D/A_G$), values of 2.17 and 1.42 were calculated for FdAC and GO-FdAC, pointing out the lower concentration of defects and larger degree of graphitization of the graphene containing sample. Additionally, the spectra also show the I and D'' band at ca. 1070 and ca. 1550 $cm^{-1}$, these bands are related to the disorder in the graphitic lattice and the presence of amorphous phases, respectively. These results are in agreement with the morphological changes induced by the incorporation of the graphene sheets into the carbon composites observed by electron microscopy.

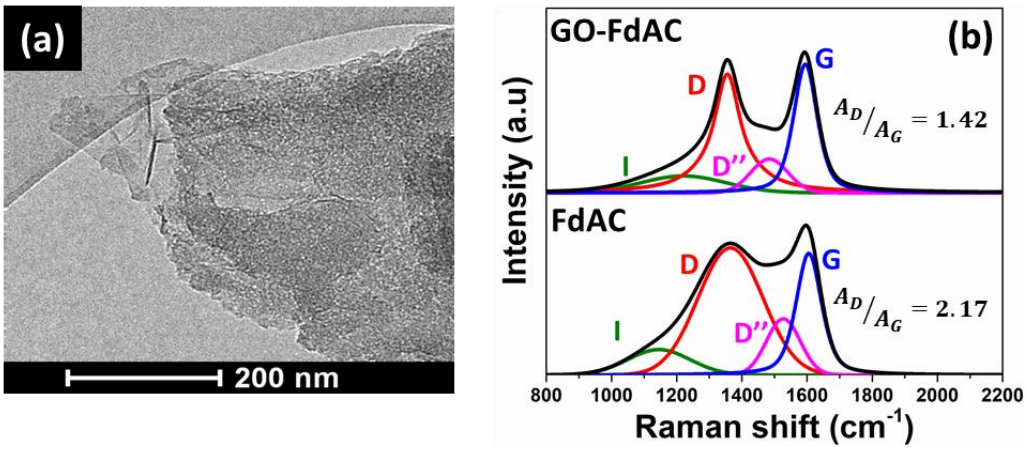


***Figure 4.2.*** *TEM image of GO-FdAC sample (**a**) and Raman spectra (**b**) of noted activated carbons.*

Textural properties of the activated carbons were determined by nitrogen adsorption/desorption isotherms, which are included in **Figure 4.3a**. According to the IUPAC classification [54], the isotherm of the FdAC sample can be indexed as type-I, which corresponds to microporous carbons, while GO-FdAC exhibits a profile in between type-I and IV, characteristic of samples containing a combination of both micropores and mesopores. FdAC and GO-FdAC activated carbons show BET specific

surface areas of 2,266 and 2,252 $m^2 g^{-1}$, respectively. Pore size distributions calculated from the isotherms are depicted in **Figure 4.3b**. Most of the total pore volume of FdAC sample corresponds to the microporous contribution, showing a large amount of small-sized micropores (0.7 nm). On the other hand, the pore size distribution calculated for the GO-FdAC sample is shifted towards larger microporous ranges and small micropores coexist with medium (0.9 nm) and larger ones (2.0 nm). Differences in PSD for both samples can be ascribed to the morphological changes induced by the presence of graphene, as already observed in the SEM images (see **Figure 4.1**). Specifically, the graphene sheets act as support for the cellulose acetate fibers, limiting the carbon particle growth and leading to composites with smaller particle size. Under these circumstances the impregnation with KOH is favored leading to the collapse of contiguous micropores into larger size pores.

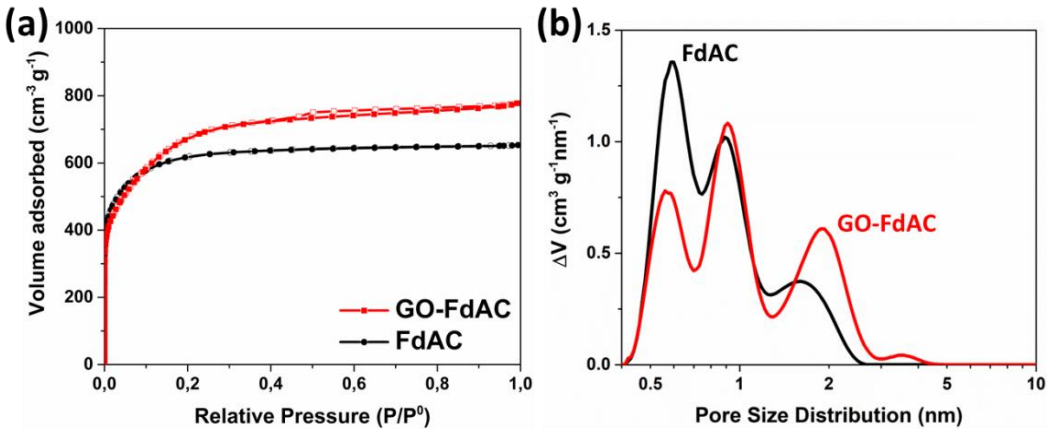


***Figure 4.3.*** *Nitrogen adsorption/desorption isotherms (**a**) and corresponding pore size distributions (**b**) of noted activated carbons.*

### 4.2.3. Electrochemical characterization of the ACs

Activated carbon electrodes were first electrochemically evaluated using a two electrode symmetric configuration in one organic electrolyte (1M $Et_4N$ $BF_4$ in ACN) and two bare ionic liquids (EMIN $BF_4$ and EMIN TFSI). The determination of the stable operating voltage window for each electrolyte is depicted in **Figure 4.4**. As expected, the higher electrochemical stability of the imidazolium-based ionic liquids enables a much wider operational window than that of conventional EDLC organic electrolyte.

Specifically, operating voltage windows of 2.8, 3.3 and 3.4 V were determined for the 1M $Et_4N$ $BF_4$ / ACN (**Figure 4.4a**), EMIN $BF_4$ (**Figure 4.4b**) and EMIN TFSI (**Figure 4.4c**) electrolytes, respectively. Same voltage windows determined for GO-FdAC electrodes were applied to FdAC-based EDLCs for the sake of comparison (**Figure 4.4d**, **e** and **f**).

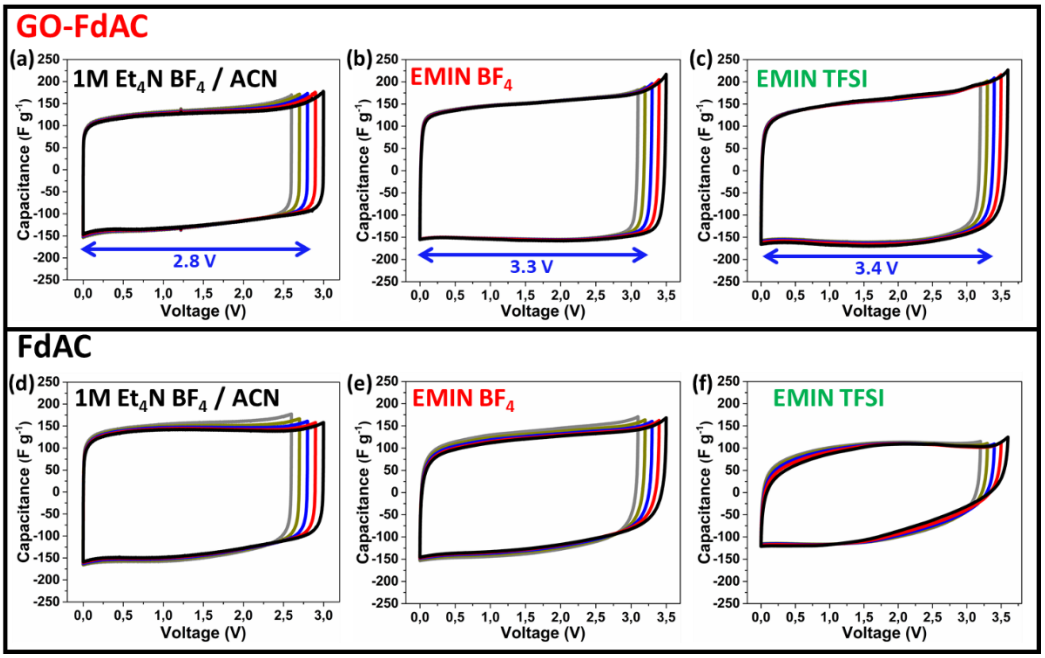


***Figure 4.4.*** *CVs of symmetric EDLCs measured at 5 mV $s^{-1}$ using GO-FdAC electrodes at different voltage windows in $Et_4N$ $BF_4$ (**a**), EMIN $BF_4$ (**b**) and EMIN TFSI (**c**), as well as corresponding measurements for FdAC electrodes (**d**, **e** and **f**).*

CVs at different sweep rates included in **Figure 4.5** illustrate the performance of both ACs in those operating voltage ranges. At a first sight, the rectangular-shaped voltammograms reveal the capacitive storage electrostatic mechanism in both of the samples whatever the electrolyte tested. However, the graphene containing sample- GO-FdAC- (**Figure 4.5a, b** and **c**) outperforms pristine activated carbon- FdAC- (**Figure 4.5d, e** and **f)** in terms of specific capacitance values and capacitance retention. This fact is much more prominent in the ionic liquid systems. A deeper analysis in the performance of the GO-FdAC in ILs (**Figure 4.5b** and **c**) shows its good capacitance retention, evidenced by the rectangular-shaped profile of CV curves even at very high

sweep rates. In contrast, when the graphene-free FdAC sample is tested in ILs, its CV curves get distorted and specific capacitance strongly decays when increasing the sweep rates (**Figure 4.5e** and **f**). The good electrochemical performance of GO-FdAC can be ascribed, on one hand to its wider porosity, which enables a fast access of the electrolyte ions to the whole surface of the carbon composite, and, on the other hand, to its better electronic conductivity. On the contrary, the narrow micropores (mainly pores below 0.7 nm) present on the FdAC sample restrict the access of the large $EMIN^+$ and $TFSI^-$ ions.

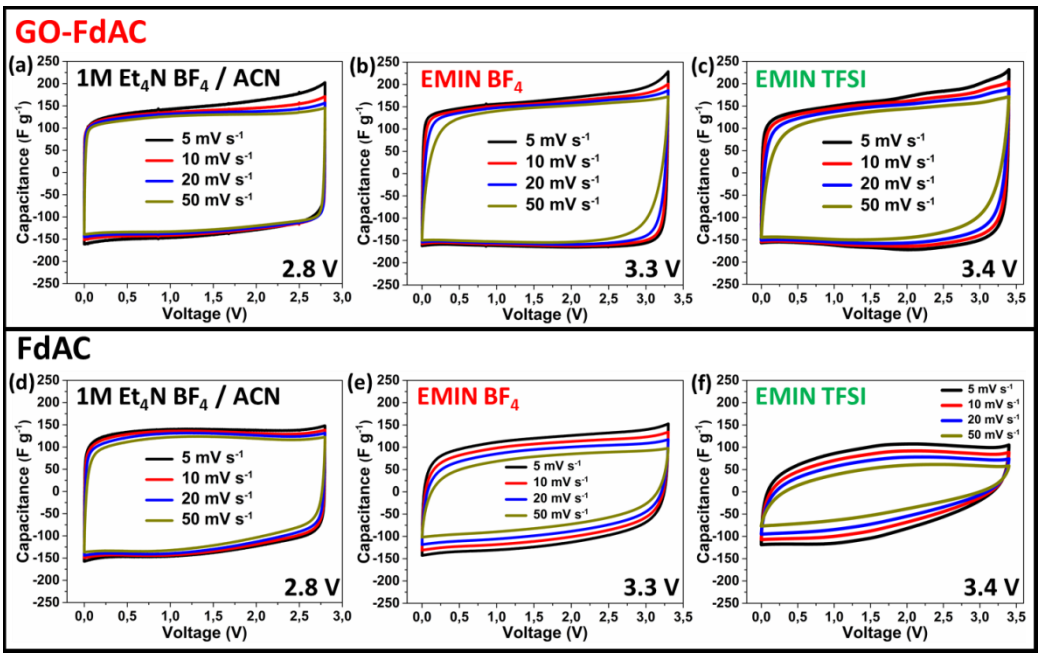


***Figure 4.5.*** *CVs at different scan rates for symmetric EDLCs using GO-FdAC electrodes in $Et_4N\ BF_4$ (**a**), EMIN $BF_4$ (**b**) and EMIN TFSI (**c**), as well as corresponding measurements for FdAC sample (**d**, **e** and **f**)*

Galvanostatic charge/discharge curves registered for the GO-FdAC and FdAC samples in the different electrolytes are included in **Figure 4.6**. In agreement with the CVs measurements, the triangular shape of the charge/discharge curves confirms the electrostatic charge storage mechanism and the absence of faradaic processes on these EDLC systems. More in detail, the GO-FdAC sample when measured at current

density of 1 A $g^{-1}$ shows a negligible ohmic drop whatever the electrolyte tested (**Figure 4.6a**). Only a small voltage decay is observed in the IL-based systems when the current density is increased to 10 A $g^{-1}$ (**Figure 4.6b**). These results support the outstanding electric conductivity of the graphene-containing sample. In the case of the 1M $Et_4NBF_4$/ACN electrolyte, no significant voltage drop is observed whatever the current rate tested. Regarding the pristine sample, FdAC shows more pronounced ohmic drops either at 1 (**Figure 4.6c**) and 10 A $g^{-1}$ (**Figure 4.6d**) in all the tested electrolytes.

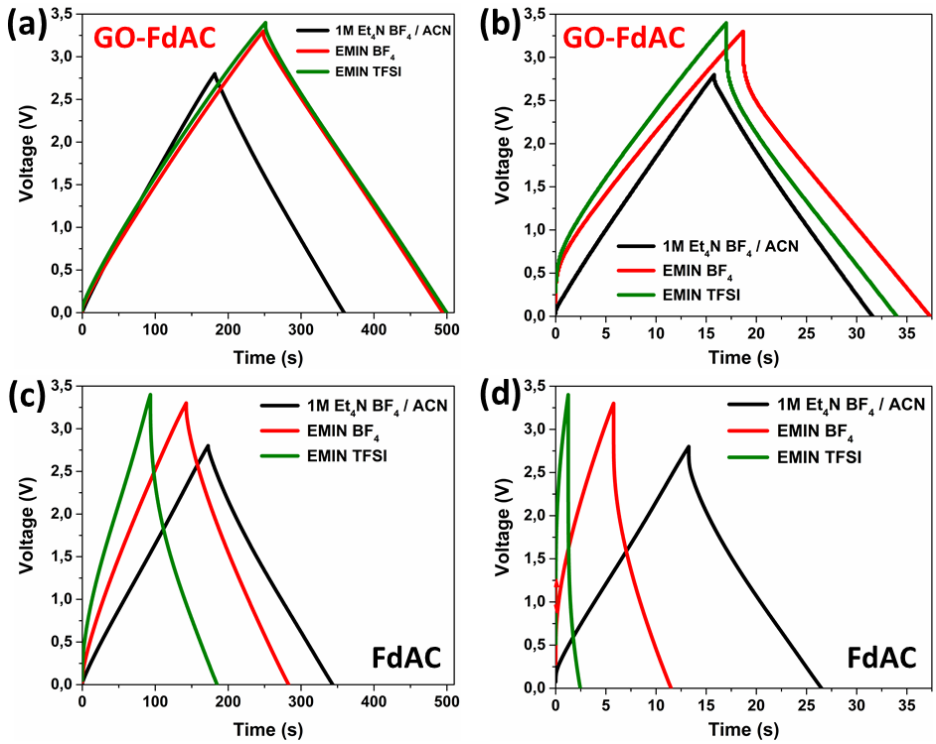


***Figure 4.6.*** *Galvanostatic charge/discharge curves at 1 A $g^{-1}$ (**a**) and 10 A $g^{-1}$ (**b**) for Go-FdAC sample in noted electrolytes; and corresponding measurements for FdAC sample (**c** and **d**).*

The specific capacitance values for the GO-FdAC sample calculated from the discharge branch of galvanostatic curves at different current rates for all the electrolytes are shown in **Figure 4.7a**. At low current densities (0.25 A $g^{-1}$), the specific capacitance in ionic liquids is larger than for the conventional organic electrolyte (160 F $g^{-1}$ vs.

132 F $g^{-1}$). However, $Et_4N$ $BF_4$ electrolyte shows better capacitance retention at high current densities than ILs. At 10 A $g^{-1}$, around 86% of the initial capacitance is retained in the organic electrolyte while 75 and 69% are retained in EMIN $BF_4$ and EMIN TFSI systems, respectively. This trend is directly related to the viscosity and ionic conductivity values, summarized in **Table 4.1**, associated to each of the electrolytes. Conventional organic electrolyte has significant lower viscosity (0.57 mPa s) and higher conductivity (63 mS $cm^{-1}$) than ILs. And in the case of imidazolium-based electrolytes with similar viscosity (35-37 mPa s), the $BF_4^-$-based salt has higher conductivity compared to the $TFSI^-$-based electrolyte (14 vs. 9 mS $cm^{-1}$ respectively), as reported elsewhere [55].

***Table 4.1.*** *Representative physicochemical properties of the electrolytes used in this study.*

| Electrolyte | Viscosity (mPa s) | Conductivity (mS $cm^{-1}$) | Cation size (nm) | Anion size (nm) | References |
|---|---|---|---|---|---|
| 1M $Et_4N$ $BF_4$ in ACN | 0.57 | 63 | 0.69 | 0.46 | [55,56] |
| EMIN $BF_4$ | 37 | 14 | 0.76 | 0.46 | [57] |
| EMIN TFSI | 35.55 | 9 | 0.76 | 0.79 | [58] |

Specific capacitance values calculated for the pristine FdAC sample (**Figure 4.7b**) follow the same electrolyte-dependent trend. However, as also observed in the CV curves, FdAC shows a low performance in IL-based electrolytes, which is especially pronounced in the case of the EMIN TFSI. At the current density of 10 A $g^{-1}$, a capacitance retention of just 34 and 10% are measured for the FdAC systems tested in EMIN $BF_4$ and EMIN TFSI electrolytes, respectively. In the case of the conventional organic electrolyte (1M $Et_4NBF_4$ in ACN) the FdAC sample also shows lower capacitance retention compared with the graphene containing sample (74 vs. 86%, respectively).

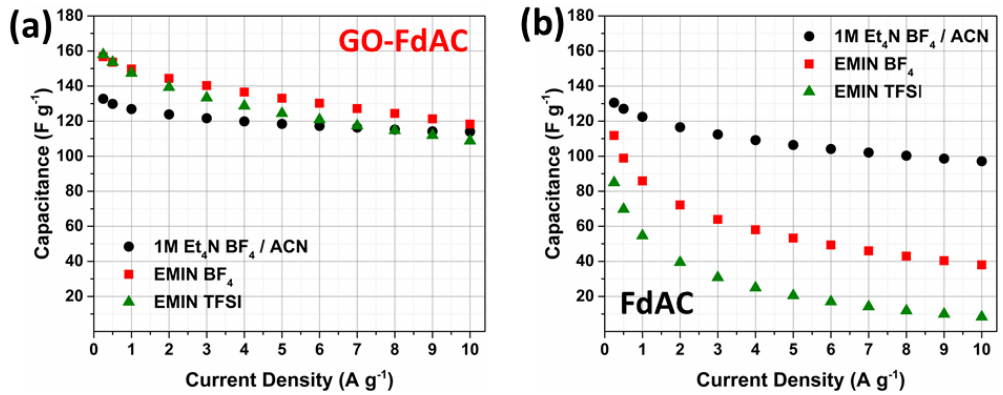


***Figure 4.7.*** *Specific capacitance values at different current densities measured for GO-FdAC (**a**) and FdAC (**b**) activated carbons in noted electrolytes.*

So, in an overall aspect, the incorporation of graphene within the carbon composite improves the electrochemical performance of the EDLC systems regardless the electrolyte used. As mentioned above, the presence of the graphene oxide sheets promotes morphological changes during carbonization, which leads to composites with slightly larger micropores that favor the fast adsorption/desorption of large electrolyte ions. Additionally, graphene sheets create a conductive network all along the different AC particles that significantly increases the electric conductivity. Electronic impedance spectroscopy studies, depicted in **Figure 4.8**, further confirm the increase of the electronic conductivity and the enhancement of the ionic diffusion for the graphene-containing carbon composite regardless the electrolyte used. The vertical line in the low-medium frequencies regime is characteristic of the capacitive behavior. The semicircle registered at high frequencies is related to the resistances of the system. The first cut with the X-axis is ascribed to the resistance of the electrolyte and the amplitude of the semicircle with the contacts and internal resistances. The $45^0$ slope region at middle frequencies (Warburg) is related to diffusion processes of the ions into the pores. In the case of the systems tested in the conventional organic electrolyte (1M $Et_4N$ $BF_4$/ACN), they show an almost ideal behavior, which is associated to its very low resistance values. When samples are tested in EMIN $BF_4$ the resistance increases in both of the samples, but it is worth mentioning that, at medium-low frequencies, GO-FdAC (**Figure 4.8a**) shows a slightly steeper slope than FdAC (**Figure 4.8b**), which indicates a better ionic diffusion into the pores due to the improved conductivity and the more appropriate textural properties developed in the

graphene containing composites. In the case of EMIN TFSI, the resistance measured is the largest one. At high frequencies both materials show a semicircle mainly related to the formation of a parasitic interphase film between the current collector and the materials. This unwanted artifact is smaller for the GO-FdAC sample. Nevertheless, at medium-low frequencies GO-FdAC shows more vertical features than FdAC pointing out the better access of $TFSI^-$ anions in the wider pores.

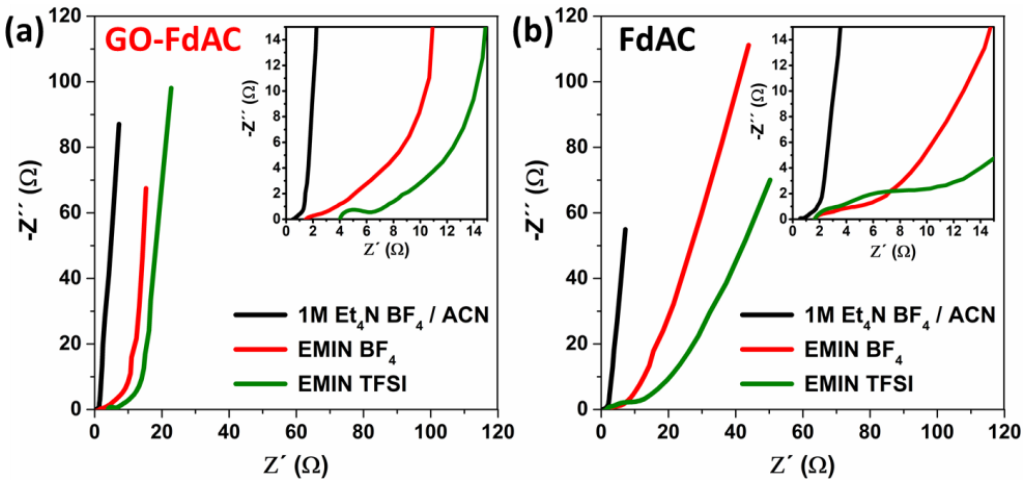


***Figure 4.8.*** *EIS measurements recorded for GO-FdAC (**a**) and FdAC (**b**) electrodes as symmetric EDLCs in the labeled electrolytes at full discharge state.*

Energy-to-power density plots for the GO-FdAC-based symmetric EDLCs are included in **Figure 4.9a**. The extension of the operating voltage range to 3.3 and 3.4 V leads to outstanding energy densities of 60 and 63 Wh $kg^{-1}$ at 206 and 212 W $kg^{-1}$ for the EMIN $BF_4$ and EMIN TFSI electrolytes, respectively. At high current densities, EMIN $BF_4$-based systems overperform the EMIN TFSI-based ones in both energy and power densities due to the better capacitance retention measured in the former electrolyte (41 vs. 37 Wh $kg^{-1}$ at 7,863 and 7,816 W $kg^{-1}$, respectively). When using the conventional organic electrolyte ($Et_4N$ $BF_4$ in ACN), the GO-FdAC sample exhibits a slightly lower energy density at low current rates, 36 Wh $kg^{-1}$ at 175 W $kg^{-1}$, due to its narrower operating voltage window (2.8 V) compared to IL-based systems. But, at high current rates conventional organic-based systems show much better capacitance retention, still delivering 25 Wh $kg^{-1}$ at 26,888 W $kg^{-1}$. In contrast, Ragone plot for graphene-free

activated carbon (FdAC sample, **Figure 4.9b**) shows significantly lower energy densities regardless the electrolyte tested. Specifically, initial energy densities of 36, 42 and 34 Wh $kg^{-1}$ are obtained for $Et_4N$ $BF_4$, EMIN $BF_4$ and EMIN TFSI electrolytes, respectively. While the conventional organic electrolyte retains 15 Wh $kg^{-1}$ at the high-power density of 25,000 W $kg^{-1}$, ionic liquids show abrupt energy density drops at high power values.

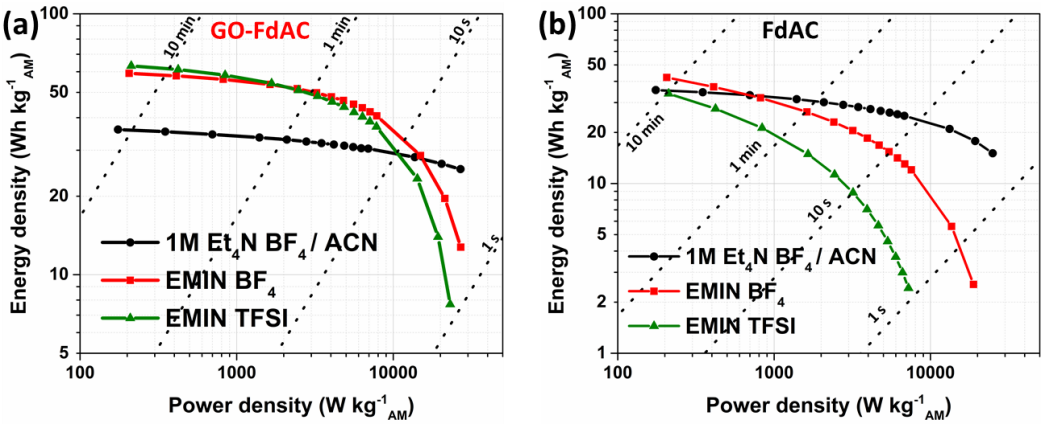


***Figure 4.9.*** *Ragone plots of GO-FdAC (**a**) and FdAC (**b**) activated carbons measured in noted electrolytes as symmetric EDLCs.*

Stability of the GO-FdAC-based EDLC systems were evaluated through repetitive galvanostatic charge/discharge measurements at 10 A $g^{-1}$ (**Figure 4.10a**). It is worth highlighting that in all the cases, graphene-containing system still provides ca. 78% of the initial capacitance after 11,000 cycles. On the other hand, FdAC sample retains only 40-50% of the initial capacitance after 11,000 cycles for $Et_4N$ $BF_4$ and EMIN $BF_4$ electrolytes (**Figure 4.10b**). Nevertheless, an unexpectedly high capacitance retention value is observed for the EMIN TFSI electrolyte. It can be related to the fact that at this current density, FdAC delivered specific capacitance is almost negligible (see last point in **Figure 4.7b** for EMIN TFSI).

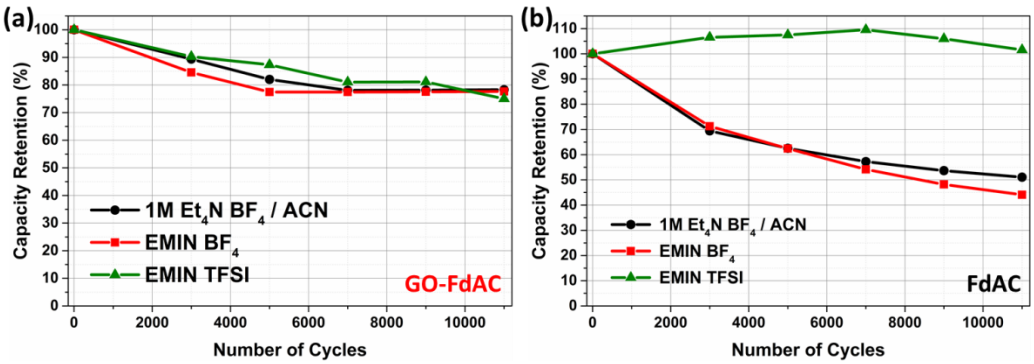


***Figure 4.10.*** *Capacitance retention evolution upon cycling at 10 A $g^{-1}$ measured in noted electrolytes for GO-FdAC (**a**) and FdAC (**b**) activated carbons.*

In **Table 4.2** some representative performance values reported for EDLC systems based on biowaste-derived ACs are summarized. It is worth mentioning, that under these circumstances, EDLC cells assembled using GO-FdAC outperform most of the values reported in literature.

***Table 4.2.*** *Summary of some relevant EDLC parameters reported in representative works using biomass-derived ACs in organic and ionic liquid electrolytes.*

| Material | Surface area ($m^2 g^{-1}$) | Electrolyte | Voltage window (V) | Capacitance ($F g^{-1}$) | Energy Density ($Wh kg^{-1}_{AM}$) | Power Density ($W kg^{-1}_{AM}$) | Cyclability (%) | Ref |
|---|---|---|---|---|---|---|---|---|
| Orange peel derived AC | 2160 | EMIN $BF_4$ | 3.0 | 140 ($0.2 A g^{-1}$) | 43 ($300 W kg^{-1}$) | 1,180 ($25 Wh kg^{-1}$) | 79% (500 cy) | [38] |
| Aloe Vera derived AC | 1890 | EMIN $BF_4$ | 3.0 | 126 ($0.1 A g^{-1}$) | 40 ($150 W kg^{-1}$) | 800 ($15 Wh kg^{-1}$) | 83% (500 cy) | [59] |
| Rice Straw derived AC | 1007 | EMIN $BF_4$ | 2.5 | 80 ($0.1 A g^{-1}$) | 17 ($126 W kg^{-1}$) | 650 ($6 Wh kg^{-1}$) | 78% (5,000 cy) | [60] |
| Cherry derived AC | 1612 | EMIN $BF_4$ | 3.6 | 173 ($1 A g^{-1}$) | 81 ($446 W kg^{-1}$) | 13,650 ($25 Wh kg^{-1}$) | 93% (6,000 cy) | [61] |
| Bamboo derived AC | 1472 | EMIN TFSI | 3.5 | 146 ($0.2 A g^{-1}$) | 59 ($166 W kg^{-1}$) | 42,000 ($43 Wh kg^{-1}$) | 95% (5,000 cy) | [62] |
| Thiourea derived AC | 2561 | EMIN TFSI | 3.0 | 41 ($1 A g^{-1}$) | 62 ($300 W kg^{-1}$) | 7,560 ($26 Wh kg^{-1}$) | 92% (5,000 cy) | [63] |
| Cellulose derived AC | 2285 | EMIN TFSI | 3.0 | 132 ($1 A g^{-1}$) | 44 ($746 W kg^{-1}$) | 20,000 ($18 Wh kg^{-1}$) | 90% (20,000 cy) | [64] |
| Paper pulp derived AC | 2980 | 1M $Et_4N$ $BF_4$ in ACN | 2.3 | 162 ($0.1 A g^{-1}$) | 30 ($57 W kg^{-1}$) | 5,450 ($20 Wh kg^{-1}$) | - | [41] |
| | | EMIN TFSI | 3.0 | 162 ($0.1 A g^{-1}$) | 51 ($371 W kg^{-1}$) | 7,000 ($31 Wh kg^{-1}$) | 91% (5,000 cy) | |
| Capsicum derived AC | 2201 | EMIN TFSI | 3.0 | 116 ($1 A g^{-1}$) | 37 ($600 W kg^{-1}$) | 3,000 ($25 Wh kg^{-1}$) | 100% (25,000 cy) | [65] |
| Firmiana derived AC | 3320 | EMIN TFSI | 3.0 | 100 ($0.5 A g^{-1}$) | 55 ($200 W kg^{-1}$) | 2,083 ($42 Wh kg^{-1}$) | 94% (10,000 cy) | [66] |
| **GO-FdAC** | **2252** | **1M $Et_4N$ $BF_4$ in ACN** | **2.8** | **127 ($1 A g^{-1}$)** | **36 ($175 W kg^{-1}$)** | **26,880 ($25 Wh kg^{-1}$)** | **78% (11,000 cy)** | **This Work** |
| | | **EMIN $BF_4$** | **3.3** | **150 ($1 A g^{-1}$)** | **60 ($206 W kg^{-1}$)** | **7,863 ($41 Wh kg^{-1}$)** | **78% (11,000 cy)** | |
| | | **EMIN TFSI** | **3.4** | **147 ($1 A g^{-1}$)** | **63 ($212 W kg^{-1}$)** | **7,816 ($37 Wh kg^{-1}$)** | **75% (11,000 cy)** | |

### 4.2.4. Three-electrode studio of GO-FdAC

To get insight on the adsorption processes of GO-FdAC-based EDLCs, three-electrode measurements were performed using a silver wire and oversized NORIT discs as reference and counter electrodes respectively. First, the electrochemical stability window of each ion was determined from the open circuit potential to its maximum voltage (**Figure 4.11a**, **b** and **c**). It can be observed that $Et_4N^+$ and $EMIN^+$ cations deliver similar stable voltage windows of ca. 2 V. On the other side, the stable voltage window is enlarged for the anions $BF_4^-$ and $TFSI^-$ when taking part of the ILs (**Figure 4.11b** and **c**), which can be the reason for the large operational voltage of both ionic liquids. Once the stable voltage window was determined, CVs were performed at several scan rates as depicted in **Figure 4.11d**, **e** and **f**. In good agreement with the CVs of symmetric EDLCs (see **Figure 4.5**), it can be observed that IL-based EDLCs shows more distorted profiles upon scan rate fastening. This can be ascribed to the lower conductivity and higher viscosity of the imidazolium-based electrolytes.

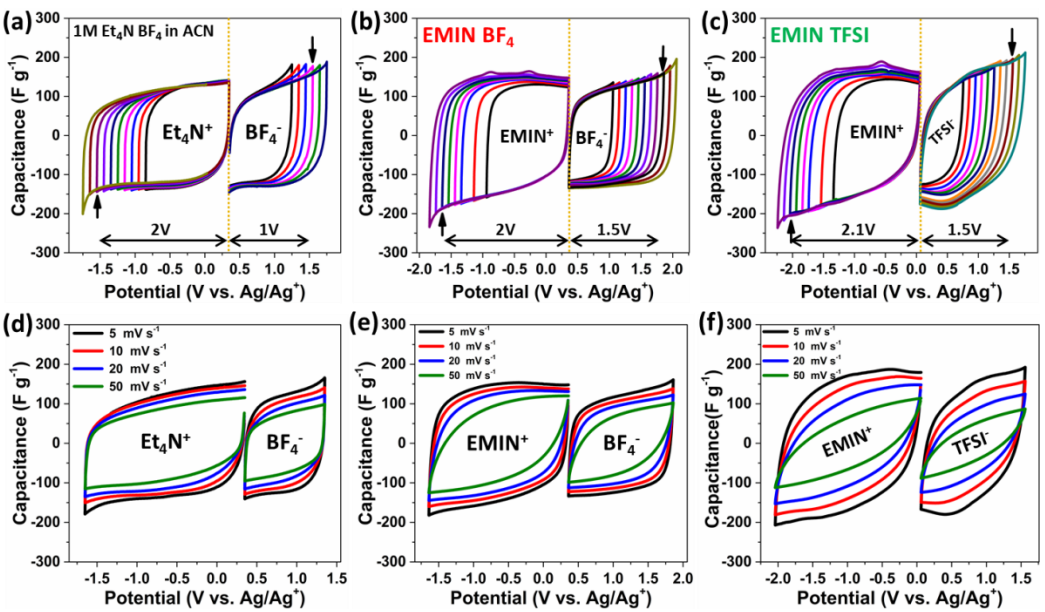


***Figure 4.11.*** *CVs measured at 5 mV $s^{-1}$ for GO-FdAC sample in a three electrode configuration in 1M $Et_4N$ $BF_4$ in ACN (**a**), EMIN $BF_4$ (**b**) and EMIN TFSI (**c**) at several voltage windows; and CVs at different scan rates for 1M $Et_4N$ $BF_4$ in ACN (**d**), EMIN $BF_4$ (**e**) and EMIN TFSI (**f**).*

Specific capacitances of GO-FdAC electrodes in the three-electrode system were calculated from the integrated area of the CV curves for each ion at different scan rates (**Figure 4.12a**, **b** and **c**). The higher specific capacitance at lower rates obtained for the ILs in symmetric cells in comparison with the conventional electrolyte (see **Figure 4.7a**) is related to the higher specific capacitance of the cation $EMIN^+$ compared with that of $Et_4N^+$ as it is evidenced by three-electrode set up (**Figure 4.12a**, **b** and **c**). Considering that the size of $Et_4N^+$ < $EMIN^+$ (**Table 4.1**) and that most of the total pore volume of GO-FdAC sample arises from pores ~0.9 nm (**Figure 4.3b**), the higher capacitance must be related to the different geometry and the better confinement in the pores of $EMIN^+$, as it has been previously reported [10,58,67,68]. From the capacitance retention values for each ion (**Figure 4.12d**, **e** and **f**), one can conclude that the conductivity of the electrolyte is the main factor limiting the performance at higher rates rather than the viscosity or even the size of the ions.

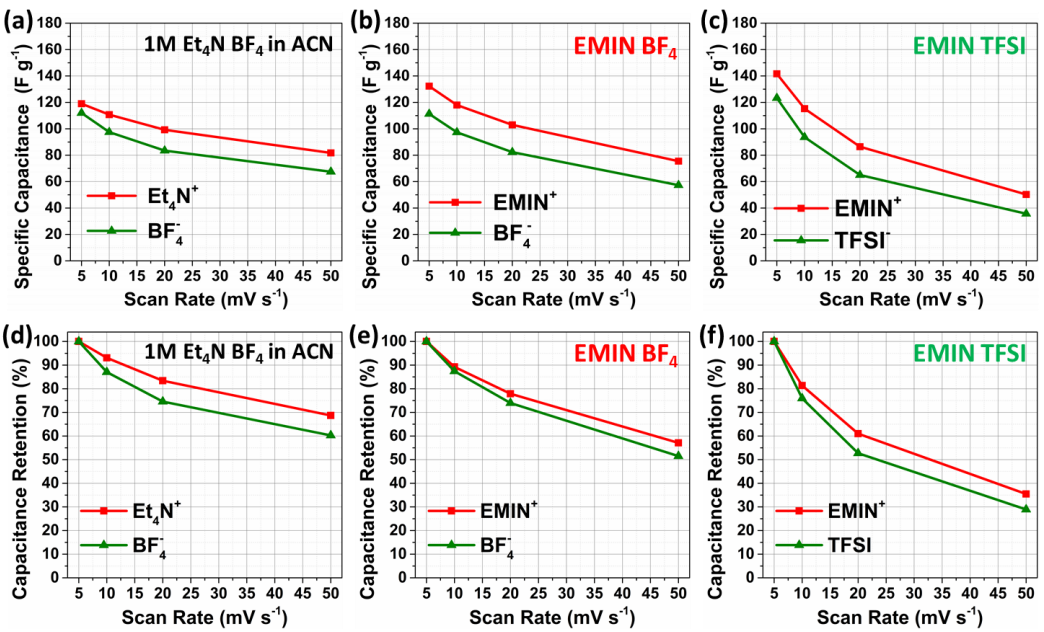


***Figure 4.12.*** *Specific capacitance evolution upon scan rate fastening for GO-FdAC sample measured in 1M $Et_4N$ $BF_4$/ACN (**a**), EMIN $BF_4$ (**b**) and EMIN TFSI (**c**) in a three electrode configuration and corresponding capacitance retention values (**d**, **e** and **f**).*

### 4.2.5. GO-FdAC measured in diluted ionic liquids

With the aim of improving the rate performance and power of GO-FdAC-based EDLCs, dilutions of 1M EMIN $BF_4$ and 1M EMIN TFSI were prepared from pure ionic liquids in ACN. As previously reported [69,70], dilution of ILs can enhance the performance of EDLCs thanks to it lowered resistance and viscosity. To support this argument, EIS spectra were measured in pure (dotted line) and diluted ionic liquids (solid line) for GO-FdAC sample in a symmetric configuration (**Figure 4.13a)**. As expected, diluted electrolytes show lower electrolyte resistance than that of pure ILs. Moreover, it is worth to remark the evolution of a $45^0$ slope region at middle frequencies for pure ILs, indicating hindered molecular diffusion in the EDL formation. GO-FdAC electrodes were galvanostatically charge/discharged at different rates in the different ILs using a symmetric configuration as represented in **Figure 4.13b**. It can be observed that GO-FdAC deliver lower initial capacitances in diluted ILs (ca. 140 F $g^{-1}$) when compared to that measured for pure ILs (ca. 160 F $g^{-1}$). As reported elsewhere [71], this phenomenon can be ascribed to the solvation of the ionic liquid molecules in ACN. Nevertheless, thanks to their higher conductivity, diluted ILs show larger specific capacitance values at faster rates (>10 A $g^{-1}$). Even 76 and 59 F $g^{-1}$ are retained at 40 A $g^{-1}$, corresponding to a 56 and 43% retention of the initial capacitance for 1M EMIN $BF_4$ and EMIN TFSI in ACN, respectively. Conversely, pure ionic liquids only retain the 32 and 26% of the initial capacitance at 40 A $g^{-1}$ for $BF_4$ and TFSI based electrolytes, respectively.

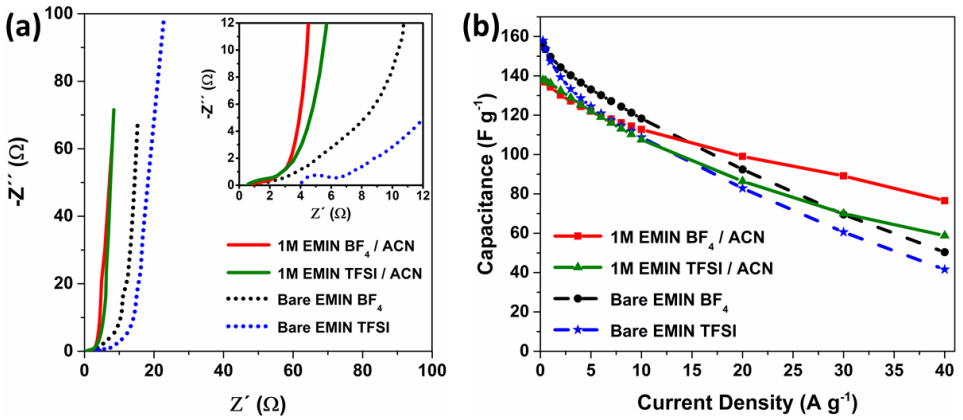


***Figure 4.13.*** *Nyquist plot (**a**) and capacitance evolution at different current densities (**b**) for GO-FdAC electrodes evaluated in bare (dotted) and diluted (solid) ionic liquids in a symmetric configuration.*

Ragone plot of GO-FdAC in diluted and pure ILs (**Figure 4.14a**) shows higher energy values for the pure ionic liquids at low power densities. However, this trend is reversed from 5 kW $kg^{-1}_{AM}$ onwards, which is in good agreement with the minor resistance and improved capacitance retention recorded for dilutions at higher rates. More in detail, EDLCs measured in diluted EMIN $BF_4$ and EMIN TFSI electrolytes deliver initial energy densities of 52 and 55 Wh $kg^{-1}$ (290 and 230 W $kg^{-1}$), respectively and high power densities of 29,200 and 30,700 W $kg^{-1}$ (23 and 19 Wh $kg^{-1}$). Unfortunately, long-term cycling stability at 10 A $g^{-1}$ (**Figure 4.14b**) reveals that while 78% of the initial capacitance is retained after 11,000 cycles for the pure EMIN $BF_4$ and EMIN TFSI only 26% and 41% is retained for their respective dilutions. This is related to the lower electrochemical stability of acetonitrile compared to that of the used ionic liquids.

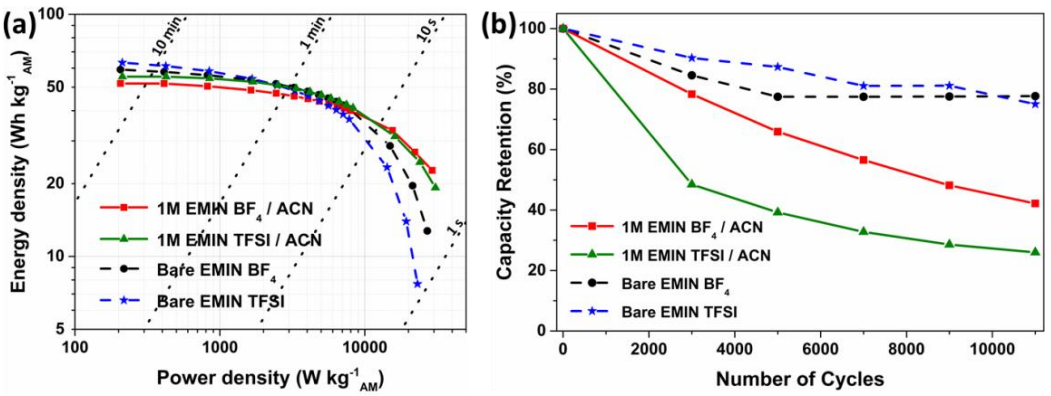


***Figure 4.14.*** *Ragone plots (**a**) and long-term stability tests at 10 A $g^{-1}$ (**b**) registered for GO-FdAC in bare (dotted) and diluted (solid) ionic liquids using a symmetric EDLC configuration.*

Therefore, performance at higher rates is improved for diluted ILs at the cost of sacrificing their capacitance retention upon cycling, disabling them for long-term applications. In order to increase the stability, a narrower voltage window would be needed. However, this would considerably affect their energy density performance. A correct balance between energy, power and cycling stability is still required in this study for the correct performance of EDLCs based on GO-FdAC and diluted ILs.

## 4.3. Summary and conclusions

The potential of this ecofriendly and easy-scalable route for the preparation of activated carbons from wasted cigarette filters to be used as electrodes for high voltage EDLCs have been demonstrated. It was found that graphene significantly improves the performance of the devices evaluated in ILs and organic electrolytes. The presence of graphene (i) increases the conductivity of the carbon composites, (ii) performs as a template, leading to flat-shaped structures that favors the ions diffusion and (iii) promotes textural modifications, extending the micropores size and thus enabling the adsorption of large-sized electrolyte ions such $EMIN^+$ or $TFSI^-$. Symmetric EDLCs assembled using this nanostructured carbon composite delivered ca. 160 F $g^{-1}$ at low current rate, and still ca. 120 F $g^{-1}$ at 10 A $g^{-1}$ when tested in ILs, leading to energy densities of ca. 63 Wh $kg^{-1}$ at 210 W $kg^{-1}$ and 40 Wh $kg^{-1}$ at 7,800 W $kg^{-1}$ in EMIN $BF_4$ and EMIN TFSI, respectively. In addition, even when operating above 3.3 V, these systems reach 11,000 charge-discharge cycles with ca. 80% retention of the initial capacitance. Besides, a comprehensive three-electrode study disclosed that the enhanced capacitance observed for these carbon composites ILs is related to the optimized textural properties, which improves the imidazolium-cation adsorption. Moreover, graphene-based electrodes were also evaluated in diluted ILs, improving the rate performance and power delivered. However, the lower electrochemical stability of the diluted ILs results in a poor capacitance retention upon cycling.

## 4.4. Bibliography

[1] S.W. Bokhari, A.H. Siddique, P.C. Sherrell, X. Yue, K.M. Karumbaiah, S. Wei, A.V. Ellis, W. Gao, Advances in graphene-based supercapacitor electrodes, Energy Rep. 6 (2020) 2768–2784. https://doi.org/10.1016/j.egyr.2020.10.001.

[2] X. Shi, S. Zheng, Z.-S. Wu, X. Bao, Recent advances of graphene-based materials for high-performance and new-concept supercapacitors, J. Energy Chem. 27 (2018) 25–42. https://doi.org/10.1016/j.jechem.2017.09.034.

[3] Q. Ke, J. Wang, Graphene-based materials for supercapacitor electrodes – A review, J. Materiomics. 2 (2016) 37–54. https://doi.org/10.1016/j.jmat.2016.01.001.

[4] Z.-S. Wu, Y. Sun, Y.-Z. Tan, S. Yang, X. Feng, K. Müllen, Three-Dimensional Graphene-Based Macro- and Mesoporous Frameworks for High-Performance Electrochemical Capacitive Energy Storage, J. Am. Chem. Soc. 134 (2012) 19532–19535. https://doi.org/10.1021/ja308676h.

[5] Y. Gao, Y. Zhang, Y. Zhang, L. Xie, X. Li, F. Su, X. Wei, Z. Xu, C. Chen, R. Cai, Three-dimensional paper-like graphene framework with highly orientated laminar structure as binder-free supercapacitor electrode, J. Energy Chem. 25 (2016) 49–54. https://doi.org/10.1016/j.jechem.2015.11.011.

[6] Y. Zhang, J.-Y. Zhu, H.-B. Ren, Y.-T. Bi, L. Zhang, Facile synthesis of nitrogen-doped graphene aerogels functionalized with chitosan for supercapacitors with excellent electrochemical performance, Chin. Chem. Lett. 28 (2017) 935–942. https://doi.org/10.1016/j.cclet.2017.01.023.

[7] Y. Xu, Z. Lin, X. Zhong, X. Huang, N.O. Weiss, Y. Huang, X. Duan, Holey graphene frameworks for highly efficient capacitive energy storage, Nat. Commun. 5 (2014) 4554. https://doi.org/10.1038/ncomms5554.

[8] Y.B. Pottathara, H.R. Tiyyagura, Z. Ahmad, K.K. Sadasivuni, Graphene Based Aerogels: Fundamentals and Applications as Supercapacitors, J. Energy Storage. 30 (2020) 101549. https://doi.org/10.1016/j.est.2020.101549.

[9] L.L. Zhang, X. Zhao, M.D. Stoller, Y. Zhu, H. Ji, S. Murali, Y. Wu, S. Perales, B. Clevenger, R.S. Ruoff, Highly Conductive and Porous Activated Reduced Graphene Oxide Films for High-Power Supercapacitors, Nano Lett. 12 (2012) 1806–1812. https://doi.org/10.1021/nl203903z.

[10] G. Moreno-Fernández, N. Boulanger, A. Nordenström, A. Iakunkov, A. Talyzin, D. Carriazo, R. Mysyk, Ball-milling-enhanced capacitive charge storage of activated graphene in aqueous, organic and ionic liquid electrolytes, Electrochimica Acta. 370 (2021) 137738. https://doi.org/10.1016/j.electacta.2021.137738.

[11] H.-X. Yang, R.-Z. Gao, H. Pu, Y. Yang, Y.-Q. Wu, W.-J. Meng, D.-L. Zhao, Hierarchical porous activated graphene nanosheets with an ultra-high potential as electrode material for symmetric supercapacitors, Microporous Mesoporous Mater. 306 (2020) 110430. https://doi.org/10.1016/j.micromeso.2020.110430.

[12] Y.H. Kim, Y.J. Choi, B.H. Park, S.B. Choi, S.-G. Kim, K.-B. Kim, Competing effects of potassium hydroxide activation of graphene on gravimetric and volumetric capacitances, J. Power Sources. 479 (2020) 229076. https://doi.org/10.1016/j.jpowsour.2020.229076.

[13] H. Zhang, D. Yang, A. Lau, T. Ma, H. Lin, B. Jia, Hybridized Graphene for Supercapacitors: Beyond the Limitation of Pure Graphene, Small. 17 (2021) 2007311. https://doi.org/10.1002/smll.202007311.

[14] W. Li, Y. Bu, H. Jin, J. Wang, W. Zhang, S. Wang, J. Wang, The Preparation of Hierarchical Flowerlike NiO/Reduced Graphene Oxide Composites for High Performance Supercapacitor Applications, Energy Fuels. 27 (2013) 6304–6310. https://doi.org/10.1021/ef401190b.

[15] S.P. Lim, N.M. Huang, H.N. Lim, Solvothermal synthesis of SnO 2 /graphene nanocomposites for supercapacitor application, Ceram. Int. 39 (2013) 6647–6655. https://doi.org/10.1016/j.ceramint.2013.01.102.

[16] M. Liu, M. Shi, W. Lu, D. Zhu, L. Li, L. Gan, Core–shell reduced graphene oxide/MnO @carbon hollow nanospheres for high performance supercapacitor electrodes, Chem. Eng. J. 313 (2017) 518–526. https://doi.org/10.1016/j.cej.2016.12.091.

[17] C. Yang, J.-L. Lan, C. Ding, F. Wang, S.H. Siyal, Y. Yu, X. Yang, Three-dimensional hierarchical ternary aerogels of ultrafine TiO2 nanoparticles@porous carbon nanofibers-reduced graphene oxide for high-performance lithium-ion capacitors, Electrochimica Acta. 296 (2019) 790–798. https://doi.org/10.1016/j.electacta.2018.10.037.

[18] X. Meng, L. Lu, C. Sun, Green Synthesis of Three-Dimensional $MnO_2$ /Graphene Hydrogel Composites as a High-Performance Electrode Material for Supercapacitors, ACS Appl. Mater. Interfaces. 10 (2018) 16474–16481. https://doi.org/10.1021/acsami.8b02354.

[19] A.K.R. Police, M. Chennaiahgari, R. Boddula, S.V.P. Vattikuti, K.K. Mandari, B. Chan, Single-step hydrothermal synthesis of wrinkled graphene wrapped TiO2 nanotubes for photocatalytic hydrogen production and supercapacitor applications, Mater. Res. Bull. 98 (2018) 314–321. https://doi.org/10.1016/j.materresbull.2017.10.034.

[20] Z. Song, W. Liu, N. Sun, W. Wei, Z. Zhang, H. Liu, G. Liu, Z. Zhao, One-step self-assembly fabrication of three-dimensional copper oxide/graphene oxide aerogel composite material for supercapacitors, Solid State Commun. 287 (2019) 27–30. https://doi.org/10.1016/j.ssc.2018.10.007.

[21] M. Yang, J.-M. Jeong, Y.S. Huh, B.G. Choi, High-performance supercapacitor based on three-dimensional MoS2/graphene aerogel composites, Compos. Sci. Technol. 121 (2015) 123–128. https://doi.org/10.1016/j.compscitech.2015.11.004.

[22] Y. Ji, Q. Wei, Y. Sun, Superior Capacitive Performance Enabled by Edge-Oriented and Interlayer-Expanded $MoS_2$ Nanosheets Anchored on Reduced Graphene Oxide Sheets, Ind. Eng. Chem. Res. 57 (2018) 4571–4576. https://doi.org/10.1021/acs.iecr.7b05342.

[23] Z. Yang, H. Zhang, B. Ma, L. Xie, Y. Chen, Z. Yuan, K. Zhang, J. Wei, Facile synthesis of reduced graphene oxide/tungsten disulfide/tungsten oxide nanohybrids for high performance supercapacitor with excellent rate capability, Appl. Surf. Sci. 463 (2019) 150–158. https://doi.org/10.1016/j.apsusc.2018.08.185.

[24] T. Zhao, W. Yang, X. Zhao, X. Peng, J. Hu, C. Tang, T. Li, Facile preparation of reduced graphene oxide/copper sulfide composite as electrode materials for supercapacitors with high energy density, Compos. Part B Eng. 150 (2018) 60–67. https://doi.org/10.1016/j.compositesb.2018.05.058.

[25] J.Ph. Mensing, A. Wisitsoraat, D. Phokharatkul, T. Lomas, A. Tuantranont, Novel surfactant-stabilized graphene-polyaniline composite nanofiber for supercapacitor applications, Compos. Part B Eng. 77 (2015) 93–99. https://doi.org/10.1016/j.compositesb.2015.03.004.

[26] X. Hong, B. Zhang, E. Murphy, J. Zou, F. Kim, Three-dimensional reduced graphene oxide/polyaniline nanocomposite film prepared by diffusion driven layer-by-layer assembly for high-performance supercapacitors, J. Power Sources. 343 (2017) 60–66. https://doi.org/10.1016/j.jpowsour.2017.01.034.

[27] S. Zhu, M. Wu, M.-H. Ge, H. Zhang, S.-K. Li, C.-H. Li, Design and construction of three-dimensional CuO/polyaniline/rGO ternary hierarchical architectures for high performance supercapacitors, J. Power Sources. 306 (2016) 593–601. https://doi.org/10.1016/j.jpowsour.2015.12.059.

[28] X. Cai, K. Sun, Y. Qiu, X. Jiao, Recent Advances in Graphene and Conductive Polymer Composites for Supercapacitor Electrodes: A Review, Crystals. 11 (2021) 947. https://doi.org/10.3390/cryst11080947.

[29] L. Xu, M. Jia, Y. Li, S. Zhang, X. Jin, Design and synthesis of graphene/activated carbon/polypyrrole flexible supercapacitor electrodes, RSC Adv. 7 (2017) 31342–31351. https://doi.org/10.1039/C7RA04566B.

[30] S.K. Tiwari, A.K. Thakur, A.D. Adhikari, Y. Zhu, N. Wang, Current Research of Graphene-Based Nanocomposites and Their Application for Supercapacitors, Nanomaterials. 10 (2020) 2046. https://doi.org/10.3390/nano10102046.

[31] N. Wang, J. Wang, J. Zhao, J. Wang, J. Pan, J. Huang, Synthesis of porous-carbon@reduced graphene oxide with superior electrochemical behaviors for lithium-sulfur batteries, J. Alloys Compd. 851 (2021) 156832. https://doi.org/10.1016/j.jallcom.2020.156832.

[32] X. He, J. Wang, G. Xu, M. Yu, M. Wu, Synthesis of microporous carbon/graphene composites for high-performance supercapacitors, Diam. Relat. Mater. 66 (2016) 119–125. https://doi.org/10.1016/j.diamond.2016.04.005.

[33] H. Xia, J. Hu, J. Li, K. Wang, Electrochemical performance of graphene-coated activated mesocarbon microbeads as a supercapacitor electrode, RSC Adv. 9 (2019) 7004–7014. https://doi.org/10.1039/C8RA09382B.

[34] Y. Li, T.-X. Shang, J.-M. Gao, X.-J. Jin, Nitrogen-doped activated carbon/graphene composites as high-performance supercapacitor electrodes, RSC Adv. 7 (2017) 19098–19105. https://doi.org/10.1039/C7RA00132K.

[35] J. Wang, Q. Li, C. Peng, N. Shu, L. Niu, Y. Zhu, To increase electrochemical performance of electrode material by attaching activated carbon particles on reduced graphene oxide sheets for supercapacitor, J. Power Sources. 450 (2020) 227611. https://doi.org/10.1016/j.jpowsour.2019.227611.

[36] Q. Zhou, J. Gao, C. Li, J. Chen, G. Shi, Composite organogels of graphene and activated carbon for electrochemical capacitors, J. Mater. Chem. A. 1 (2013) 9196. https://doi.org/10.1039/c3ta11438d.

[37] M. Sevilla, R. Mokaya, Energy storage applications of activated carbons: supercapacitors and hydrogen storage, Energy Environ. Sci. 7 (2014) 1250–1280. https://doi.org/10.1039/C3EE43525C.

[38] K. Subramani, N. Sudhan, M. Karnan, M. Sathish, Orange Peel Derived Activated Carbon for Fabrication of High-Energy and High-Rate Supercapacitors, ChemistrySelect. 2 (2017) 11384–11392. https://doi.org/10.1002/slct.201701857.
[39] J.L. Gómez-Urbano, G. Moreno-Fernández, M. Arnaiz, J. Ajuria, T. Rojo, D. Carriazo, Graphene-coffee waste derived carbon composites as electrodes for optimized lithium ion capacitors, Carbon. 162 (2020) 273–282. https://doi.org/10.1016/j.carbon.2020.02.052.
[40] T.S. Blankenship, R. Mokaya, Cigarette butt-derived carbons have ultra-high surface area and unprecedented hydrogen storage capacity, Energy Environ. Sci. 10 (2017) 2552–2562. https://doi.org/10.1039/C7EE02616A.
[41] H. Wang, Z. Li, K.T. Tak, C.M.B. Holt, X. Tan, Z. Xu, B.S. Amirkhiz, D. Harfield, A. Anyia, T. Stephenson, D. Mitlin, Supercapacitors based on carbons with tuned porosity derived from paper pulp mill sludge biowaste, Carbon. 57 (2013) 317–328. https://doi.org/10.1016/j.carbon.2013.01.079.
[42] F. Cheng, X. Yang, S. Zhang, W. Lu, Boosting the supercapacitor performances of activated carbon with carbon nanomaterials, J. Power Sources. 450 (2020) 227678. https://doi.org/10.1016/j.jpowsour.2019.227678.
[43] G. Moreno-Fernández, J.L. Gómez-Urbano, M. Enterría, T. Rojo, D. Carriazo, Flat-shaped carbon–graphene microcomposites as electrodes for high energy supercapacitors, J. Mater. Chem. A. 7 (2019) 14646–14655. https://doi.org/10.1039/C9TA03295A.
[44] G. Moreno-Fernández, M. Granados-Moreno, L. Gómez-Urbano, D. Carriazo, Phosphorus-functionalized graphene for power and cyclability improved lithium-ion capacitors, Batter. Supercaps. 4 (2021) 469–478. https://doi.org/10.1002/batt.202000247.
[45] C. Zhong, Y. Deng, W. Hu, J. Qiao, L. Zhang, J. Zhang, A review of electrolyte materials and compositions for electrochemical supercapacitors, Chem. Soc. Rev. 44 (2015) 7484–7539. https://doi.org/10.1039/C5CS00303B.
[46] S. Marinello, F. Lolli, R. Gamberini, B. Rimini, A second life for cigarette butts? A review of recycling solutions, J. Hazard. Mater. 384 (2020) 121245. https://doi.org/10.1016/j.jhazmat.2019.121245.
[47] Q. Meng, W. Chen, L. Wu, J. Lei, X. Liu, W. Zhu, T. Duan, A strategy of making waste profitable: Nitrogen doped cigarette butt derived carbon for high performance supercapacitors, Energy. 189 (2019) 116241. https://doi.org/10.1016/j.energy.2019.116241.
[48] M. Lee, G.-P. Kim, H. Don Song, S. Park, J. Yi, Preparation of energy storage material derived from a used cigarette filter for a supercapacitor electrode, Nanotechnology. 25 (2014) 345601. https://doi.org/10.1088/0957-4484/25/34/345601.
[49] Q. Xiong, Q. Bai, C. Li, D. Li, X. Miao, Y. Shen, H. Uyama, Nitrogen-doped hierarchical porous carbons from used cigarette filters for supercapacitors, J.

Taiwan Inst. Chem. Eng. 25 (2019) 315–323. https://doi.org/10.1016/j.jtice.2018.07.019.
[50] L. Li, C. Jia, X. Zhu, S. Zhang, Utilization of cigarette butt waste as functional carbon precursor for supercapacitors and adsorbents, J. Clean. Prod. 256 (2020) 120326. https://doi.org/10.1016/j.jclepro.2020.120326.
[51] Environmental protection authorities of Westhern Australia, Waste Management in Australia, 2013. https://wastemanagementausttralia.weebly.com/cigarette-butts.html (accessed September 17, 2021).
[52] C.H. Yun, Y.H. Park, C.R. Park, Effects of pre-carbonization on porosity development of activated carbons from rice straw, Carbon. 39 (2001) 559–567. https://doi.org/10.1016/S0008-6223(00)00163-9.
[53] M.S. Reza, C.S. Yun, S. Afroze, N. Radenahmad, M.S.A. Bakar, R. Saidur, J. Taweekun, A.K. Azad, Preparation of activated carbon from biomass and its' applications in water and gas purification, a review, Arab J. Basic Appl. Sci. 27 (2020) 208–238. https://doi.org/10.1080/25765299.2020.1766799.
[54] M. Thommes, K. Kaneko, A.V. Neimark, J.P. Olivier, F. Rodriguez-Reinoso, J. Rouquerol, K.S.W. Sing, Physisorption of gases, with special reference to the evaluation of surface area and pore size distribution (IUPAC Technical Report), Pure Appl. Chem. 87 (2015) 1051–1069. https://doi.org/10.1515/pac-2014-1117.
[55] J. Krummacher, C. Schütter, S. Passerini, A. Balducci, Characterization of Different Conductive Salts in ACN-Based Electrolytes for Electrochemical Double-Layer Capacitors, ChemElectroChem. 4 (2017) 353–361. https://doi.org/10.1002/celc.201600534.
[56] S. Pohlmann, R.-S. Kühnel, T.A. Centeno, A. Balducci, The Influence of Anion-Cation Combinations on the Physicochemical Properties of Advanced Electrolytes for Supercapacitors and the Capacitance of Activated Carbons, ChemElectroChem. 1 (2014) 1301–1311. https://doi.org/10.1002/celc.201402091.
[57] T. Nishida, Y. Tashiro, M. Yamamoto, Physical and electrochemical properties of 1-alkyl-3-methylimidazolium tetrafluoroborate for electrolyte, J. Fluor. Chem. 120 (2003) 135–141. https://doi.org/10.1016/S0022-1139(02)00322-6.
[58] R. Singh, N.N. Rajput, X. He, J. Monk, F.R. Hung, Molecular dynamics simulations of the ionic liquid [EMIM+][TFMSI−] confined inside rutile (110) slit nanopores, Phys. Chem. Chem. Phys. 15 (2013) 16090. https://doi.org/10.1039/c3cp51266e.
[59] M. Karnan, K. Subramani, N. Sudhan, N. Ilayaraja, M. Sathish, *Aloe vera* Derived Activated High-Surface-Area Carbon for Flexible and High-Energy Supercapacitors, ACS Appl. Mater. Interfaces. 8 (2016) 35191–35202. https://doi.org/10.1021/acsami.6b10704.
[60] N. Sudhan, K. Subramani, M. Karnan, N. Ilayaraja, M. Sathish, Biomass-Derived Activated Porous Carbon from Rice Straw for a High-Energy Symmetric Supercapacitor in Aqueous and Non-aqueous Electrolytes, Energy Fuels. 31 (2017) 977–985. https://doi.org/10.1021/acs.energyfuels.6b01829.

[61] D. Yu, C. Chen, G. Zhao, L. Sun, B. Du, H. Zhang, Z. Li, Y. Sun, F. Besenbacher, M. Yu, Biowaste-Derived Hierarchical Porous Carbon Nanosheets for Ultrahigh Power Density Supercapacitors, ChemSusChem. 11 (2018) 1678–1685. https://doi.org/10.1002/cssc.201800202.

[62] W. Tian, Q. Gao, Y. Tan, K. Yang, L. Zhu, C. Yang, H. Zhang, Bio-inspired beehive-like hierarchical nanoporous carbon derived from bamboo-based industrial by-product as a high performance supercapacitor electrode material, J. Mater. Chem. A. 3 (2015) 5656–5664. https://doi.org/10.1039/C4TA06620K.

[63] L. Ji, B. Wang, Y. Yu, N. Wang, J. Zhao, N, S co-doped biomass derived carbon with sheet-like microstructures for supercapacitors, Electrochimica Acta. 331 (2020) 135348. https://doi.org/10.1016/j.electacta.2019.135348.

[64] Y. Cui, H. Wang, N. Mao, W. Yu, J. Shi, M. Huang, W. Liu, S. Chen, X. Wang, Tuning the morphology and structure of nanocarbons with activating agents for ultrafast ionic liquid-based supercapacitors, J. Power Sources. 361 (2017) 182–194. https://doi.org/10.1016/j.jpowsour.2017.06.087.

[65] D. Momodu, N.F. Sylla, M. Bridget, A. Bello, T. Masikhwa, S. Lindberg, A. Matic, N. Manyala, Stable ionic-liquid-based symmetric supercapacitors from Capsicum seed-porous carbons, J. Electroanal. Chem. 838 (2019) 119–128. https://doi.org/10.1016/j.jelechem.2019.02.045.

[66] J. Fang, D. Guo, C. Kang, S. Wan, L. Fu, Q. Liu, N, O-enriched hierarchical porous graphite carbon flake for high performance supercapacitors, J. Electroanal. Chem. 851 (2019) 113467. https://doi.org/10.1016/j.jelechem.2019.113467.

[67] C. Merlet, C. Péan, B. Rotenberg, P.A. Madden, B. Daffos, P.-L. Taberna, P. Simon, M. Salanne, Highly confined ions store charge more efficiently in supercapacitors, Nat. Commun. 4 (2013) 2701. https://doi.org/10.1038/ncomms3701.

[68] A. Elbourne, S. McDonald, K. Voïchovsky, F. Endres, G.G. Warr, R. Atkin, Nanostructure of the Ionic Liquid–Graphite Stern Layer, ACS Nano. 9 (2015) 7608–7620. https://doi.org/10.1021/acsnano.5b02921.

[69] J. Guo, M. Ye, K. Zhao, J. Cui, B. Yang, J. Meng, X. Yan, High voltage supercapacitor based on nonflammable high-concentration-ionic liquid electrolyte, Colloids Surf. Physicochem. Eng. Asp. 598 (2020) 124858. https://doi.org/10.1016/j.colsurfa.2020.124858.

[70] V.V. Chaban, I.V. Voroshylova, O.N. Kalugin, O.V. Prezhdo, Acetonitrile Boosts Conductivity of Imidazolium Ionic Liquids, J. Phys. Chem. B. 116 (2012) 7719–7727. https://doi.org/10.1021/jp3034825.

[71] E. Zhang, N. Fulik, S. Paasch, L. Borchardt, S. Kaskel, E. Brunner, Ionic liquid - Electrode materials interactions studied by NMR spectroscopy, cyclic voltammetry, and impedance spectroscopy, Energy Storage Mater. 19 (2019) 432–438. https://doi.org/10.1016/j.ensm.2019.03.015.

# Chapter V. Lithium-ion Capacitors



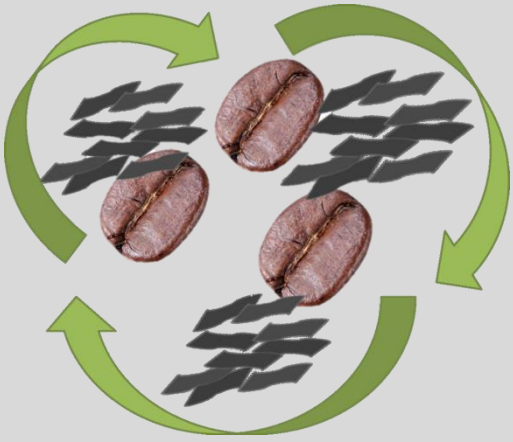

## 5.1. State-of-the-art of graphene-based Lithium-ion Capacitors

Lithium-ion capacitors are promising energy storage devices that can fill the gap between batteries and supercapacitors. However, a thorough search for safe, cheap and efficient electrode materials is still needed to overcome the imbalance electrode kinetics between the battery-type and the capacitive-type electrode. On this regard, the rational design of graphene-based electrodes has been appointed as a promising solution strategy [1,2]. Graphene can be considered an ideal capacitive-type electrode material thanks to its outstanding theoretical capacitance of 550 F $g^{-1}$. However, graphene sheets tend to suffer from restacking and aggregation, leading to a drastic reduction of its theoretical SSA. As result, graphene-based materials explored as positive electrodes of a LIC [3–10] deliver insufficient specific capacitances, limiting the energy density of the LIC. On the other hand, graphene has spurred much interest as battery-type electrode for LICs owing to its high aspect ratio, outstanding electric conductivity and low resistance to $Li^+$ diffusion [11–14]. Moreover, graphene can act as robust 2D substrates for the anisotropic growth of various battery-type compounds as electrode materials, buffering their volume changes and promoting a fast charge transfer process [15–33]. Although outstanding energy densities are achieved at low rates for graphene-based battery-type electrodes, the sluggish kinetics result in limited power output and shortened cycle life of the LICs. Among the different hybrid configurations, graphene-based dual-carbon LICs show a longer cycle life and improved power performance [34–38]. Additionally, the fabrication of carbon-graphene-composites and its integration in dual-carbon LICs has demonstrated to be a versatile and efficient approach [39–43]. On one hand, carbonaceous materials can be easily adapted to the charge storage mechanism of each electrode, matching electrodes kinetics in the LIC. On the other hand, graphene-based materials can not only serve as a conductive matrix but also tailor the morphological and textural properties of the composites. Thus, development of advanced carbon-graphene composites from safe and environmentally friendly sources can be considered a promising strategy to solve the aforementioned challenges of LICs.

## 5.2. Graphene-coffee waste derived HC as the negative electrode

This section is devoted to the preparation of graphene-coffee waste derived hard carbons and its electrochemical evaluation for its further utilization as negative

electrodes in a LIC. As already mentioned, the power performance of LICs is limited by the battery-type electrode since it involves lithium insertion/extraction mechanism which leads to a much stronger decay of capacity at high current densities compared to the capacitive electrode. Thus, in order to enhance the performance at high current densities without compromising lifetime, it is of paramount importance to find the most appropriate balance between morphology, particle size and surface area of carbons. In this section parameters such as (i) the presence of graphene, (ii) reduction of the carbon particle size and (iii) amount of active mass loading in the electrodes are carefully evaluated to improve the power performance of the battery-type electrodes.

### 5.2.1. Material and electrode preparation of the HC

In a first step, coffee waste was collected from used capsules of a well-known coffee company. Then, 2.5 g of exhausted coffee waste and 40 mL (2 mg $mL^{-1}$) of commercially available GO suspension (Graphenea) were mixed and vigorously stirred overnight. GO/Coffee waste dry precursor was obtained after freeze/freeze-drying the suspension. Graphene containing hard carbon composites were obtained by heating the powdered GO/coffee waste mixture at 950 °C for 1 h under dynamic Ar atmosphere. The sample hereafter denoted as GOCAF was obtained after ball milling (Planetary mill PULVERISETTE 5) at 250 rpm using a ball:carbon mass ratio of 1:30. Milling process (30 minutes) was repeated six times with a resting time of 5 minutes between each repetition (**Scheme 5.1**). For sake of comparison an additional sample without GO, denoted as CAF, was also prepared.

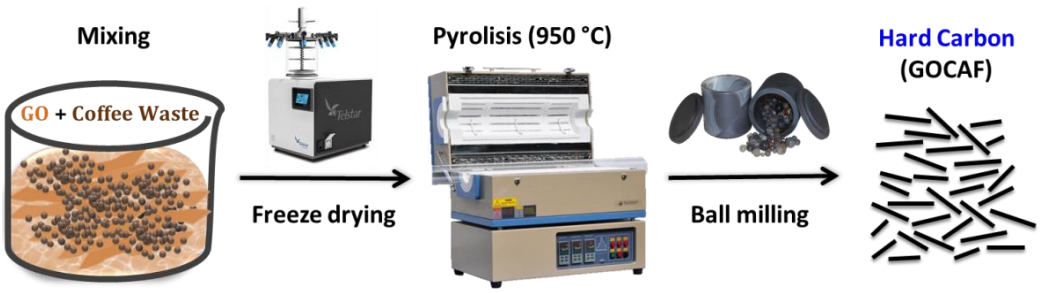


***Scheme 5.1.*** *Schematic representation of the preparation method followed for the synthesis of GOCAF.*

In order to prepare laminates for further electrochemical characterization, HCs were mixed with carbon black and PVDF in NMP using a mass ratio of 90:5:5. These slurries were then deposited onto a cupper aluminum foil using the doctor blade technique and dried at 120 °C under vacuum overnight. Electrode discs of 11 mm in diameter were cut and further dried prior to cell assembly. Two electrode type Swagelok cells were assembled in an argon-filled glovebox using lithium discs as counter and reference electrode. The electrolyte used was a 1 M solution of lithium hexafluorophosphate ($LiPF_6$), in a 1:1 (v/v) mixture of ethylene carbonate (EC) and dimethyl carbonate (DMC).

### 5.2.2. Morphological and physicochemical characterization of the HCs

SEM images registered for the coffee waste derived carbon just after its pyrolysis (**Figure 5.1a**) reveals that the materials are formed by particles of about ca. 200 µm in size, which contains macropores in a honeycomb structure. The addition of GO (**Figure 5.1b**) does not significantly modify neither the structure nor the particle size of the samples as can be observed from the SEM images. Despite its low content (6 ± 1 wt.%), reduced graphene oxide sheets, product of the thermal reduction of graphene oxide, fully cover the surface of the carbon particles in a homogeneous way, creating a conductive network along the whole sample. Controlled ball milling treatment of both samples produces a significant decrease in the particle size to 2 - 5 µm as can be observed in **Figure 5.1c** and **d**.

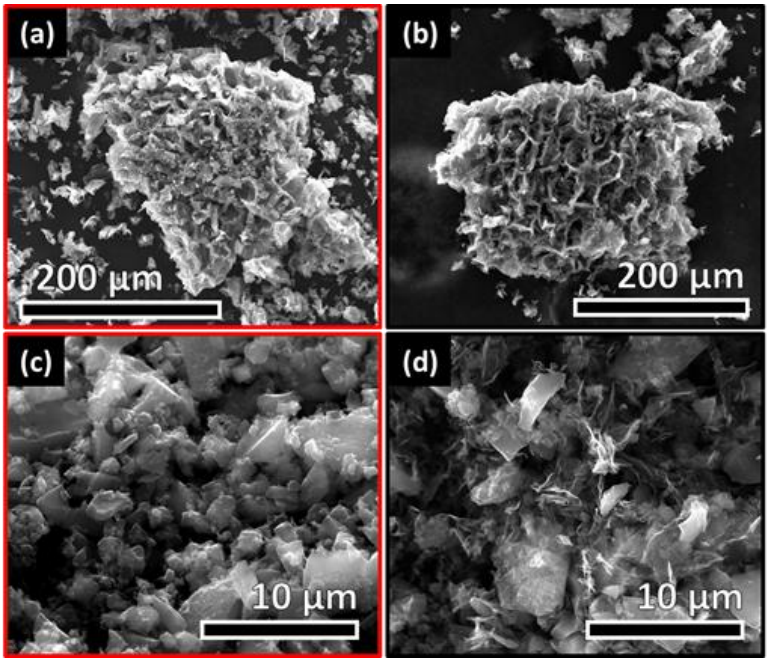


***Figure 5.1.*** *SEM images of CAF (**a**) and GOCAF (**b**) before and after (**c** and **d**) the ball milling process.*

TEM images registered for CAF (**Figure 5.2a**) and GOCAF (**Figure 5.2b**) samples furtherly show the presence of irregular-shaped hard carbon particles in both of the materials, which in the case of the GOCAF sample are embedded within the graphene sheets.

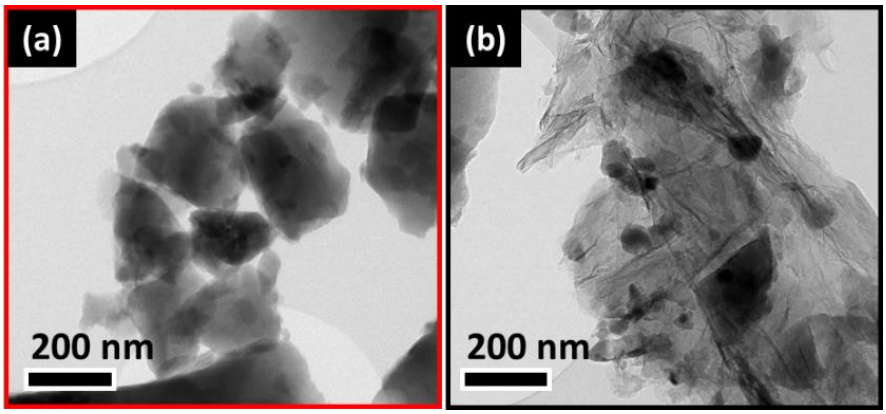


***Figure 5.2.*** *TEM images of CAF (**a**) and GOCAF (**b**).*

The XRD patterns measured for CAF and GOCAF are shown in **Figure 5.3a**. Both of them show two broad peaks assigned to the (002) and (100) diffraction planes of graphite, which in good agreement with reported literature [44], confirm the amorphous/disordered structure of the carbons. Raman spectra registered for the HCs are shown in **Figure 5.3b**. Both of them show two broad peaks at ca. 1,351 and 1,599 $cm^{-1}$, assigned to the G and D bands of carbons. From the ratio between peak integrated areas ($A_D/A_G$) values of 1.65 and 1.78 are calculated for GOCAF and CAF, respectively, indicating a lower concentration of defect and larger degree of graphitization in the graphene containing sample [45]. Textural properties were investigated through gas adsorption. Nitrogen adsorption/desorption isotherms registered for both samples are included in **Figure 5.3c**. Both of them show a similar adsorption profile ascribed to type-III isotherms, according to the IUPAC classification [46], that corresponds to the adsorption in macroporous or non-porous materials. It is worth noticing that, despite the low amount of graphene within the sample, SSA is increased from 12 to 51 $m^2 g^{-1}$ with the incorporation of graphene.

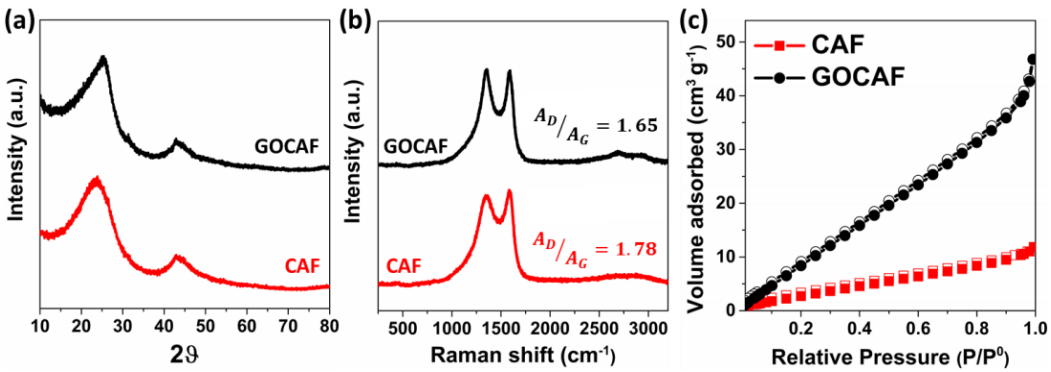


***Figure 5.3.*** *XRD (**a**), Raman (**b**) and Nitrogen adsorption-desorption isotherms (**c**) registered for labelled graphene-coffee waste HCs.*

### 5.2.3. Electrochemical characterization of the HC

HCs were submitted to a preliminary electrochemical evaluation in order to assess their performance as battery-type electrodes. For this purpose, HCs were assembled as working electrodes in a two electrode configuration against metallic lithium. Cells were galvanostatically cycled between 0.002 and 2 V to simulate their potential swing

as negative electrodes in the LIC. CAF and GOCAF samples were cycled at different C-rates (1C: 372 mA $g^{-1}$ referring to the theoretical specific capacity of graphite) to assess the impact of graphene in the composite (**Figure 5.4**). It is clearly observed that the incorporation of graphene into the carbon composite produces a significant increase on the specific capacity in the whole range of current densities investigated. Moreover, the presence of graphene does not have a negative impact over coulombic efficiency evolution.

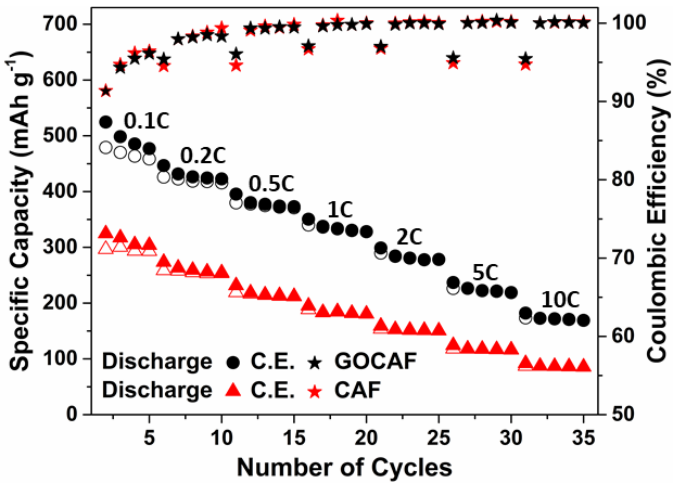


***Figure 5.4.*** *Scan rate comparing electrochemical performance of CAF and GOCAF.*

Galvanostatic charge/discharge curves registered for CAF and GOCAF samples are depicted in **Figure 5.5**. Both of them show sloping profiles without plateaus that are characteristic of $Li^+$ insertion in non-graphitic carbons, as reported elsewhere [47]. It is worth highlighting that the capacity measured when charging process is stopped at 0.2 V *vs.* $Li/Li^+$ almost reaches the 70% of the full capacity, particularly when current densities over 1C are applied. More in detail, GOCAF sample (**Figure 5.5a**) shows outstanding gravimetric discharge capacity values of 398, 356, 305 and 195 mAh $g^{-1}$ at current rates of 0.5C, 1C, 2C and 10C, respectively. At these current densities CAF sample (**Figure 5.5b**) delivered considerably lower specific capacity values (231, 195, 159 and 92 mAh $g^{-1}$). The significant improvement measured in the graphene containing sample, whatever the current rate applied is, could be ascribed to a

synergistic effect between rGO and the coffee waste derived carbon particles that enables fast insertion/extraction of lithium ions within the carbonaceous structure while graphene sheets creates a 3D conductive network that interconnects the whole sample enhancing its electronic conductivity.

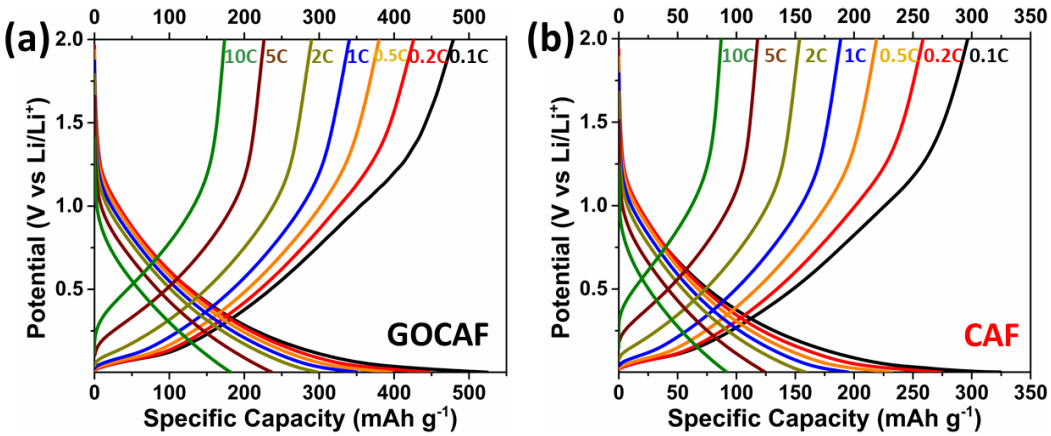


***Figure 5.5.*** *Galvanostatic charge/discharge curves at different rates for GOCAF (**a**) and CAF (**b**).*

The electrochemical impedance spectroscopy measured in the fully discharged state (2 V) was performed in a three-electrode configuration cell to monitor electrode resistance (**Figure 5.6**) for the HC-based materials. The characteristic resistances for the different electrochemical processes were calculated according to the equivalent circuit shown in **Figure 5.6** inset. EIS spectra of both materials after 5 activation cycles at 0.1C, show a semicircle at high frequency and a linear region at the low frequency range. A clear reduction in the size of the high frequency semicircle is observed for the graphene containing sample. This could be ascribed to the as-mentioned conductive network created by the incorporation of rGO which allows a faster and unimpeded charge transfer in the sample.

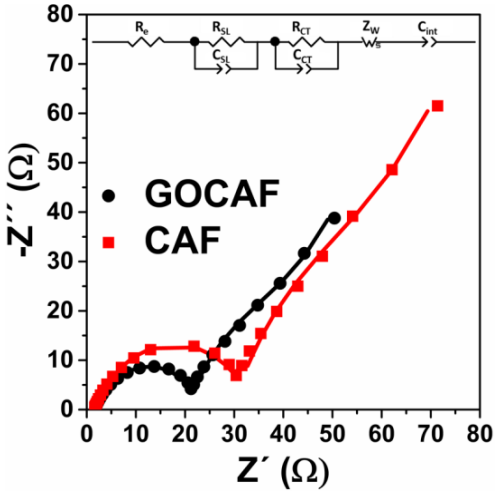


***Figure 5.6.*** *EIS spectra of labelled HCs fitted with the equivalent circuit shown inset.*

Specifically, as can be observed from (**Table 5.1**) resistance of the electrochemical processes ($R_{CT}$ values) are clearly reduced when graphene is incorporated in the sample.

***Table 5.1.*** *Resistance values goodness of the fitting calculated from fitted EIS spectra of HCs.*

| | $R_e$ (Ω) | $R_{SL}$ (Ω) | $R_{CT}$ (Ω) | $Chi^2$ |
|---|---|---|---|---|
| **CAF** | 1.3 | 26.3 | 29.1 | 5.49E-4 |
| **GOCAF** | 1.3 | 17.7 | 19.5 | 5.39E-4 |

Besides the role of incorporating graphene in the sample, some other parameters such as active mass in the electrodes and particle size where evaluated for a proper optimization of the negative electrode of the LIC. As it is generally known [48–50], the active mass loading of the electrodes plays a critical role in the electrochemical performance of the cell, and this is especially relevant at high current rates. Within this context, the performance of GOCAF was evaluated at several C-rates using different mass loadings as represented in **Figure 5.7a**. The impact of that mass loading on GOCAF sample over its electrochemical properties was studied in the mass range between 1 and 3 mg (0.9 and 2.8 mg $cm^{-2}$). As expected, the largest capacity values are obtained for the lowest mass loading whatever the C-rate applied. The specific

capacity decreases progressively as the active mass increases from 1.0 to 2.2 mg and no significant differences are observed when moving from 2.2 to 3.0 mg. This behavior could be related to the progressive increase of the electrode resistance as the electrode is thickened, and to the negligible contribution of the external particles in the capacity output.

Carbon particle size is also a critical parameter for Li-insertion anodes. On one hand, very large carbon particles can hinder $Li^+$ kinetics resulting in lower capacity values, especially at high current densities, while on the other hand, a very small particle size can result in extremely low coulombic efficiencies during the first cycle and consequently, a huge irreversible loss of active material which could be detrimental for practical applications [51]. In order to evaluate the influence of carbon particle size over electrochemical performance, graphene containing samples before (GOCAFnoBM) and after (GOCAF) the ball milling process were galvanostatically cycled at different C-rates (**Figure 5.7b**). As expected, the reduction on the carbon particle size produce a considerably increase on the specific capacity in the whole range of current densities studied.

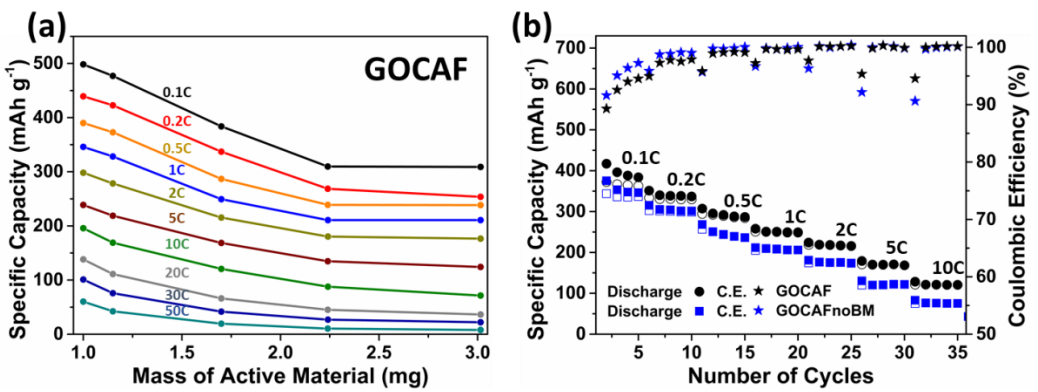


***Figure 5.7.*** *Influence of active mass over specific capacity at different current densities for GOCAF sample (**a**) and specific capacity evolution of GOCAF and GOCAFnoBM at different current densities (**b**).*

HCs capacity variations at several C-rates due to the different optimization methods followed in this section are illustrated in **Figure 5.8**. Firstly, from **Figure 5.8a** it can be appreciated that the incorporation of graphene results in an outstanding capacity improvement in the whole range of current densities. Even a 40% capacity improvement is achieved at low current densities (0.1C). Also it is worth noting that the positive impact of graphene incorporation is more pronounced at higher rates, reaching a capacity improvement of the 64% at 50C. Secondly, regarding the influence of electrodes mass loadings (**Figure 5.8b)**, the capacity loss when increasing the active mass from 1 to 3 mg is more prominent at high current rates, rising from 40% at 0.1C to 90% at 50C. Thirdly, as can be appreciated from **Figure 5.8c**, reduction of the particle size has also a beneficial influence over capacity in the whole range of scanned rates. It should be also noted that this improvement is even more prominent at high current rates. Specifically, while only a 10% capacity improvement is obtained at 0.1C, when increasing current density to 50C, capacity improvement related with the reduction of particle size increases to 50%.

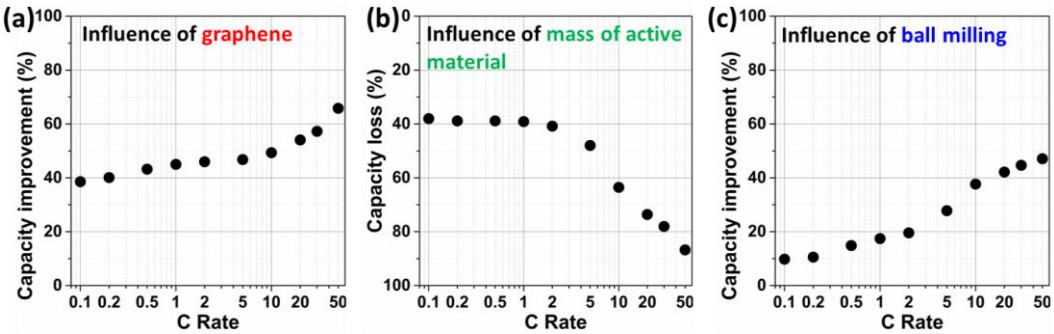


***Figure 5.8.****Percentual capacity variations due to the incorporation of graphene (**a**), increasing the mass loading from 1 mg to 3 mg (**b**) and reducing the carbon particle size by ball milling (**c**) of the HCs.*

It is also worth noting that the incorporation of graphene does not strongly impact on the first cycle coulombic efficiency (**Figure 5.9a**), and values of 50 and 52% are obtained for the GOCAF and CAF samples, respectively. This could be ascribed to the low content of rGO in this sample (6 ± 1 wt.%) which it is proved to be enough to increase the capacity and boost the rate capability compared to the CAF sample, but does not significantly increase the irreversible decomposition of the electrolyte and

the solid electrolyte interphase formation on the surface of the particles. Likewise, capacity improvement due to ball milling process does not have a detrimental effect over first cycle C. E., since as can be observed from **Figure 5.9c** and **Figure 5.9a**, values of C.E. in the first cycle for both samples (GOCAFnoBM and GOCAF respectively) are pretty similar. This could be ascribed to the optimized reduction of the particle size by the controlled ball milling process. This tailored particle size lead to an increase in the capacity compared with GOCAFnoBM sample, but does not result in excessive appearance of irreversible reactions due to the SEI formation.

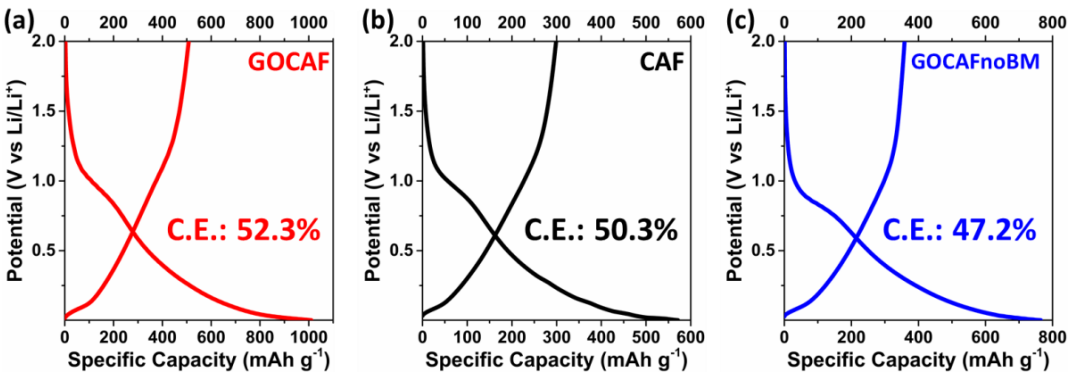


***Figure 5.9.*** *First cycle charge and discharge curves for GOCAF (**a**), CAF (**b**) and GOCAFnoBM (**c**).*

Some representative capacity values reported for different carbons obtained from the pyrolysis of biowastes when tested as anodes for LIBs are summarized in **Table 5.2**. It is worth highlighting that the specific capacity delivered by GOCAF is among the highest reported values in literature for biomass derived carbons. This can be majorly ascribed to the presence of graphene, since the HC prepared in the absence of graphene (CAF) does not stand out over the state-of-the-art.

***Table 5.2.*** *Electrochemical performance of some representative biomass waste derived carbons as negative electrodes for Li-ion energy storage systems.*

| Active material | Electrolyte | Current Density (mA $g^{-1}$) | Specific Capacity (mAh $g^{-1}$) | Reference |
|---|---|---|---|---|
| Coffee waste derived carbon | $LiPF_6$ in EC:DEC | 100 | 360 | [52] |
| Olive pits derived carbon | $LiPF_6$ in EC:DMC | 186 (0.5C) | 230 | [53] |
| Wheat straw derived carbon | $LiPF_6$ in EC:DMC | 186 (0.5C) | 250 | [54] |
| Green tea derived carbon | $LiPF_6$ in EC:DMC | 200 | 352 | [55] |
| Loofah derived carbon | $LiPF_6$ in EC:DMC | 200 | 346 | [56] |
| **rGO-Coffee waste derived carbon (GOCAF)** | **$LiPF_6$ in EC:DMC** | **186 (0.5C)** | **398** | **This work** |
| **Coffee waste derived carbon (CAF)** | **$LiPF_6$ in EC:DMC** | **186 (0.5C)** | **225** | **This work** |

## 5.3. Graphene-coffee waste derived AC as the positive electrode

Last section focused on the optimization of the battery-type electrodes to enhance the power performance of the LICs. In the same way, the positive electrode must be taking into consideration since its capacitive reactions can restrict the energy performance of the LICs. Thus, this section is devoted to the preparation of graphene-coffee waste derived activated carbons and its electrochemical evaluation for its further utilization as positive electrodes in a LIC. For this purpose, both chemistry and texture of the materials need to be optimized. Specially, textural properties should be carefully considered, since the electrochemical adsorption/desorption of charge is directly related to the available specific surface area of the electrode. For this purpose, activated carbons are prepared using GO-coffee waste as precursor and KOH as activating agent. The influence of the C:KOH activation ratio over textural properties of the ACs and its further impact over electrochemical performance are carefully evaluated to improve the energy output of the capacitive-type electrodes.

### 5.3.1. Material and electrode preparation of the AC

GO/coffee waste mixture was pre-carbonized at 400 °C in a furnace for 3 h under dynamic Ar atmosphere. Then carbon was grounded together with KOH in a mortar using two different C:KOH mass ratios: 1:4 (AC4) and 1:6 (AC6) and furtherly heated at 800 °C for 1 h under Ar atmosphere. The resulting materials were washed one time using a diluted solution of HCl and then several times with hot deionized water. Dry powder was obtained after freeze and freeze-drying the material (see **Scheme 5.2**).

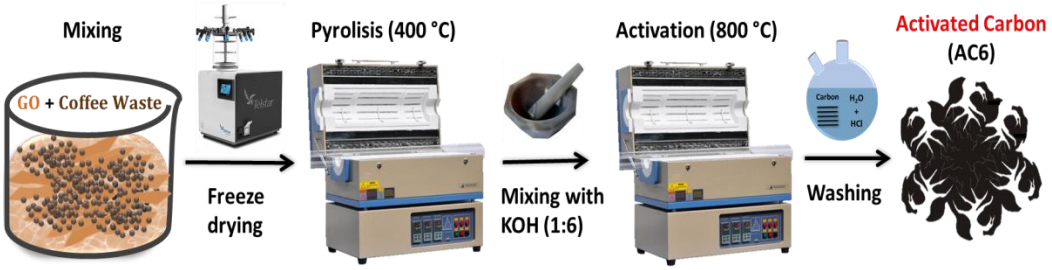


***Scheme 5.2.*** *Schematic representation of the preparation method followed for the synthesis of GOCAF.*

AC electrodes were prepared using the same method as for HC but in this case aluminum was used instead of cupper as current collector. Three electrode-type Swagelok cells were assembled in an argon-filled glovebox using a lithium disc as reference and an oversized NORIT disc as counter electrode. Three electrode cells were evaluated in the potential range of 1.5 to 4.2 V. AC-based electrodes were also tested as symmetric EDLC devices using two electrode-type Swagelok cells with AC-electrodes as working and counter electrodes. EDLCs were evaluated in the voltage range of 0 to 2.7 V. The electrolyte used was a 1 M solution of $LiPF_6$ in a 1:1 (v/v) mixture of EC and DMC.

### 5.3.2. Morphological and physicochemical characterization of the ACs

SEM images of graphene-coffee waste powdered precursor carbonized at 400 °C and derived activated carbons prepared using a C:KOH ratio of 4 (AC4) and 6 (AC6) are shown in **Figure 5.10**. All the samples show carbon particles of approximately 10 µm in size that appears homogeneously coated with rGO sheets. From these images no

significant microscopic differences are observed between the non-activated (**Figure 5.10a**) and activated samples (**Figure 5.10b** and **Figure 5.10c**). Likewise, similar morphology is observed for the ACs regardless the activation ratio.

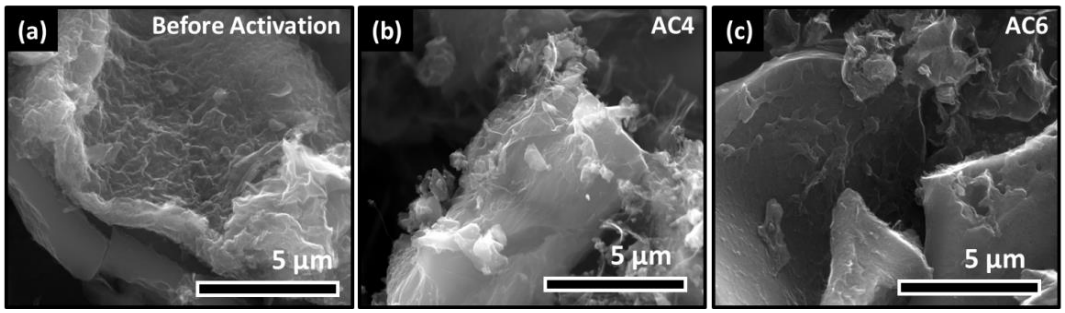


***Figure 5.10.*** *SEM images of GO/Coffee waste precursor precarbonized at 400°C (**a**) and activated carbons prepared using a C:KOH ratio of 1:4 (**b**) and 1:6 (**c**).*

Textural properties of AC4 and AC6 were investigated by nitrogen adsorption/desorption at -196 °C (**Figure 5.11a**). According to IUPAC classification [46], isotherm registered on the AC4 sample can be indexed into type-I, which corresponds to microporous carbons, while AC6 exhibits a profile in between type-I and II, characteristic of samples containing a combination of both micropores and mesopores. BET specific surface area values calculated for AC4 and AC6 are 1,650 and 2,350 $m^2$ $g^{-1}$, respectively, pointing out the significant surface increase on the AC6 sample as consequence of its larger activating agent ratio. PSD calculated from the isotherms of these two ACs are reported in **Figure 5.11b**. This plot clearly shows that increasing the amount of KOH up to 6 produces an enlargement of the pore size as consequence of the collapse of contiguous small micropores giving rise to pores ranging from 1 to 2 nm.

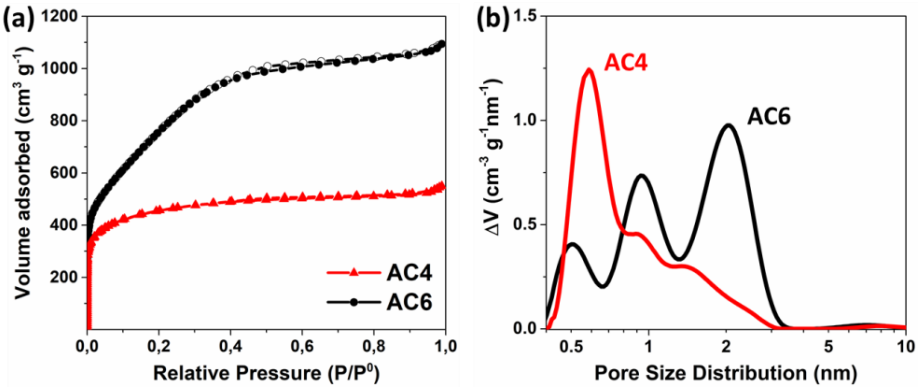


***Figure 5.11.*** *Nitrogen adsorption/desorption isotherms (**a**) and corresponding pore size distributions (**b**) for graphene-coffee waste ACs.*

### 5.3.3. Electrochemical characterization of the AC

The electrochemical performance of ACs was firstly investigated *vs.* Li/Li$^+$ in a three-electrode cell using $LiPF_6$ in EC:DMC as electrolyte and an oversized electrode made from Norit (Kuraray) carbon as counter. Electrochemical cells were evaluated in the potential range of 1.5 - 4.2 V to emulate the operation conditions of the ACs in the lithium-ion capacitor. CVs registered for AC4 (**Figure 5.12a**) and AC6 (**Figure 5.12b**) at different sweep rates, show typical rectangular shaped profiles characteristic of capacitive charge storage mechanism. Both samples show high specific capacitance and low resistance even at high sweep rates. However, lower specific capacitance is delivered by AC4, evidencing the better capacitive performance of AC6.

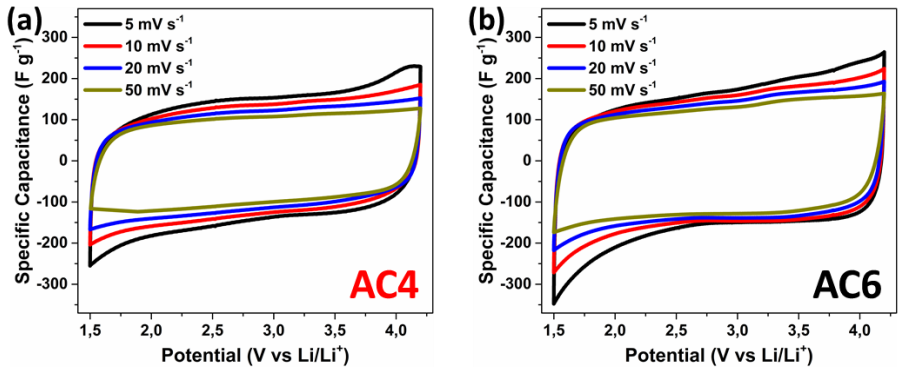


***Figure 5.12.*** *CVs of AC4 (**a**) and AC6 (**b**) measured in the three electrode configuration.*

Evolution of specific capacitance (capacity) for both ACs was measured from the galvanostatic discharge branches at different current rates (**Figure 5.13**). Larger specific capacitances measured for the AC6 sample in the whole current density range can be ascribed to its larger SSA and wider PSD than those measured for the AC4. Specifically, more than 200 F $g^{-1}$ (150 mAh $g^{-1}$) are obtained at a current density of 0.25 A $g^{-1}$, while 112 F $g^{-1}$ (84 mAh $g^{-1}$) are retained when increasing the current density to 10 A $g^{-1}$. On the other hand, AC4 delivered 187 F $g^{-1}$ (140 mAh $g^{-1}$) at 0.25 A $g^{-1}$, and 90 F $g^{-1}$ (68 mAh $g^{-1}$) at 10 A $g^{-1}$.

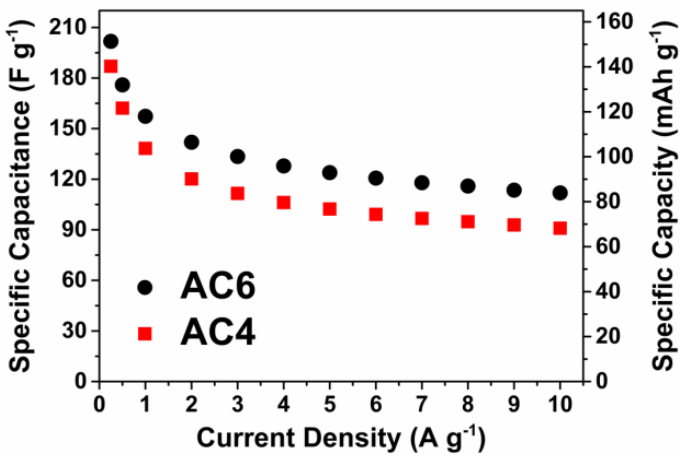


***Figure 5.13.*** *Specific capacity and capacitance evolution at different current densities for labelled activated carbons.*

The electrochemical performance of the activated carbons was also evaluated in a symmetric EDLC configuration using $LiPF_6$ in EC:DMC as organic electrolyte in a voltage window of 0 - 2.7 V (**Figure 5.14**). CVs measured at different scan rates for AC4 and AC6 are represented in **Figure 5.14a** and **Figure 5.14b**, respectively. Both ACs voltammograms display almost ideal quadratic shapes, furtherly confirming their capacitive charge storage mechanism. ACs were also galvanostatically cycled at several current densities in the symmetric EDLC configuration (**Figure 5.14c**). AC6 delivers high specific capacitances of 157 F $g^{-1}$ at 0.25 A $g^{-1}$ and 128 F $g^{-1}$ at 10 A $g^{-1}$. In contrast, AC4 shows lower capacitances in the whole range of current. From Ragone plots (**Figure 5.14d**) it can be appreciated that AC4 shows a more abrupt energy decay at higher powers when compared to AC6. Specifically, AC6 sample delivers energy density

values of 40 Wh $kg^{-1}_{AM}$ and 22 Wh $kg^{-1}_{AM}$ at the corresponding power densities of 168 W $kg^{-1}_{AM}$ and 24.68 kW $kg^{-1}_{AM}$, respectively. On the other hand, AC4 energy densities are 36 Wh $kg^{-1}_{AM}$ and 14 Wh $kg^{-1}_{AM}$ at the corresponding power densities of 168 W $kg^{-1}_{AM}$ and 22.98 kW $kg^{-1}_{AM}$, respectively. Summarizing, measurements of the ACs in the symmetric EDLC configuration furtherly confirmed the better performance of AC6 over AC4.

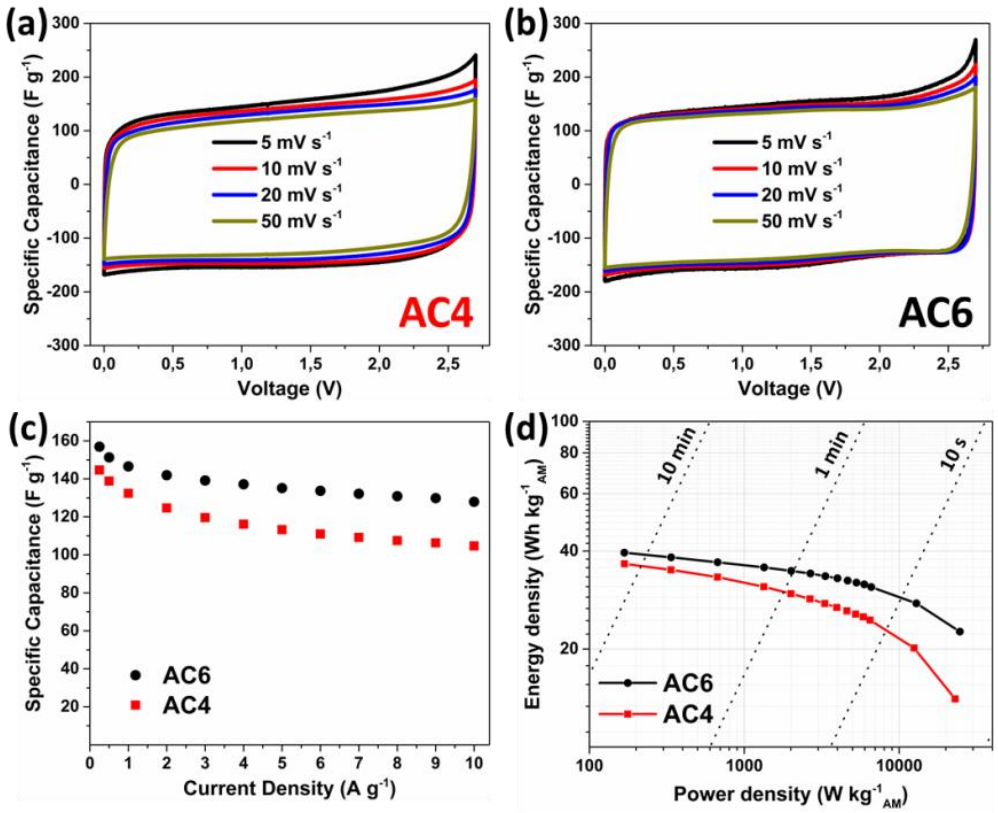


***Figure 5.14.*** *Electrochemical performance of graphene-coffee waste ACs measured as symmetric EDLCs including: cyclic voltammetry measurements of AC4 (**a**) and AC6 (**b**); specific capacitance evolution upon increasing current density (**c**) and corresponding Ragone plots (**d**) for labelled ACs.*

Some values reported recently for representative ACs obtained by the pyrolysis of different biowastes are summarized in **Table 5.3**. It is worth highlighting that under these circumstances, EDLC cells assembled using AC6 carbon outperform on

capacitance and energy densities terms (*i.e.* 128 F $g^{-1}$ and 31 Wh $kg^{-1}$) those biowaste derived ACs reported in literature, either using conventional organic EDLC or battery-based electrolytes.

***Table 5.3.*** *Textural properties and electrochemical performance of some representative biowaste derived activated carbons used as electrodes in non-aqueous symmetric EDLC systems.*

| Active material | Specific Surface Area ($m^2$ $g^{-1}$) | Electrolyte | Capacitance (F $g^{-1}$) | Energy Density (Wh $kg^{-1}$) | Reference |
|---|---|---|---|---|---|
| KOH activated olive pits | 2225 | $Et_4NBF_4$/ACN | 90 | 22 | [53] |
| $ZnCl_2$ activated coffee waste | 1021 | $TEABF_4$/ACN | 110 | 20 | [57] |
| KOH activated coffee waste | 1946 | $BMINBF_4$/ACN | 88 | 27 | [58] |
| KOH activated human hair | 1306 | $LiPF_6$/EC:DEC | 55 | 17 | [59] |
| KOH activated indian cake rusk | 1413 | $LiPF_6$/EC:DMC | 60 | 13 | [60] |
| **KOH activated rGO-coffee (AC6)** | **2350** | **$LiPF_6$/EC:DMC** | **128** | **31** | **This work** |

*Specific capacitance and gravimetric energy density values are calculated at the current density of 10 A $g^{-1}$

## 5.4. Assembly and performance of graphene-coffee waste LIC

In this section the assembly, optimization and electrochemical evaluation of the final LICs are disclosed. In view of their better performance, graphene-coffee waste derived hard carbon (GOCAF, **Section 5.2**) and the AC within a 1:6 activation ratio (AC6, **Section 5.3**) were selected as negative and positive electrode materials, respectively, for the development of the LICs.

### 5.4.1. Optimization and assembly of the LIC

In order to maximize the output capacity of the LIC, mass balance of the electrodes needs to be performed. In this regard, both electrodes must exhibit the same charge stored. For this purpose, the individual evolution of the specific capacity values calculated for GOCAF and AC6 at different current rates using similar electrode masses

are shown in **Figure 5.15**. It is clearly observed that the GOCAF exhibits a characteristic evolution of battery-type electrodes showing higher capacities at low current rates and a prominent capacity decay as the current rate is increased. In contrast, AC6 electrode shows a lower capacity at the beginning but with improved capacitance retention, characteristic of capacitive materials. Since it is impossible to define a proper mass balance for the whole applied current density range, a 1 to 1 mass balance was selected aiming at the design of an optimal system for an application that requires charge/discharge times of 30 seconds (i.e. a current density of ca. 5 A $g^{-1}$). At this current density the negative electrode is slightly oversized to avoid its full utilization, and lithium platting.

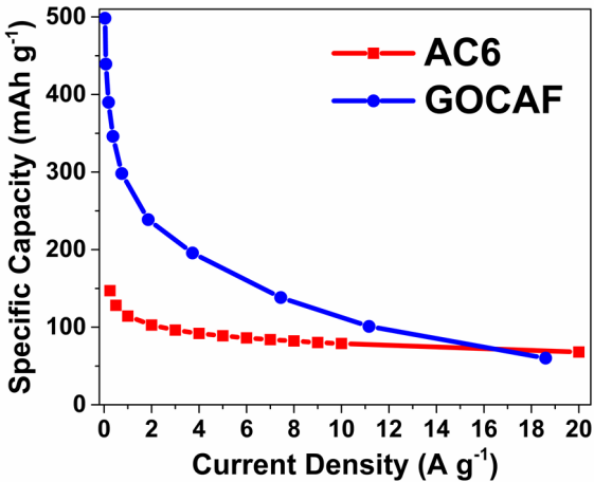


***Figure 5.15.*** *Specific capacity evolution of AC6 and GOCAF at different current densities.*

Prelithiation of the GOCAF electrode was carried out before full cell assembly. The HC electrode was cycled five times between 0.002 and 2 V vs $Li/Li^+$ at 0.1C in order to form a SEI and supply sufficient lithium to compensate for the first cycle irreversibility. For instance, the last discharge was performed at a lower current rate and the final potential was set to 0.2 V (**Scheme 5.4a**). After prelithiation process, lithiated GOCAF was assembled together with AC6 in a three-electrode Swagelok cell using lithium metal as reference electrode to monitor the potential of the cell (**Scheme 5.4b**). HC potential was set to 0.2 V *vs.* $Li/Li^+$ and AC was charged up to 4.2 V *vs.* $Li/Li^+$. The

different potential ranges of the electrodes can efficiently enlarge the operating voltage window of the LIC, enhancing its energy density.

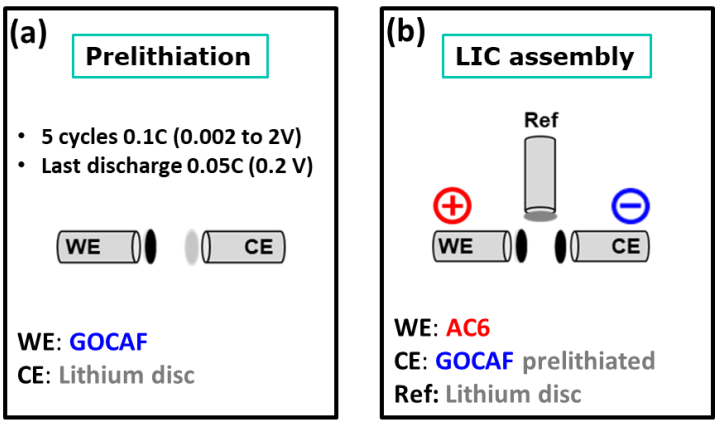


***Scheme 5.4.*** *Schematic representation of prelithiation process (**b**) and LIC assembly (**c**).*

### 5.4.2. Graphene-coffee waste LIC electrochemical performance

LICs were cycled after assembly at some representative current rates in the 1.5 - 4.2 voltage range. Galvanostatic charge/discharge curves plotted in **Figure 5.16a** show a linear voltage increase/decrease during charge and discharge, characteristic of the non-faradaic capacitive charge storage mechanism taking place. Almost unappreciable ohmic drop are observed up to 5 A $g^{-1}$, pointing out the low internal resistance of the LIC. To get insight on the contribution of each electrode into the full cell, individual galvanostatic charge/discharge profiles were monitored at representative current rates. It is observed that at 0.5 A $g^{-1}$ (discharge time of 5 minutes, **Figure 5.16b**), the positive electrode potential swings 2.1 V, while the negative electrode only fluctuates 0.6 V. When the current rate is increased to 5 A $g^{-1}$ (**Figure 5.16c**), the discharge time is reduced to *ca.* 25 seconds and the potential swing of the GOCAF-based negative electrode increases to *ca.* 1.0 V, while the potential swing of the AC decreases to 1.7 V. It is worth mentioning that even at 5 A $g^{-1}$, no lithium platting is observed, ensuring a safe operation of the cell. When current rate is increased over 8 A $g^{-1}$ the potential of the GOCAF-based negative electrode reaches negative values (**Figure 5.16d**), which can be risky not only affecting cyclability but also from a safety point of view. Taking

this into account only values below 6 A $g^{-1}$ were considered for the Ragone plot calculation.

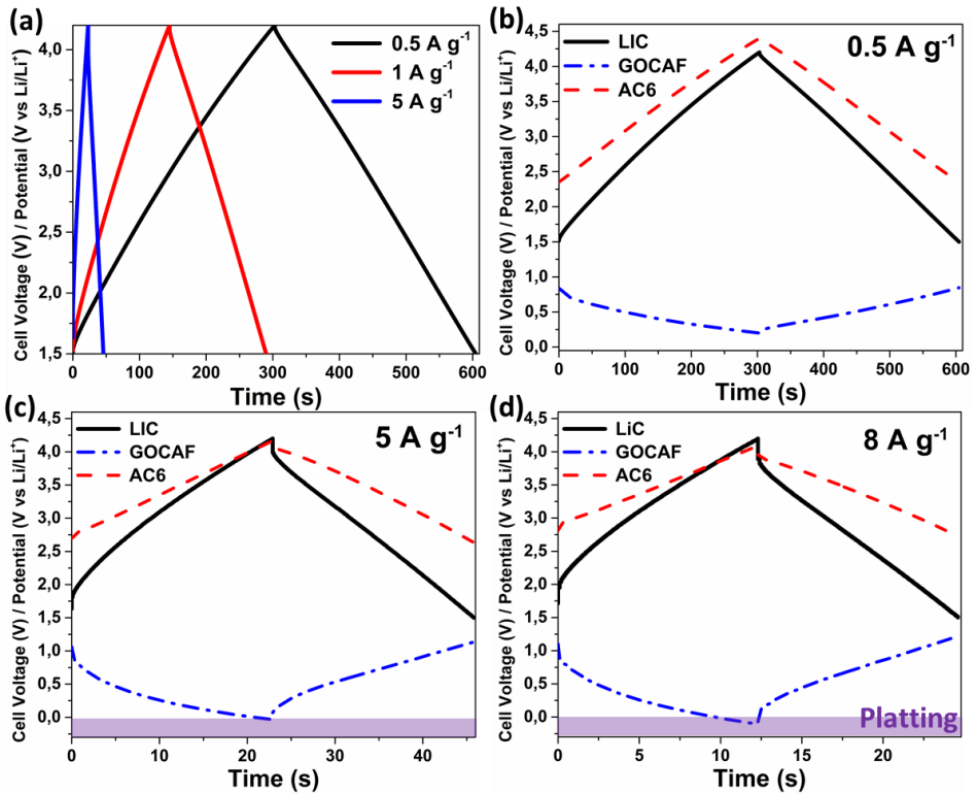


***Figure 5.16.*** *Galvanostatic charge/discharge curve for the LIC measured from 1.5 to 4.2 V at representative current rates (**a**), and galvanostatic charge/discharge profiles registered at 0.5 (**b**), 5 (**c**) and 8 A $g^{-1}$ (**d**) for the LIC (black), the negative electrode (blue) and the positive electrode (red).*

Energy-to-power ratio of the LIC calculated from the galvanostatic charge/discharge curves in the voltage range of 1.5 - 4.2 V is represented in **Figure 5.17a**. Empty points of the curve represent energy/power values, for which the negative electrode reaches negative potential values (from 6 A $g^{-1}$ onwards). It can be observed that for a similar power density, the LIC can deliver more than three times of the energy corresponding to its EDLC counterpart (0 – 2.7V), and still shows impressive energy retention (100 Wh $kg^{-1}_{AM}$ at 9 kW $kg^{-1}_{AM}$). **Figure 5.17b** shows the capacitance retention of the LIC tested within the 1.5 - 4.2 V cell voltage. As it can be observed, herein developed

LIC reaches 80% of the initial capacitance after 3,000 charge/discharge cycles at 5 A $g^{-1}$ (discharge time less than 30 seconds).

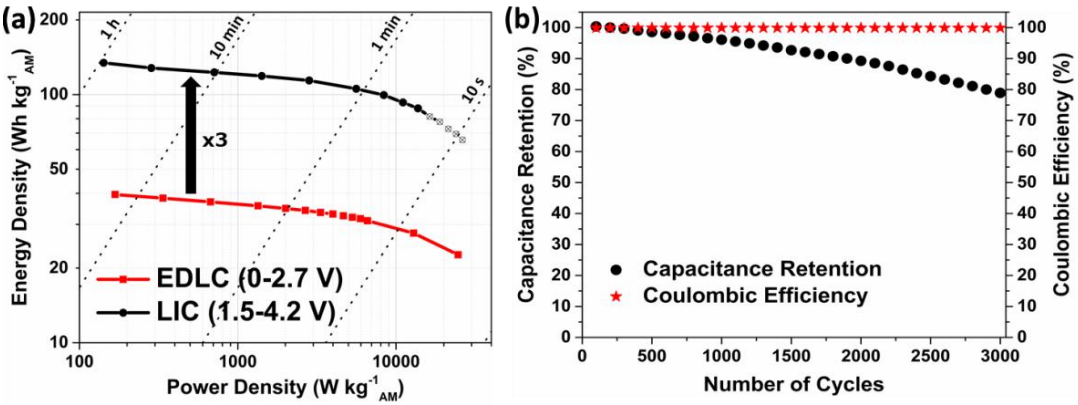


***Figure 5.17.*** *Ragone plot (**a**) and long-term cycling at 5 A $g^{-1}$ (**b**) of LIC assembled using GOCAF and AC6 as negative and positive electrode respectively. Measurements were carried out in the 1.5 – 4.2 V window.*

It is worth mentioning that this LIC shows superior performance in terms of power compared to the biomass derived dual carbon based LICs reported so far in the state-of-the-art, as summarized in **Table 5.4**.

***Table 5.4.*** *Electrochemical performance of representative reported biowaste derived dual-carbon LICs.*

| Positive electrode | SSA ($m^2 g^{-1}$) | Positive electrode capacity* ($mAh g^{-1}$) | Negative electrode | Negative electrode capacity ($mAh g^{-1}$) | LIC Voltage window (V) | LIC Power density** ($kW kg^{-1}_{AM}$) | N° Cycles (% Retention) | Ref |
|---|---|---|---|---|---|---|---|---|
| KOH activated olive pits | 2225 | 120 | Olive pits derived carbon | 250 (0.2 A $g^{-1}$) | 1.5 - 4.2 | 2 | 5000 (70%) | [53] |
| KOH activated juliflora | 2083 | 146 | Juliflora derived carbon | 400 (0.2 A $g^{-1}$) | 1.8 - 4.4 | 2 | 5000 (94%) | [61] |
| KOH activated juliflora | 2448 | 95 | Natural graphite | 373 (0.1 A $g^{-1}$) | 2.0 - 4.0 | 3 | 7000 (80%) | [62] |
| $ZnCl_2$ activated coconut shell | 1795 | 81 | Coconut shell derived carbon | 250 (0.1 A $g^{-1}$) | 1.7 - 4.2 | 3 | 8000 (83%) | [63] |
| KOH activated orange peel | 1901 | - | Graphite | - | 2.0 - 4.0 | 0.5 | 1000 (80%) | [64] |
| KOH activated teak wood | 2108 | 70 | Graphite | - | 2.0 - 4.0 | 0.2 | 1000 (80%) | [65] |
| KOH activated natural sisal | 3104 | 60 | Mesocarbon microbeads | 375 (0.1 A $g^{-1}$) | 2.0 - 4.0 | 1.3 | 1000 (93%) | [66] |
| **KOH activated rGO-coffee waste (AC6)** | **2350** | **150** | **rGO-coffee waste derived carbon(GOCAF)** | **398 (0.2 A $g^{-1}$)** | **1.5 - 4.2** | **9** | **3000 (80%)** | - |

*Positive electrode capacity corresponding to the current density of 0.1 A $g^{-1}$

**Power density values corresponding to energy density values of *ca.* 100 Wh $kg^{-1}$

Despite the great energy and power density values achieved, cyclability still need to be improved to find the requirements of possible industrial applications. Additionally, lithium platting observed from 6 A $g^{-1}$ onwards could result in serious safety risks due to the appearance of metallic lithium in the cell. Thus, with the aim of expanding the cycle life of the cell and avoid premature platting, LICs were assembled following the previous method but cycled in a shortened voltage window of 2.0 – 4.0 V. Galvanostatic charge/discharge curves measured at representative current rates in **Figure 5.18a** evidences the low internal resistance of the cell, since almost negligible ohmic drops are appreciated. However, due to the shortening of the voltage window, around half of the discharge time is attained when compared with the LIC measured in the 1.5 – 4.2 V window (**Figure 5.16a**). Discharge time reduction of the LIC can be ascribed to the lower utilization of the negative electrode, which potential swings from 0.84 to 0.46 V at 0.5 A $g^{-1}$ (**Figure 5.18b**) and from 0.87 to 0.43 V at 5 A $g^{-1}$ (**Figure 5.18c**). Nevertheless, since GOCAF-based negative electrode is not fully utilized, potentials below 0 V are not reached, avoiding lithium platting in the whole range of

current densities applied. It can be observed from **Figure 5.18d** that even at the current density of 10 A $g^{-1}$, the potential swing of the negative electrode is far from reaching negative potential values, whereas the LIC tested from 1.5 to 4.2 V suffers from metallic lithium formation from 6 A $g^{-1}$ onwards.

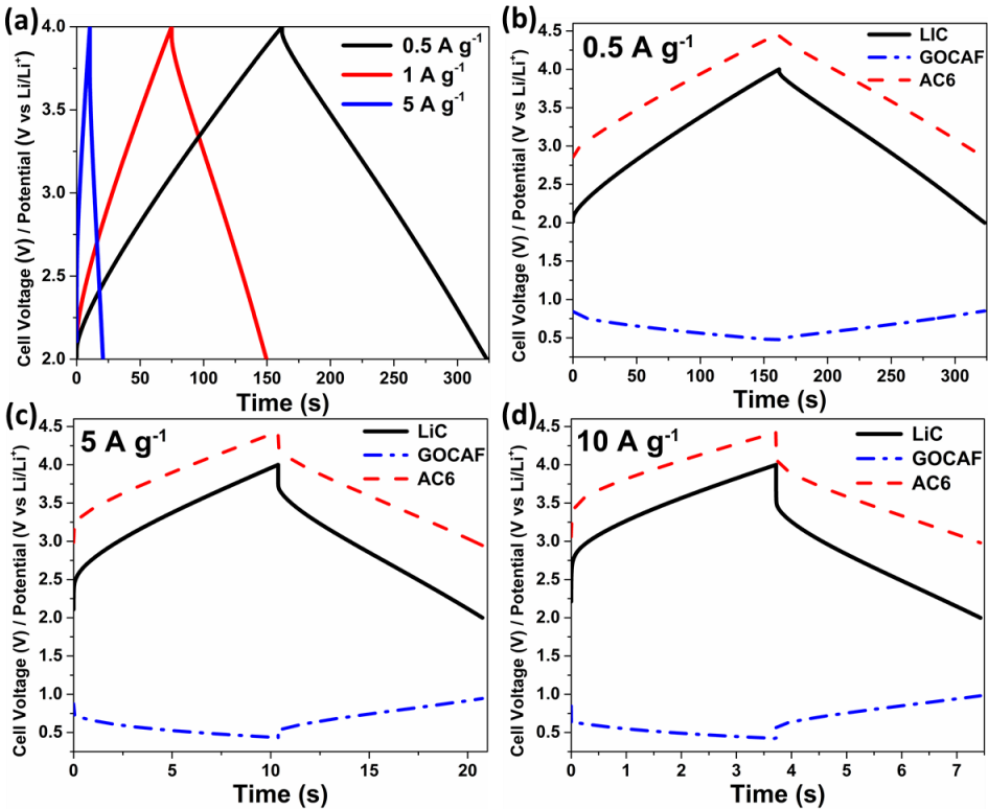


***Figure 5.18.*** *Galvanostatic charge/discharge curve for the LIC measured from 2.0 to 4.0 V at representative current rates (**a**), and galvanostatic charge/discharge profiles registered at 0.5 (**b**), 5 (**c**) and 10 A $g^{-1}$ (**d**) for the LIC (black), the negative electrode (blue) and the positive electrode (red).*

Ragone plot for the LICs measured in the shortened voltage window is depicted in **Figure 5.19a**. Due to the reduced discharge time and since energy is quadratically proportional to the voltage window, the device tested from 2.0 to 4.0 V displays lower energy densities when compared to the LIC measured in the extended voltage window (1.5 to 4.2 V; **Figure 5.17a**). Still, the device is capable to double the energy density

delivered by the corresponding EDLC (measured from 0 to 2.7 V). Nevertheless, at the cost of scarifying part of the energy density, cyclability is considerably enhanced. Specifically, even 15,000 cycles can be reached at 5 A $g^{-1}$ before the initial capacitance decays to 80% (**Figure 5.19b**). This can be ascribed to the lower electrochemical degradation degree of the electrolyte at the selected voltage window. These results evidence the flexibility of LIC storage devices since, by simply adjusting some operational parameters, the electrochemical performance can be tailored to the required application.

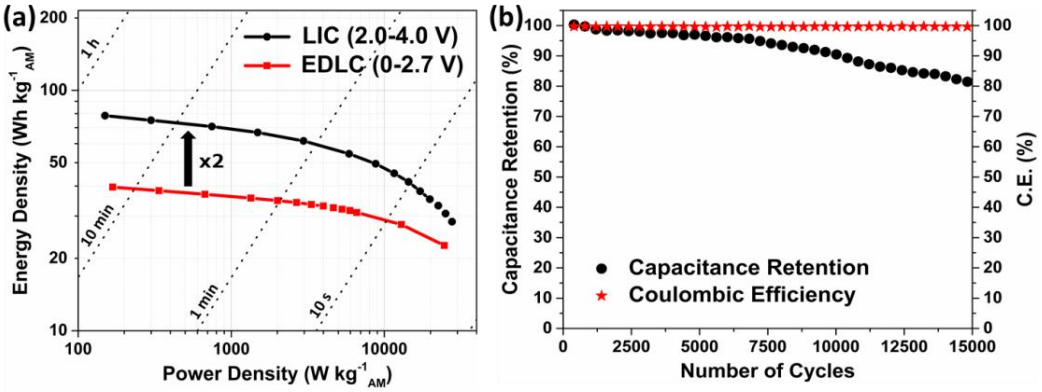


***Figure 5.19.*** *Ragone plot (**a**) and long-term cycling at 5 A $g^{-1}$ (**b**) of LIC assembled using GOCAF and AC6 as negative and positive electrode respectively. Measurements were carried out in the 2.0 – 4.0 V window.*

## 5.5. General summary and conclusions

The potential of ecofriendly and easy-scalable carbons derived from the pyrolysis and/or activation of coffee waste combined with graphene oxide and their application in lithium ion capacitors was demonstrated. It was shown that the optimization of different parameters such as particle size, electronic conductivity or activation degree in the corresponding materials have a great impact on the performance of the final electrodes. Specifically, it was found that the incorporation of graphene oxide into the hard carbon leads to a 40 to 70% increase of the capacity depending on the applied current rate. With regard to the activated carbon, AC6 showed specific capacitance values of 200 F $g^{-1}$ at low rates while 128 F $g^{-1}$ are retained at 10 A $g^{-1}$. LICs assembled with these activated carbons and graphene-carbon composites show high energy

density values of *ca.* 100 Wh $kg^{-1}_{AM}$ at a high power density of 9,000 W $kg^{-1}_{AM}$, accounting for more than three times the energy corresponding to the EDLC system. In addition, the device was able to reach 3,000 cycles with an 80% retention of the initial capacitance when operating between 1.5 - 4.2 V, and 15,000 cycles when voltage window is fixed to 2.0 – 4.0 V.

## 5.6. Bibliography

[1] J. Lang, X. Zhang, B. Liu, R. Wang, J. Chen, X. Yan, The roles of graphene in advanced Li-ion hybrid supercapacitors, J. Energy Chem. 27 (2018) 43–56. https://doi.org/10.1016/j.jechem.2017.11.020.

[2] C. Li, X. Zhang, C. Sun, K. Wang, X. Sun, Y. Ma, Recent progress of graphene-based materials in lithium-ion capacitors, J. Phys. Appl. Phys. 52 (2019) 143001. https://doi.org/10.1088/1361-6463/aaff3a.

[3] J.H. Lee, W.H. Shin, M.-H. Ryou, J.K. Jin, J. Kim, J.W. Choi, Functionalized Graphene for High Performance Lithium Ion Capacitors, ChemSusChem. 5 (2012) 2328–2333. https://doi.org/10.1002/cssc.201200549.

[4] V. Aravindan, D. Mhamane, W.C. Ling, S. Ogale, S. Madhavi, Nonaqueous Lithium-Ion Capacitors with High Energy Densities using Trigol-Reduced Graphene Oxide Nanosheets as Cathode-Active Material, ChemSusChem. 6 (2013) 2240–2244. https://doi.org/10.1002/cssc.201300465.

[5] H. Li, L. Shen, J. Wang, S. Fang, Y. Zhang, H. Dou, X. Zhang, Three-dimensionally ordered porous $TiNb_2O_7$ nanotubes: a superior anode material for next generation hybrid supercapacitors, J. Mater. Chem. A. 3 (2015) 16785–16790. https://doi.org/10.1039/C5TA02929E.

[6] R. Gokhale, V. Aravindan, P. Yadav, S. Jain, D. Phase, S. Madhavi, S. Ogale, Oligomer-salt derived 3D, heavily nitrogen doped, porous carbon for Li-ion hybrid electrochemical capacitors application, Carbon. 80 (2014) 462–471. https://doi.org/10.1016/j.carbon.2014.08.086.

[7] L. Ye, Q. Liang, Y. Lei, X. Yu, C. Han, W. Shen, Z.-H. Huang, F. Kang, Q.-H. Yang, A high performance Li-ion capacitor constructed with Li4Ti5O12/C hybrid and porous graphene macroform, J. Power Sources. 282 (2015) 174–178. https://doi.org/10.1016/j.jpowsour.2015.02.028.

[8] H. Wang, C. Guan, X. Wang, H.J. Fan, A High Energy and Power Li-Ion Capacitor Based on a $TiO_2$ Nanobelt Array Anode and a Graphene Hydrogel Cathode, Small. 11 (2015) 1470–1477. https://doi.org/10.1002/smll.201402620.

[9] M.D. Stoller, S. Murali, N. Quarles, Y. Zhu, J.R. Potts, X. Zhu, H.-W. Ha, R.S. Ruoff, Activated graphene as a cathode material for Li-ion hybrid supercapacitors, Phys. Chem. Chem. Phys. 14 (2012) 3388. https://doi.org/10.1039/c2cp00017b.

[10] D. Mhamane, V. Aravindan, M.-S. Kim, H.-K. Kim, K.C. Roh, D. Ruan, S.H. Lee, M. Srinivasan, K.-B. Kim, Silica-assisted bottom-up synthesis of graphene-like high surface area carbon for highly efficient ultracapacitor and Li-ion hybrid capacitor applications, J. Mater. Chem. A. 4 (2016) 5578–5591. https://doi.org/10.1039/C6TA00868B.

[11] J.J. Ren, L.W. Su, X. Qin, M. Yang, J.P. Wei, Z. Zhou, P.W. Shen, Pre-lithiated graphene nanosheets as negative electrode materials for Li-ion capacitors with high power and energy density, J. Power Sources. 264 (2014) 108–113. https://doi.org/10.1016/j.jpowsour.2014.04.076.

[12] T. Zhang, F. Zhang, L. Zhang, Y. Lu, Y. Zhang, X. Yang, Y. Ma, Y. Huang, High energy density Li-ion capacitor assembled with all graphene-based electrodes, Carbon. 92 (2015) 106–118. https://doi.org/10.1016/j.carbon.2015.03.032.

[13] Y. Sun, J. Tang, F. Qin, J. Yuan, K. Zhang, J. Li, D.-M. Zhu, L.-C. Qin, Hybrid lithium-ion capacitors with asymmetric graphene electrodes, J. Mater. Chem. A. 5 (2017) 13601–13609. https://doi.org/10.1039/C7TA01113J.

[14] W. Ahn, D.U. Lee, G. Li, K. Feng, X. Wang, A. Yu, G. Lui, Z. Chen, Highly Oriented Graphene Sponge Electrode for Ultra High Energy Density Lithium Ion Hybrid Capacitors, ACS Appl. Mater. Interfaces. 8 (2016) 25297–25305. https://doi.org/10.1021/acsami.6b08298.

[15] C. Lu, X. Wang, X. Zhang, H. Peng, Y. Zhang, G. Wang, Z. Wang, G. Cao, N. Umirov, Z. Bakenov, Effect of graphene nanosheets on electrochemical performance of Li 4 Ti 5 O 12 in lithium-ion capacitors, Ceram. Int. 43 (2017) 6554–6562. https://doi.org/10.1016/j.ceramint.2017.02.083.

[16] N. Xu, X. Sun, X. Zhang, K. Wang, Y. Ma, A two-step method for preparing $Li_4Ti_5O_{12}$–graphene as an anode material for lithium-ion hybrid capacitors, RSC Adv. 5 (2015) 94361–94368. https://doi.org/10.1039/C5RA20168C.

[17] R. Xue, J. Yan, L. Jiang, B. Yi, Fabrication of lithium titanate/graphene composites with high rate capability as electrode materials for hybrid electrochemical supercapacitors, Mater. Chem. Phys. 160 (2015) 375–382. https://doi.org/10.1016/j.matchemphys.2015.04.055.

[18] X. Zhang, C. Lu, H. Peng, X. Wang, Y. Zhang, Z. Wang, Y. Zhong, G. Wang, Influence of sintering temperature and graphene additives on the electrochemical performance of porous Li4Ti5O12 anode for lithium ion capacitor, Electrochimica Acta. 246 (2017) 1237–1247. https://doi.org/10.1016/j.electacta.2017.07.014.

[19] T. Yuan, W.-T. Li, W. Zhang, Y.-S. He, C. Zhang, X.-Z. Liao, Z.-F. Ma, One-Pot Spray-Dried Graphene Sheets-Encapsulated Nano-Li4Ti5O12 Microspheres for a Hybrid BatCap System, Ind Eng Chem Res. 53 (2014) 10849–10857. https://doi.org/10.1021/ie501287a.

[20] G. Wang, Toward Ultrafast Lithium Ion Capacitors_ a Novel Atomic Layer Deposition Seeded Preparation of Li4Ti5O12/Graphene Anode, Nano Energy. 36 (2017) 46–57. https://doi.org/10.1016/j.nanoen.2017.04.020.

[21] X. Li, Y. Tang, M. Wang, Y. Huang, L. Liu, J. Zheng, Self-supporting lithium titanate nanorod/carbon nanotube/reduced graphene oxide flexible electrode for high performance hybrid lithium-ion capacitor, J. Alloys Compd. 790 (2019) 1157–1166. https://doi.org/10.1016/j.jallcom.2019.03.151.

[22] Z. Guoyin, L. Ma, H. Lin, P. Zhao, L. Wang, Y. Hu, R. Chen, T. Chen, Y. Wang, Z. Tie, Z. Jin, High-performance Li-ion capacitor based on black-TiO2-x/graphene aerogel anode and biomass-derived microporous carbon cathode, Nano Res. 12 (2019) 1713–1719. https://doi.org/10.1007/s12274-019-2427-3.

[23] C. Yang, J.-L. Lan, C. Ding, F. Wang, S.H. Siyal, Y. Yu, X. Yang, Three-dimensional hierarchical ternary aerogels of ultrafine TiO2 nanoparticles@porous carbon nanofibers-reduced graphene oxide for high-performance lithium-ion capacitors, Electrochimica Acta. 296 (2019) 790–798. https://doi.org/10.1016/j.electacta.2018.10.037.

[24] H. Kim, M.-Y. Cho, M.-H. Kim, K.-Y. Park, H. Gwon, Y. Lee, K.C. Roh, K. Kang, A Novel High-Energy Hybrid Supercapacitor with an Anatase $TiO_2$ -Reduced Graphene Oxide Anode and an Activated Carbon Cathode, Adv. Energy Mater. 3 (2013) 1500–1506. https://doi.org/10.1002/aenm.201300467.

[25] H. Song, J. Fu, K. Ding, C. Huang, K. Wu, X. Zhang, B. Gao, K. Huo, X. Peng, P.K. Chu, Flexible Nb2O5 nanowires/graphene film electrode for high-performance hybrid Li-ion supercapacitors, J. Power Sources. 328 (2016) 599–606. https://doi.org/10.1016/j.jpowsour.2016.08.052.

[26] J.-L. Huang, L.-Q. Fan, Y. Gu, C.-L. Geng, H. Luo, Y.-F. Huang, J.-M. Lin, J.-H. Wu, One-step solvothermal synthesis of high-capacity Fe3O4/reduced graphene oxide composite for use in Li-ion capacitor, J. Alloys Compd. 788 (2019) 1119–1126. https://doi.org/10.1016/j.jallcom.2019.03.004.

[27] F. Zhang, T. Zhang, X. Yang, L. Zhang, K. Leng, Y. Huang, Y. Chen, A high-performance supercapacitor-battery hybrid energy storage device based on graphene-enhanced electrode materials with ultrahigh energy density, Energy Environ. Sci. 6 (2013) 1623. https://doi.org/10.1039/c3ee40509e.

[28] Q. Xia, H. Yang, M. Wang, Q. Guo, L. Wan, H. Xia, Y. Yu, High Energy and High Power Lithium-Ion Capacitors Based on Boron and Nitrogen Dual-Doped 3D Carbon Nanofibers as Both Cathode and Anode, Adv. Energy Mater. 7 (2017) 1701336. https://doi.org/10.1002/aenm.201701336.

[29] M. Ulaganathan, V. Aravindan, W.C. Ling, Q. Yan, S. Madhavi, High energy Li-ion capacitors with conversion type Mn3O4 particulates anchored few layer graphene as negative electrode, J. Mater. Chem. A. 4 (2016) 15134–15139. https://doi.org/10.1039/C6TA05944A.

[30] M. Liu, L. Zhang, P. Han, X. Han, H. Du, X. Yue, Z. Zhang, H. Zhang, G. Cui, Controllable Formation of Niobium Nitride/Nitrogen-Doped Graphene Nanocomposites as Anode Materials for Lithium-Ion Capacitors, Part. Part. Syst. Charact. 32 (2015) 1006–1011. https://doi.org/10.1002/ppsc.201500095.

[31] Z.-K. Chen, J.-W. Lang, L.-Y. Liu, L.-B. Kong, Preparation of a NbN/graphene nanocomposite by solution impregnation and its application in high-performance Li-ion hybrid capacitors, RSC Adv. 7 (2017) 19967–19975. https://doi.org/10.1039/C7RA01671A.

[32] J. Ajuria, M. Arnaiz, C. Botas, D. Carriazo, R. Mysyk, T. Rojo, A.V. Talyzin, E. Goikolea, Graphene-based lithium ion capacitor with high gravimetric energy and power densities, J. Power Sources. 363 (2017) 422–427. https://doi.org/10.1016/j.jpowsour.2017.07.096.

[33] M. Arnaiz, C. Botas, D. Carriazo, R. Mysyk, F. Mijangos, T. Rojo, J. Ajuria, E. Goikolea, Reduced graphene oxide decorated with SnO2 nanoparticles as negative electrode for lithium ion capacitors, Electrochimica Acta. 284 (2018) 542–550. https://doi.org/10.1016/j.electacta.2018.07.189.

[34] C. Li, X. Zhang, K. Wang, X. Sun, Y. Ma, High-power and long-life lithium-ion capacitors constructed from N-doped hierarchical carbon nanolayer cathode and mesoporous graphene anode, Carbon. 140 (2018) 237–248. https://doi.org/10.1016/j.carbon.2018.08.044.

[35] H. Kim, K.-Y. Park, J. Hong, K. Kang, All-graphene-battery: bridging the gap between supercapacitors and lithium ion batteries, Sci. Rep. 4 (2015) 5278. https://doi.org/10.1038/srep05278.

[36] R. Wang, Q. Zhao, W. Zheng, Z. Ren, X. Hu, J. Li, L. Lu, N. Hu, J. Molenda, X. Liu, C. Xu, Achieving high energy density in a 4.5 V all nitrogen-doped graphene based lithium-ion capacitor, J. Mater. Chem. A. 7 (2019) 19909–19921. https://doi.org/10.1039/C9TA06316A.

[37] J.H. Lee, W.H. Shin, S.Y. Lim, B.G. Kim, J.W. Choi, Modified graphite and graphene electrodes for high-performance lithium ion hybrid capacitors, Mater. Renew. Sustain. Energy. 3 (2014) 8. https://doi.org/10.1007/s40243-014-0022-9.

[38] L. Jin, X. Guo, R. Gong, J. Zheng, Z. Xiang, C. Zhang, J.P. Zheng, Target-oriented electrode constructions toward ultra-fast and ultra-stable all-graphene lithium ion capacitors, Energy Storage Mater. 23 (2019) 409–417. https://doi.org/10.1016/j.ensm.2019.04.027.

[39] N.-W. Li, X. Du, J.-L. Shi, X. Zhang, W. Fan, J. Wang, S. Zhao, Y. Liu, W. Xu, Y.-G. Guo, C. Li, Graphene@hierarchical meso-/microporous carbon for ultrahigh energy density lithium-ion capacitors, Electrochimica Acta. 281 (2018) 459–465. https://doi.org/10.1016/j.electacta.2018.05.147.

[40] C. Aphirakaramwong, N. Phattharasupakun, P. Suktha, A. Krittayavathananon, M. Sawangphruk, Lightweight Multi-Walled Carbon Nanotube/N-Doped Graphene Aerogel Composite for High-Performance Lithium-Ion Capacitors, J. Electrochem. Soc. 166 (2019) A532–A538. https://doi.org/10.1149/2.0251904jes.

[41] J. Ajuria, M. Zarrabeitia, M. Arnaiz, O. Urra, T. Rojo, E. Goikolea, Graphene as Vehicle for Ultrafast Lithium Ion Capacitor Development Based on Recycled Olive

Pit Derived Carbons, J. Electrochem. Soc. 166 (2019) A2840–A2848. https://doi.org/10.1149/2.0361913jes.
[42] E. Adelowo, A. Baboukani, C. Chen, C. Wang, Electrostatically Sprayed Reduced Graphene Oxide-Carbon Nanotubes Electrodes for Lithium-Ion Capacitors, C. 4 (2018) 31. https://doi.org/10.3390/c4020031.
[43] B. Li, H. Zhang, D. Wang, H. Lv, C. Zhang, Agricultural waste-derived activated carbon for high performance lithium-ion capacitors, RSC Adv. 7 (2017) 37923–37928. https://doi.org/10.1039/C7RA06680E.
[44] J. Ni, Y. Huang, L. Gao, A high-performance hard carbon for Li-ion batteries and supercapacitors application, J. Power Sources. 223 (2013) 306–311. https://doi.org/10.1016/j.jpowsour.2012.09.047.
[45] I. Childres, L.A. Jauregui, W. Park, H. Cao, Y.P. Chen, RAMAN SPECTROSCOPY OF GRAPHENE AND RELATED MATERIALS, (n.d.) 20.
[46] M. Thommes, K. Kaneko, A.V. Neimark, J.P. Olivier, F. Rodriguez-Reinoso, J. Rouquerol, K.S.W. Sing, Physisorption of gases, with special reference to the evaluation of surface area and pore size distribution (IUPAC Technical Report), Pure Appl. Chem. 87 (2015) 1051–1069. https://doi.org/10.1515/pac-2014-1117.
[47] B.N. Loeffler, D. Bresser, S. Passerini, M. Copley, Secondary Lithium-Ion Battery Anodes: From First Commercial Batteries to Recent Research Activities, Johns. Matthey Technol. Rev. 59 (2015) 34–44. https://doi.org/10.1595/205651314X685824.
[48] Y. Lee, The Effect of Active Material, Conductive Additives, and Binder in a Cathode Composite Electrode on Battery Performance, Energies. 12 (2019) 658. https://doi.org/10.3390/en12040658.
[49] W. Mei, H. Chen, J. Sun, Q. Wang, The effect of electrode design parameters on battery performance and optimization of electrode thickness based on the electrochemical–thermal coupling model, Sustain. Energy Fuels. 3 (2019) 148–165. https://doi.org/10.1039/C8SE00503F.
[50] J. Smekens, R. Gopalakrishnan, N. Steen, N. Omar, O. Hegazy, A. Hubin, J. Van Mierlo, Influence of Electrode Density on the Performance of Li-Ion Batteries: Experimental and Simulation Results, Energies. 9 (2016) 104. https://doi.org/10.3390/en9020104.
[51] F. Béguin, F. Chevallier, C. Vix-Guterl, S. Saadallah, V. Bertagna, J.N. Rouzaud, E. Frackowiak, Correlation of the irreversible lithium capacity with the active surface area of modified carbons, Carbon. 43 (2005) 2160–2167. https://doi.org/10.1016/j.carbon.2005.03.041.
[52] F. Luna-Lama, D. Rodríguez-Padrón, A.R. Puente-Santiago, M.J. Muñoz-Batista, A. Caballero, A.M. Balu, A.A. Romero, R. Luque, Non-porous carbonaceous materials derived from coffee waste grounds as highly sustainable anodes for lithium-ion batteries, J. Clean. Prod. 207 (2019) 411–417. https://doi.org/10.1016/j.jclepro.2018.10.024.

[53] J. Ajuria, E. Redondo, M. Arnaiz, R. Mysyk, T. Rojo, E. Goikolea, Lithium and sodium ion capacitors with high energy and power densities based on carbons from recycled olive pits, J. Power Sources. 359 (2017) 17–26. https://doi.org/10.1016/j.jpowsour.2017.04.107.

[54] P. Yan, F. Ai, C. Cao, Z. Luo, Hierarchically porous carbon derived from wheat straw for high rate lithium ion battery anodes, J. Mater. Sci. Mater. Electron. 30 (2019) 14120–14129. https://doi.org/10.1007/s10854-019-01778-z.

[55] S. Sekar, Y. Lee, D.Y. Kim, S. Lee, Substantial LIB Anode Performance of Graphitic Carbon Nanoflakes Derived from Biomass Green-Tea Waste, Nanomaterials. 9 (2019) 871. https://doi.org/10.3390/nano9060871.

[56] H. Hou, C. Yu, X. Liu, Y. Yao, Q. Liao, Z. Dai, D. Li, Waste-loofah-derived carbon micro/nanoparticles for lithium ion battery anode, Surf. Innov. 6 (2018) 159–166. https://doi.org/10.1680/jsuin.17.00068.

[57] T.E. Rufford, D. Hulicova-Jurcakova, E. Fiset, Z. Zhu, G.Q. Lu, Double-layer capacitance of waste coffee ground activated carbons in an organic electrolyte, Electrochem. Commun. 11 (2009) 974–977. https://doi.org/10.1016/j.elecom.2009.02.038.

[58] Y.S. Yun, M.H. Park, S.J. Hong, M.E. Lee, Y.W. Park, H.-J. Jin, Hierarchically Porous Carbon Nanosheets from Waste Coffee Grounds for Supercapacitors, ACS Appl. Mater. Interfaces. 7 (2015) 3684–3690. https://doi.org/10.1021/am5081919.

[59] W. Qian, F. Sun, Y. Xu, L. Qiu, C. Liu, S. Wang, F. Yan, Human hair-derived carbon flakes for electrochemical supercapacitors, Energy Env. Sci. 7 (2014) 379–386. https://doi.org/10.1039/C3EE43111H.

[60] T. Kesavan, T. Partheeban, M. Vivekanantha, M. Kundu, G. Maduraiveeran, M. Sasidharan, Hierarchical nanoporous activated carbon as potential electrode materials for high performance electrochemical supercapacitor, Microporous Mesoporous Mater. 274 (2019) 236–244. https://doi.org/10.1016/j.micromeso.2018.08.006.

[61] P. Sennu, N. Arun, S. Madhavi, V. Aravindan, Y.-S. Lee, All carbon based high energy lithium-ion capacitors from biomass: The role of crystallinity, J. Power Sources. 414 (2019) 96–102. https://doi.org/10.1016/j.jpowsour.2018.12.089.

[62] P. Sennu, V. Aravindan, M. Ganesan, Y.-G. Lee, Y.-S. Lee, Biomass-Derived Electrode for Next Generation Lithium-Ion Capacitors, ChemSusChem. 9 (2016) 849–854. https://doi.org/10.1002/cssc.201501621.

[63] S. Jayaraman, A. Jain, M. Ulaganathan, E. Edison, M.P. Srinivasan, R. Balasubramanian, V. Aravindan, S. Madhavi, Li-ion vs. Na-ion capacitors: A performance evaluation with coconut shell derived mesoporous carbon and natural plant based hard carbon, Chem. Eng. J. 316 (2017) 506–513. https://doi.org/10.1016/j.cej.2017.01.108.

[64] M. Maharjan, M. Ulaganathan, V. Aravindan, S. Sreejith, Q. Yan, S. Madhavi, J.-Y. Wang, T.M. Lim, Fabrication of High Energy Li-Ion Capacitors from Orange Peel

Derived Porous Carbon, ChemistrySelect. 2 (2017) 5051–5058. https://doi.org/10.1002/slct.201700574.

[65] A. Jain, S. Jayaraman, M. Ulaganathan, R. Balasubramanian, V. Aravindan, M.P. Srinivasan, S. Madhavi, Highly mesoporous carbon from Teak wood sawdust as prospective electrode for the construction of high energy Li-ion capacitors, Electrochimica Acta. 228 (2017) 131–138. https://doi.org/10.1016/j.electacta.2017.01.060.

[66] Z. Yang, H. Guo, X. Li, Z. Wang, Z. Yan, Y. Wang, Natural sisal fibers derived hierarchical porous activated carbon as capacitive material in lithium ion capacitor, J. Power Sources. 329 (2016) 339–346. https://doi.org/10.1016/j.jpowsour.2016.08.088.

# Chapter VI. General overview, conclusions and perspectives



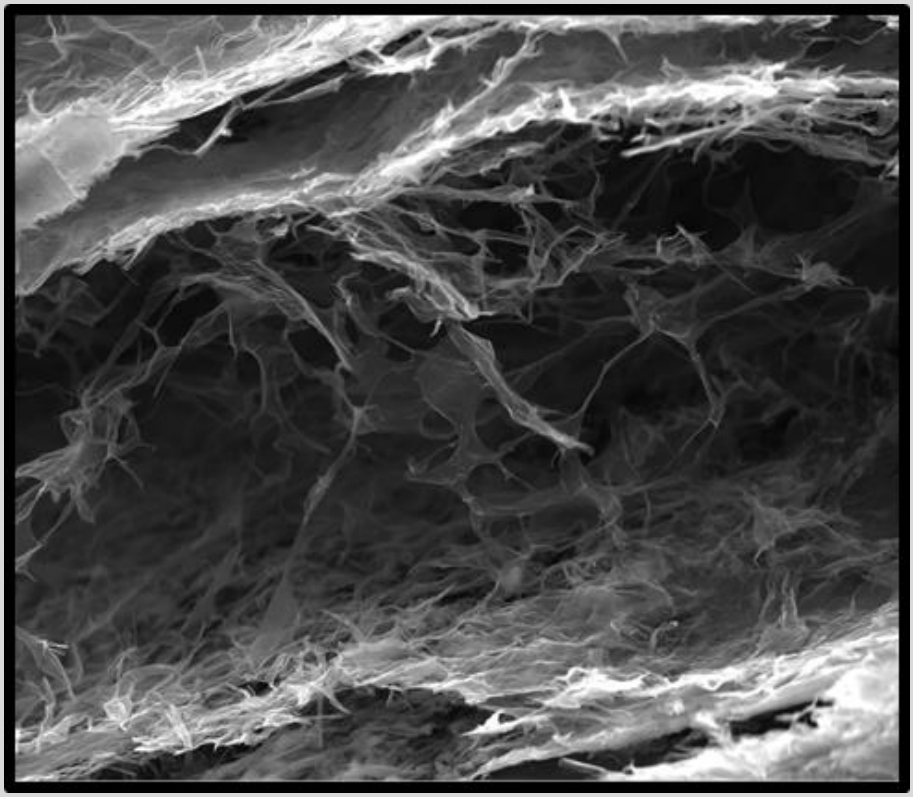

## 6.1. General overview

With the aim of improving the performance of different energy storage systems, graphene has been rationally used to overcome some of the challenges associated to each of the technologies. Graphene oxide was chosen as precursor due to its availability and its easy processability for the fabrication of electrodes. It was found that graphene structures play an important role to circumvent some of the handicaps of **Li-S batteries** (Chapter II). The insulating nature of sulfur, the volume changes undergone upon cycling and/or polysulfide migration have been partially mitigated by incorporation of graphene into the cathode. Moreover, graphene allows hosting large sulfur contents and to process high sulfur loadings cathodes. In contrast, the direct use of graphene oxide for the preparation of sulfur composites results in poor electrochemical performances due to its large oxidation degree, which contribute to polysulfide trapping but, at the same time, decrease the electronic conductivity of the composite. Taking this into account, a partial reduction of the oxygen functionalities through hydrothermal treatment was proved to be an effective route for the preparation of graphene suspensions. Combination of hydrothermally reduced GO and in-situ synthesized sulfur particles (ca. 500 μm) result in well performing Li-S cathode, reaching 500 charge-discharge cycles with a very low-capacity loss (0.07% per cycle) when cycled at 1.675 A $g^{-1}$. However, even if the sulfur content in these cathodes is higher than most of the reported works until now (70%), the sulfur loading is not yet enough to outperform the energy densities of current lithium-ion batteries. For this propose, GO-based self-standing cathodes with sulfur loadings as high as 4 mg $cm^{-2}$ were prepared. The combination of this high loading with the increased conductivity of the GO-based aerogels due to thermal treatment or incorporation of CNTs resulted in high areal capacities (2 mAh $cm^{-2}$) with almost no capacity loss after 100 cycles. Results show that the interconnected framework created by the CNTs in the GO-based matrix enables a better electrochemical stability of the cathode. On the other hand, thermally treated supports show a better performance at high rates due to its higher conductivity.

The performances of thermally reduced GO-based aerogels were furtherly investigated as electrocatalyst in **Na-$O_2$ batteries** (Chapter III). In this particular case, it was found that the textural properties of graphene-based oxygen cathodes can be modified by adjusting the freezing temperature of the GO suspensions before the freeze-drying. A quick freezing with liquid nitrogen leads to the formation of randomly

orientated small aggregates which results in a well-developed porosity. Total pore volume and pore size distribution of the material frozen at lower temperatures (faster freezing) resulted to be higher than that of the material frozen at higher temperatures (slower freezing). It was found that pore size distribution plays an important role on the performance of these materials as electrocatalyst support for the oxygen cathodes. The graphene-based porous material that was frozen at lower temperatures shown the best electrochemical performance in terms of higher discharge capacity (6.6 mAh $cm^{-2}$), lower charge overpotential (260 mV) and extended cycle life (38 cycles). Moreover, cycle life was extended to even 128 cycles by shortening the capacity limitation. These results, which show a much better performance over the scarce state-of-the-art results, are mainly ascribed to the well-distributed mesoporosity of the carbonaceous matrix, which allows the deposition of large amounts of discharge products and provides active sites for ORR and OER reactions. It is worth noting that sodium superoxide ($NaO_2$) was found as the major discharge product, which enables a greater stability than $Na_2O_2$. This finding brings some light over the topic, since, which is the preferentially formed discharge product in $NaO_2$ batteries is still controversial.

According to the results, it was proved that graphene can promote faradaic reactions in Li-S and Na-$O_2$ batteries, improving the specific capacity, rate capability and cycle life. Besides, graphene also has shown to have a great impact over the electrochemical performance of non-faradaic devices like **EDLCs** (Chapter IV). The sustainable combination of used cigarettes and graphene oxide precursors resulted in the formation of highly porous graphene-carbon composites (2,252 $m^2$ $g^{-1}$). It was found that graphene can act as a template for the growth of the carbon precursors, which after carbonization leads to carbon composites with a flat-shaped morphologies. Tailored morphology and textural properties provided by the presence of graphene enabled the use of large-sized electrolyte ions such as imidazolium-based ionic liquids. This suitable combination leads to stable operational voltage windows of even 3.3 and 3.4 V when using EMIN $BF_4$ an EMIN TFSI, respectively. Moreover, graphene-carbon composites delivered capacitance values of ca. 160 F $g^{-1}$ at low current rate, and still ca. 120 F $g^{-1}$ at 10 A $g^{-1}$ when tested in ILs. As result, energy densities of ca. 63 Wh $kg^{-1}$ at 210 W $kg^{-1}$ and 40 Wh $kg^{-1}$ at 7,800 W $kg^{-1}$ were obtained in EMIN $BF_4$ and EMIN TFSI, respectively. In addition, these systems reach 11,000 charge-discharge cycles with ca. 80% retention of the initial capacitance. Three-electrode study disclosed that the enhanced capacitance observed for these carbon composites in ionic liquids is

related to the optimized textural properties, which improves the imidazolium-cation adsorption. Evaluation of graphene-based electrodes in diluted ILs shown that the rate performance and power delivered can be furtherly increased. However, the lower electrochemical stability of the diluted ILs results in poor capacitance retention upon cycling.

The experience acquired from the preparation of graphene-carbon composites starting from biowaste precursors was transferred to the preparation of active materials for **DC-LICs** (Chapter V). In this case, coffee waste was selected as precursor for the preparation of both battery-type and capacitive-type electrodes. It was shown that some parameters such as carbon particle size or active mass loading have a great impact on the rate capability of the battery-type electrodes. Additionally, it was found that the incorporation of graphene oxide into the hard carbon leads to a 40 to 70% increase of the capacity depending on the applied current rate. Regarding the capacitive-type electrode, the influence of the amount of activation agent over the EDL formation was demonstrated. The sample prepared with a larger carbon:KOH ratio delivered higher capacitance values in the whole range of current densities due to its higher SSA (2,350 $m^2$ $g^{-1}$) and wider PSD. Individual optimization of the electrodes according to their charge storage mechanism enabled the smooth operation of the LIC, delivering *ca.* 100 Wh $kg^{-1}_{AM}$ at a high-power density of 9,000 W $kg^{-1}_{AM}$. In addition, the device was able to reach 3,000 cycles with an 80% retention of the initial capacitance. Moreover, at the cost of sacrificing some energy density, the shortening of the voltage window from 1.5 – 4.2 V to 2.0 – 4.0 V demonstrates to greatly enhances the cyclability to 15,000 cycles and avoid lithium platting.

## 6.2. Conclusions

### Lithium-Sulfur Batteries

1. Graphene-based materials effectively create a conductive matrix for the wrapping of sulfur particles, alleviating the major challenges of Li-S technology: isolating nature of sulfur, volume changes during cycling and polysulfides migration.

2. Partial reduction of GO through hydrothermal treatment allows the creation of stable aqueous suspensions with higher conductivity and maintaining some polarity for the efficient wrapping of polysulfides, which allows a long-cycle life of the cells at high rates.

3. Sub-micrometer size sulfur particles produced by a green and scalable process using sodium thiosulfate as precursor and PVP as capping agent improve the electrochemical stability of Li-S batteries.

4. Graphene-based aerogels allow the incorporation of larger amounts of sulfur, leading to higher areal capacities.

5. Addition of carbon nanotubes and thermal reduction of GO-based aerogels result in enhanced electrochemical performance due to its higher conductivity. Graphene-CNT/S composites show better stability but lower rate performance than thermally treated ones.

### Sodium-Oxygen Batteries

6. Graphene-based supports demonstrate to be versatile oxygen cathodes for Na-$O_2$ batteries.

7. Textural properties of the rGO-based aerogels can be tuned by simply adjusting the freezing temperature of GO suspensions before freeze-drying.

8. Pore size distribution of graphene-based oxygen cathodes greatly influences the electrochemical performance of Na-$O_2$ batteries in terms of cycle life, delivered capacity and energy efficiency. Especially, a quick freezing of the GO suspension guarantees the presence of active sites for ORR and OER reactions and provides enough channels for the diffusion of $O_2$ and $Na^+$ ions.

**9.** Sodium superoxide was found to be the major discharge product. Size and distribution of $NaO_2$ have a high dependence on the textural properties of the carbon matrix used

## Electric Double Layer Capacitors

**10.** Cigarette butts waste showed to be an effective green source to prepare high specific surface area activated carbons.

**11.** Graphene acts as a template during activation of acetate cellulose, leading to a flat morphology of the activated carbons. This modified morphology enables a better access of the activation agent, which provides a wider pore size to the composite.

**12.** Wide PSD of the graphene-AC composite facilitates the access of large-sized electrolyte ions of ionic liquids, allowing a stable performance even at 3.4 V.

**13.** Diluted ionic liquids increase the power performance of graphene-based EDLCs at the cost of reducing capacity retention upon cycling due to its lower electrochemical stability.

**14.** Three-electrode study disclosed that the enhanced capacitance observed for these carbon composites in ionic liquids is related to the optimized textural properties, which improves the imidazolium-cation adsorption.

## Lithium-ion Capacitors

**15.** Novel ecofriendly and easy-scalable production approach for the preparation of carbon-graphene composites from coffee wastes is demonstrated.

**16.** The presence of graphene creates a conductive matrix that interconnects the carbon particles enhancing the electrode conductivity and enabling fast $Li^+$ diffusion.

**17.** Particle size and mass loading optimization in the negative electrode improve electrochemical performance, especially at high rates.

**18.** Activated carbon materials obtained from the highest 1:6 ratio (carbon:KOH) exhibit the highest pore sizes and the larger specific surface area, thus, showing the highest specific capacitance values

**19.** Individual optimization of both positive and negative electrodes of the LIC according to their charge storage mechanisms has a great impact on the energy and power performance of the full cell.

**20.** Cyclability of the LIC can be extended from 3,000 to 15,000 cycles, at the cost of the energy just by decreasing the voltage window from 1.5 - 4.2 V to 2.0 - 4.0 V.

## 6.3. Perspectives

The investigations presented in this thesis, in agreement with most of the recent bibliographic studies, have shown that the integration of graphene can improve some of the most relevant metrics of different energy storage technologies when tested at lab-scale. However, these promising findings should be taken with caution because it takes time and efforts to implement them into commercial energy storage devices.

Although graphene produced through the graphite exfoliation is a very promising route for its mass production, it still has associated some important drawbacks such as high cost and the poor physical and chemical reproducibility. In addition, the low density of graphenic materials may limit its use in those applications where high volumetric energy density is needed.

Taking all of this into account, it seems that there is still a long way until some of the graphene-based next generation energy storage devices reach the maturity and gets into the market. To make this possible advanced large-scale production processes that can guarantee reproducible, high quality and low-cost graphene is still required and the engineering processes of electrodes in battery cells should be also adapted for the integration of the graphene-based new formulations.

# Appendix



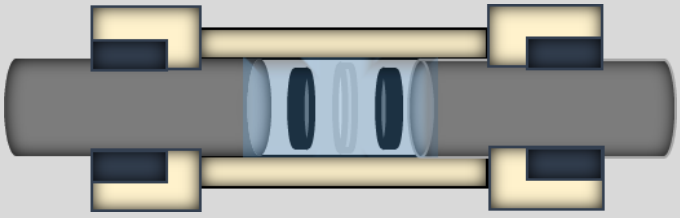

# Appendix I. List of abbreviations

| | |
|---|---|
| **2D-NLFDT** | Bidimensional non-local density functional theory |
| **AC** | Activated Carbon |
| **ACN** | Acetonitrile |
| **AM** | Active Mass |
| **BET** | Brunauer–Emmett–Teller |
| **CB** | Cigarette Butt |
| **CNT** | Carbon Nanotube |
| **CT** | Charge Transfer |
| **CVD** | Chemical Vapor Deposition |
| **C.E.** | Coulombic Efficiency |
| **CTAB** | Cetyl Trimethyl Ammonium Bromide |
| **CV** | Cyclic Voltammetry |
| **DC-LIC** | Dual Carbon Lithium-ion Capacitor |
| **DME** | 1,2-Dimethoxyethane |
| **DMC** | Dimethyl Carbonate |
| **DOL** | 1,3-Dioxolane |
| **EC** | Electrochemical Capacitor |
| **EDL** | Electric Double Layer |
| **EDLC** | Electric Double Layer Capacitor |
| **EES** | Electrochemical Energy Storage |
| **EIS** | Electrochemical Impedance Spectroscopy |
| **EMIN** | 1-Ethyl-3-Methylimidazolium |
| **$Et_4N$** | Tetraethylammonium |
| **ESS** | Energy Storage System |
| **EV** | Electric Vehicle |
| **GNS** | Graphene nanosheets |
| **GO** | Graphene Oxide |

| | |
|---|---|
| **HC** | Hard Carbon |
| **HrGO** | Hydrothermally Reduced Graphene Oxide |
| **IL** | Ionic Liquid |
| **IUPAC** | International Union of Pure and Applied Chemistry |
| **LiB** | Lithium-ion Battery |
| **LIC** | Lithium-ion Capacitor |
| **Li-S** | Lithium-Sulfur |
| **LTO** | Lithium titanate Oxide |
| **LiTFSI** | Lithium bis(trifluoromethanesulfonyl) imide |
| **M-$O_2$** | Metal Oxygen |
| **NLDFT** | Non-Local Density Functional Theory |
| **NMP** | N-Methyl-2-Pyrrolidone |
| **NMR** | Nuclear Magnetic Resonance |
| **OCP** | Open Circuit Potential |
| **OER** | Oxygen evolution reaction |
| **ORR** | Oxygen reduction reaction |
| **PC** | Porous Carbon |
| **PPY** | Polypyrrole |
| **PSD** | Pore Size Distribution |
| **PVDF** | Polyvinyilidene fluoride |
| **PVP** | Polyvinyl Pyrrolidone |
| **rGO** | Reduced Graphene Oxide |
| **SEI** | Solid electrolyte interface |
| **SEM** | Scanning Electron Microscopy |
| **SL** | Surface Layer |
| **SSA** | Specific Surface Area |
| **TEM** | Transmission Electron Microscopy |
| **VN** | Vanadium Nitride |
| **XRD** | X-Ray Diffraction |

# Appendix II. Experimental

## AII.1. Physicochemical characterization techniques

### AII.1.1. X-Ray Diffraction

In XRD measurements, X-ray beam is directed to the surface of the studied material, interacting with the atoms in the crystal. A portion of the X-ray beam is scattered/diffracted, at a well-defined angle (*2*θ) and detected by the instrument. The diffraction pattern for an element or compound is unique, which is related to the crystal structure. The average spacing *d* between layers or rows of atoms can be determined by the incident X-ray wavelength (λ*)* and angle θ, following Bragg's Law (see **Scheme AII.1**):

$$n\lambda = 2d \cdot sen(\theta) \qquad \textbf{(}\boldsymbol{AII.1}\textbf{)}$$

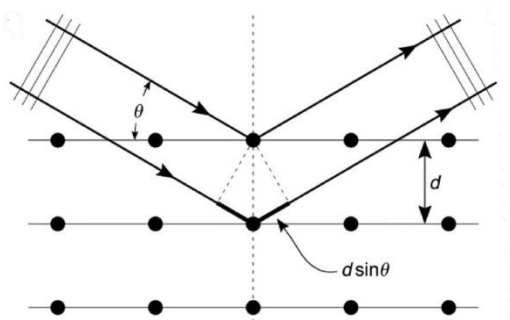


***Scheme AII.1.*** *Diagram of Bragg reflection by a set of parallel planes with interplanar distance d [1].*

X-ray diffraction (XRD) patterns were registered for powdered samples in a Bruker D8 X-ray diffractometer; data were collected at 40 kV and 30 mA using CuKα radiation over 2θ within the range from 10 to 80° at steps of 0.02° and a residence time of 5 s.

### AII.1.2. Raman

Raman spectroscopy is a light scattering technique where the sample is irradiated by a monochromatic, high intensity laser light source. Incident light interacts with the

atoms of the materials and scattered light is detected. Much of the scattered radiation has the same frequency of the incident radiation; this is the so-called Rayleigh scattering. On the other hand, a much smaller fraction of the scattered light has a different frequency from the irradiated one, this constitutes the Raman scattering. The Raman scattering process leads to absorption of energy by the molecule and its promotion to a higher energy excited vibrational state. As result, scattered light, also known as Stokes scattering, presents a higher wavelength than irradiated one. In contrast, due to thermal energy, some molecules might be presented in an excited state. Scattering from this state to the initial state, is called anti-Stokes scattering and in this process energy is transferred to the scattered photon, resulting a lower wavelength when compared to that of original radiation (see **Scheme AII.2**).

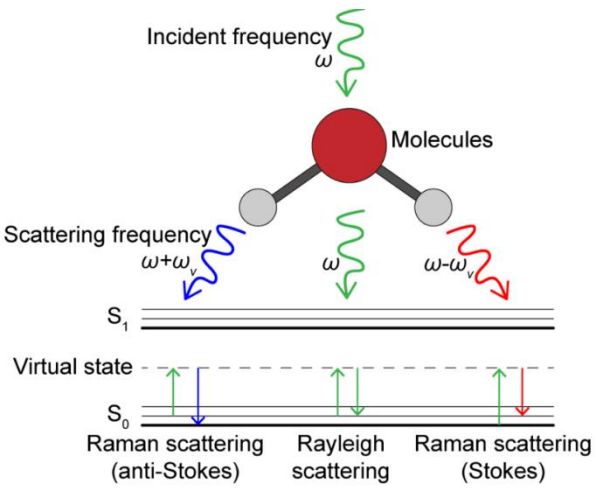


***Scheme AII.2.*** *Scheme and Jablonski diagram illustrating Raman and Rayleigh scattering [2].*

When measuring graphene-based materials, two broad Raman peaks appears at ca. 1600 and 1350 $cm^{-1}$, commonly denoted as D-band and G-band, respectively. D-band is associated to the disordered structure of graphene, representing the dispersive, defect induced vibrations, while the G-band is related to vibration of $sp^2$-bound carbon atoms [3]. The relative area ratio ($A_D/A_g$) or maximum intensity pick ratio ($I_D/I_g$) of the D and G bands are measures of the defects formed in the sample and is inversely proportional to the average size of the $sp_2$ domains [4].

Raman spectra were recorded with a Renishaw spectrometer (Nanonics Multiview 2000) operating with an excitation wave-length of 532 nm. The spectra were acquired with 30 s of exposition time of the laser beam to the sample. The ratio between the integral of D and G peaks was calculated in Origin software by fitting the experimental curve with Gaussian and Lorentz equations.

### AII.1.3. Nitrogen adsorption isotherms

Among the different gas adsorption methods, $N_2$ adsorption at -195.8 °C (77 K) is the most commonly used technique owing to the large pore range that can cover and its weak interaction with most solids. The surface adsorption capacity of nitrogen in a solid surface depends on the nitrogen-relative pressure ($P/P_0$), where $P$ is the partial pressure of nitrogen and $P_0$ is the saturated vapor pressure of nitrogen under temperature of liquid nitrogen [5]. The information related to the specific surface area and pore size distribution of the material can be extracted from the adsorption-desorption isotherm.

Nitrogen adsorption/desorption isotherms were registered at -196 °C in an ASAP 2460 and ASAP 2020 from micromeritics. Already thermally treated samples (AC, HC, rGO) were degassed at 250 °C during 3 h under vacuum while non-reduced samples (GO, GO-CNT) were degassed at 90 °C for 12 h under vacuum. The specific surface area was calculated according to the Brunauer–Emmett–Teller (BET) method [6] from the nitrogen isotherms in the relative pressure range of 0.05-0.25. The t-plot method was used to the external surface area ($S_{EXT}$) in the relative pressure range of 0.07–0.25. The total volume of micro-mesopores ($V_T$) was calculated as the amount of $N_2$ adsorbed at the relative pressure of 0.99. The pore size distribution was determined by using 2D-NLDFT heterogeneous surface method (equilibrium/desorption branch) and fitting with SAIEUS software. The average mesopore ($D_{meso}$) and macropore sizes ($D_{macro}$) were calculated as specify above:

$$D_{meso} = {}^{4V_T}/_{S_{BET}} \qquad \textbf{(}\textit{AII.2}\textbf{)}$$

$$D_{macro} = {}^{4V_P}/_{S_{EXT}} \qquad \textbf{(}\textit{AII.3}\textbf{)}$$

where $V_P$ is the total pore volume of micro-meso macropores calculated by He pycnometry at room temperature ($cm^3\ g^{-1}$).

## AII.1.4. Helium Pycnometry

A gas pycnometer operates by detecting the pressure change resulting from displacement of gas by a solid object. Expanding a quantity of gas at known pressure into an empty chamber and measuring the pressure establishes a baseline. Then a sample is placed in the chamber and the chamber is resealed. The same quantity of gas at the same pressure is again expanded into the sample chamber, and the pressure is measured. The difference in the two pressure combined with the known volume of the empty sample chamber allows the volume of the sample to be determined by way of the gas law. Helium is usually used because is not adsorbed by almost any solid at normal conditions [7].

In this work, AccuPyc II 1340 pycnometer (Micromeritics) was used to measure the true density ($\rho_t$) of graphene-based materials. The total pore ($V_P$) volume of micro-meso and macropores was calculated by the formula:

$$V_P = \frac{1}{\rho_a} - \frac{1}{\rho_t} \qquad \textbf{(}\boldsymbol{AII.4}\textbf{)}$$

where $\rho_a$ is the apparent density ($g\ cm^{-3}$) calculated by weighting and measuring the dry materials and $\rho_t$ is the true density ($g\ cm^{-3}$).

## AII.1.5. Elemental Analysis

Elemental analysis is a well-known method for determining the elemental composition of a substance. Elemental analysis commonly refers to CHNX analysis, where X is a heteroatom like halogens or sulfur. Generally, for EA measurements, samples are heated at very high temperatures in the presence of catalysts, leading to the total combustion of the samples in the form of gases, which are detected by the equipment. The total amount of gases detected can be quantitatively related with the atomic composition of the sample. Elemental analysis was carried out using a flash 2000 Thermo Scientific CHNS-O analyzer to determine the sulfur content in the composites

## AII.1.6. Solid-State NMR

NMR is the oscillatory response of nuclei with non-zero spins in a magnetic field to resonant excitation by radiofrequency irradiation. The NMR transition frequencies are sensitive to the electron distribution around the nucleus, which shields the nucleus from the applied magnetic field. The shielding constant, $\sigma$, varies for different nuclei of a given isotope in a molecule, causing slightly different frequencies. Thus, NMR frequencies reveal the chemical structure of the sample. NMR frequencies are commonly reported as a chemical shift, $\delta$, which is the fractional difference between the frequency of a particular nucleus and a standard compound [8]. In solution NMR, spectra consist of a series of very sharp transitions, due to averaging of anisotropic NMR interactions by rapid random tumbling. By contrast, solid-state NMR spectra are very broad, as the full effects of anisotropic or orientation-dependent interactions are observed in the spectrum. These anisotropic dipolar interactions can be suppressed by introducing artificial motions on the solid - this technique involved rotating the sample about an axis oriented at 54.74° with respect to the external magnetic field. This became known as magic-angle spinning. Samples are finely powdered and packed tightly into rotors, which are then spun at rates from 1 to 35 kHz, depending on the rotor size and type of experiment being conducted (**Scheme AII.3**).

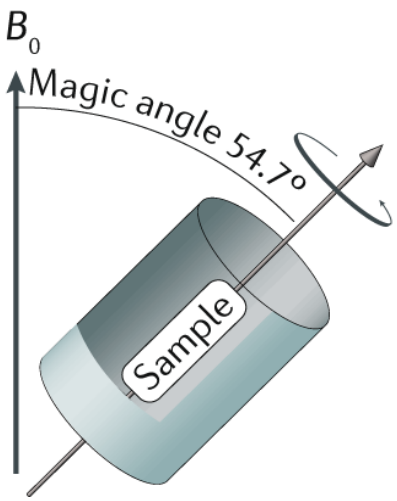


***Scheme AII.3.*** *Diagram representing Magic Angle Spinning configuration [8].*

Solid state NMR experiments were performed in a WB 500 MHz spectrometer equipped with a Bruker standard 2.5 mm probe. Experiments were carried out using a rotor-synchronized Hahn echo pulse sequence using a 90° pulse duration of 3 µs. The pulse delay was set to 10 s, as this was observed in our sample, and previously to be sufficient to avoid signal saturation allowing the quantitative characterization of the signals in the spectra. A total of 25,920 scans were accumulated with a total experimental time of 72 h. The Magic Angle Spinning frequency was set to 20 kHz in all experiments. The experimental data were deconvoluted using the Dmfit software.

### AII.1.7. Scanning Electron Microscope

Scanning Electron Microscope is a technique used to evaluate the morphology and chemical features of the surface of a certain material. A high-energy laser beam irradiates electrons to the sample and then the signals produced are collected and analyzed from the secondary electrons, back-scattered electrons, characteristic X-rays, transmitted electrons, etc. Analysis of each signal can provide different information about the sample's surface. For example, analysis of the dispersed X-Rays can give qualitative information about the elemental composition of the sample. On the other hand, most common SEM images are created from the secondary electrons that arise from the sample and are attracted to the sample holder through a positive potential. Thus, when electrons cross the sample and impact on the sample holder, a light that is converted by a photomultiplier in a voltage signal is generated and converted into an image. Similarly, detection of elastically reflected electrons of the laser beam after interacting with the sample, also known as backscattered electrons, can give information about the chemical composition of the sample.

In this work, SEM measurements were performed using a Quanta200 FEI (3 kV, 30 kV) microscope.

### AII.1.8. Transmission Electron Microscope

TEM relies on the detection and analysis of transmitted electrons after passing through a thin sample. For this purpose, high energy electrons (up to 300 kV) are accelerated and focused into a thin beam thanks to the use of condenser lens. After the electron beam strikes the sample, transmitted electrons are focused by the

objective lens into a phosphor screen to convert the electron image information to a visible form. This configuration allows considerably greater magnification than that obtained from SEM imaging. Additionally, since high-energy electrons pass through the sample, crystallographic and atomic information of the sample can be obtained from this technique. However, samples need to be processed into thin films to perform the measurements. **Scheme AII.4** compares the configuration of most commonly employed SEM and TEM instruments.

TEM measurements were carried out in a FEI -TECNAI G2 F20 S-TWIN microscope at an acceleration voltage of 200 kV and a spot size of 3. Samples were dispersed in acetone and transferred onto a holey carbon film fixed on a 3 mm copper grid.

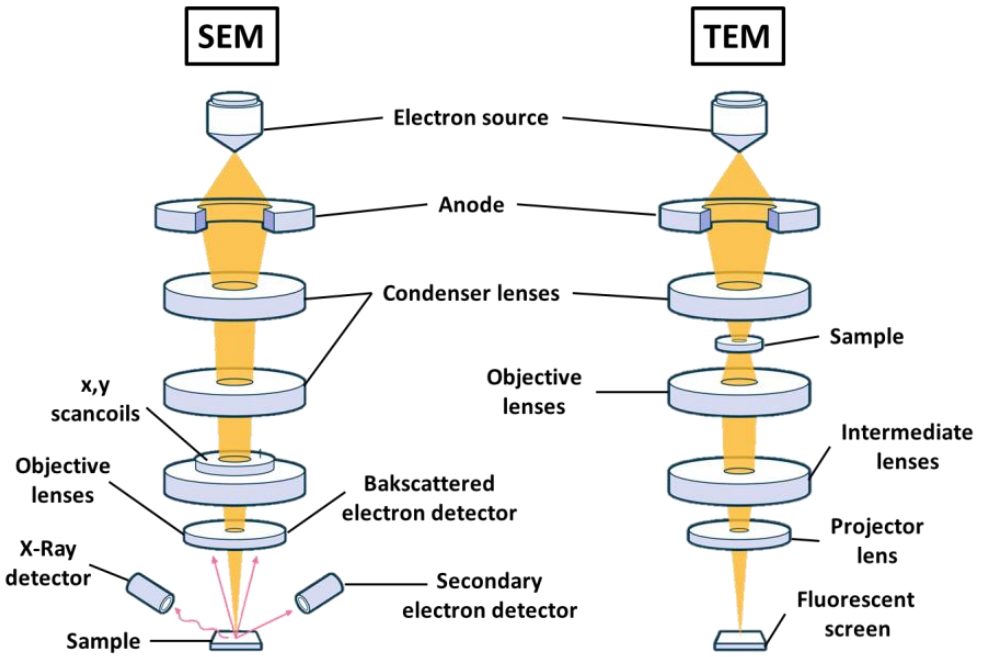


***Scheme AII.4.*** *Diagram of the most representative parts in SEM and TEM instruments (modified from [9]).*

## AII.2. Electrochemical characterization techniques

### AII.2.1. Electrode preparation

In **Section 2.2**, active materials (HrGO-PVP/S, HrGO/S, and GO/S) are mixed with PVDF and C65 conductive carbon (IMERYS Graphite & Carbon) in NMP using an 80:10:10 ratio. These slurries were then deposited onto a carbon-coated aluminum foil using the doctor blade technique with a coating thickness of 300 µm and dried at 50 °C under vacuum overnight. Electrode discs of 12 mm in diameter and typical sulfur mass loadings of 1.3-1.6 mg $cm^{-2}$ were cut and further dried prior to cell assembly.

In **Section 2.3**, composites (GO/S, GO-CNT/S and rGO/S) were processed as self-standing discs and directly used as electrodes. The electrodes, accounting with a diameter of 12 mm and typical thickness values of 300 ± 20 µm, were dried at 50 °C under vacuum overnight prior their assembly into the cell. The same electrode preparation process was followed in **Chapter III** for graphene-based materials ($N_2$-rGO, F-rGO and Film). In this case, self-standing electrodes of 11 mm in diameter and 1.77 ± 0.44 mg $cm^{-2}$ were dried at 120 °C under vacuum overnight prior to cell assembly.

In **Chapter IV**, electrodes of active materials (both GO-FdAC and FdAC) were processed by rolling and pressing a mixture formed by these materials together with Super P C65 and polytetrafluoroethylene in ethanol according to the 90:5:5 mass ratio. Self-standing electrode discs (4 ± 1 mg $cm^{-2}$, 150 ± 30 µm) of 11 mm in diameter were punched out from the paste and dried at 120 °C under vacuum overnight prior to cell assembly.

In **Chapter V**, hard carbon (both GOCAF and CAF) and activated carbon (both AC4 and AC6) electrodes were processed by mixing the active materials together with Super P C65 and PVDF in NMP according to the 90:5:5 mass ratio. Hard and activated carbon NMP-based inks were coated on copper and aluminum foil, respectively, using doctor blade technique with a coating thickness of 150 µm and then the laminates were dried at 80 °C under vacuum overnight. Electrode discs of 11 mm in diameter were punched out and dried at 120 °C overnight under vacuum prior the cell assembly.

## AII.2.1. Cell Assembly and Electrochemical Conditions

Different cell assembly configurations were used according to the needs of each technology. CR2032 coin cells were used for galvanostatic measurements of Li-S batteries (**Scheme AII.5a**). Electric double layer capacitors and lithium-ion capacitors were assembled in two (**Scheme AII.5b**) and three (**Scheme AII.5c**) electrode Swagelok-type cells. A clamp was attached to the Swagelok-type cells during the electrochemical measurements to ensure a good pressure in the cell.

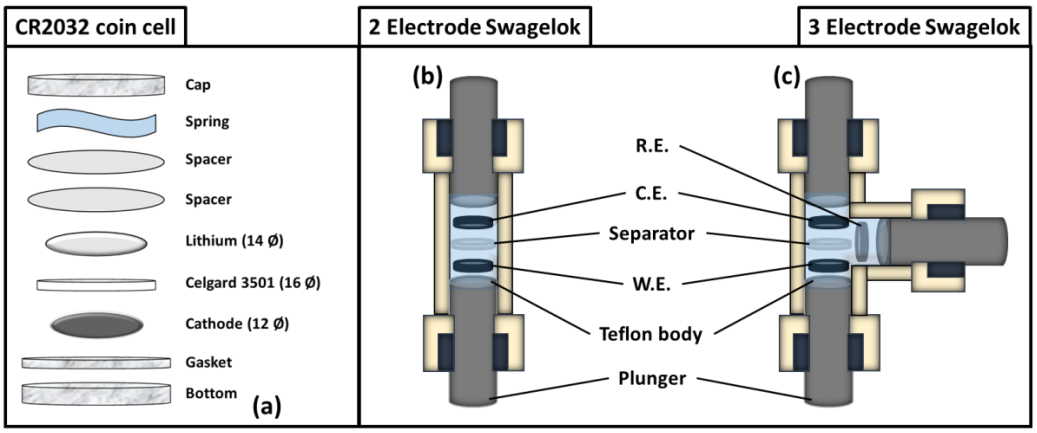


***Scheme AII.5.*** *Representation of different cell parts in CR2032 coin cells (**a**); and two (**b**) and three (**c**) electrodes Swagelok-type cells.*

For $NaO_2$ batteries, a pressurized Swagelok-type cell with an entry for gases was used (**Scheme AII.6a**). Since geometrical disposition of the electrodes in the cell has a great influence when performing EIS measurements [10]. EL-cells were used for this purpose, since a homogenous distribution of the current is guaranteed thanks to the coaxial ring-shaped reference electrode (**Scheme AII.6b**). In all the cases, cells were assembled inside an Ar-filled glovebox.

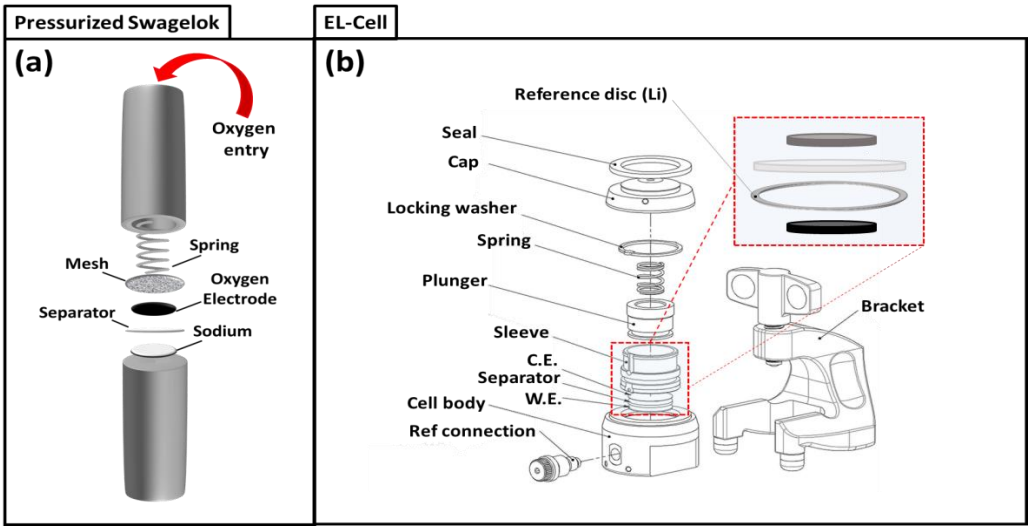


***Scheme AII.6**. Set up of a pressurized Swagelok-type cell (**a**) and an EL-cell (**b**).*

In **Section 2.2**., CR2032 type coin cells were assembled using lithium discs (Ø= 14 mm) as counter and reference electrode and graphene-sulfur materials as working electrodes (Ø= 12 mm). Celgard 3105 (Ø= 16 mm) was used as separator and a 1 M solution of LiTFSI, in a 1:1 (v/v) mixture of DME/DOL containing 2 wt.% $LiNO_3$ as electrolyte. The sulfur/electrolyte ratio was optimized to 1/20 for this kind of composites. Electrochemical measurements were carried out using a Maccor 4000 series potentiostat. The working electrodes were galvanostatically cycled between 2.6 V and 1.7 V vs $Li^+$/Li. EIS measurements were carried out in an EL-cell at the fully charged state over frequency ranges from 200 kHz to 10 mHz with a BioLogic VMP3 station. Specific and areal capacity values are referred to the mass of elemental sulfur in the electrodes. The same procedure was followed in **Section 2.3.**, but in this case a 1/30 sulfur/electrolyte ratio was stablished.

In **Chapter III**, pressurized 2-electrode Swagelok-type cell were assembled using a sodium metal anode (Ø= 12 mm) and graphene-based materials as oxygen electrode (Ø= 12 mm). The electrolyte was a 0.1 M $NaClO_4$ in DME solution prepared in the glove box with final water content below 20 ppm, determined by C20 Karl Fisher coulometer (Mettler Toledo). DME was dried over molecular sieves (3 Å) for one week and $NaClO_4$ under vacuum at 80 °C for 24 h prior to electrolyte preparation. Before the assembly of the cell, graphene-based electrode and Celgard H2010 separators (Ø= 13 mm) were

soaked overnight in 150 µl of electrolyte. After the assembly, cells were pressurized with pure oxygen to ~1 atm before the electrochemical measurements. Galvanostatic measurements were performed with a potential cut-off between 1.8 to 3.2 V vs $Na^+/Na$ in a BioLogic VMP3 station.

In **Chapter IV**, AC-based electrodes (Ø= 11 mm) were assembled in a two-electrode Swagelok-type cell as working and counter/reference electrodes (symmetric configuration). AC-based electrodes were also evaluated in a three-electrode Swagelok-type cell using an oversized Norit (Kuraray) disc as counter electrode and a silver wire as reference electrode ($Ag/Ag^+$). Whatman D-type glass fiber discs (Ø= 13 mm) were used as separator, while 1M $Et_4N\ BF_4$ (Sigma Aldrich, ≥99.0%) in acetonitrile, EMIN $BF_4$ (Sigma Aldrich, ≥99.0%) and EMIN TFSI (Solvionic, 99.9%) were chosen as electrolytes. Electrochemical impedance spectroscopy (signal amplitude 10 mV, frequency range 1 MHz-10 mHz), cyclic voltammetry and galvanostatic charge-discharge measurements were performed in a multichannel VMP3 generator from Biologic.

In **Chapter V**, HC-based electrodes (Ø= 11 mm) were assembled in a two-electrode Swagelok-type cell using a lithium disc (Ø= 10 mm) as counter and reference electrode. Galvanostatic charge/discharge measurements were carried between 0.002 and 2.0 V *vs.* $Li/Li^+$. AC-based electrodes were evaluated in a three-electrode Swagelok-type cell using an oversized Norit disc (Ø= 11 mm) as counter electrode and a lithium disc (Ø= 10 mm) as reference electrode. Galvanostatic charge/discharge measurements and cyclic voltammetries were carried between 1.5 and 4.2 V *vs.* $Li/Li^+$. AC-based electrodes were also evaluated in a symmetric configuration using a two-electrode Swagelok-type cell. Galvanostatic charge/discharge and CV measurements for EDLCs were performed within the 0-2.7 V cell voltage range. Before the assembly of the LIC, hard carbon electrode was pre-lithiated in a two electrode Swagelok-type cell using lithium metal disc as counter and reference electrode. The pre-lithiation process involved 5 charge/discharge cycles at 0.1 C between 0.002 and 2.0 V *vs.* $Li/Li^+$, an then a slow discharge at 0.025 C from 2.0 V to 0.2 V. LICs were assembled using the pre-lithiated HC as battery-type counter electrode *vs.* an AC as the capacitive-type working electrode in three-electrode Swagelok-type cell using metallic lithium as reference electrode. HC potential was set to 0.2 V *vs.* $Li/Li^+$ and AC was charged up to 4.2 V *vs.* $Li/Li^+$. Galvanostatic charge/discharge measurements for the LIC were performed within the 1.5-4.2 V cell voltage range in a multichannel VMP3 generator

from Biologic. Whatman D-type glass fibers discs (Ø= 13 mm) in diameter and 1 M $LiPF_6$ in 1:1 in volume of ethylene carbonate (EC) and dimethyl carbonate (DMC) were used as separator and electrolyte, respectively in all the measurements. Specific capacity and current density values were calculated with respect to the total mass of active material.

In **Table AII.1** are summarized the most relevant set-up parameters employed for the construction of the studied energy storage devices.

***Table AII.1.*** *Most relevant set-up parameters for the construction of the studied energy storage devices.*

| Technology | Type of Cell | Electrolyte | Evaluation | Electrode preparation | Binder | Current Collector |
|---|---|---|---|---|---|---|
| Li-S batteries | CR2032 | 1M LiTFSI in DME/DOL with 2 wt.% $LiNO_3$ | Half Cell (Vs. Li) | Lamination* | PVDF | Carbon coated Al |
| | | | | Self-standing aerogel** | None | None |
| Na-$O_2$ batteries | Pressurized Swagelok | 0.1M $NaClO_4$ in DME | Half Cell (Vs. Na) | Self-standing aerogel | None | None |
| Electric Double Layer Capacitors | Swagelok | 1M $Et_4N$ $BF_4$/ACN<br>EMIN $BF_4$<br>EMIN TFSI | Full Cell (AC vs. AC) | Self-standing film | PTFE | None |
| Lithium-ion Capacitors | Swagelok | 1M $LiPF_6$ in EC/DMC | Full Cell (AC vs. HC) | Lamination | PVDF | Al (AC)<br>Cu (HC) |

*Section 2.2, **Section 2.3

## AII.2.2. Cyclic Voltammetry

Cyclic Voltammetry is a powerful technique to evaluate the existence of redox processes, reaction mechanisms or intermediate reactions in electrochemical cells. When performing a CV, a lineal change in the electric potential (mV $s^{-1}$) is imposed to the cell between certain voltage ranges, generating a current which is measured. The potential change as a function of time is usually called “scan rate”. Voltammograms usually represents the generated current (Y-axis) versus the voltage of the cell (X-axis). Essential information regarding the nature of the electrochemical processes can be attained from the intensity of the current generated, and most importantly, from the shape of the voltammogram. In the case of faradaic materials, a peak in the voltammogram is observed due to the appearance of an electrochemical reaction at a

certain voltage. On the other hand, ideal capacitive-type materials show rectangular shaped curves due to the formation of the EDL.

In this thesis, CV was employed for the initial evaluation of the electrochemical performance of EDLCs. For example, the stable operational voltage window in each electrolyte was determined by this technique. This is possible since rectangular shaped voltammograms are attained for capacitive-type materials, but when electrolyte starts to decompose, a gradual increase in the current is observed [11]. Moreover, current axis of the voltammograms can be easily expressed in terms of electrodes specific capacitance ($C_e$ = F $g^{-1}$) by:

$$C_e = 2 \cdot \frac{I}{V_{scan\,rate} \cdot m_{act}} \qquad \textbf{(}\boldsymbol{AII.5}\textbf{)}$$

Where $V_{scan\ rate}$ is the applied scan rate in mV $s^{-1}$, $m_{act}$ is the mass of active material in the electrode in grams and I correspond to the measured current in amperes. By applying progressively faster scan rates, the variation in the shape of the voltammograms can give a clear idea about the resistivity of the system towards the formation of the EDL. In order to exactly extract the capacitance value from CV measurements in three-electrode cells, the next formula was applied:

$$C_e = \int \frac{I \cdot dE}{V_{scan\,rate} \cdot m_{act}} \qquad \textbf{(}\boldsymbol{AII.6}\textbf{)}$$

Where *I* is the instant current, *E* is the instant working potential and $V_{Scan\ rate}$ is the applied scan rate in millivolts per second.

### AII.2.3. Galvanostatic Charge/Discharge Measurements

In galvanostatic measurements a fixed current is applied and change in potential with time is recorded. Curves describing the variation of the potential *vs.* time allow calculating the stored charge, the capacity, the capacitance, the specific energy and power from the working electrode or the overall device. This electrochemical technique has been employed in this thesis for all the evaluated systems.

In the case of batteries, charge/discharge overpotential, voltage hysteresis, specific capacity and coulombic efficiency are calculated from the galvanostatic curves.

Charge/discharge overpotential is the difference between the theoretical reaction voltage, calculated from list standard potentials, and the practical potential measured in the cell. In an idealized case, charge and discharge should take place at the same potential. However, due to internal resistance and various polarizations, charge and discharge may present a difference in potential for the same reaction. This difference between charge potential and discharge potential is usually called as "voltage hysteresis". Specific capacity ($C_g$ = mAh $g^{-1}$) is calculated by multiplying the time for the reaction to occur (service life) to the fixed current density applied.

$$C_g = \left(\frac{A}{g}\right) \cdot (h) = \frac{Ah}{g} \qquad \textbf{(AII.7)}$$

Coulombic efficiency is the ratio between charge and discharge capacity. CE is often an indication of the loss of capacity per cycle and thus an important parameter for predicting the battery life [12]. Moreover, monitoring CE evolution is useful to evaluate the appearance of irreversible process, such as the formation of the SEI.

Galvanostatic measurements were also applied to capacitive-type devices to extract their specific capacitance, energy and power density values. Applied current density values were calculated on the basis of the total mass of active material in the electrodes. Specific capacitance values of the two electrode symmetric cells were calculated from the discharge galvanostatic plots, following the equation:

$$C_e = 2 \cdot \frac{I_g \cdot t_d}{\Delta V} \qquad \textbf{(\textit{AII.8})}$$

where $t_d$ and $\Delta V$ are the discharge time and the operational voltage window, respectively, once the total resistance drop is subtracted. Gravimetric energy ($E_g$) and power densities ($P_g$) were calculated according to the following equations:

$$E_g = \frac{1}{3.6}\left[\frac{1}{8} C_g \cdot (V_{Max}^2 - V_{Min}^2)\right] \qquad \textbf{(\textit{AII.9})}$$

$$P_g = \frac{E_g}{t_d} \qquad \textbf{(}\boldsymbol{AII.10}\textbf{)}$$

where $V_{Max}$ and $V_{Min}$ are the maximum and the minimum of the cell potential, once discarded the corresponding resistance drop.

## AII.2.4. Electrochemical Impedance Spectroscopy

Electrochemical impedance spectroscopy (EIS) measures the impedance (Z) of a system with a small alternating current potential applied over a range of frequencies. It can reveal the electrochemical processes in an electrode material such as electron transfer mass transport or diffusion processes. Data obtained by EIS can be expressed graphically in a Nyquist plot where the real part of impedance is represented on the X-axis and the imaginary part on the Y-axis of a chart. The experimental impedance diagrams fit mathematically to the representation of an equivalent electrical circuit, thus the profile can be decomposed in parameters with physical sense.

# Appendix III. Contributions

## Publications

During this PhD a total of thirteen articles were published in indexed Q1 journals. Impact factor (IF) of the journals was updated in January 2022.

**1-** **J. L. Gómez-Urbano**, J. L. Gómez-Cámer, C. Botas, N. Díez, J. M. López del Amo, L. M. Rodríguez-Martínez, D. Carriazo, T. Rojo. *Hydrothermally reduced graphene oxide for the effective wrapping of sulfur particles showing long term stability as electrodes for Li-S batteries.* Carbon. 139 (**2018)** 226-233. (IF: 7.794).

**2-** M. Enterría, C. Botas, **J. L. Gómez-Urbano**, B. Acebedo, J. M. López del Amo, D. Carriazo, T. Rojo, N. Ortiz-Vitoriano. *Pathways towards high performance Na-O2 batteries: tailoring graphene aerogel cathode porosity & nanostructure.* Journal of Materials Chemistry A. 6 **(2018)** 20778-20787. (IF: 10.721).

**3-** N. Díez, M. Qiao, **J. L. Gómez-Urbano**, C. Botas, D. Carriazo, M. Magdalena-Titirici. *High density graphene–carbon nanosphere films for capacitive energy storage.* Journal of Materials Chemistry A. 7 **(2019)** 6126-6133. (IF: 11.301).

***4-*** **J. L. Gómez-Urbano**, J. L. Gómez-Cámer, C. Botas, T. Rojo, D. Carriazo**.** *Graphene oxide-carbon nanotubes aerogels with high sulfur loadings suitable as binder-free cathodes for high performance lithium-sulfur batteries.* Journal of Power Sources. 412 **(2019)** 408-415. (IF: 8.247).

**5-** Z. Zhao, G. Tian, A. Sarapulova, G. Melinte, **J. L. Gómez-Urbano**, C. Li, S. Liu, E. Welter, M. Etter, S. Dsoke. *Mechanism Study of Carbon Coating Effects on Conversion-Type Anode Materials in Lithium-Ion Batteries: Case Study of ZnMn2O4 and ZnO–MnO Composites.* ACS applied materials & interfaces. 11 **(2019)** 29888-29900. (IF: 8.491).

**6-** G. Moreno-Fernández, **J. L. Gómez-Urbano**, M. Enterría, T. Rojo, D. Carriazo. *Flat-shaped carbon-graphene microcomposites as electrodes for high energy supercapacitors.* Journal of Materials Chemistry A. 7 **(2019)** 14646-14655. (IF: 11.301).

**7-** **J. L. Gómez-Urbano**, M. Enterría, I. Monterrubio-Santín, I. Ruiz de Larramendi, D. Carriazo, N. Ortiz-Vitoriano, T. Rojo**.** *An Overview of Engineered Graphene-based Cathodes: Boosting Oxygen Reduction and Evolution Reactions in Lithium and Sodium Oxygen Batteries.* ChemSusChem. 13 **(2020)** 1203-1225. (IF: 8.928).

**8-** **J. L. Gómez-Urbano**, G. Moreno-Fernández, M. Arnaiz, J. Ajuria, T. Rojo, D. Carriazo. *Graphene-coffee waste derived carbon composites as electrodes for optimized lithium ion capacitors.* Carbon 162 **(2020)** 273-282. (IF: 9.594).

**9-** G. Moreno-Fernández, **J. L. Gómez-Urbano**, M. Enterría, R. Cid, J. M. López del Amo, R. Mysyk, D. Carriazo. *Understanding enhanced charge storage of phosphorus-functionalized graphene in aqueous acidic electrolytes.* Electrochimica Acta. 361 **(2020)** 136985. (IF: 6.215).

**10-** M. Enterría, **J. L. Gómez-Urbano**, J. M. Munuera, S. Villar-Rodil, D. Carriazo, J. I. Paredes, N. Ortiz-Vitoriano. *Boosting the performance of graphene cathodes in Na-$O_2$ batteries by exploiting the multifunctional character of small biomolecules.* Small. 14 **(2021)** 2005034. (IF: 13.281).

**11-** **J. L. Gómez-Urbano**, G. Moreno-Fernández, M. Granados-Moreno, T. Rojo, D. Carriazo. *Optimized graphene-cigarrette filter derived carbon composites as electrodes for high voltage supercapacitors.* Batter. Supercaps **(2021)**. (IF: 7.093).

**12-** G. Moreno-Fernández, M. Granados-Moreno, **J. L. Gómez-Urbano**, D. Carriazo. *Phosphorus-functionalized graphene for power and cyclability improved lithium-ion capacitors.* Batteries and Supercaps. 4 **(2021)** 469-478. (IF: 7.093).

**13-** M. Granados-Moreno, G. Moreno-Fernández, R. Cid, **J.L. Gómez-Urbano**, D. Carriazo, *Microstructured nitrogen-doped graphene-Sn composites as a negative electrode for high performance lithium-ion hybrid supercapacitors*. Sustain. Energy Fuels. Online version available **(2022)** (IF: Not available).

## Oral presentations

The following works were presented as oral presentations in conferences:

**1-** **J. L. Gómez-Urbano**, J. L. Gómez-Cámer, C. Botas, N. Díez, L. M. Rodríguez-Martínez, D. Carriazo, T. Rojo. High sulfur loading graphene composites as cathodes for Li-S batteries. *Carbon 2018, Madrid, Spain (International).*

**2-** **J. L. Gómez-Urbano**, J. L. Gómez-Cámer, C. Botas, N. Díez, L. M. Rodríguez-Martínez, D. Carriazo, T. Rojo. The role of graphene-based materials in Li-S batteries. *Graphene Week 2018, Donostia, Spain (International).*

**3-** **J. L. Gómez-Urbano**, J. L. Gómez-Cámer, C. Botas, N. Díez, L. M. Rodríguez-Martínez, D. Carriazo, T. Rojo. El papel del grafeno en las grafeno en las baterías litio-azufre. *Multimat 2019, Granada, Spain (National).*

**4-** **J. L. Gómez-Urbano**, J. L. Gómez-Cámer, C. Botas, N. Díez, T. Rojo, D. Carriazo. High Sulfur loading graphene composites as self-standing cathodes for advanced Li-S batteries. *Power Our Future 2019, Vitoria-Gasteiz, Spain (International).*

**5-** **J. L. Gómez-Urbano**, J. L. Gómez-Cámer, C. Botas, N. Díez, T. Rojo, D. Carriazo. Graphene-based self-standing composites as promising candidates as cathodes for Li-S batteries. *Graphene Week 2019, Helsinki, Finland (International).*

**6-** **J. L. Gómez-Urbano**, J. L. Gómez-Cámer, C. Botas, N. Díez, T. Rojo, D. Carriazo. El papel del grafeno en las baterías del futuro. *VII Jornadas Doctorales G9 2019, Logroño, Spain (National).*

**7-** **J. L. Gómez-Urbano**, G. Moreno-Fernández, M. Arnaiz, J. Ajuria, T. Rojo, D. Carriazo. El papel del grafeno en la preparación de electrodos avanzados para su aplicación en condensadores híbridos de doble capa. *QIES* 2022, Sevilla, Spain (National).

# Co-author conferences

The following works with participation of the PhD candidate were presented in conferences:

**1-** G. Moreno-Fernández, **J. L. Gómez-Urbano**, M. Enterría, D. Carriazo. Electrodos de carbono funcionalizados con fosfatos para supercondensadores de alta energía. *Multimat 2018, Granada, Spain (National, oral presentation).*

**2-** G. Moreno-Fernández, **J. L. Gómez-Urbano**, M. Enterría, D. Carriazo. Lamellar-shaped carbon-graphene composites as electrodes for high energy supercapacitors. *Graphene Conference 2019, Rome, Italy (International, oral presentation).*

**3-** G. Moreno-Fernández, **J. L. Gómez-Urbano**, M. Enterría, D. Carriazo. Carbon graphene microcomposites for high energy supercapacitors. *Power Our Future 2019, Vitoria-Gasteiz, Spain (International, poster).*

**4-** G. Moreno-Fernández, **J. L. Gómez-Urbano**, M. Enterría, D. Carriazo. Flat-shaped carbon-graphene microcomposites for high energy supercapacitors. *LeStadium Conference 2020, Tours, France (International, oral presentation).*

**5-** M. Enterría, **J. L. Gómez-Urbano**, J. M. Munuera, J. I. Paredes, S. Villar-Rodil, D. Carriazo, A. Martínez-Alonso, J. M. Díez-Tascón, N. Ortiz-Vitoriano. The use of nucleotides for the sustainable manufacture of high-performing graphene cathodes for NaO2 batteries. *ISE Conference 2020, Online congress (International, poster).*

# Appendix Bibliography

[1] R. Terzano, M.A. Denecke, G. Falkenberg, B. Miller, D. Paterson, K. Janssens, Recent advances in analysis of trace elements in environmental samples by X-ray based techniques (IUPAC Technical Report), Pure Appl. Chem. 91 (2019) 1029–1063. https://doi.org/10.1515/pac-2018-0605.

[2] L. Lin, X. Bi, Y. Gu, F. Wang, J. Ye, Surface-enhanced Raman scattering nanotags for bioimaging, J. Appl. Phys. 129 (2021) 191101. https://doi.org/10.1063/5.0047578.

[3] J.-B. Wu, M.-L. Lin, X. Cong, H.-N. Liu, P.-H. Tan, Raman spectroscopy of graphene-based materials and its applications in related devices, Chem. Soc. Rev. 47 (2018) 1822–1873. https://doi.org/10.1039/C6CS00915H.

[4] M. Sethi, H. Bantawal, U.S. Shenoy, D.K. Bhat, Eco-friendly synthesis of porous graphene and its utilization as high performance supercapacitor electrode material, J. Alloys Compd. 799 (2019) 256–266. https://doi.org/10.1016/j.jallcom.2019.05.302.

[5] F. Fu, L. Lin, E. Xu, Functional pretreatments of natural raw materials, in: Adv. High Strength Nat. Fibre Compos. Constr., Elsevier, 2017: pp. 87–114. https://doi.org/10.1016/B978-0-08-100411-1.00004-2.

[6] F. Rouquerol, Adsorption by powders and porous solids : principles, methodology and applications, Academic P, 2013.

[7] E.Y.H. Keng, Air and helium pycnometer, Powder Technol. 3 (1969) 179–180. https://doi.org/10.1016/0032-5910(69)80070-7.

[8] B. Reif, S.E. Ashbrook, L. Emsley, M. Hong, Solid-state NMR spectroscopy, Nat. Rev. Methods Primer. 1 (2021) 2. https://doi.org/10.1038/s43586-020-00002-1.

[9] Nicole Gleichmann, SEM frente a TEM, 2020. http://www.news-courier.com/analysis/articles/sem-vs-tem-331262 (accessed April 10, 2021).

[10] S. Klink, E. Madej, E. Ventosa, A. Lindner, W. Schuhmann, F. La Mantia, The importance of cell geometry for electrochemical impedance spectroscopy in three-electrode lithium ion battery test cells, Electrochem. Commun. 22 (2012) 120–123. https://doi.org/10.1016/j.elecom.2012.06.010.

[11] D. Weingarth, H. Noh, A. Foelske-Schmitz, A. Wokaun, R. Kötz, A reliable determination method of stability limits for electrochemical double layer capacitors, Electrochimica Acta. 103 (2013) 119–124. https://doi.org/10.1016/j.electacta.2013.04.057.

[12] W. Wang, X. Wei, D. Choi, X. Lu, G. Yang, C. Sun, Electrochemical cells for medium- and large-scale energy storage, in: Adv. Batter. Medium Large-Scale Energy Storage, Elsevier, 2015: pp. 3–28. https://doi.org/10.1016/B978-1-78242-013-2.00001-